Spectropolarimetric behaviour of a selection of high-energy blazars

Joleen Barnard

Submitted in fulfillment of the requirements for the degree
Magister Scientiae
in the Faculty of Natural and Agricultural Sciences
Department of Physics
The University of the Free State
South Africa

Submission date: 30 November 2022

Supervised by: Prof. B. van Soelen, Department of Physics

The financial assistance of the National Research Foundation (NRF) towards this research is hereby acknowledged. Opinions expressed and conclusions arrived at, are those of the author and are not necessarily to be attributed to the NRF.

Abstract

Blazars form part of the jetted class of Active Galactic Nuclei (AGN), with a relativistic jet closely aligning to the observer's line of sight. Due, in part, to this viewing angle, these sources are characterised by Doppler-boosted emission across the entire electromagnetic spectrum that is variable on timescales from years down to minutes. These are some of the most numerous extragalactic γ-ray sources, dominated by polarised non-thermal emission produced by relativistic leptons and/or hadrons moving within the jet-component. Blazars are subdivided into two categories: BL Lac-type objects (BLLs), and Flat-Spectrum Radio Quasars (FSRQs). They are classified based on the presence/absence and equivalent widths of optical spectral features, as well as the location of their synchrotron peak frequencies. Blazar SEDs are characterised by two broad, non-thermal components, along with an underlying thermal contribution at optical/ultraviolet wavelengths due to the accretion disc, host galaxy, and broad-line region of the blazar. However, the nature and origin of the non-thermal, high-energy emission remains unclear, as it can be reproduced by two different models, each assuming different particle populations and emission regions that produce the emission. Polarimetry provides a unique diagnostic tool to probe the polarisation signatures of the emission at optical wavelengths. The investigation of the polarisation of blazar emission aides in constraining the particle populations and acceleration mechanisms responsible for the non-thermal emission at lower energies, and constraining the high-energy emission and polarisation. It also places constraints on the accretion disc component and mass of the supermassive black hole, and sheds light on the structure of the jet's magnetic field. Here, an optical spectropolarimetric study of a selection of high-energy blazars was undertaken. The aims of this project was to: first, investigate the change in the degree of polarisation from high to low states, second, monitor the evolution of polarisation in BLLs and FSRQs over a long period of time, and last, investigate overall trends in the behaviour of the sample of blazars, and compare it to what has been found in other population studies. To achieve these goals, optical spectropolarimetric observations were taken of eighteen blazars (six BLLs and twelve FSRQs) using the Southern African Large Telescope (SALT), complemented by optical photometric data from the Las Cumbres Observatory (LCO), and γ-ray data from the *Fermi* Large Area Telescope (LAT). For the population of blazars investigated, it was found that FSRQs tend to reach higher degrees of polarisation than BLLs during high states. More regular occurrences of high states and a wider range of polarisation levels were observed for FSRQs. For both BLLs and FSRQs, the average degree of polarisation was higher while the γ-ray fluxes were still on the rise than while it was decreasing to a lower state. In agreement with what was found by the RoboPol monitoring campaign, the degree of polarisation showed no clear correlation with the γ-ray luminosity or redshift of the source, but showed a significant anti-correlation with the location of the synchrotron peak frequency ($\nu_{\rm sy}$) of the sources. Two sources with noteworthy results were AP Lib and PKS 1510–089. For AP Lib, long-term variations in the optical and γ-ray fluxes were detected, with the same behaviour mirrored in the degree of polarisation, but lagging by ~ 54 days. PKS 1510–089 was observed multiple times in 2022, during an unprecedented low-state in which the non-thermal emission from the jet diminished completely. This project serves as a good basis for further investigation of blazar polarisation, both in optical/ultraviolet and X-ray/γ-ray regimes.

Key words: galaxies: active, Galaxy: nucleus, quasars: supermassive black holes, BL Lacertae objects: general, quasars: general, polarisation, techniques: photometric, techniques: polarimetric, techniques: spectroscopic

Acknowledgements

I hereby acknowledge and express my sincere gratitude to the following parties for their valuable contributions:

- The National Research Foundation: for their financial assistance towards this research. Opinions expressed and conclusions arrived at, are those of the author and are not necessarily to be attributed to the NRF.
- The Department of Physics at the University of the Free State: for the opportunity to conduct this research.
- The South African Astronomical Observatory: Some of the observations reported in this paper were obtained with the Southern African Large Telescope (SALT) under program 2021-2-LSP-001 (PI: D.A.H. Buckley) and program 2019-2-MLT-001 (PI: B. van Soelen).
- My colleague and dear friend Natalie Matchett: for six years of companionship, without whom I would not have been able to do this.
- Prof. P.J. Meintjies: for the years of support and encouragement to pursue my research.
- My supervisor and mentor, Prof. Brian van Soelen: for his guidance, support and trust in my work during the completion of this study, as well as the countless opportunities which he has granted me.
- My father in law: for the hours of reading my work, without whose love and encouragement I would not have been able to complete this study.
- My parents and my sister: for their unconditional love, support and countless sacrifices they have made for me over the years.
- My loving husband, Barend: for everything that I cannot put into words.

"The heavens tell of the glory of God; And their expanse declares the work of His hands." - Psalm 19:1

Contents

List of Acronyms

3FGL	Third *Fermi* Gamma-ray LAT source catalogue
4FGL	Fourth *Fermi* Gamma-ray LAT source catalogue
4LAC	Fourth LAT AGN Catalogue
AGN	Active Galactic Nuclei
APASS9	AAVSO Photometric All-Sky Survey
BBB	Big Blue Bump
BCU	Blazar Candidates of an Unknown type
BH	Black Hole
BLL	BL Lac-type objects
BLR	Broad-Line Region
CCD	Charge-Coupled Device
CDF	Cumulative Distribution Function
CMB	Cosmic Microwave Background
DCF	Discrete Correlation Function
EC	External Compton
EVPA	Electric Vector Polarisation Angle
FoV	Field of View
FR-I	Fanaroff–Riley class I
FR-II	Fanaroff–Riley class II
FSRQ	Flat-Spectrum Radio Quasar
GBM	Gamma-ray Burst Monitor
GL	Gamma-ray Loud
GQ	Gamma-ray Quiet
GUI	Graphical User Interface
HBL	High synchrotron-peaked BL Lac-type object
HESS	High Energy Stereoscopic System
HRS	High Resolution Spectrograph
HSP	High Synchrotron-Peaked

IBL	Intermediate synchrotron-peaked BL Lac-type object
IC	Inverse Compton
IR	Infrared
ISM	Interstellar Medium
ISP	Intermediate Synchrotron-Peaked
IXPE	Imaging X-ray Polarimetry Explorer
LAT	Large Area Telescope
LBL	Low synchrotron-peaked BL Lac-type object
LCO	Las Cumbres Observatory
LCR	Light Curve Repository
LSP	Low Synchrotron-Peaked
NED	NASA Extragalactic Database
NLR	Narrow-Line Region
ODR	Orthogonal Distance Regression
PI	Principle Investigator
QSO	Quasi-Periodic Oscillation
Quasar	Quasi-stellar radio source
RMHD	Relativistic Magnetohydrodynamics
RSS	Robert Stobie Spectrograph
SAAO	South African Astronomical Observatory
SALT	Southern African Large Telescope
SED	Spectral Energy Distribution
SMBH	Supermassive Black Hole
SSC	Synchrotron-Self Compton
ToO	Target-of-Opportunity
TS	Test Statistic
UV	Ultraviolet
VHE	Very High Energy

Chapter 1

Introduction

What drives the formation and evolution, as well as what the structure of galaxies emitting vast amounts of radiation from a small central region is, are pivotal questions in the study of galactic cores. These sources have a long and complicated history. It was first proposed that these central active cores of galaxies, or Active Galactic Nuclei (AGN), are powered by the accretion of material onto a central, supermassive black hole (SMBH) in the 1960s (Lynden-Bell, 1969; Lynden-Bell and Rees, 1971; Salpeter, 1964; Zel'dovich and Novikov, 1964). Today, this model is widely accepted, as it explains much of the observed phenomena of AGN. The study of AGN is an important facet of astrophysics, as it presents a unique astrophysical laboratory to study accretion phenomena and relativistic jet physics in an environment that cannot be reproduced on Earth.

AGN are detected in nearly every wavelength regime (radio to γ-ray bands), with large energy outputs across the electromagnetic spectrum and variability on short timescales (Beckmann and Shrader, 2012b). This led to a myriad of different types of AGN being reported over the years, leading to a "zoo" of different AGN being identified, as seen in Figure 1.1. In an attempt to unify all the different flavours of AGN, a unified model has been developed, in which the observed type of AGN is determined mainly by three parameters, namely the orientation of the AGN with respect to an observer, the presence or absence of a relativistic jet, and the accretion rate of material onto the central SMBH. In the unified model, all AGN broadly have the same underlying physical structure: a central SMBH, an accretion disc, broad- and narrow-line regions, dusty torus, and (in some cases), a strong, collimated, relativistic jet.

Blazars form part of the jetted class of AGN, with the relativistic jet closely aligning with the observer's line of sight. Due to the presence of the jet, the observed emission from blazars is highly Doppler boosted, characterised by rapid, multi-wavelength outbursts/flares occurring on timescales from years down to seconds in extreme cases (see e.g. Albert et al., 2007, on the second-scale variability of Mrk 501). The bulk of the emission originates from within the jet-component, and the resulting emission is, by definition, non-thermal and polarised in nature, consisting of a lower- and higher energy contribution, with an underlying thermal (unpolarised) contribution from other components of the galaxy superimposed at optical/UV wavelengths (Böttcher, 2019). For a more detailed discussion on AGN and blazars see, for example, Beckmann and Shrader (2012b); Boettcher et al. (2012), and Shields (1999).

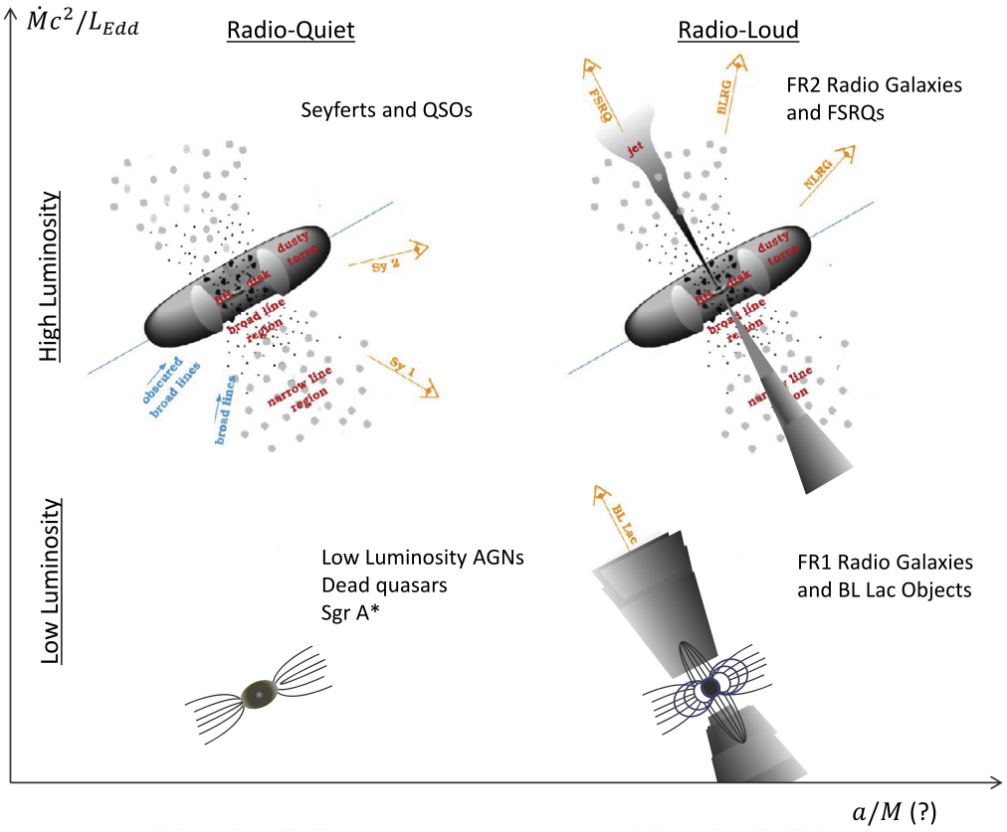

Figure 1.1: A cartoon illustration of the types of active galaxies – the so-called AGN zoo – in an attempt at unification based on accretion rate and black-hole rotation. Figure adopted from Dermer and Giebels (2016).

However, the problem remains that the precise origin and nature of the non-thermal, high-energy emission in blazars is still unclear, as it can be reproduced by two different models, each assuming different particle populations and emission regions that produce the emission (see e.g. Böttcher et al., 2017; Mannheim, 1993; Zhang, 2019, for a discussion on leptonic and hadronic models). Since there still exists so much uncertainty in the nature and origin of the particle population producing the observed radiation, disentangling blazar emission is a challenge not yet fully met. Consequently, there is a gap in the knowledge and understanding of blazars, their jets, and accretion mechanisms, and since no two blazars behave in exactly the same way, models are unable to fully explain the behaviour of the blazar population as a whole.

To bridge this gap, polarimetry can be used to disentangle the thermal, unpolarised and non-thermal, polarised emission in the optical/UV wavelength regime. This will aide in constraining the particle population and acceleration mechanisms responsible for the non-thermal emission at lower energies, and potentially constrain the high-energy emission as well (Schutte et al., 2022). The polarisation signatures of blazars will also allow for constraints to be indirectly placed on the SMBH-mass and the structure and evolution of the jet's magnetic field.

This project is an optical spectropolarimetric study of a selection of high-energy blazars, with the aims of a) investigating the change in the polarisation as blazars transition from high/flaring states to low/quiescent states, b) monitoring the evolution of polarisation in different types of blazars over a longer period of time, c) determining the

overall trends in the behaviour of the selected blazars, and d) investigating the possible link between blazars and radio galaxies and how polarisation can be included in the study of astrophysical jets in future work. This will address the problem of understanding the physics of AGN jets.

The study was undertaken by performing both photometric and spectropolarimetric observations of blazars in the optical regime, using the Las Cumbres Observatory (LCO) Telescope Network and the Southern African Large Telescope (SALT), respectively. Observations were done in two different ways. The first was to investigate sources during various states of activity, requiring two SALT spectropolarimetric observations (a low-state and high-state observation). The second was to investigate some blazars over a longer period, which required multiple SALT spectropolarimetry observations to track the changes in the polarisation over time. To complement the spectropolarimetric observations, optical photometric lightcurves from the LCO Telescope Network, and long-term γ-ray lightcurves were taken from the publicly available *Fermi* Large Area Telescope (LAT) to investigate the change in the optical and γ-ray fluxes around the period of the SALT observations.

The structure of this dissertation is as follows. Chapter 2 contains a literature review of the historical development of AGN-theory, the composition of AGN, the development of a unified model of AGN, and an outline of blazars and their classification, along with a discussion on the multifaceted nature of blazar emission and its underlying emission mechanisms. Chapter 3 provides a detailed discussion of the various observations performed on the selection of blazars reported in this text, including information on the telescopes and science instruments used, the data reduction processes, and the resulting data obtained from the various observational campaigns. Chapter 4 provides a brief literature review of selected sources of interest, along with the results from the observations outlined in the previous chapter. Thereafter, Chapter 5 discusses possible trends from the behaviour of the blazars investigated in this project as a whole. Chapter 6 provides concluding remarks on the results from this study, and how it can be improved upon in future work.

Appendix A includes the results of the blazars not discussed in detail in the main body of the text. The research done in the duration of this study has been presented at several local and international conferences, and the conference proceedings published so far are shown in Appendix B.

Chapter 2

Active Galactic Nuclei

In this chapter, the historical development of the theory of Active Galactic Nuclei will be briefly discussed in Section 2.1, along with an outline of the main components of Active Galactic Nuclei and how they fit into a unified model in Section 2.2. The last section will focus on blazars and their observational signatures (Section 2.3).

2.1 Historical Development of AGN-Theory

Extragalactic Astronomy

In the known universe, there are an estimated 2×10^{12} galaxies within the observable limits. Of all of these galaxies, only about 1% can be classified as Active Galactic Nuclei (AGN) by the presence of an additional emitting component in its centre (i.e. more than just stellar related contributions). These sources are some of the most exotic and violent sources in the extragalactic sky, characterised by the production of high luminosities in a small emitting region, as well as extreme underlying physics that produces the observed emission (Urry and Padovani, 1995). However, many of the physical mechanisms that produce the non-thermal emission of these energetic sources are still unclear. Here, the historical development of the theory of AGN is briefly summarised, which, for the purposes of this dissertation, will mainly focus on the development in the optical wavelength regime. For a more detailed discussion see, for example, Beckmann and Shrader (2012b, pp. 1–9) and Shields (1999).

The idea of extragalactic astronomy dates back to the 18th century, with the likes of philosophers Immanuel Kant and Thomas Wright, introducing the concept of *island universes* (Kant, 1755), which are observed nebulae that do not form part of the Milky Way Galaxy (Wright, 1750). This was the first time our understanding of the universe expanded beyond the Milky Way Galaxy (Pigatto, 2005). These island universes were observed as "fixed stars", or faint, disc-like nebulae. However, at the time, it was largely accepted that these nebulae were of a Galactic origin and some, in fact, are (for example globular clusters and planetary nebulae). Hence, an argument for extragalactic nebulae seemed far-fetched at the time, and proper arguments for it were difficult to produce.

Unfortunately, for many years, these insights into the extragalactic nature of some "nebulae" were practically forgotten, until François Arago called the attention of astronomers back to Immanuel Kant and his idea of extragalactic island universes in 1854

(Arago and Barral, 1854). At this time great strides were made observationally, with the emergence of large catalogues of the so-called nebulae (see e.g. Dreyer, 1888; Herschel, 1864, 1785). In addition to Galactic nebulae, these catalogues also listed strange nebulae, with redshifts indicating velocities greater than the escape velocity of the Milky Way (Slipher, 1913), implying that they might have an extragalactic nature.

The argument over the galactic or extragalactic nature of these nebulae reached its peak in the April of 1920, when H.D. Curtis and H. Shapley entered the famous "Great Debate" (Pigatto, 2005). In this debate, hosted by the National Academy of Science in Washington, D.C., the existence of other galaxies was discussed, with Shapley arguing for nebulae as part of the Milky Way, and Curtis leaning towards an extragalactic interpretation. In the end, neither viewpoints won, and the debate served only to highlight the issues, rather than solve the dilemma (Beckmann and Shrader, 2012b). The debate was only settled some years later, when Edwin Hubble detected Cepheid variable stars in M31 and M33, two nearby spiral "nebulae" (Hubble, 1926). From the absolute brightness of these Cepheids, he was able to determine their distance from the Earth, and that M31 and M33 must be extragalactic, with stars similar to that of the Milky Way Galaxy (Heckman and Best, 2014). With this, the scene for extragalactic astronomy was set.

Active Galaxies

In 1909, Edward A. Fath found that most spiral nebulae had continuous spectra with stellar absorption lines, indicating that the emission was formed by a collection of unresolved extragalactic stars. However, one of the nebulae he observed, NGC 1068, had a composite spectrum displaying both emission and absorption lines (Carroll and Ostlie, 1996). The composite spectrum of NGC 1068 was confirmed in 1917 by Vesto M. Slipher, and Edwin Hubble was able to show a similar result for two other galaxies in 1926 (Shields, 1999). Then, in 1943, almost 20 years after the existence of extragalactic sources was proven, Carl Seyfert found the first evidence that some galaxies display an additional emitting, stellar-type component in their centres (Beckmann and Shrader, 2012b; Shields, 1999). He took spectrograms of six of the brightest galaxies and found that broad, high-excitation nuclear emission lines were superimposed on the typical (G-type) absorption spectra (Seyfert, 1943). This led to the coining of the term *Seyfert Galaxies*, which are characterised by these high-excitation nuclear emission lines (Shields, 1999).

Concurrently, significant progress was made in radio astronomy, leading to Grote Reber publishing a map of the radio sky at 160 MHz. This showed that some of the *local maxima* present in the radio-sky map were in fact discrete extragalactic sources, like Cygnus A (Reber, 1944). Some of these local maxima would later be connected to Seyfert Galaxies; a crucial step for the development of AGN-theory (Padovani et al., 2017). Hence, correlating radio-sources with optical counterparts was at the forefront of astronomy in the 1940s and 1950s, and many surveys and catalogues were produced, highlighting the nature of extragalactic nebulae in both wavelength bands. These surveys made it clear that the emission was non-thermal in nature, with synchrotron processes being the main driver in the radio-band. During this time, it was also discovered that some of these *radio galaxies* showed evidence of strong magnetic fields, with a double-lobed structure surrounding its centre (Shields, 1999). Studies of the spectra of radio galaxies led to the discovery that some of these sources were star-like, and showed broad emission lines at

very high redshifts. These are the so-called "quasi-stellar radio sources", or *quasars* for short (Kellermann, 2015; Schmidt, 1963; Shields, 1999).

One of the first proposals was that the emission of quasars could be reproduced by a large cluster of stars. However, the central 100 pc of the galaxies would have to have an accumulated mass of a few $\times 10^8\,\mathrm{M}_\odot$ (Woltjer, 1959). Hoyle and Fowler suggested that, instead, there resided a hypermassive, stellar-type object driven by accretion processes from a disc surrounding it (Hoyle and Fowler, 1963), but this hypothesis was not able to fully explain the immense amounts of energy emitted from these sources. Finally, it was put forward that instead of a stellar-type object, the nucleus contained a *Supermassive Black Hole* (SMBH) at their centre, with an accretion disc surrounding it (Lynden-Bell, 1969; Lynden-Bell and Rees, 1971; Salpeter, 1964; Zel'dovich and Novikov, 1964). The model suggesting that active galactic nuclei housed an accreting SMBH at its centre is a powerful one, as it explains not only the large energy output across multiple wavelength bands, but also the small emitting region and the short variability timescales (Beckmann and Shrader, 2012b).

By the 1960s, radio to optical observations of AGN were well established, while X-ray and γ-ray astronomy was still in the early stages of its development. Today, high-energy observations are at the forefront of AGN studies, and for a review of the development of X-ray and γ-ray astronomy of AGN see, for example, Bassani and Dean (1983), Degrange and Fontaine (2015), and Dermer and Giebels (2016). These historical events, along with many more, led to immense progress in both the observational and theoretical understanding of AGN, and AGN became part of typical astronomical terminology. In a short period of time, AGN became a prominent field of research in astrophysics, as it allows for the study of accretion phenomena, thermal and non-thermal emission mechanisms, and relativistic jet physics.

2.2 Towards a Unified Model of AGN

As has already been mentioned, AGN are highly luminous objects emitting across the entire electromagnetic spectrum from a very small region. Since AGN are detected in nearly every wavelength/energy regime (from the radio to the γ-ray band), a significant, and ever increasing, number of AGN-types have been recorded. This led to a number of different "flavours" with different characteristics being identified – from Seyfert Galaxies and quasars/quasi-stellar objects (QSOs) to narrow- and broad-line radio galaxies and blazars (Urry and Padovani, 1995). This made it very challenging to form a unified theory of AGN.

In order to create "order out of chaos", many attempts at unification and identifying the various components within AGN were undertaken by, for example, Antonucci and Miller (1985), Osterbrock (1993a), Antonucci (1993), and Urry and Padovani (1995). By the end of the 20th century, the basic structure of AGN was known, and it was generally accepted that AGN are split into two main classes, namely radio-loud AGN, and radio-quiet AGN (Antonucci, 1993). However, the picture was – and still is – far from complete, as their intrinsic rarity, the precise nature of the SMBH, dominant accretion mechanisms, origin and presence/absence of collimated jets, nature and morphology of the dust torus,

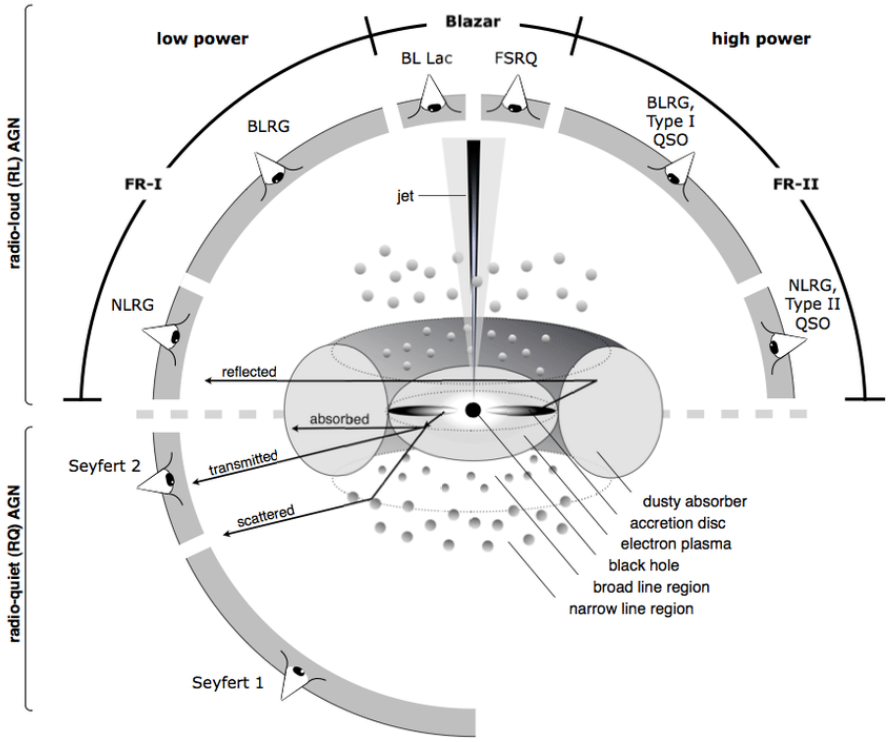

Figure 2.1: A schematic representation of the unified model of AGN. The diagram is separated into two main sub-classes: radio-loud AGN, and radio-quiet AGN. The radio-loud class comprises AGN with a prominent jet structure present, and the radio-quiet class consists of AGN with a negligible or non-existent jet-component. From this figure, it is evident that the observer's line of sight also plays a significant role in AGN classification. Figure adopted from Beckmann and Shrader (2012b).

etc. are still open issues (see e.g Beckmann and Shrader, 2012a; Böttcher, 2019; Padovani, 2017a; Zhang, 2019, for a detailed overview of unanswered questions in AGN studies).

It is now accepted that, despite of the different appearances across the electromagnetic spectrum, all AGN have the same basic underlying physical structure and nature. This *Unified Model* is shown in Figure 2.1 (Osterbrock, 1993a,b). This structure is axisymmetric, with components aligning to the central axis along the jet. Below follows a brief discussion on some of the main individual components of the unified model, as well as the effect each component has on the observational features.

Central Supermassive Black Hole

At the centre of all AGN ($10^{-7} - 10^{-3}$ pc), there is an actively accreting central SMBH ($M > 10^5\,\mathrm{M}_\odot$), driven by a continuous supply of material (Netzer, 2015; Padovani et al., 2017). This process of accretion onto the central SMBH is the main driver of an AGN's large energy output (Ho, 2008). In general, black holes (BHs) have two defining traits, namely mass and spin, and both of these traits play a crucial role in the observational features of AGN.

The bolometric luminosity of an AGN is (in part) proportional to the mass of the central SMBH. Therefore, the luminosity is often characterised in terms of the Eddington ratio $L_{\mathrm{AGN}}/L_{\mathrm{Edd}}$ where L_{Edd} is the Eddington luminosity; the maximum luminosity

a body can have and still remain in pressure equilibrium. The Eddington luminosity is $\approx 1.3 \times 10^{38} M_{\rm BH}/{\rm M}_{\odot}$ erg s^{-1}. However, because the emission from AGN is not necessarily isotropic, super-Eddington luminosities have been reported for some sources (Castelló-Mor et al., 2016).

The spin, or angular momentum, of the SMBH affects the inner radius of the accretion disc of the AGN, as a rapidly spinning SMBH may have an accretion disc extending closer towards it than a non-rotational SMBH of similar mass (Padovani et al., 2017). For AGN to conserve total angular momentum, the SMBH has to be rotating (from the Kerr Metric), which impacts the radiative efficiency and accretion rate of the accretion disc, and, therefore, affects the emission of the AGN as a whole.

Accretion Disc

Material from the outer regions of the AGN is accreted onto the SMBH through an accretion disc that is generally modelled by an optically thick (but geometrically thin) type disc as in the Shakura and Sunyaev (1973) model. Note that there are many different accretion disc models of varying optical and geometrical characteristics, but it is beyond the scope of this dissertation to discuss these in detail (see e.g. Yuan and Narayan, 2014). The accretion of matter onto the SMBH converts gravitational potential energy to electromagnetic radiation through viscous and turbulent processes (Urry and Padovani, 1995).

The radiation originating from the disc is thermal as it is produced by the loss of angular momentum via viscous heating/radiation processes through the rotationally dominated inflow of material onto the SMBH (Carroll and Ostlie, 1996; Netzer, 2015). The accretion disc produces continuum emission at optical, ultraviolet (UV), and soft X-ray wavelengths (Urry and Padovani, 1995), and is observed as the "big blue bump" (BBB), an underlying thermal component in the typical spectral energy distribution of AGN (e.g. Shang et al., 2005).

Broad-Line Region

The broad-line region (BLR) is located between the SMBH's accretion disc and the inner ring of the dust torus (0.01−1 pc), and this is where the strong, kinematically broadened emission lines observed in the optical/ultraviolet (UV) wavelength regimes are produced (Netzer, 2015; Urry and Padovani, 1995). It is one of two identified regions of ionised gas in the structure of AGN (Bennert et al., 2002). The BLR consists of a collection of individual, high density clouds of turbulent photoionised gas moving at high velocities $\geq$1000 km s^{-1} (Padovani et al., 2017). The produced emission lines are broadened by the motion of the high velocity gas clouds (Kollatschny and Zetzl, 2013). It is likely formed by the evaporation of dust from the dusty torus surrounding the central engine, and the material spirals inwards to later form part of the accretion disc (Gaskell, 2009).

The BLR emits both high-ionisation and low-ionisation broad emission lines that are typically emitted in the optical regime (e.g. high-ionisation He II, He I, O VI, and low-ionisation Mg II, Ca II, O I, Fe II, respectively, along with H I Balmer lines). The broad emission lines provide an aide in estimating the masses of the central SMBHs, since the

motions in the BLR are predominantly Keplerian, and therefore, directly related to the BH mass (Tran, 2003). It has been found that the BLR has a flattened structure with cylindrical symmetry (Gaskell, 2009). Thus, due to obscuration from the dust torus, the BLR is not visible in all AGN, which is part of the reason why different classes of AGN are observed.

Dust Torus

Surrounding the accretion disc and BLR is the dust torus, extending from 0.1 – 10 pc from the central SMBH (Netzer, 2015). Depending on the inclination angle, it can completely obscure the central SMBH, accretion disc and BLR (Antonucci, 1993; Urry and Padovani, 1995). At high inclination angles, the radiation from the central region of the AGN is absorbed by the dust torus, and re-emitted as continuum emission in the infrared (IR) wavelength regime (Mor et al., 2009).

The structure, shape and kinematics of dust tori in AGN are still uncertain and complex – since it is not a fixed structure universal to all AGN, but can vary from AGN type to AGN type (Padovani et al., 2017). The structure and dust distribution in the torus vary from smooth to clumpy, and the underlying kinematics vary from static to in- or outflowing models (Padovani et al., 2017). However, recent reviews indicate that most AGN tori are thick, clumpy, and axisymmetric structures that surround the accretion disc and SMBH (see Netzer, 2015, for a full review).

Narrow-Line Region

The second region of ionised gas and dust in the AGN structure is the narrow line region (NLR). It is located just beyond the dust torus, extending out to hundreds of parsecs beyond the torus (Netzer, 2015). It is a conical, symmetrical structure due to the so-called "ionisation cones" caused by escaping photons being funneled by the dust torus encircling the accretion disc (Osterbrock, 1993b). The NLR is a universal optically thin component in the AGN structure, that scales with photoionisation (luminosity-size) from Seyfert galaxies to quasars (Bennert et al., 2002).

The NLR is where the narrow emission lines observed in optical AGN spectra are produced. It consists of low density ionised gas and dust, moving at relatively low velocities from approximately 300 to 1000 km s^{-1} (Padovani et al., 2017). The most prominent emission lines produced in the NLR are the forbidden [O III] and [N II] lines, along with the H_α line (Bennert et al., 2002). The dust in the NLR can also greatly contribute to the infrared continuum (Bennert et al., 2002; Netzer, 2015).

Radio Jet

For a few AGN (less than 10% Netzer, 2015), strong, highly collimated jets, generally occurring at the poles of the disc/torus are produced (Urry and Padovani, 1995). The expulsion of energetic particles in a collimated stream – or jet – is common in any instance where matter accretes onto a central object, and becomes relativistic when the central

object is compact, like a neutron star, stellar-mass black hole, or SMBH (Romero et al., 2017). In AGN, these relativistic jets are the main energy transport mechanism from the SMBH outward, and produce highly Doppler-boosted non-thermal emission that can range from the radio to the γ-ray energy regimes. The emission from the jet is highly variable across the electromagnetic spectrum, with no apparent periodicity (Romero et al., 2017). However, much about the jets in AGN is still poorly understood, as the jet formation, magnetic fields, radiation mechanisms, and population of particles producing the non-thermal emission are still unclear. Jet-physics remains one of the main fields of research in the field of radio-loud AGN (Beckmann and Shrader, 2012a; Romero et al., 2017).

Host Galaxy

Current research indicates that there are no "standalone" supermassive black holes, i.e. all SMBHs reside at the centre of a galaxy (Beckmann and Shrader, 2012a). Therefore, the effects of the host galaxy on the central engine of AGN, and vice versa, cannot be ignored. The type of AGN observed is dependent on the type of the host galaxy, e.g. elliptical galaxies host AGN with strong radio jets, and gas-rich spiral galaxies host AGN with weak or no radio jets (Urry and Padovani, 1995). It is now known that a SMBH exists in almost all galactic bulges and, provided the central SMBH is not dormant, AGN are observable from all types of galaxies (Beckmann and Shrader, 2012a; Heckman and Best, 2014; Urry and Padovani, 1995). Due to the symbiotic relationship between the host galaxy and the SMBH, AGN play a critical role in the formation and evolution of galaxies, as the AGN phenomenon forms part of the typical lifespan of galaxies (Best et al., 2005; Heckman and Best, 2014). One of the main observational effects the host galaxy has on the study of AGN, is that there is a selection effect, or observational bias, tending towards higher-luminosity AGN. Hence, there is an intrinsic uncertainty in the population of faint AGN (Padovani et al., 2017).

Evidently, AGN are by no means simple objects – they have a complex, composite structure, exhibiting a wide array of diverse observational features across the electromagnetic spectrum. Yet, however complex the classification of AGN might become, in the unification of AGN, there are only three main parameters that determine the type of AGN that is observed: the orientation of the AGN, or viewing/inclination angle of the observer; the presence or absence of a relativistic jet; and the accretion rate of material onto the central SMBH.

From this, and from the basic components of AGN, all of the various AGN classes can be typified into a single, unified model as represented in Figure 2.1. As mentioned before, AGN can be split into two main classes, radio-loud and radio-quiet. However, there is a push to change the nomenclature from radio-loud/radio-quiet to something more accurate and descriptive of the physical scenario, as radio-loudness is a vague and inaccurate naming scheme, kept only for its historical importance (Padovani, 2017b). Therefore, from hereon out, we will refer to jetted AGN, and non-jetted AGN. Then, following from the unified model in Figure 2.1, Seyfert 1 and 2 type AGN are non-jetted (radio-quiet) sources, whereas blazars are jetted (radio-loud) AGN (Mor et al., 2009).

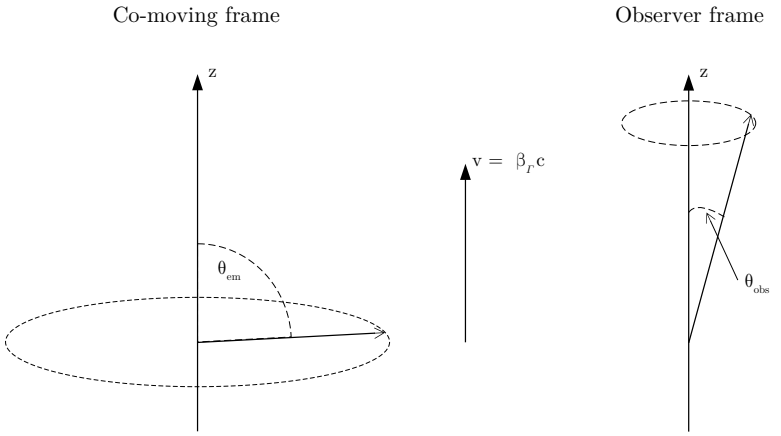

Figure 2.2: The viewing geometry of an AGN jet in the co-moving (left) and observer (right) frames, with the jet-component in the z-direction. Figure adapted from Boettcher et al. (2012).

2.3 Blazars

As shown in Figure 2.1, blazars form part of the jetted class of AGN, with a jet-component closely aligning with the observer's LOS (with a viewing angle of $\theta_{\rm obs} \lesssim 15-20^{\circ}$, Padovani et al., 2017). These jets are highly collimated, relativistic outflows that extend outward to kiloparsec or megaparsec scales (Zhang, 2019). The observed non-thermal emission is highly Doppler boosted and, therefore, highly luminous, and extends across a wide range of energies (radio to γ-ray). At an angle $\theta_{\rm obs}$ (in the observer frame) with respect to the line of sight, the frequency emitted from a region moving with a bulk Lorentz factor of $\Gamma \equiv (1-\beta_{\Gamma}^{2})^{-\frac{1}{2}}$, at speed $v = \beta_{\Gamma} c$, will be Doppler boosted by a factor of:

$$\nu = \delta \nu^{'}, \tag{2.1}$$

where $\delta = (\Gamma[1-\beta_{\Gamma}\cos\theta_{\rm obs}])^{-1}$ is the Doppler factor. The observed luminosity will be Doppler boosted by:

$$L_{\nu} = \delta^{3} L^{'}_{\nu^{'}}, \tag{2.2}$$

and the observed flux of the emission will be Doppler boosted by a factor of:

$$F_{\nu} = \delta^{3} F^{'}_{\nu^{'}}, \tag{2.3}$$

while any timescale variability in the observed emission will be shortened by:

$$t = \delta^{-1} t^{'}. \tag{2.4}$$

In Equations (2.2) – (2.4), the primed quantities are in the co-moving frame and the unprimed quantities are in the observer frame (see Figure 2.2 exhibiting the viewing geometry of blazars; Böttcher, 2019).

Blazars are rare sources, since only about 10% of all AGN can be classified as jetted sources. Of these, it is often stated that only one in every 100 000 is a blazar. Despite the intrinsic scarcity of blazars, as seen by the *Fermi*-LAT, the relativistic beaming effects of

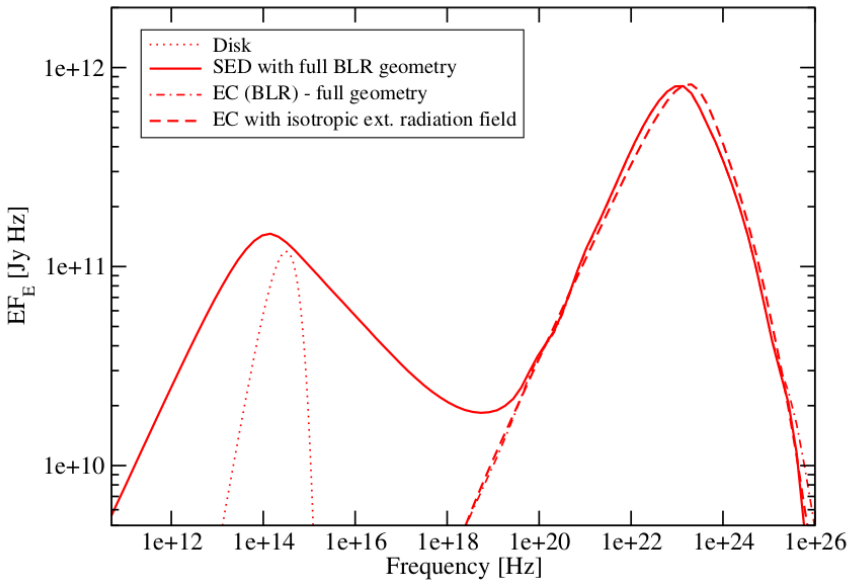

Figure 2.3: A generic SED model for typical blazar emission, indicating various contributions that led to the characteristic double-humped spectrum. Figure adapted from Böttcher et al. (2013).

the jet-emission make them the most numerous and brightest extragalactic γ-ray sources in the universe, as well as the most extreme type of known AGN (according to the *Fermi*-LAT 4FGL 8-year source catalogue, blazars formed $> 98\%$ of the observed AGN population; Ackermann et al., 2015; Böttcher, 2019). Blazars are characterised by extreme, rapid variability in both flux and polarisation, with the emission varying throughout the electromagnetic spectrum on timescales from years down to minutes, with high-energy outbursts, or "flares" occurring at seemingly random intervals (Beckmann and Shrader, 2012b; Marscher, 2013). These flares are generally observed in multiple wavelength bands, but in some instances, so-called *orphan flares* have been observed, in which the flare is only observable in one wavelength band (e.g. Błażejowski et al., 2005).

2.3.1 Spectral Energy Distributions of Blazars

The broad-band continuum spectral energy distributions (SEDs) of blazars are dominated by non-thermal emission radiating from the jet-component (Böttcher, 2019). They display a characteristic double-humped, composite structure as shown in Figure 2.3, consisting of a low-energy and high-energy component.

The low-energy component extends from radio to optical/UV frequencies, but can sometimes extend into the soft X-ray frequencies (Zhang, 2019). It is generally accepted that this component is produced by leptonic synchrotron emission from relativistic electrons in the jet, and that the emission is intrinsically polarised. The lower-energy component of blazar SEDs also has an underlying thermal contribution at infrared-UV wavelengths due to emission originating in the accretion disc, dusty torus, BLR, and host galaxy itself. Hence, the low-energy component is a superposition of both thermal and non-thermal contributions, leading to the highly variable degree of polarisation in blazars, as the dominance of the non-thermal, polarised synchrotron contribution fluctuates with jet-activity (Böttcher et al., 2017).

The high-energy component of blazar SEDs spans the X-ray to γ-ray wavelength bands, and can be reproduced by two different models, generally referred to as the leptonic or hadronic models (Böttcher et al., 2013). In the leptonic scenario, it is assumed that any protons present in the jet have a negligible contribution, and the high-energy emission is produced by the inverse-Compton (IC) scattering of low-energy (soft) photons by the same population of relativistic electrons that produce the low-energy component (Boettcher, 2010; Böttcher et al., 2013; Degrange and Fontaine, 2015). In the leptonic scenario, the jet magnetic field strength is relatively low (mG to G levels), and the target photons that are upscattered can originate either within the jet itself, or from an external region (Zhang, 2019).

The photons originating in the jet are the direct result of the synchrotron emission producing the low-energy component, and are upscattered via IC processes (e.g. Bloom and Marscher, 1996; Maraschi et al., 1992). In this Synchrotron-Self Compton (SSC) scenario, the radio-optical/UV seed photons provided by the synchrotron emission are upscattered to X-ray and/or γ-ray frequencies (Beckmann and Shrader, 2012b; Rybicki and Lightman, 1985). When the target photons originate externally to the jet, this is known as External Compton (EC) emission. The photons can originate from a number of regions, for example, radiation from the accretion disc (the BBB) and the BLR could contribute optical, UV, and soft X-ray photons (Dermer and Schlickeiser, 1993; Dermer et al., 1997), and the dusty torus contributes infrared seed photons (Błażejowski et al., 2000). These seed photon fields, both external and from within the jet itself, produce the high-energy component of blazar SEDs in the leptonic scenario.

Leptonic models have been largely successful in recreating the high-energy component of the SEDs, as well as the spectral variability of blazars (e.g. Boettcher, 2010; Celotti and Ghisellini, 2008; Ghisellini et al., 1998). They are also successful in explaining the strong radio-γ-ray correlation, since both are produced by the same population of electrons (Lister et al., 2015). However, some blazars are characterised by extremely rapid TeV variability, and others are characterised by orphan flares, in which TeV γ-ray flares happen days before activity becomes apparent at lower energies (e.g. Aharonian et al., 2007; Albert et al., 2007; Błażejowski et al., 2000). These characteristics are difficult to explain with the standard leptonic model (Dermer and Giebels, 2016).

In the hadronic scenario, it is assumed that hadrons (i.e. protons and/or nuclei) are sufficiently accelerated to produce the high-energy emission via proton initiated synchrotron cascade emission and/or photomeson processes (photo-pion production; Mannheim, 1993; Zhang, 2019). To achieve this, the protons must be accelerated in a highly magnetised environment (several tens of G; Boettcher, 2010) to overcome the threshold for secondary particle production (Mannheim and Biermann, 1992). These secondary particles are neutral muons and mesons – generally pions (π^0) – that form high-energy γ-rays through pion-decay (Degrange and Fontaine, 2015).

These processes are able to explain the orphan flares, as well as the rapid very high energy (VHE $> 100\,\mathrm{GeV}$) variability of some blazars. It can also explain the detection of high-energy neutrinos (as seen in TXS 0506+056, Tanaka et al., 2017), pointing to the multi-messenger nature of blazars (e.g. Böttcher, 2019; Dermer and Giebels, 2016).

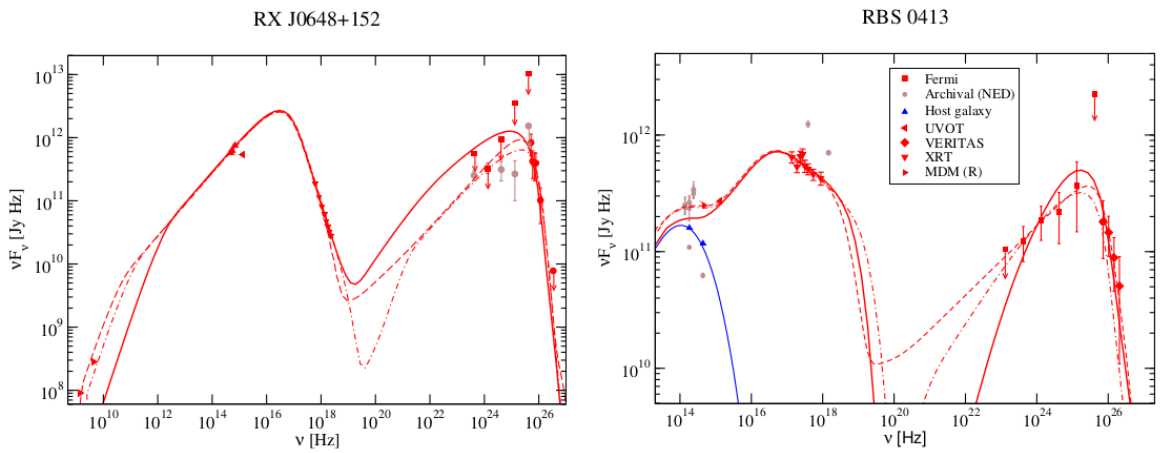

Figure 2.4: Modelling of the SEDs of two different blazars, RX J0648.7+1516 (left), and RBS 0413 (right), fitted with three different models. First, the solid curve was fitted with a leptonic SSC model. Second, the dot-dashed curve is a leptonic SSC + EC fit, and third, the dashed curve was fitted with a semi-analytical hadronic model. Figure adopted from Boettcher (2012).

However, the strong magnetic fields required to accelerate the protons to sufficiently high energies, is challenging (Zhang, 2019).

Due to the multitude of various contributing radiation components, uncertainty of the particle population, and acceleration mechanisms at high energies, disentangling blazar emission from the SEDs alone can be very challenging (Boettcher, 2010; Böttcher et al., 2017; Zhang, 2019). For example, as shown in Figure 2.4, the observed SEDs of some blazars can be well reproduced by both leptonic and hadronic models. However, since the low energy component is accepted to be produced by synchrotron processes, this provides a way of constraining the electron (leptonic) population of particles. Combined with polarisation, the thermal and non-thermal contributions at optical wavelengths can be disentangled. This not only allows for constraints on the SMBH-mass, but also more successful modelling of the high-energy component (see e.g. Schutte et al., 2022). When coupled with polarisation signatures of the emission at higher frequencies (X-ray and γ-ray), the optical – γ-ray connection can be explained, and will promote a better understanding of what produces the high-energy emission observed in blazars.

2.3.2 Blazar Classification and the Blazar Sequence

Even though all blazars broadly have the same properties, blazars can be further subdivided into two different classes, namely *BL Lacertae type objects* (BLLs) and *Flat-Spectrum Radio Quasars* (FSRQs). BLLs and FSRQs have some intrinsic differences, and can be classified based on a number of different features (Fossati et al., 1998).

Firstly, BLLs and FSRQs are classified based on the spectral features in their optical/UV spectra. The optical spectra of BLLs display a largely featureless continuum, with – in some cases – weak, narrow absorption features or weak emission lines with equivalent widths typically set at $|W_\lambda| < 5\,\text{Å}$. This indicates that the thermal contribution from the accretion disc, BLR, and dust torus is diminished due to the strong presence of the jet-component (Dermer and Giebels, 2016). Contrastingly, FSRQs tend to have strong, broad emission features with $|W_\lambda| > 5\,\text{Å}$ due to the BLR- and dust torus emission. Note

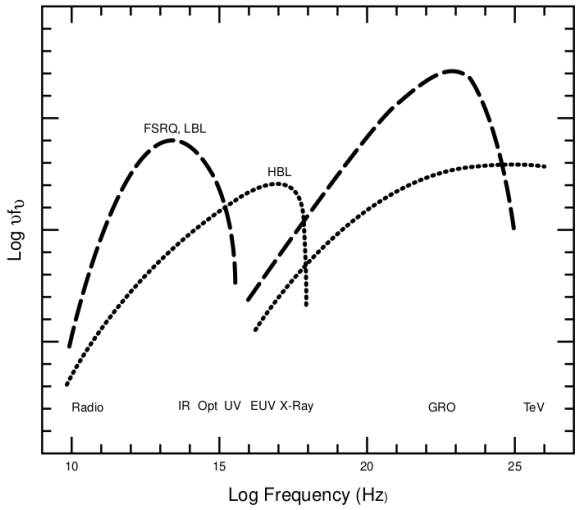

Figure 2.5: The SEDs of LSP and HSP blazars, with the shift in the synchrotron peak frequency from FSRQs to HBLs clearly visible. Figure taken from Urry (1998).

that, despite the practical application of the 5 Å dividing line, it is an arbitrary value that does not point to a physical distinction (Ghisellini et al., 2011; Meyer et al., 2011; Padovani and Giommi, 1995a,b). BLLs have weak or, in some cases, a total absence of spectral features. These spectral features often arise from the host galaxy itself, making BLLs hard to distinguish from normal galaxies. To distinguish BLLs from normal galaxies, the presence of a Ca II H/K break with a ratio < 0.4 is often used (Abdo et al., 2010b; Dermer and Giebels, 2016).

Secondly, blazars can be classified based on their flux variability over all wavelengths, γ-ray dominance, and photon indices, etc. For example, it is expected that FSRQs will be more variable than BLLs, with rapid outbursts or flares being a more regular occurrence in FSRQs than in BLLs (Boettcher, 2012). This is due to the suggested difference in the accretion discs of FSRQs and BLLs, as FSRQs have radiatively efficient (thin) accretion discs, leading to the radiation being dominated by External Compton emission, whereas BLLs have less radiatively efficient discs and therefore more synchrotron dominated emission (Ruan et al., 2012). A more detailed summary of the spectral properties and SEDs of blazars can be found in Abdo et al. (2010a,b).

Lastly, blazars (both BLLs and FSRQs) can be further subdivided based on the frequency at which the low-energy component peaks ($\nu_{\rm sy}$), as shown in Figure 2.5. The more luminous FSRQs generally have lower synchrotron peak frequencies than the less luminous BLLs. Thus, blazars can be divided into three different categories; *Low-Synchrotron-Peaked* (LSP) blazars, *Intermediate-Synchrotron-Peaked* (ISP) blazars, and *High-Synchrotron-Peaked* (HSP) blazars, as originally proposed by Padovani and Giommi (1995a). The population of LSP blazars consists of both FSRQs and low-frequency peaked BLLs, or LBLs, with $\nu_{\rm sy} < 10^{14}$ Hz, whereas ISP- and HSP blazars are mostly BLLs (IBLs, HBLs), with $10^{14} \leq \nu_{\rm sy} \leq 10^{15}$ Hz and $\nu_{\rm sy} > 10^{15}$ Hz, respectively (Böttcher et al., 2013; Rani et al., 2011). The different types of blazars can then be arranged as a continuous sequence: FSRQ $\rightarrow$ LBL $\rightarrow$ IBL $\rightarrow$ HBL.

The phenomenon connecting the location of $\nu_{\rm sy}$ to the observational signatures of

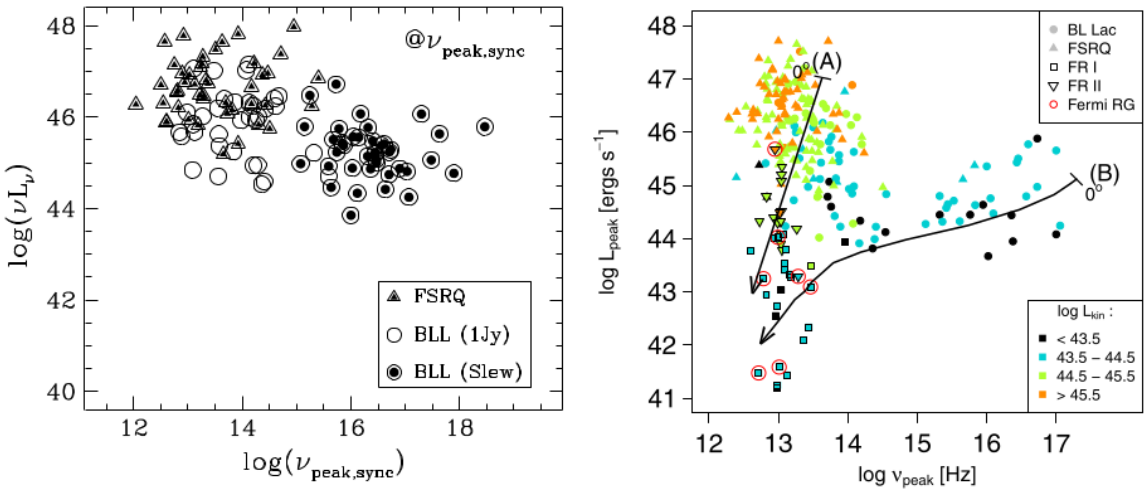

Figure 2.6: Two versions of the blazar sequence. The panel on the left shows the original blazar sequence as proposed by Fossati et al. (1998), consisting of a sample of 126 blazars. In contrast, the panel on the right shows a more recent version of the blazar sequence by Meyer et al. (2011), suggesting a blazar "envelope", rather than the original blazar "sequence".

blazars is known as the so-called *blazar sequence*. It was first pointed out by Fossati et al. (1998) as shown in the left panel of Figure 2.6, and was later reproduced by Ghisellini et al. (1998). Fossati et al. (1998) used a sample of 126 blazars (mostly LSP FSRQs and HSP BLLs), and found an anti-correlation between the observed bolometric luminosity and location of the synchrotron peak frequencies in different types of blazars; with increasing luminosity, ν_{sy} moves to lower frequencies. It was proposed by Ghisellini et al. (1998) that this could be due to the differences in the radiative cooling processes in FSRQs and BLLs, respectively.

Meyer et al. (2011) revisited the original blazar sequence, but with a much larger sample of BLLs and FSRQs at a wider range of observation angles (therefore including FR I and FR II radio galaxies).[1] From this, Meyer et al. (2011) showed that the "updated" blazar sequence forms an *L*-shaped envelope, contradicting the original sequence proposed by Fossati et al. (1998). This could also explain the "missing" ISP population in the blazar sequence, as ISPs are possibly just more misaligned versions of HSPs at similar jet powers (for a more detailed overview on the blazar sequence, see e.g. Dermer and Giebels, 2016; Meyer et al., 2011).

The blazar sequence may, therefore, point to an evolutionary track where blazars evolve from FSRQs, to HBLs, and might be due to intrinsic differences in the jet structure or SMBH's accretion mechanisms (e.g. Böttcher and Dermer, 2002). However, its existence and whether or not it points to a true evolutionary sequence or any intrinsic physical difference, is still widely debated. For example, the blazar sequence predicts HBLs should be more numerous than LBLs, but observationally, this is not the case. It might also be that the anti-correlation between the synchrotron peak frequency and observed power and the clear divide between BLLs and FSRQs based on ν_{sy}, is largely due to selection

[1] Radio galaxies (FR I and FR II type radio galaxies) are believed to be the misaligned counterparts of BLLs and FSRQs, respectively (see Figure 2.7; Fanaroff and Riley, 1974; Meyer et al., 2011; Urry and Padovani, 1995)

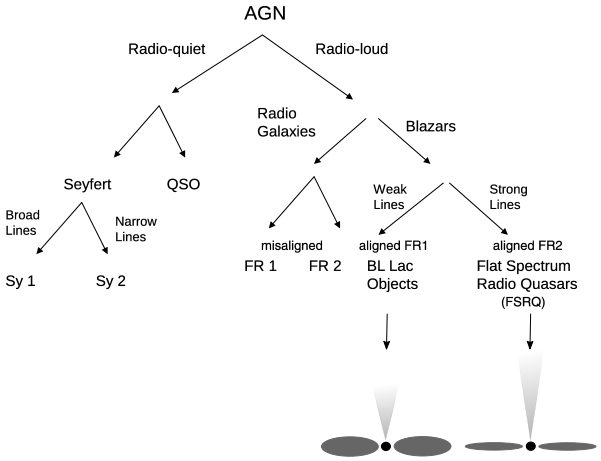

Figure 2.7: The dichotomy of AGN. Here the connection between blazars and Fanaroff-Riley (FR) radio galaxies is highlighted. It is believed that FR I radio galaxies are the misaligned counterparts of BLLs, and FR II radio galaxies are misaligned counterparts to FSRQs. This connection between blazars and FR radio galaxies provide a plausible explanation to the connection between the synchrotron peak frequency ($\nu_{\rm sy}$) and the jet kinetic power ($L_{\rm kin}$), as well as the missing population of ISPs in the blazar sequence. Figure adapted from Dermer and Giebels (2016).

effects (Padovani, 2007).

The above discussion about blazar SEDs and the widely debated blazar sequence implies that much of blazars is still unclear. It is evident that new ways of investigating them are required to gauge information from blazars to understand their SEDs and the way they evolve or link together. One of these improved means of investigating blazars, is the polarisation signatures in blazar emission. Polarisation can be used as an additional diagnostic tool to aide in disentangling the emission components and constraining the particle population responsible for producing said emission. *Polarimetry* is defined as the measurement of polarisation in electromagnetic radiation, and can be used to understand the underlying particle populations and acceleration mechanisms in blazars, as well as probe AGN jets, their magnetic field and the central SMBH (Zhang, 2019).

2.3.3 Optical Polarisation Signatures of Blazars

This section contains a brief introduction to the polarisation of electromagnetic waves, followed by the definition of synchrotron radiation and polarisation, and how it can be applied to the specific case of blazars. Lastly, there will be a brief discussion on the recent observational and theoretical progress in blazar polarimetry studies.

Polarisation

Following the discussion by Jackson (1975, pp. 202–207) and Rybicki and Lightman (1985, pp. 62–69), Maxwell's equations in a vacuum fully describes the electric ($\mathbf{E}$) and magnetic ($\mathbf{B}$) fields of plane electromagnetic waves (light). These are given by:

$$\begin{aligned} \bigtriangledown \cdot \mathbf{E} &= 0 && (2.5)\\ \bigtriangledown \cdot \mathbf{B} &= 0 && (2.6)\\ \bigtriangledown \times \mathbf{E} &= -\frac{1}{c}\frac{\partial \mathbf{B}}{\partial t} && (2.7)\\ \bigtriangledown \times \mathbf{B} &= \frac{1}{c}\frac{\partial \mathbf{E}}{\partial t}, && (2.8) \end{aligned}$$

where c is the speed of light in a vacuum. The **E**-field has a possible vector wave solution of the form:

$$\bigtriangledown^2 \mathbf{E} - \frac{1}{c^2}\frac{\partial^2 \mathbf{E}}{\partial t^2} = 0, \tag{2.9}$$

and, since Equations (2.5) to (2.8) are invariant under the transformation $\mathbf{E} \rightarrow \mathbf{B}$ and $\mathbf{B} \rightarrow -\mathbf{E}$, the **B**-field can have a similar wave solution:

$$\bigtriangledown^2 \mathbf{B} - \frac{1}{c^2}\frac{\partial^2 \mathbf{B}}{\partial t^2} = 0. \tag{2.10}$$

From this, it follows that the plane-wave solutions to Equations (2.9) and (2.10) have the form:

$$\begin{aligned} \mathbf{E}(\mathbf{r}, t) &= \hat{\varepsilon}_1 E_0 e^{i(\mathbf{k}\cdot\mathbf{r} - \omega t)} && (2.11)\\ \mathbf{B}(\mathbf{r}, t) &= \hat{\varepsilon}_2 B_0 e^{i(\mathbf{k}\cdot\mathbf{r} - \omega t)}, && (2.12) \end{aligned}$$

where $\hat{\varepsilon}_1$ and $\hat{\varepsilon}_2$ are constant real unit vectors, E_0, B_0 are the complex wave amplitudes at a time t, $\mathbf{k} = k\mathbf{n}$ is the wave vector, and $\omega = 2\pi\nu$ the angular frequency of the wave. From Equations (2.5) to (2.12) it is clear that the wave propagates in the direction **n**, and that the wave motion is transverse (i.e. perpendicular) to the direction of propagation, and that the electric **E** and magnetic **B** fields are always in-phase and perpendicular to one another.

For a more generalised solution, consider two electromagnetic waves oscillating in perpendicular directions. The observed electromagnetic radiation can be in various stages of polarisation. Since the magnetic field vector **B** is always perpendicular to the **E**, and has the same amplitude, we can consider only the electric field vectors to describe the general state of polarisation. For a given wave of **k** and ω, the electric field vector can be described by:

$$\mathbf{E}(\mathbf{r}, t) = (\hat{\varepsilon}_1 E_1 + \hat{\varepsilon}_2 E_2) e^{i(\mathbf{k}\cdot\mathbf{r} - \omega t)}, \tag{2.13}$$

where the complex wave amplitudes E_1 and E_2 are given by:

$$\begin{aligned} E_1 &= \mathcal{E}_1 e^{i\phi_1} && (2.14)\\ E_2 &= \mathcal{E}_2 e^{i\phi_2}, && (2.15) \end{aligned}$$

with real components:

$$\begin{aligned} E_{\varepsilon_1} &= \mathcal{E}_1 \cos(\omega t - \phi_1) && (2.16)\\ E_{\varepsilon_2} &= \mathcal{E}_2 \cos(\omega t - \phi_2). && (2.17) \end{aligned}$$

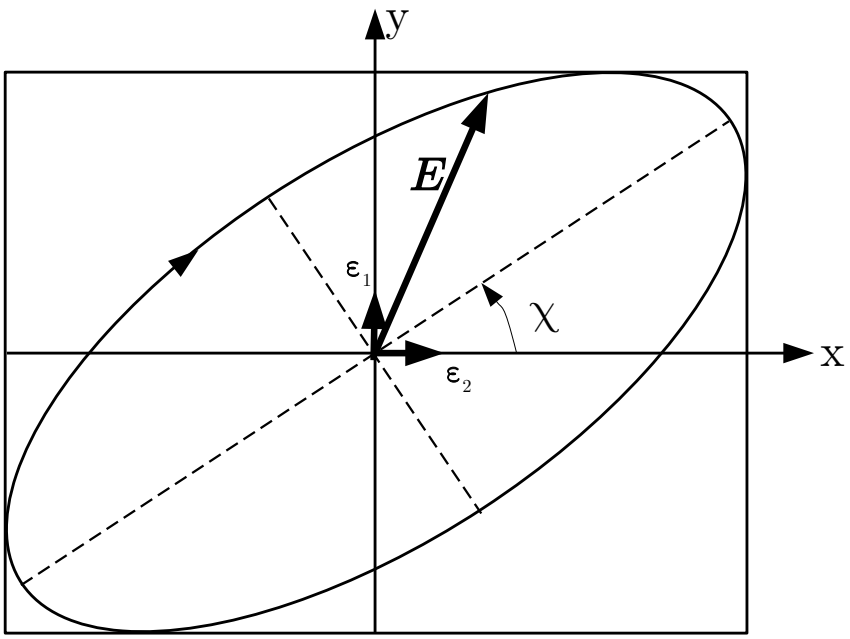

Figure 2.8: The polarisation ellipse tracing the rotation of the x and y components of an **E**-field vector through an angle χ. This defines the plane of rotation and the type of polarisation that an observer will see. Figure adapted from Jackson (1975); Rybicki and Lightman (1985).

The rotation of the electric field components described by Equations (2.13) to (2.17) traces out the *polarisation ellipse* as seen in Figure 2.8, implying that the general state of polarisation for electromagnetic waves is *elliptically polarised*.

Two special cases arise for the polarisation of electromagnetic waves. The first is where $\mathbf{E}_1$ and $\mathbf{E}_2$ have the same orientation (i.e. with a phase difference of $\phi = \phi_2 - \phi_1 = 0$), oscillating only in one plane. The observed emission for such a case will be *linearly polarised*. The second case is *circular polarisation*, when $\mathbf{E}_1$ and $\mathbf{E}_2$ have a phase difference of $\phi = \pi/2$. For any other phase difference ϕ, the polarisation is elliptical (Griffiths, 2013; Jackson, 1975). Elliptical and circular polarisation can be further defined by the "handedness" or direction of rotation as viewed by the observer (see the polarisation ellipse in Figure 2.8), as the rotation can be clockwise (right-handed) or counterclockwise (left-handed).

The polarisation of electromagnetic radiation can be described by the *Stokes parameters*. The Stokes parameters can be expressed in terms of the averaged product of the x and y components of the linearly combined **E**-field vectors of a beam of radiation (e.g. Landi Degl'Innocenti et al., 2007). For the general case of incoherent/partially polarised light, the Stokes parameters can be expressed as:

$$I(\omega) \propto [\langle \varepsilon_x(\omega)^* \varepsilon_x(\omega) \rangle + \langle \varepsilon_y(\omega)^* \varepsilon_y(\omega) \rangle] \tag{2.18}$$
$$Q(\omega) \propto [\langle \varepsilon_x(\omega)^* \varepsilon_x(\omega) \rangle - \langle \varepsilon_y(\omega)^* \varepsilon_y(\omega) \rangle] \tag{2.19}$$
$$U(\omega) \propto [\langle \varepsilon_x(\omega)^* \varepsilon_y(\omega) \rangle + \langle \varepsilon_y(\omega)^* \varepsilon_x(\omega) \rangle] \tag{2.20}$$
$$V(\omega) \propto [\langle \varepsilon_x(\omega)^* \varepsilon_y(\omega) \rangle - \langle \varepsilon_y(\omega)^* \varepsilon_x(\omega) \rangle], \tag{2.21}$$

or, when considering only the real components of the electric field vector, by:

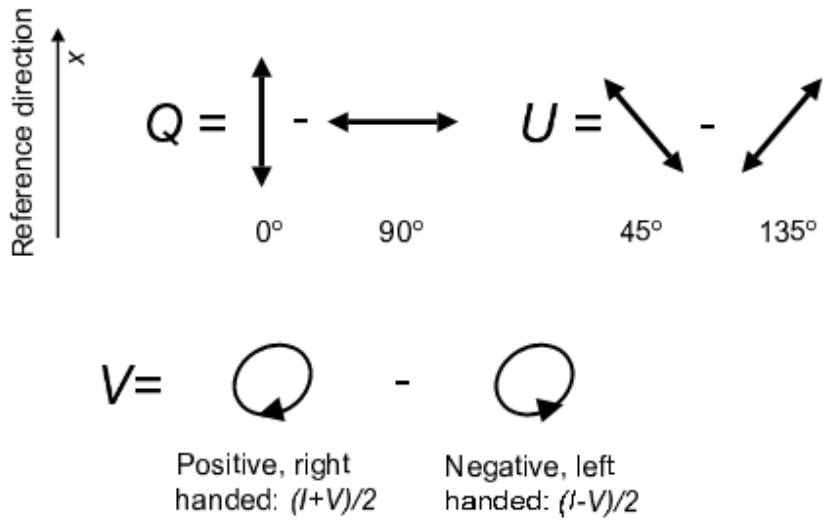

Figure 2.9: Visualisation of the definition of the Stokes Parameters Q, U, and V. Figure taken from Landi Degl'Innocenti et al. (2007).

$$I = \langle E_x^2 + E_y^2 \rangle \tag{2.22}$$
$$Q = \langle E_x^2 - E_y^2 \rangle \tag{2.23}$$
$$U = \langle 2E_x E_y \cos(\phi_y - \phi_x) \rangle \tag{2.24}$$
$$V = \langle 2E_x E_y \sin(\phi_y - \phi_x) \rangle, \tag{2.25}$$

where $\phi_y - \phi_x$ is the phase difference between E_x and E_y. Here, I represents the total intensity of the observed emission, Q is the difference between the **E**-fields oscillating along and perpendicular to the reference direction, U is the difference between the **E**-fields oscillating at 45° and 135° with respect to the reference direction, and lastly, V is defined as the difference between the right-handed and left-handed circular polarisation of the observed emission (see Figure 2.9).

Spectropolarimetry is defined as the measurement of the state of polarisation of light as a function of wavelength (Landstreet, 2015). Depending on the method of observation (see Section 3.1 for the full details of the SALT observations), it is possible to measure both linear and circular polarisation. However, in blazar emission the contribution of circular polarisation is negligible, and only the linear degree of polarisation is measured. Then, when performing linear spectropolarimetry, I gives the total intensity of the observed emission as a function of wavelength, and the degree of linear polarisation is given by:

$$P_{\rm L} = \sqrt{P_Q^2 + P_U^2}, \tag{2.26}$$

where $P_Q = Q/I$ and $P_U = U/I$ are the reduced Stokes parameters. The polarisation angle θ is the angle of maximum polarisation relative to the celestial meridian (Landi Degl'Innocenti et al., 2007), and is given by:

$$\theta = \frac{1}{2}\text{sign}(P_U)\arccos\left(\frac{P_Q}{\sqrt{P_Q^2 + P_U^2}}\right), \tag{2.27}$$

as outlined in a discussion by Landi Degl'Innocenti et al. (2007).

The linear spectropolarimetric data can then be represented by intensity (I) as with normal spectroscopy, degree of linear polarisation (P_L), and linear polarisation angle (θ) as a function of wavelength (λ). These results are of immense importance in polarisation studies, as it gives valuable information regarding the nature of the observed emission, as well as underlying activity and emission mechanisms in astrophysical sources.

Synchrotron Radiation and Polarisation

When relativistic charged particles are accelerated by a magnetic field, they will radiate and lose energy via a process called synchrotron emission. Relativistic electrons moving within a magnetic field **B**, will be accelerated because the magnetic field exerts a force perpendicular to the electrons' original direction of motion. An electron travelling with some velocity will be accelerated to follow a circular motion around the magnetic field lines. This will result in the particles following a helical path, *gyrating* around the magnetic field at a frequency $\omega_B = qB/\gamma mc$. As shown in many standard texts, such as Rybicki and Lightman (1985, pp. 167–191), for an isotropic distribution of velocities, averaged over all pitch angles (α, the angle at which the particle is moving with respect to the magnetic field) for a given speed β, the total power of the radiation is given by:

$$P = \frac{4}{3}\sigma_T c\beta^2\gamma^2 U_B, \tag{2.28}$$

where σ_T is the Thomson scattering cross section, and $U_B = B^2/8\pi$ the magnetic energy density. A more detailed analysis shows that the total emitted power per unit frequency for a single particle can be separated into its parallel and perpendicular components (with respect to the projection of the magnetic field on the plane of the sky) as:

$$P_\perp(\omega) = \frac{\sqrt{3}q^3 B\sin\alpha}{4\pi mc^2}\left[F(x) + G(x)\right] \tag{2.29}$$

$$P_\parallel(\omega) = \frac{\sqrt{3}q^3 B\sin\alpha}{4\pi mc^2}\left[F(x) - G(x)\right] \tag{2.30}$$

where:

$$F(x) = x\int_x^\infty K_{5/3}(\xi)d\xi \tag{2.31}$$

is an integral over a modified Bessel function of order 5/3 with $x = \omega/\omega_c$, and,

$$G(x) = xK_{\frac{2}{3}}(x), \tag{2.32}$$

is a modified Bessel function of order 2/3. Here, ω_c is the critical or peak frequency of the emitted synchrotron radiation, and is defined as:

$$\omega_c = \frac{3}{2}\gamma^2\omega_B\sin\alpha. \tag{2.33}$$

The total emitted power per unit frequency is given by the sum of its perpendicular and parallel components from Equations (2.29) and (2.30); i.e.:

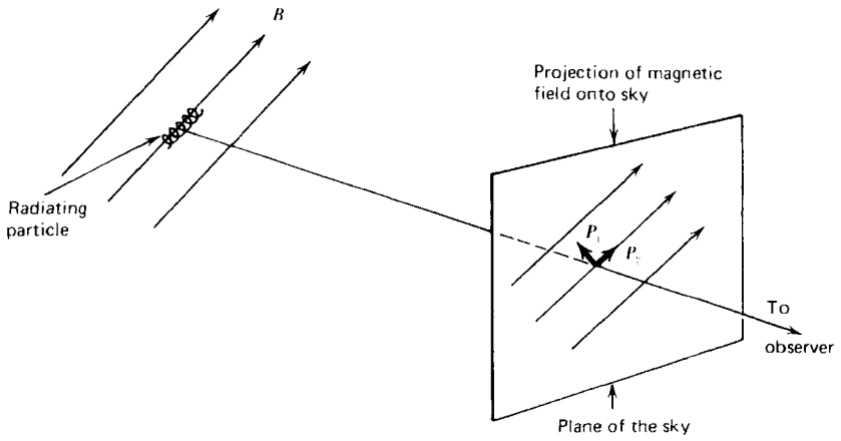

Figure 2.10: Synchrotron polarisation as projected on the plane of the sky, following Equation (2.38). Figure adopted from Rybicki and Lightman (1985).

$$\begin{aligned} P(\omega) &= P_{\perp}(\omega) + P_{\parallel}(\omega) \\ &= \frac{\sqrt{3}}{2\pi}\frac{q^3 B \sin\alpha}{mc^2} F(x)\,, \end{aligned} \tag{2.34}$$

For astrophysical sources, synchrotron radiation is often produced by a power-law distribution of electrons. In this case, the number density of particles with energies (γ to $\gamma + d\gamma$) is approximated by:

$$N(\gamma) = C\gamma^{-p} d\gamma, \tag{2.35}$$

where p is the particle distribution index, and C is a constant. The total power radiated per unit volume per unit frequency is then found by the integral:

$$P_{\rm tot}(\omega) = \int_0^{\infty} P(\omega) N(\gamma) d\gamma, \tag{2.36}$$

where the power per unit frequency per particle is given by Equation (2.34). It can then be shown that Equation (2.36) scales as:

$$P_{\rm tot} \propto \omega^{-\frac{p+1}{2}} \propto \omega^{-s}, \tag{2.37}$$

where s is the observed spectral index.

As already mentioned, synchrotron radiation from a single charged particle is inherently elliptically polarised. In a relativistic plasma, the contributions of all the individual, elliptically polarised photons can be summed up, with each photon having a different "handedness". The elliptically polarised contributions from each individual particle will effectively cancel out, and the ensemble will not produce any circularly or elliptically polarised emission. Instead, the observed synchrotron emission will be partially linear polarised. The synchrotron radiation of the jet plasma can be fully described by the power per unit frequency in directions parallel and perpendicular to the projection of the magnetic field on the plane of the sky (Figure 2.10). The degree of polarisation is determined by:

$$\Pi(\omega) = \frac{P_\perp(\omega) - P_\parallel(\omega)}{P_\perp(\omega) + P_\parallel(\omega)} = \frac{G(x)}{F(x)}. \tag{2.38}$$

which can be simplified by some assumptions. For an electron population with a power-law distribution in a uniform magnetic field, Equation (2.38) reduces to:

$$\Pi = \frac{p+1}{p+\frac{7}{3}}, \tag{2.39}$$

The allowed polarisation is quite high, and can go up to as high as $\sim 75\%$ (for $p < 3$). The observed polarisation of blazars does not reach such high levels, as it typically remains below 20 to 30% (Zhang, 2019). Since the synchrotron polarisation in blazars is always linear, for the remainder of this dissertation, the term "polarisation" will refer to linear polarisation unless otherwise specified.

2.3.4 Synchrotron Polarisation in Blazars

As already discussed in Section 2.3.1, the synchrotron radiation producing the low-energy component of blazar SEDs, and possibly the high-energy component via leptonic processes, is intrinsically polarised. Due to the underlying thermal (unpolarised) contribution from the host galaxy and dust torus at lower frequencies, as well as the accretion disc towards the bluer end, the degree of linear polarisation in these frequency ranges will be reduced slightly (Böttcher et al., 2017). From this, it is clear that the non-thermal emission in the radio-optical/UV wavelength bands will be partially linear polarised emission originating in the jet of the blazar (see e.g. Beckmann and Shrader, 2012b; Rybicki and Lightman, 1985, for a detailed overview of synchrotron emission in jet plasmas).

The degree of synchrotron polarisation (radio - optical wavelength bands) in blazars can vary from a few to tens of percent in a partially ordered magnetic field (Zhang et al., 2014). The polarisation of blazars is highly variable in both degree and angle, especially during outbursts or flares, and can increase up to 50% during very high-energy or TeV flares (Smith, 2017), and large ($\gtrsim 180°$) polarisation angle swings have been reported during flaring activity (Marscher et al., 2008, 2010).

Polarisation signatures in blazars can be used to directly probe the evolution, composition, and magnetic field structure of AGN jets, aide in identifying periodic variability in blazar activity (e.g. Zhang and Wang, 2022). However, blazar polarimetry is still a fairly new field, and has yet to expand fully into the high-energy (X-ray and γ-ray) regimes (see Liodakis et al., 2019; Zhang and Böttcher, 2013, for an overview on the expected/theoretical X-ray and γ-ray polarisation signatures of blazars). Below, the recent progress in polarimetry, both observational and theoretical, is briefly discussed.

Observational findings by RoboPol

The RoboPol programme[2] (2014 - present) is the first large-scale data collection attempt at studying statistical trends in blazars connected to the polarisation signatures in their

[2]https://robopol.physics.uoc.gr/

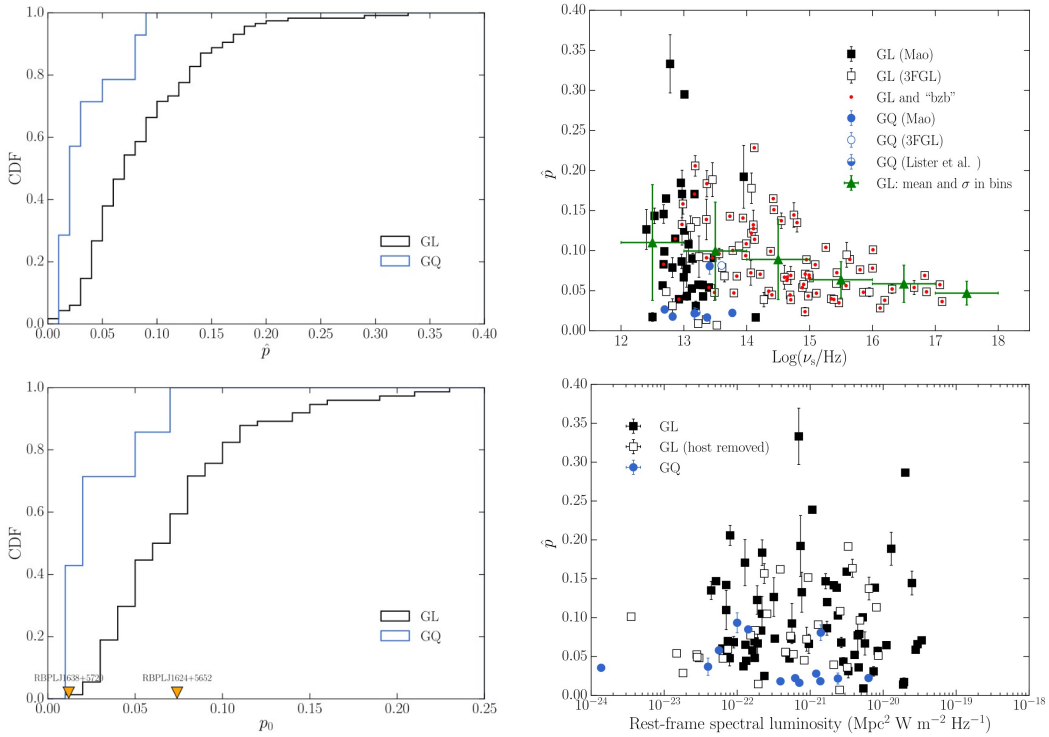

Figure 2.11: Findings by Angelakis et al. (2016) from the RoboPol programme. The left column (top and bottom) shows the cumulative distribution function (CDF) of the median (top) and intrinsic (bottom) fraction of polarisation in γ-ray loud (GL) and γ-ray quiet AGN (GQ). The top right panel shows the median polarisation fraction versus the logarithm of the synchrotron peak frequency, whereas the bottom right panel gives the median polarisation fraction as a function of emitted rest-frame luminosity.

emission. RoboPol is a specialised photopolarimeter designed to have high observing efficiency and automated operations. One of the RoboPol Collaboration's primary science goals is to monitor the optical linear polarisation of γ-ray bright blazars over a long period of time and identify trends in their overall behaviour. This programme has significantly boosted the field of polarisation studies in AGN – and specifically blazars – with the myriad of information it presents. Below is a short summary of some of the RoboPol Collaboration's main findings.

A comparison of γ-ray loud and γ-ray quiet AGN shows that there seems to be a general trend for the polarisation levels to increase with increased γ-ray activity, with γ-ray loud AGN displaying systematically higher polarisation fractions than γ-ray quiet AGN (Angelakis et al., 2016). This is shown in the left column of Figure 2.11, which gives the cumulative distribution function for the observed AGN. This is likely due to γ-ray loud AGN's emission being highly Doppler boosted, jet-dominated, and highly variable, leading to higher observed degrees of polarisation than for γ-ray quiet AGN. There is also an anti-correlation between the median fraction of polarisation and the location of the synchrotron peak frequency ($\nu_{\rm sy}$; top right plot in Figure 2.11), where HSP sources have lower polarisation fractions compared to LSPs. Since LSP sources peak in the infrared, the optical regime represents the high-frequency portion of the synchrotron radiation, and is, therefore, more polarised than HSPs (Angelakis et al., 2016). The average degree of linear polarisation does not seem to depend on the observed rest-frame spectral luminosity, indicating that the difference in polarisation fraction of γ-ray quiet and γ-ray loud sources cannot be traced to differences in the jet luminosity at optical wavelengths (see

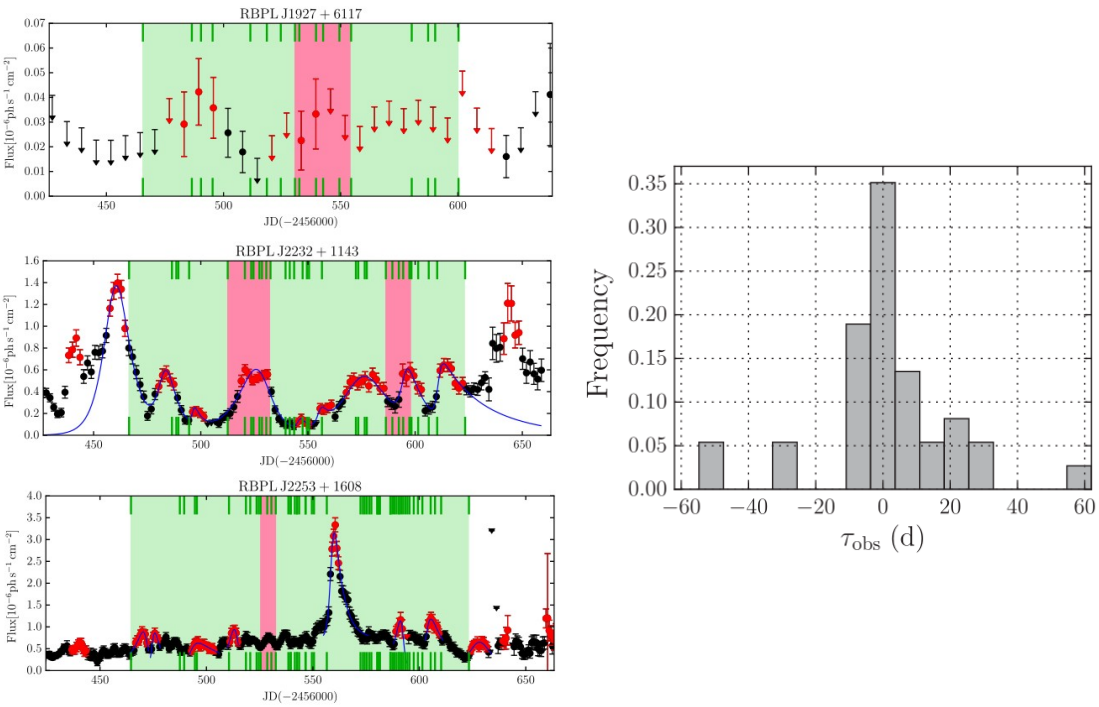

Figure 2.12: Results from Blinov et al. (2018) on the link between polarisation angle rotations and γ-ray flares. The figures on the left show the γ-ray lightcurves with detected Electric Vector Polarisation Angle (EVPA) rotations of three sources (of a larger sample of 24) observed with the RoboPol programme in 2013. The red datapoints indicate periods of flaring activity, and the green ticks indicate when EVPA measurements were taken. The pink shaded area indicates the duration of the polarisation angle rotation, and the green shaded area gives the season interval. The histogram to the right shows the distribution of the observed time lags ($\tau_{\rm obs}$, not yet redshift-corrected) between the γ-ray flares and EVPA rotations.

the bottom right plot in Figure 2.11; Angelakis et al., 2016).

RoboPol found no significant difference in the overall polarisation properties of TeV-detected and non-TeV-detected BLLs. This indicates that the TeV loudness of blazars, or BLLs in particular, is not directly linked to their polarisation properties. Rather, the TeV loudness of BLLs is more likely a consequence of flaring activity, redshifts, and the location of the synchrotron peak frequency ($\nu_{\rm sy}$; Hovatta et al., 2016). All of these trends hint towards a possible connection to the blazar sequence (Fossati et al., 1998; Meyer et al., 2011).

A major achievement of the RoboPol monitoring programme, is that it has measured polarisation angle swings in blazars. Although polarisation angle swings are very rare and do not occur in all blazars, it was found to happen in BLLs and FSRQs with equal probability (Blinov et al., 2016). In blazars that show polarisation angle rotations, there is a decrease in the average degree of polarisation during the rotation. There is also a correlation with higher and more variable γ-ray emission during the polarisation angle rotation.

A connection between the RoboPol observed polarisation angle swings and γ-ray flaring activity detected by the *Fermi*-LAT in blazars was also found. This was detected for a total of 24 sources, and the figures on the left of Figure 2.12 show the *Fermi*-LAT lightcurves for three of these sources, indicating both the periods associated with γ-ray flares (red datapoints), and the periods associated with polarisation angle swings (pink shaded areas).

A cross correlation between the polarisation angle rotations and γ-ray flares gives the distribution of the time lags between the two events in the plot to the right in Figure 2.12. This distribution has a peak around $\tau_{\rm obs} = 0$, with an average delay consistent with zero when the lags are redshift-corrected ($\langle\tau_{\rm corr}\rangle = 1.5 \pm 3.1$d, where $\tau_{\rm corr}$ is the redshift-corrected time lags), indicating that these events occur with a time-lag between the flare and polarisation angle swing consistent with zero (see Figure 2.12; Blinov et al., 2018). The authors suggest that, in principle, every γ-ray flare should be accompanied by a polarisation angle rotation, but more continuous monitoring of blazars would be required to test this hypothesis.

Progress in Blazar Spectropolarimetry

Another example of the importance of including polarimetry and multi-wavelength observational data can be seen in Figure 2.13, where Schutte et al. (2022) simultaneously fitted the thermal and non-thermal components of the observed blazar flux, as well as the degree of optical linear polarisation. This model was applied to the FSRQ 4C+01.02 during both a flaring (top plots in Figure 2.13) and quiescent state (bottom plots), during which the emission was dominated by the jet-synchrotron emission, and accretion disc emission, respectively. The authors were able to not only constrain the thermal accretion disc emission component and determine the mass of the SMBH ($M_{\rm SMBH} \sim 3 \times 10^9\,{\rm M}_\odot$), but also shed some light on the electron distribution in the jet. The degree of ordering of the jet magnetic field, $F_{\rm B}$, was also constrained. Here, $F_{\rm B}$ is a unitless parameter such that the polarisation is given by,

$$\Pi_\omega^{\rm sy} = F_{\rm B} \cdot \frac{\langle G(x)\rangle}{\langle F(x)\rangle}, \tag{2.40}$$

and it was found that the magnetic field was partially ordered, with ordering of the magnetic field $F_{\rm B} < 1$ during both flaring ($F_{\rm B} = 0.188$) and quiescent ($F_{\rm B} = 0.040$) states.

There has also been significant progress in theoretical polarimetry studies regarding the long and short-term polarisation signatures, the physical structure of the jet-magnetic field, as well as fluid-dynamical simulations of blob-injections, shocks and particle acceleration within the jet (e.g. Marscher, 2014; Marscher et al., 2008; Zhang et al., 2014, to name just a few).

By investigating the degree of polarisation in frequency space, one can use the slope of the polarisation to gauge what is happening in the jet-component at the time of observation. As shown in e.g. Schutte et al. (2022), a decrease in the degree of linear polarisation toward the blue/higher frequency end of the optical spectrum is due to the contribution of the thermal (unpolarised) accretion disc emission (see Figure 2.13).

In contrast, an increase in the degree of linear polarisation toward the blue/higher frequency end might be due to a shock in the jet. This is the so-called "shock-in-jet" model, as outlined by Tavecchio et al. (2018) as a possible jet energy dissipation mechanism, and is shown in Figure 2.14. In this model, a rapidly decaying B-field component perpendicular to the direction of the shock's motion is generated by instabilities in the vicinity of the shock front. Due to the highly ordered $B_\perp$, one expects the emission from the highly energetic electrons (e.g. emitting at X-ray wavelengths in the case of HBLs)

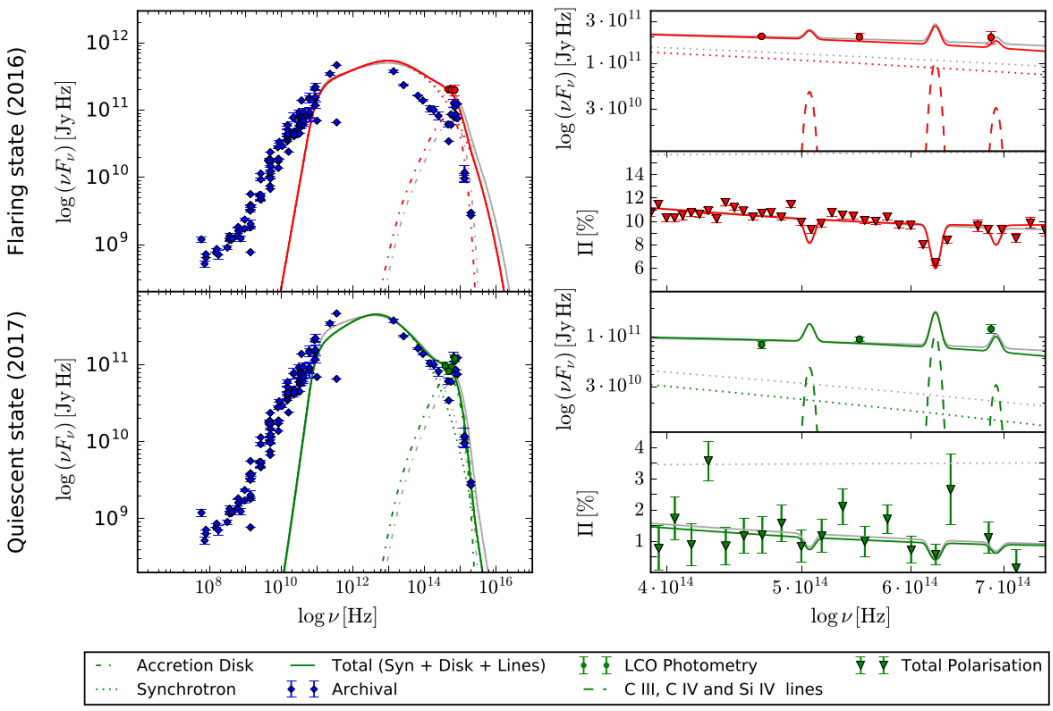

Figure 2.13: An example of simultaneous SED and spectropolarimetry modelling of the emission of blazar 4C+01.02 during flaring and quiescent states by Schutte et al. (2022). The figures in the left column gives the SED model fitted to the blazar during a flaring (top) and quiescent (bottom) state, whereas the figures in the right column give the model fit to the degree of polarisation in the optical/UV regime.

to be characterised by a high degree of polarisation. However, due to strong radiative losses, the electrons cool rapidly, and the highly polarised emission is only emitted in a small volume close to the shock region. At lower energies (optical/IR), the emission is produced by low-energy electrons that fill the post-shock region. The quasi-parallel B field is dominant over $B_\perp$, and the electrons, therefore, experience a less ordered magnetic field and lower degrees of polarisation.

An implementation of this model is shown in Figure 2.15. Here, the shock-in-jet model is implemented with a fixed viewing angle of $\theta_\mathrm{v} = 0.1°$, with the degree of polarisation (Π_v) and polarisation angle (χ_v) modelled for a wide range of frequencies (IR – X-ray), and various decay rates (m) of the perpendicular component of the magnetic field (scaling as a power-law). Here, the predicted high degrees of polarisation at X-ray wavelengths are seen, along with a gradual (for $m = 0.4$, $m = 1$) decrease in the degree of polarisation towards lower frequencies, reaching a plateau in the optical regime (for $m = 1$, $m = 3$). The low degree of polarisation in the optical regime is in agreement with what is observed for typical HBLs ($\Pi \leq 10\%$). For a more detailed discussion on the shock-in-jet model and its implications for optical and X-ray polarimetry, see, for example, Schutte et al. (2022); Tavecchio et al. (2018) and Paliya et al. (2018).

Evidently, polarimetry proves to be especially useful in blazar research in the optical wavelength regime. Recently, the *Imaging X-ray Polarimetry Explorer*[3] (IXPE) has been launched (2021, December 9) in an attempt to expand polarimetry studies into the higher energy regime. One of the IXPE's main science objectives is to provide simultaneous spec-

[3] `https://ixpe.msfc.nasa.gov/`

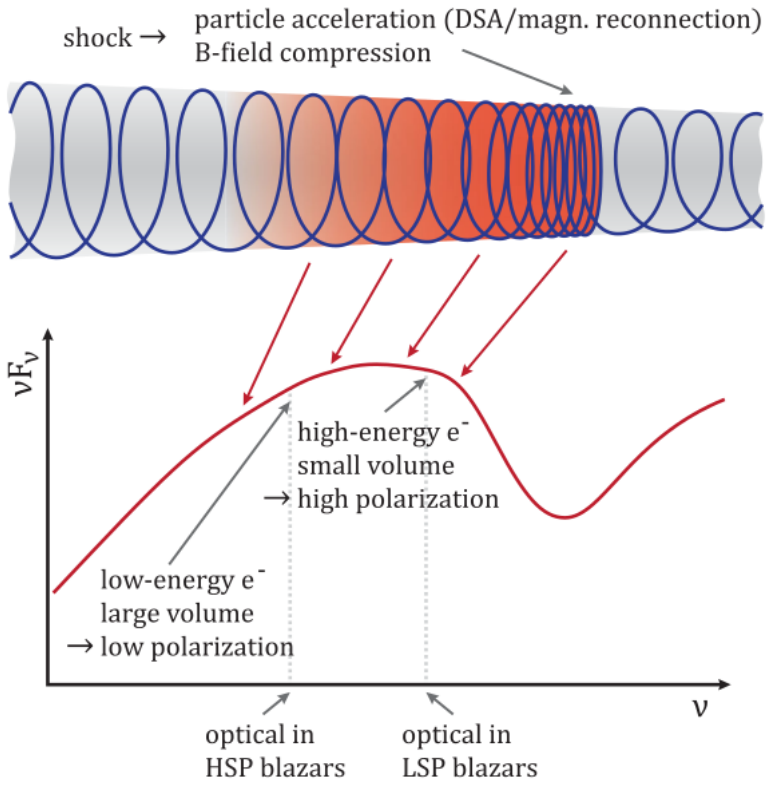

Figure 2.14: An illustration of the shock-in-jet model proposed to explain the concentration of synchrotron polarisation around the shock (red region) at higher (X-ray) frequencies. Here, the downstream direction is to the left. Figure taken from Angelakis et al. (2016).

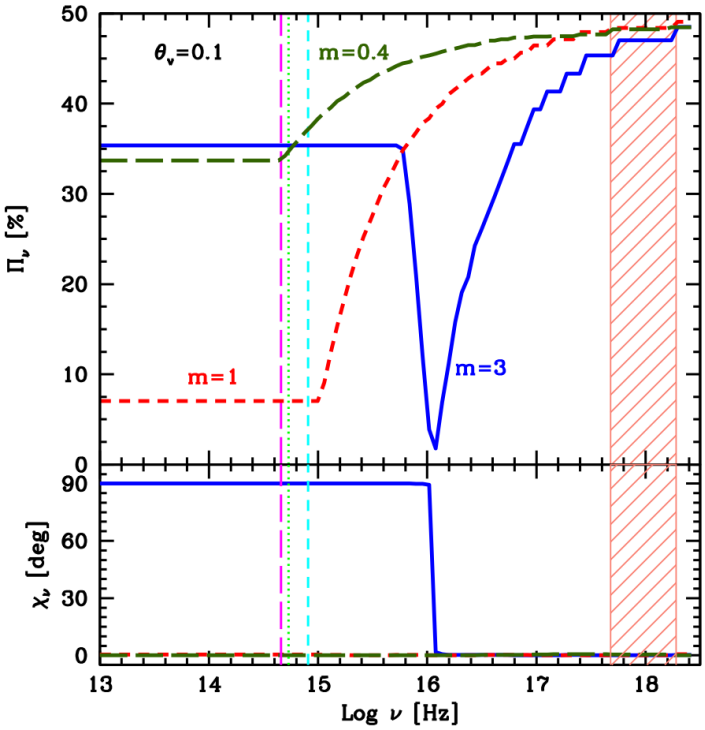

Figure 2.15: The behaviour of the degree of polarisation (top panel) and polarisation angle (bottom panel) as a function of frequency in HBL sources when considering the shock-in-jet model from Tavecchio et al. (2018). These results were obtained with a fixed viewing angle, but varying decay rates for the magnetic field component perpendicular to the shock normal ($B_\perp$), where m indicates the power-law index with which the $B_\perp$ intensity is fitted. The vertical dashed lines indicate the central frequencies of Johnson R, V, and U optical filters, and the orange shaded region indicate the energy range covered by the IXPE.

tral, spatial and temporal X-ray measurements to determine the geometry and emission mechanisms of AGN. This will provide crucial information about the particle population producing the high-energy component of blazar SEDs, and will lead to a clearer understanding of the behaviour of these highly energetic sources.[4]

In the chapters to follow, an optical spectropolarimetric study of the behaviour of a selection of high-energy blazars will be presented. In the following chapter, a summary of the optical spectropolarimetric observations taken with SALT, as well as the complementary photometric observations performed with the Las Cumbres Observatory telescope network, and the *Fermi*-LAT γ-ray lightcurves, will be given.

[4]While finalising this dissertation, the first-ever X-ray polarisation was detected from the blazar Mrk 501 with the IXPE ($\Pi_{\rm X}\,(2-8{\rm keV}) = 10 \pm 2\,\%$, twice that of the optical degree of polarisation; Liodakis et al., 2022). These results are in agreement with the shock-in-jet model as proposed by Tavecchio et al. (2018).

Chapter 3

Observations of selected sources

This chapter provides an overview of the telescopes and science instruments, observations, and data reduction processes that were used/performed to obtain the observational data for this project. This covers a selection of eighteen blazars, of which six were BLLs and twelve were FSRQs. Section 3.1 will summarise the optical spectropolarimetric observations, Section 3.2 will outline the optical photometry, and Section 3.3 will cover the γ-ray monitoring of the selection of blazars.

3.1 Optical Spectropolarimetry

As already mentioned in Chapter 2, spectropolarimetry is the measurement of the total intensity and polarisation in electromagnetic radiation as a function of wavelength (Landstreet, 2015). Spectropolarimetry provides insight into the geometrical structure and physical nature of astrophysical sources like, for example, blazars. For this project, all optical spectropolarimetric observations were taken with the Southern African Large Telescope (SALT; Buckley et al., 2006) using the Robert Stobie Spectrograph (RSS; Burgh et al., 2003; Kobulnicky et al., 2003), located at the South African Astronomical Observatory (SAAO) near Sutherland in the Northern Cape province of South Africa.

The observations used in this project were taken under two different SALT observing programmes. The first is "Observing the Transient Universe" (2021-2-LSP-001) with Principle Investigator (P.I.) David A.H. Buckley. It is an ongoing Target-of-Opportunity (ToO) observing campaign that aims at investigating virtually all of the major transient classes. For studying the transient behaviour of blazars, this project relies on triggers from the *Fermi* Large Area Telescope (LAT) and the High Energy Stereoscopic System (H.E.S.S.) of enhanced γ-ray activity in blazars, and then utilises SALT's capabilities for follow-up observations in the optical regime. Ideally, observations in both high and low states are required to monitor the change in flux and polarisation. From the start of the campaign in 2016 up to 2022, twenty-four blazars have been observed, of which seventeen were FSRQs, six were BLLs, and one was a blazar candidate of unidentified classification (BCU). The aim is to obtain quasi-contemporaneous optical and γ-ray observations of blazars during various states of activity to track the change in flux, degree of polarisation and polarisation angle.

[1]The NASA/IPAC Extragalactic Database (NED) is funded by the National Aeronautics and Space Administration and operated by the California Institute of Technology.

Table 3.1: Coordinates, type, redshift and apparent visual magnitude of all of the blazars studied in this dissertation. Note that most of the information comes from already published data from the Simbad database (Wenger et al., 2000), and the NASA/IPAC Extragalactic Database.[1]Note that, since blazars are highly variable sources, the state during which the catalogue apparent visual magnitudes were taken is not necessarily quiescent. The synchrotron peak frequencies ($\nu_{\rm sy}$) were taken from the Fourth Catalog of Active Galactic Nuclei detected by the LAT (4LAC; Ajello et al., 2020; Lott et al., 2020).

Target	RA (J2000)	Dec. (J2000)	Type	Redshift	V-mag	$\nu_{\rm sy}$ (Hz)
PKS 0426–380	04:28:40.42	-37:56:19.56	BLL	1.111	19.00	4.79×10^{12}
PKS 0447–439	04:49:24.70	-43:50:08.96	BLL	0.107	15.24	4.47×10^{15}
TXS 0506+056	05:09:25.96	+05:41:35.33	BLL	0.337	14.78	3.55×10^{14}
PKS 0537–441	05:38:50.36	-44:05:08.94	BLL	0.894	16.48	6.24×10^{12}
PKS 1454–354	14:57:26.71	-35:39:09.98	BLL	1.424	19.50	1.01×10^{13}
AP Lib	15:17:41.81	-24:22:19.48	BLL	0.049	14.00	9.06×10^{13}
PKS 0035–252	00:38:14.74	-24:59:02.23	FSRQ	0.498	17.29	2.57×10^{12}
PKS 0131–522	01:33:05.76	-52:00:03.95	FSRQ	0.020	20.30	4.37×10^{12}
PKS 0208–512	02:10:46.20	-51:01:01.89	FSRQ	1.003	16.93	8.61×10^{12}
4FGL J0231.2–4745	02:31:11.80	-47:46:11.58	FSRQ	0.765	17.87	1.31×10^{12}
PKS 0346–279	03:48:38.14	-27:49:13.56	FSRQ	0.991	18.63	1.41×10^{13}
PKS 0837+012	08:39:49.61	+01:04:26.74	FSRQ	1.123	19.09	3.24×10^{12}
PKS 0907–023	09:09:44.92	-02:31:30.36	FSRQ	0.957	18.56	5.56×10^{13}
PKS 1034–293	10:37:16.08	-29:34:02.82	FSRQ	0.310	16.46	6.92×10^{12}
3C 273	12:29:06.70	+02:03:08.60	FSRQ	0.158	14.83	7.00×10^{13}
PKS 1424–418	14:27:56.30	-42:06:19.44	FSRQ	1.522	17.70	1.40×10^{13}
PKS 1510–089	15:12:50.53	-09:05:59.83	FSRQ	0.360	16.54	1.10×10^{13}
PKS 2023–07	20:25:40.66	-07:35:52.69	FSRQ	1.388	18.23	4.16×10^{12}

The second observing programme is a pilot project named "Untangling variability in blazars through spectropolarimetry and relativistic magnetohydrodynamic (RMHD) simulations" (2019-2-MLT-001) with P.I. Brian van Soelen. This observing campaign was a long-term monitoring of two sources – a BLL (AP Lib) and an FSRQ (PKS 1034-293) – over the course of ∼1 year (from 2020 May to 2021 July). The aim of the long-term observing campaign is to correlate the variability signatures (in flux, spectral features, and polarisation) of BLLs and FSRQs with dynamical variations in the jet structure.

The complete list of all the sources included in this project is given in Table 3.1.

SALT and the RSS

SALT (see Figure 3.1) is an optical 10m-class segmented-mirror telescope, and is the largest single optical telescope in the southern hemisphere. It is capable of high time-resolution observations and dynamic scheduling with rapid response times, and is able to change between observing modes in less than a minute.[2] SALT houses three main science instruments, namely SALTICAM, the fibre-fed High-Resolution Spectrograph (HRS), and the Robert Stobie Spectrograph (RSS). Thus, it is well-suited for observing faint and/or transient sources in various modes (Buckley et al., 2006).

The RSS (Figure 3.2) is the main, all-purpose spectroscopic instrument on SALT, with an $8'$ Field of View (FoV), operating between 3200 Å (UV cutoff due to the atmosphere)

[2]See e.g. `https://astronomers.salt.ac.za/proposals/`

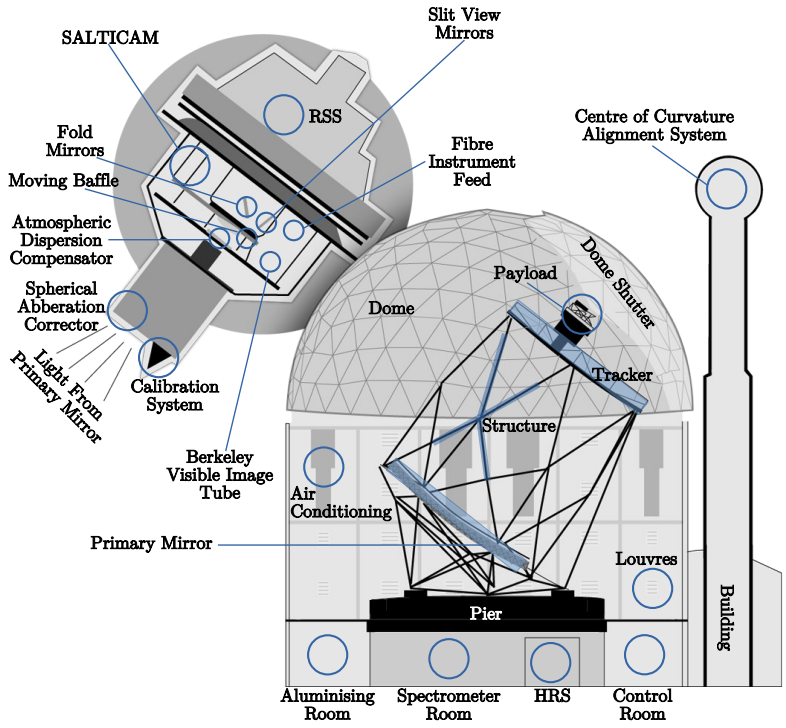

Figure 3.1: A schematic diagram of the Southern African Large Telescope, highlighting its various components and instruments. The Payload is enlarged to the left of the diagram, indicating the position of the Robert Stobie Spectrograph. Figure adapted from `https://www.salt.ac.za/telescope/`.

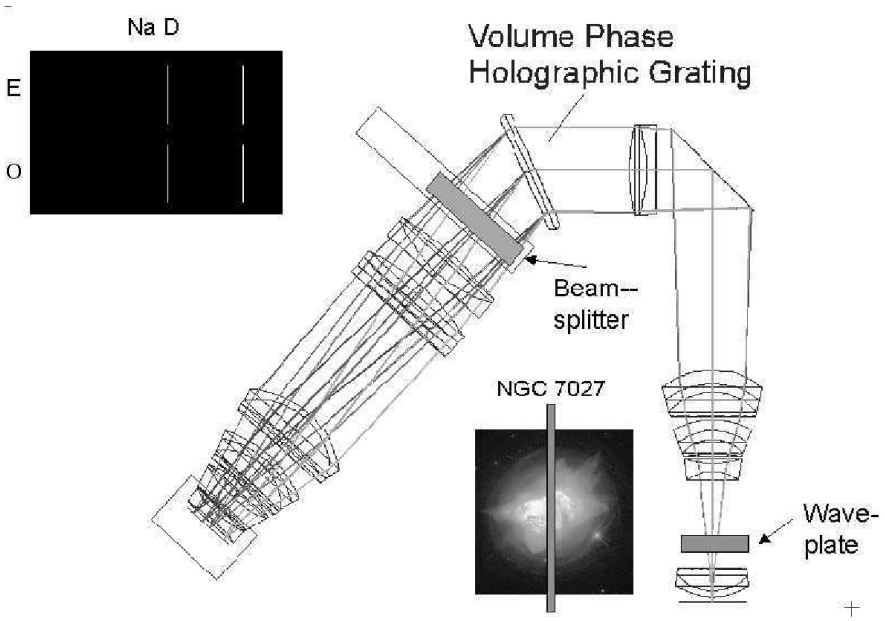

Figure 3.2: The optical layout of the RSS in longslit spectropolarimetry mode. Figure taken from Buckley et al. (2005).

Table 3.2: All the possible imaging and spectroscopy configurations when using SALT and the RSS.

Imaging Modes	Waveplates used
Filter Imaging	N
Fabry-Perot Imaging	N
Imaging Polarimetry	Y
Fabry-Perot Polarimetry	Y
Spectroscopy Modes	**Waveplates used**
Longslit Spectroscopy	N
Multi-slit Spectroscopy	N
Longslit Spectropolarimetry	Y
Multi-slit Spectropolarimetry	Y

to 9000 Å (IR/instrument response cutoff) at a resolving power of between $R = 1000$ and $R = 10000$, depending on the diffraction grating and slit width used. The RSS is capable of various modes of observations: medium-band imaging, Fabry-Perot narrow-band imaging, long-slit grating spectroscopy, and multi-slit grating spectroscopy (see Table 3.2 for all the possible observing modes when using the RSS; Kobulnicky et al., 2003). All polarimetry observations can be taken in LINEAR, LINEAR-HI, CIRCULAR, CIRCULAR-HI, and ALL-STOKES modes.

The basic layout of the RSS can be seen in Figure 3.2 in longslit spectropolarimetry mode. The RSS consists of the field lens, followed by a slot for a modulator/retarder used in polarimetric modes, consisting of two rotating, superachromatic mosaic 1/2 and 1/4 waveplates. Then, the beam passes through the collimator groups and folding flat mirror that redirects the beam by 90°. For polarimetric modes, the beam is passed through a polarising beamsplitter, which is an array of calcite Wollaston prisms. The beam is then passed through a shutter and disperser (either a rotatable transmission grating, or a double-etalon Fabry-Perot system). Lastly, to utlise the gratings at various angles (see, for example, the articulation of the grating in Figure 3.2), the mosaicked detector of three CCD 2048×4096 cameras is mounted in a tube that articulates around an axis that coincides with the grating rotation axis (Burgh et al., 2003; Kobulnicky et al., 2003; Nordsieck et al., 2003; Potter et al., 2016).

The subsystem used in polarimetric modes, therefore, consists of two elements, the polarising beamsplitter, and the waveplate modulator. The purpose of the polarising beamsplitter is to separate the collimated beam along its centre into two orthogonally polarised fields (the *Ordinary* (O) and *Extraordinary* (E) beams; see Figure 3.3). The waveplates precede the beamsplitter, and modulate the difference in the intensities between the O- and E-beams with time. The waveplates are rotated (with different configurations depending on the mode of polarimetry), and the difference between the O- and E-beam intensities are measured for each waveplate orientation/step. After the full waveplate pattern is completed, the Stokes parameters are calculated from the relative intensity of the O- and E-beams of the observed emission (Burgh et al., 2003; Kobulnicky et al., 2003).

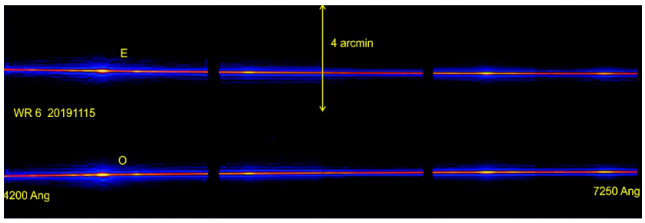

Figure 3.3: An example of an image frame taken with the RSS in long-slit spectropolarimetry linear mode. Indicated on this figure are the orthogonally polarised O- and E-beams that the original light is dispersed into. Figure adapted from Nordsieck and Groenewald (2019).

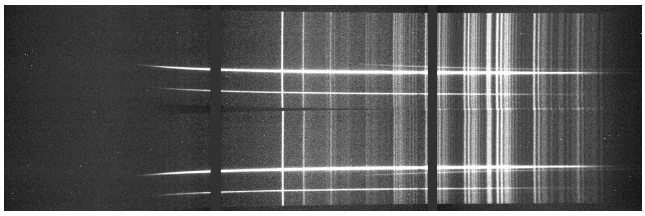

Figure 3.4: A reduced image frame for AP Librae, taken with the RSS in long-slit spectropolarimetry linear mode. This frame has been passed through the original polSALT pipeline for basic image reduction, and is ready to be split into its separate O- and E-beam frames by the modification to the polSALT pipeline.

RSS Data Reduction

The optical spectropolarimetric observations taken with the SALT RSS were reduced using a modified version of the pySALT/polSALT pipeline (Crawford et al., 2010).[3] The original polSALT reduction pipeline handles the basic CCD reductions of the raw images, which includes bias subtraction, gain and cross-talk correction, distortion correction and the mosaicking of the CCD chips. After the basic data reductions are complete, the image frames resemble that of Figure 3.4, which are passed to the modification of the pipeline for wavelength calibration.

The modification to the polSALT pipeline is three-fold (see Figure 3.5; Cooper et al., 2022). Firstly, since the image frames contain both the orthogonally polarised O-beam and E-beam (as seen in Figure 3.4), the frames are split into two along a central axis so that each frame contains only one spectral trace on the dispersion axis (either O- or E-beam). This is done so that the image frames are recognisable by IRAF/NOAO,[4,5] which is the image reduction package used for the wavelength calibration of spectroscopic data. This allows the user to use IRAF in conjunction with the polSALT pipeline, and allows for a more "hands-on" approach to the wavelength calibration. This proves to be especially useful when using an observational setup (i.e. grating, grating angle and corresponding arc lamp) that provides very few arc-lines to perform wavelength calibrations with. A user-defined wavelength solution is then found for the O- and E-beams separately in IRAF, using the standard wavelength calibration, namely `identify`, `reidentify` and `fitcoords` tasks.

The second leg of the pipeline allows the user to perform an optional cross-correlation of the O- and E-beams to ensure that the wavelength calibration was done correctly, without affecting the polarisation signatures of the original data. Since the wavelength

[3] `https://github.com/saltastro/` & `http://pysalt.salt.ac.za/`
[4] `https://iraf.net/`
[5] `http://ast.noao.edu/data/software`

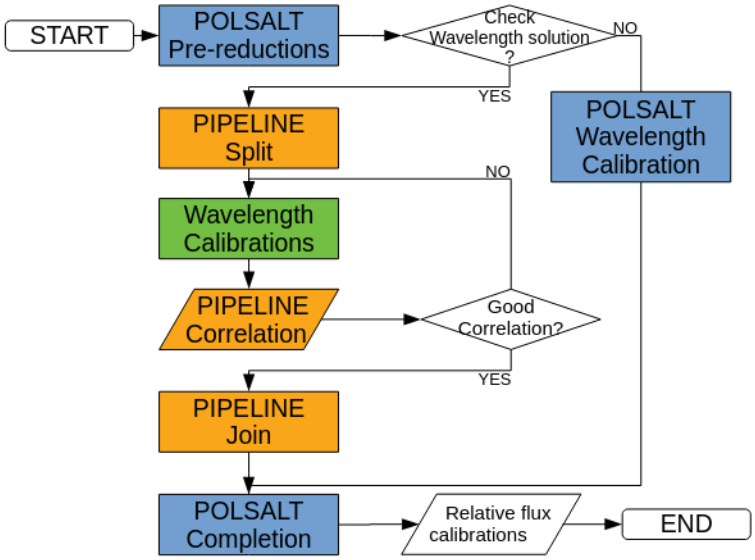

Figure 3.5: A flow chart explaining the modification to the original pySALT/polSALT reduction pipeline. Figure adopted from Cooper et al. (2022).

calibration is performed for the O- and E-beams separately and then later recombined, such a cross-correlation is necessary to ensure that the O- and E-beam's wavelength solutions are identical. An example of good cross-correlation between the O- and E-beam's wavelength solutions for each 1/2 waveplate orientation is shown in Figure 3.6. Here, the features of the wavelength callibrated spectra align perfectly, and no wavelength shift is seen. In such a scenario, the user may proceed to the next step of the modified pipeline.

Lastly, the modified pipeline performs enhanced cosmic ray rejection for each frame using the python-based LACOSMIC cosmic ray cleaning package.[6] After the frames underwent cosmic ray cleaning, the modified pipeline rejoins the O- and E-beams for each image, and attaches a wavelength solution to the image frames as an extra extension that will be recognised by the original polSALT pipeline.

After the wavelength calibration and rejoining of the data, the original polSALT pipeline is used to perform spectral extraction (with beamsplitter distortion and tilt correction applied before extraction), raw- and final Stokes calculations. The polSALT graphical user interface (GUI) allows for the visualisation of the results: intensity, linear degree of polarisation, and equatorial polarisation angle, all as a function of wavelength.

Observations

All spectropolarimetric observations for this project were taken with the RSS in either spectropolarimetry LINEAR or LINEAR-HI mode. This is performed using the 1/2 waveplate at angles 0°, 45°, 22.5°, and 67.5° for LINEAR mode; with 11.25°, 56.25°, 33.75°, and 78.75° added for the LINEAR-HI mode. Each observation was taken using either the PG0300 or PG0900 grating, at varying grating angles, depending on the source. Arc frames were taken immediately after the science cycle using an Ar, ThAr, Xe, or Ne arc lamp, depending on the spectrograph setup. The different observational setups for all of

[6] `https://github.com/larrybradley/lacosmic`

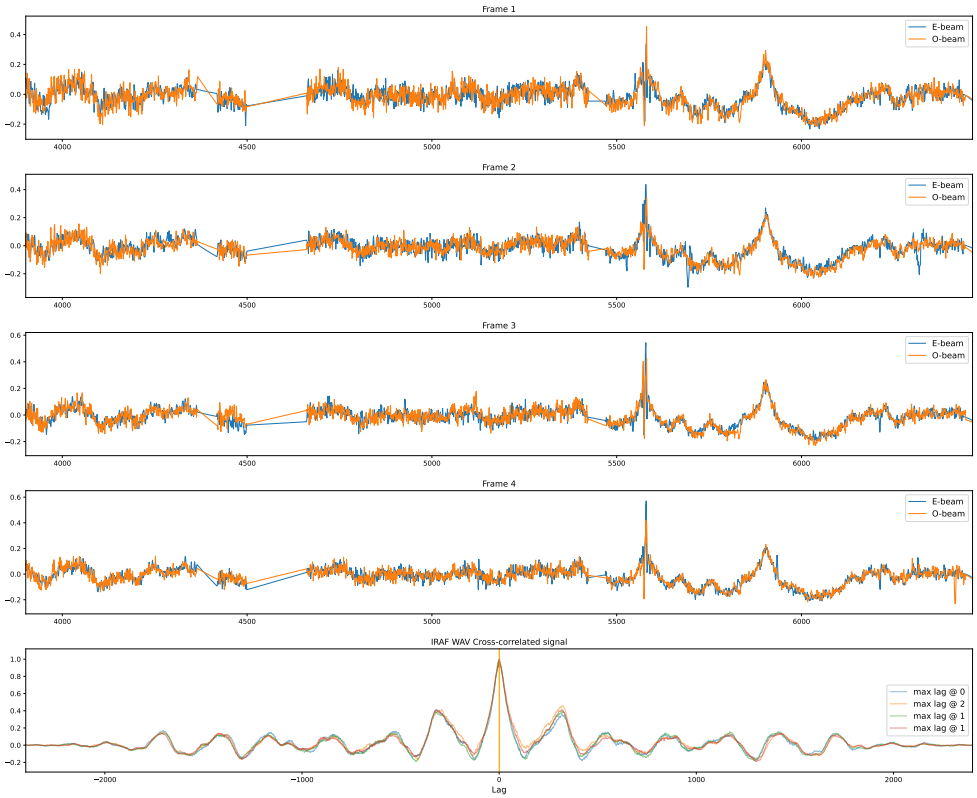

Figure 3.6: An example of the cross-correlation between the O- and E-beams of the image frames performed before the rejoining of the separate frames. Frames 1 to 4 give the wavelength callibrated spectra of the O- and E-beams for each 1/2 waveplate orientation. The last panel gives the cross-correlated signal between the O- and E-beams per 1/2 waveplate orientation, along with the maximum lag (in Å), or shift between the two solutions, given by the vertical lines.

the sources are summarised in Table 3.3.

Since the SALT pupil changes during observations, the amount of light collected by the telescope during the observations does not remain constant. Because of this, absolute flux calibration of SALT spectroscopic data is not possible without independent photometric measurements. Relative flux calibration, however, is possible by using additional spectropolarimetric observations of spectrophotometric standard stars. For the data presented in this project, the flux calibrations of a selection of sources were performed using the standard polSALT pipeline, with spectrophotometric standard star LTT 7987 observed in three different observational setups (see Table 3.4).

3.2 Optical Photometry

The purpose of photometry as it relates to this project, is to serve as a complement to the SALT spectropolarimetric observations, and to investigate the optical fluxes of the blazars as they enter a high/active state. To this end, optical photometric observations were taken with the LCO Telescope Network.

The LCO Telescope Network

The LCO is an optical photometric telescope network consisting of twenty-five telescopes at seven different sites around the world. The network consists of various 2-metre, 1-metre and 0.4-metre telescopes, each designed and suited for the observation of transient

Table 3.3: The SALT RSS spectropolarimetry observational setups for all sources. The observation dates, grating, grating angle, arc lamp used and exposure time of all of the blazars observed in both observing campaigns (2021-2-LSP-001, 2019-2-MLT-001) are given. Note that the exposure time is given as the exposure time per 1/2 waveplate angle, multiplied by the number of 1/2 waveplate angles used, with four corresponding to LINEAR mode, and eight corresponding to LINEAR-HI mode.

Target	Obs. Dates	Grating	Grating Angle (°)	Arc Lamp	Exp. Time (s)
PKS 0426–380	2017-01-21	PG0300	5.375	Ar	600×4
	2017-02-20				
PKS 0447–439	2017-02-21	PG0900	19.625	Ne	120×4
			12.500	ThAr	
TXS 0506+056	2017-10-15	PG0900	14.000	Ar	600×4
	2017-10-21		12.875	ThAr	
PKS 0537–441	2019-01-14	PG0900	14.375	Ar	650×4
	2019-03-05				
PKS 1454–354	2021-06-13	PG0300	5.375	Ar	600×4
AP Lib	2020-05-14 -	PG0300	5.375	Ar	30×8
	2021-07-31				
PKS 0035–252	2018-07-21	PG0300	5.375	Ar	625×4
PKS 0131–522	2017-11-19	PG0300	5.375	Ar	800×4
	2017-11-22				
PKS 0208–512	2019-12-05	PG0300	5.750	Ar	300×8
	2019-12-19				
4FGL J0231.2–4745	2019-10-23	PG0900	15.500	Xe	274×8
	2019-10-29				
PKS 0346–279	2018-02-09	PG0300	5.375	Ar	500×4
	2021-11-05				600×4
PKS 0837+012	2021-03-16	PG0300	5.375	Ar	500×4
PKS 0907–023	2017-01-19	PG0300	5.375	Ar	600×4
PKS 1034–293	2020-05-15 -	PG0300	5.375	Ar	600×4
	2021-06-11				
3C 273	2017-06-13	PG0300	5.375	Ar	20×8
	2017-06-14				
PKS 1424–418	2022-07-26	PG0900	12.875	ThAr	600×4
	2022-08-15				
PKS 1510–089	2021-04-06 -	PG0900	12.875	ThAr	300×4
	2022-07-31				
PKS 2023–07	2016-04-16	PG0300	5.375	Ar	300×8
	2018-10-04				

Table 3.4: The observational setup with which the spectrophotometric standard LTT 7987 was observed with the SALT RSS.

Spectrophotometric Standard	Grating	Grating Angle (°)	Obs. date
	PG0300	5.375	
LTT 7987	PG0300	5.750	2022-09-03
	PG0900	12.875	

astronomical events.[7]

All the optical photometry observations for this project were taken as a quasi-contemporaneous, ToO complement to the SALT spectropolarimetric observations of strongly variable sources detectable by H.E.S.S. and the *Fermi*-LAT in the high-energy (γ-ray) regime. The observations were taken with the various 1.0 m telescopes using Sinistro CCD (charge-coupled device) cameras at various observatories within the telescope network. All of the observational details are summarised in Table 3.5, including observation dates, exposure times, filters, and observatories used.

Data Reduction

The raw LCO photometry data is first processed through the automated BANZAI[8] pipeline, which performs the initial reduction steps. This includes bad pixel masking, bias and dark subtraction, flat-field correction, source extraction, and astrometric calibration. Corrections are also done to standardise the CCD response across the multiple instruments/telescopes that form part of the LCO telescope network. The final data are multi-extension FITS frames, and these image frames are available from the LCO observing portal.

Photometry was performed on all LCO data frames using a python-based pipeline, built on ASTROPY,[9] PHOTUTILS,[10] and ASTROQUERY.[11] First, using ASTROQUERY, all sources within a radius of $0°13'01''$ around the target are found in the AAVSO[12] Photometric All Sky Survey (APASS) DR9 catalogue (accessed via Vizier[13]). The APASS9 survey was conducted in eight different filters (Johnson B and V, and Sloan g', r', i', z_s, and Z), and currently contains photometric information for 128 million objects over 99% of the sky (Henden et al., 2016, 2018). The position and magnitude of all found sources in the preferred filters is then downloaded.

To avoid faint and overexposed sources, the source list is trimmed to sources between $\sim 7^{\text{th}}$ and 16^{th} magnitude, since this falls within the magnitude range that APASS9 is valid for. Sources that did not have any repeat measurements, and/or had bad measurements, were removed. Where needed, the Johnson-Cousins R and I magnitudes were found by converting the Sloan magnitudes using the conversion functions for Sloan to Johnson-Cousin filters for stars:[14]

$$R = r' - 0.2936\,(r' - i') - 0.1439 \tag{3.1}$$

$$\sigma(R) = \sqrt{(0.7064 \times \sigma(r'))^2 + (0.2936 \times \sigma(i'))^2}, \tag{3.2}$$

and:

[7] https://lco.global/
[8] `https://github.com/LCOGT/banzai`
[9] `https://www.astropy.org/`
[10] `https://pypi.org/project/photutils/`
[11] `https://www.astropy.org/astroquery/`
[12] The American Association of Variable Star Observers, `https://www.aavso.org/`
[13] `https://vizier.u-strasbg.fr/viz-bin/VizieR-2`
[14] `https://www.sdss3.org/dr8/algorithms/sdssUBVRITransform.php#Lupton2005`

Table 3.5: Observational setup for each source observed with the LCO. The observatory acronyms refer to Siding Spring Observatory (coj), SAAO (cpt), McDonald Observatory (elp), Cerro Tololo Interamerican Observatory (lsc), Haleakala Observatory (ogg), and Teide Observatory (tfo). Note that the number of exposures for each source, in each filter, is given in brackets after the filter name.

Target	Obs. Dates	Exp. Time per Obs. (s)	Observatory	Filters
TXS 0506+056	2017-10-15 - 2018-12-08	50	coj, lsc, cpt	B(5), V(5), R(5), I(5)
PKS 0537–441	2019-03-05 - 2019-03-10	10	cpt, lsc	B(30), V(30), R(30)
AP Lib	2020-05-15 - 2021-06-29	10	coj, cpt, lsc	B(38), V(52), R(50), I(47)
PKS 0035–252	2018-07-15 - 2018-07-19	250	coj, cpt, lsc	B(17), V(18), R(18), I(17)
PKS 0131–522	2017-11-19 - 2017-11-27	400	coj, cpt, lsc	B(3), V(24), R(24), I(3)
PKS 0208–512	2019-12-09 - 2019-12-25	30	coj, lsc	B(10), V(9), R(10), I(7)
4FGL J0231.2–4745	2019-10-22 - 2019-11-14	30	coj, cpt, lsc	B(190), V(189), R(338
PKS 0346–279	2018-02-08 - 2021-11-08	250	coj, cpt, lsc	g'(2), r'(9), i'(2)
PKS 0837+012	2021-03-16 - 2021-03-18	150	coj, cpt, lsc	g'(5)
PKS 1034–293	2021-11-30 - 2021-07-21	100	coj, cpt, lsc	B(33), V(32), R(31), I(32)
3C 273	2017-05-12 - 2017-06-14	10	coj, cpt, elp, lsc	B(9), V(9), R(10), g'(18), r'(18), i'(17)
PKS 1424–418	2022-07-22 - 2022-07-30	120	coj, cpt	B(3), V(6)
PKS 1510–089	2018-08-05 - 2020-06-22	60	coj, cpt, elp, lsc, ogg, tfn	B(247), V(235), R(94), I(44), r'(61)
PKS 2023–07	2017-10-13 - 2017-10-15	250	coj, cpt	B(6), V(6), R(6), i'(6)

$$I = r' - 1.2444\,(r' - i') - 0.3820 \tag{3.3}$$

$$\sigma(I) = \sqrt{(-0.2444 \times \sigma(r'))^2 + (1.2444 \times \sigma(i'))^2}. \tag{3.4}$$

Next, the pipeline calculates the instrumental magnitude, using standard aperture photometry with PHOTUTILS, for all sources for a range of aperture and annulus sizes (1 – 20 for aperture radii, and 25 or 30 for annulus radii, both in pixels). The aperture and annulus radii which give the highest average signal-to-noise ratio, $\langle \mathrm{S/N} \rangle$, are used for the final magnitude calculations.

The instrumental magnitude of the target is converted to the apparent magnitude by performing a linear fit of the instrumental to catalogue (apparent) magnitudes of the other measured sources. The fit is performed with an orthogonal distance regression (ODR) method, using the implementation in SCIPY.[15] The ODR method is used in order to obtain a residual from the fit that takes into account the errors for both the dependent and independent variables. Thus, when fitting a straight line to the apparent magnitude (m_{app}) as a function of the instrumental magnitude (m_{inst}):

$$m_{\mathrm{app}} = a\, m_{\mathrm{inst}} + b, \tag{3.5}$$

the error in both a and b will be calculated and given along with the diagonal ab term from the covariance matrix. The final error in the target magnitude is then calculated as an error propagation of a possibly nonlinear combination, $m_{\mathrm{app}}(a, b)$, in the form of a truncated series expansion:

$$\sigma\left(m_{\mathrm{app}}\right) = \left[\left|\frac{\partial m_{\mathrm{app}}}{\partial a}\right|^2 \sigma(a)^2 + \left|\frac{\partial m_{\mathrm{app}}}{\partial b}\right|^2 \sigma(b)^2 + \left|\frac{\partial m_{\mathrm{app}}}{\partial a}\right| \left|\frac{\partial m_{\mathrm{app}}}{\partial b}\right| \sigma(ab)\right]^{1/2}. \tag{3.6}$$

Sigma-clipping is also performed to remove any outliers above a 3σ level, and the target's apparent magnitude is calculated from the resulting fit. An example of a successful fit of the catalogue magnitude versus the instrumental magnitude, with sigma-clipping implemented, is shown in Figure 3.7.

From the apparent magnitudes for the source in the various filters produced by this pipeline, the apparent magnitude lightcurves can be converted to flux lightcurves by using flux zero point values[16] and Galactic extinction parameters for each filter.[17] The formulae used for the magnitude-to-flux conversion are given by:

$$F_\nu = F_0 \times 10^{\frac{A_\lambda - m_{\mathrm{app}}}{2.5}} \tag{3.7}$$

$$\sigma\left(F_\nu\right) = -\frac{\ln(10)}{2.5} \times F_\nu \times \sigma(m_{\mathrm{app}}), \tag{3.8}$$

where m_{app} is the apparent magnitude, F_0 is the flux zero point, and A_λ is the galactic extinction coefficient. The flux zero point values depend only on the filter in question, and

[15] `https://scipy.org`

[16] `http://coolwiki.ipac.caltech.edu/index.php/Central_wavelengths_and_zero_points`

[17] `https://irsa.ipac.caltech.edu/applications/DUST/`

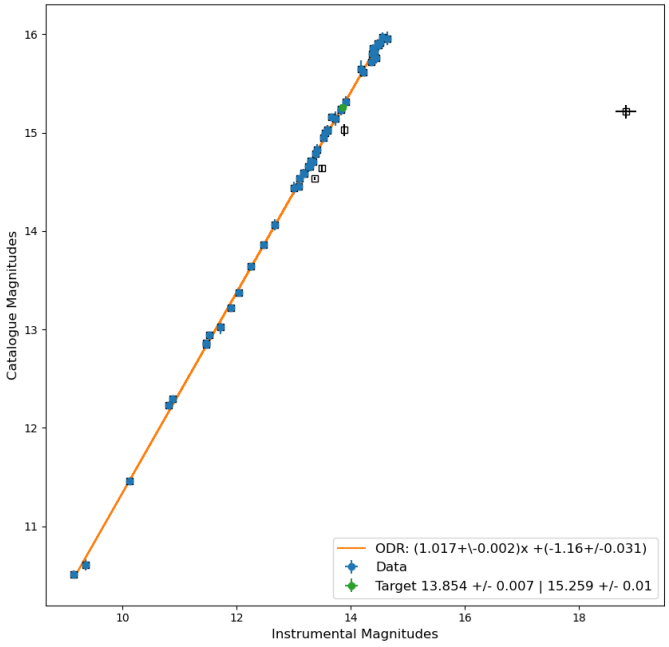

Figure 3.7: An example of the fit to the catalogue magnitudes as a function of the instrumental magnitudes for all the comparison stars within the defined search radius on the image, with sigma-clipping implemented (black squares are the data points thrown out by the sigma-clipping). From this fit, the magnitude of the target is calculated, and indicated by the green datapoint.

the values for each filter used are listed in Table 3.6. Note that the Sloan filters (g', r', and i') are all in the AB magnitude system, and, therefore, one flux zero point value is used for all of them. The Galactic extinction coefficients give the amount of extinction due to Galactic dust reddening, which is dependent on both the filter/bandpass and the region of the sky that the source is located in (line of sight towards the source; Schlafly and Finkbeiner, 2011; Schlegel et al., 1998). Hence, these values are unique for each source, and are tabulated in Table 3.7.

3.3 Gamma-ray Observations

Gamma-ray observations were obtained from the *Fermi* Gamma-ray Space Telescope, a space-based observatory that covers an energy range from 8 keV to ∼300 GeV. Launched

Table 3.6: The flux zero point values used to convert apparent magnitudes to flux values using Equations 3.7 and 3.8. Note that, since the Sloan filters are already in the AB magnitude system (i.e. with reference to a flat spectrum source), the flux zero point is the same for all bands.

Filter	Flux Zero Point F_0 (Jy)
B	4000.87
V	3597.28
R_C	3080.00
I_C	2432.84
All Sloan Filters	3631.00

Table 3.7: Galactic extinction coefficients for each source, in each bandpass/filter it was observed in. These are the extinction coefficients used to convert apparent magnitudes to flux values using Equations 3.7 and 3.8.

Target	Filter	Extinction Coefficient A_λ (mag)
TXS 0506+056	B	0.466
	V	0.349
	R	0.284
	I	0.211
PKS 0537–441	B	0.162
	V	0.122
	R	0.099
AP Lib	B	0.596
	V	0.446
	R	0.363
	I	0.270
	g'	0.523
PKS 0035–252	B	0.063
	V	0.047
	R	0.039
	I	0.029
PKS 0131–522	B	0.111
	V	0.083
	R	0.067
	I	0.050
PKS 0208–512	B	0.087
	V	0.065
	R	0.053
	I	0.039
4FGL J0231.2–4745	B	0.064
	V	0.048
	R	0.039
PKS 0346–279	g'	0.041
	r'	0.030
	i'	0.023
PKS 0837+012	g'	0.178
PKS 1034–293	B	0.223
	V	0.167
	R	0.136
	I	0.101
3C 273	B	0.089
	V	0.067
	R	0.054
	g'	0.078
	r'	0.057
	i'	0.043
PKS 1424–418	B	0.529
	V	0.396
PKS 1510–089	B	0.437
	V	0.327
	R	0.266
	I	0.198
	r'	0.278
PKS 2023–07	B	0.163
	V	0.122
	R	0.100
	i'	0.079

Table 3.8: The Likelihood Analysis Summary used to extract the information given on the *Fermi* LCR.

Time bins	3 day, 1 week, and 1 month
Energy bins	100 MeV - 100 GeV
Event selection	P8R3_SOURCE
Instrument response function	P8R3_SOURCE_V3
Acceptance cone (ROI)	12 deg (radius)
Zenith angle cut (zmax)	90 deg
Fit optimizer	MINUIT
Galactic interstellar emission model	gll_iem_v07.fits
Isotropic spectral template	iso_P8R3_SOURCE_V3_v1
4FGL-DR2 catalog	gll_psc_v27.fit
Upper limits confidence level	95% (Bayesian profile)
Minimum detection threshold	TS = 1-4 ($\sim$1-2σ)

in 2008, it houses two science instruments: the Large Area Telescope (LAT), and the Gamma-ray Burst Monitor (GBM). Its main instrument, the LAT, is a pair-production telescope with a large field of view (covering $\sim 20\%$ of the sky at any given instant), and an angular resolution of $\sim 0.6^{\circ}$ at 1 GeV (Abdo et al., 2009; Atwood et al., 2009). It is a continuously monitoring instrument, covering the entire sky roughly every three hours. All *Fermi*-LAT data are publicly available, and can be freely accessed and reduced with standard analysis software provided by the *Fermi* Science Support Centre.[18]

A new database of light-curves for over 1500 variable γ-ray sources in the 10-year *Fermi*-LAT point source catalogue has been launched in 2021, called the *Fermi* Light Curve Repository (LCR).[19] The likelihood analysis summary of the LCR's operation is given in Table 3.8. The LCR provides flux-calibrated lightcurves on 3-day, 1-week or 1-month binned timescales covering the entire *Fermi* mission (2008 – present, Fermi Large Area Telescope Collaboration, 2021). All *Fermi*-LAT γ-ray light-curves presented in this project were taken from the *Fermi*-LCR to complement the optical photometric and spectropolarimetric data from SALT and LCO. All of the data for this project was downloaded from the LCR with 3-day binning, a minimum detection significance (test-statistic, or TS-value) of TS = $4(2\sigma)$, and was fitted with a fixed photon index. An additional selection cut to exclude any datapoints with TS > 0, was performed on the data prior to plotting the γ-ray lightcurves.

It should be noted that, while the LCR is advantageous if the user wants a quick view of the γ-ray lightcurves of a source, care should be taken when using the the information given by the LCR, as there are some caveats in the resulting data produced by the LCR. For example, while the likelihood analysis summarised in Table 3.8 works well for most time bins, there is no set strategy recommended by the *Fermi*-LAT collaboration, and higher level analyses are required to verify the fit convergence. Although contamination from solar flares and/or gamma-ray bursts are accounted for, the effects of the Sun and Moon during quiescence, however, are not. Lastly, since the data is made available on the LCR in real-time, the resulting data is not validated by the LAT collaboration, and it is up to the user to perform sanity checks on the data prior to use.

[18] https://fermi.gsfc.nasa.gov/ssc/

[19] `https://fermi.gsfc.nasa.gov/ssc/data/access/lat/LightCurveRepository/`

Above was a detailed discussion on the instruments and observational setup for all the data used in this project. In the next chapter, the observational results will be presented and discussed, along with a brief literature review of some highlighted sources. Additional results for sources not highlighted in the main body of the text are given in Appendix A.

Chapter 4

Summary of Observational Results

This chapter will provide a detailed, source-specific outline of the results for a selection of blazars that formed part of the larger sample of eighteen blazars (see Table 3.1 in Chapter 3). These were selected due to the presence of interesting or compelling behaviour, generally characterised by the increase in activity in the optical and γ-ray regime, or good observational coverage. Section 4.1 will cover the results for three BLLs (TXS 0506+056, PKS 0537–441 and AP Lib); two that presented flaring activity as observed under the transient SALT programme (as outlined in Chapter 3), and one that was observed over a long period under the long-term SALT observing campaign. Section 4.2 will cover six FSRQs (PKS 0131–522, PKS 0208–512, 4FGL J0231.2–4745, PKS 1034–293, PKS 1510–089 and PKS 2023–07), of which five were observed under the transient monitoring programme, and one was observed under the long-term monitoring campaign. The results for the other sources are summarised in Appendix A.

4.1 BL Lac-Type Objects

Three BLLs will be highlighted in this section. TXS 0506+056 and PKS 0537–441 formed part of the ToO SALT transients observing campaign, and was observed during a period of enhanced activity. AP Lib is the chosen BLL for the long-term observing campaign, and was observed eighteen times over a period of approximately one year (from 2020 May to 2021 July).

4.1.1 TXS 0506+056

TXS 0506+056 is a BLL with a redshift of $z = 0.337$, apparent visual magnitude of $V = 14.78$ and synchrotron peak frequency $\nu_{\rm sy} = 3.55 \times 10^{14}\,$Hz. It has most famously been associated with neutrino production (as detected by ICE Cube) during an enhanced/flaring γ-ray state in 2017 (see e.g. de Naurois and H. E. S. S. Collaboration, 2017; Dornic and Coleiro, 2017; Evans et al., 2017; Franckowiak et al., 2017; Lucarelli et al., 2017; Mirzoyan, 2017; Steele, 2017; Tanaka et al., 2017; van Soelen et al., 2017).

The γ-ray lightcurve for TXS 0506+056 from 2017 July to 2018 February is shown in Figure 4.1, where the enhanced γ-ray activity is visible from ∼MJD 57985, having increased by a factor of ~ 6 when compared to the average flux reported in the 3FGL *Fermi*-LAT catalogue (Tanaka et al., 2017). To investigate the behaviour of the optical

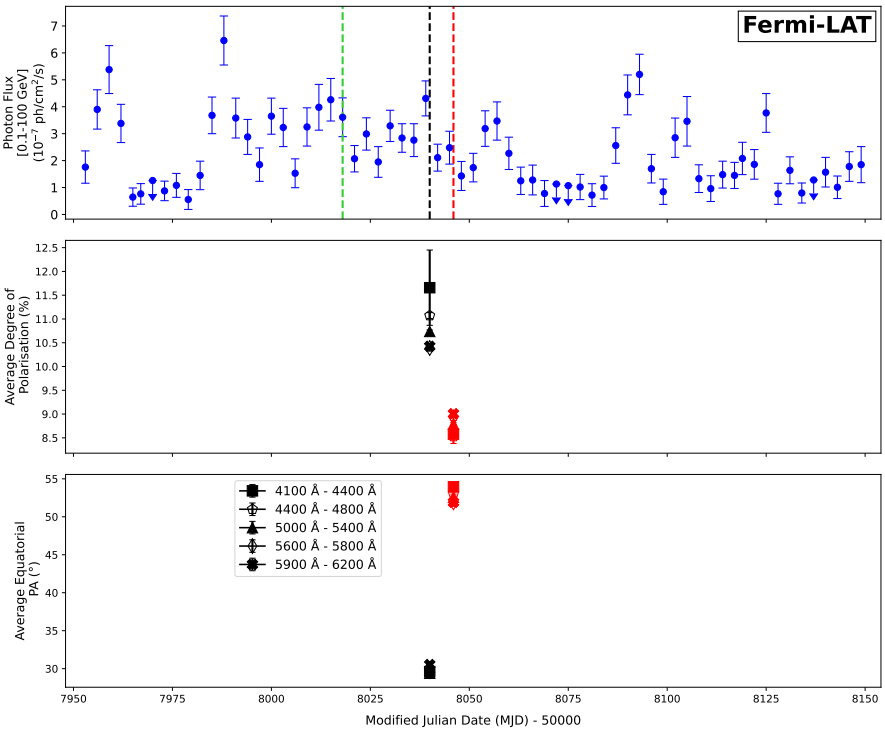

Figure 4.1: Gamma-ray lightcurve (top panel) for the BLL, TXS 0506+056, where the black and red dashed lines indicate the dates of the SALT spectropolarimetric observations, and the green dashed line indicates the date of neutrino detection from this source. The second and third panels give the averaged degree of polarisation and equatorial polarisation angle in five different wavelength bands, reported for each of the two SALT observations.

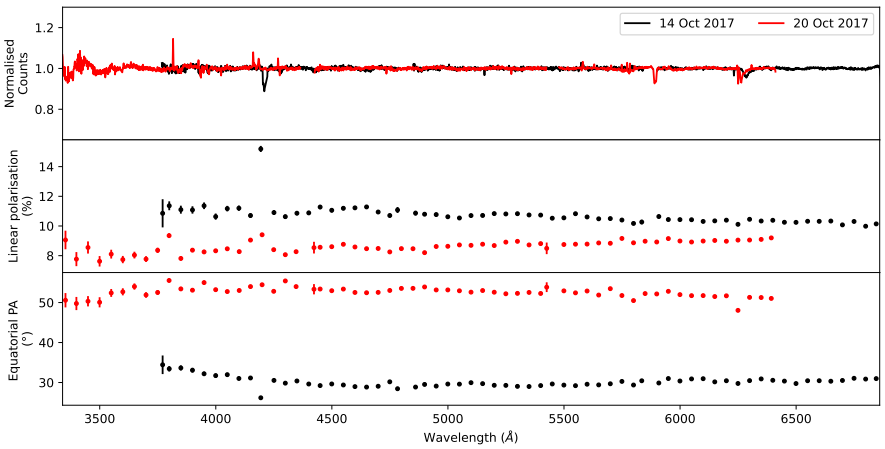

Figure 4.2: Spectropolarimetric observations for the BLL, TXS 0506+056, observed on 2017 October 14 and 2017 October 20. The top panel gives the normalised counts spectra of the two observations, where the middle and bottom panels give the degree of linear polarisation, and the equatorial polarisation angle, respectively. The gaps in the black spectrum in the top panel from $\lambda = 4790 - 4850$ Å, $\lambda = 5845 - 5895$ Å and $\lambda = 6250 - 6325$ Å are due to the removal of the two chip gaps of the CCD detector mosaic and a skyline, respectively. The gaps in the red spectrum from $\lambda = 4365 - 4425$ Å, $\lambda = 5420 - 5575$ Å and $\lambda = 6250 - 6325$ Å are due to the removal of the two chip gaps of the CCD detector mosaic and a skyline, respectively.

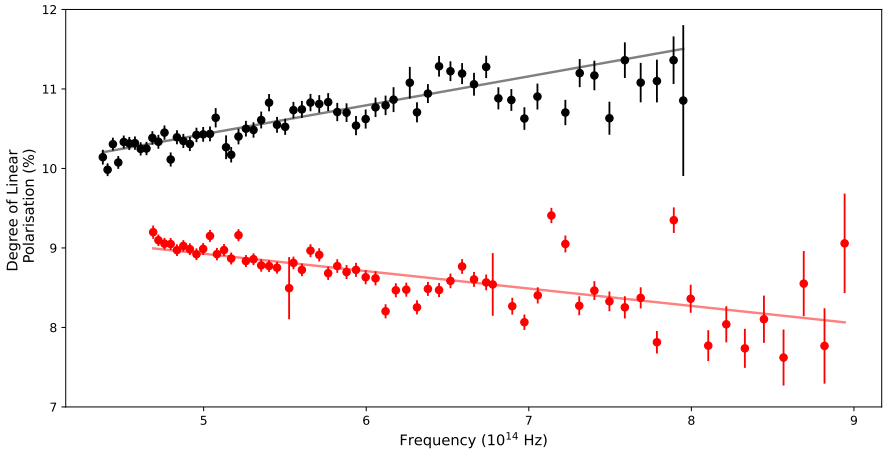

Figure 4.3: The degree of linear polarisation as a function of frequency for the BLL, TXS 0506+056, on both of the SALT observation dates. The black and red datapoints indicate the polarisation as observed on 2017 October 14 and 2017 October 20, respectively.

polarisation during this period of enhanced γ-ray activity and associated neutrino production, two SALT spectropolarimetric observations were taken on 2017 October 14 and October 20, respectively, as shown in Figure 4.2.

The redshift was determined by Paiano et al. (2018) from high S/N spectra (S/N = 650 – 1200), exhibiting three weak emission lines in the range of $\lambda = 4100 - 9000\,\text{Å}$. The emission lines were [O II] at $\lambda = 4981.14\,\text{Å}$, [O III] at $\lambda = 6691.86\,\text{Å}$, and [N II] at $\lambda = 8798.18\,\text{Å}$. Given the wavelength range of the observations, the [O II] and [O III] emission lines should, therefore, be visible in the spectra shown in Figure 4.2, but do not seem to appear. This could be due to a number of reasons. Firstly, the SALT optical spectra do not have high enough S/N ratios. Secondly, since the observational data had substantial cosmic-ray contamination, it may be that some cosmic rays were on the trace of the target, and cosmic ray cleaning was not sufficient to extract "clean" spectra.

During the first spectropolarimetric observation, the averaged degree of polarisation was observed to be $\langle \Pi \rangle = 10.73 \pm 0.34\,\%$[1] (from $\lambda = 4000 - 6400\,\text{Å}$), with an average polarisation angle of $29.92 \pm 0.86°$. The second observation displayed a slightly lower degree of polarisation of $\langle \Pi \rangle = 8.65 \pm 0.36\,\%$, with a polarisation angle of $52.43 \pm 1.49°$.

Note that the optical lightcurve for this source is not shown, as only one observation was taken during the 2017 flaring period. To investigate the jet activity during the reported period, the degree of linear polarisation is shown in Figure 4.3. During the first spectropolarimetric observation, the degree of polarisation increased towards higher frequencies, and during the second observation, it decreased towards higher frequencies. This might indicate that the observed emission transitioned from shock-dominated to accretion disc dominated between the two observations. Note that nearly all sources (excluding PKS 0131–522 and PKS 0907–023), were observed with an accompanying comparison star on the slit to compare the polarisation of the blazars to the general degree – and slope – of polarisation within that region of the sky. The slope of the frequency

[1]The errors in the reported values for the averaged degree of polarisation and polarisation angle are taken as the standard deviation of the data. However, note that some spectra show an intrinsic frequency dependent slope in the degree of polarisation.

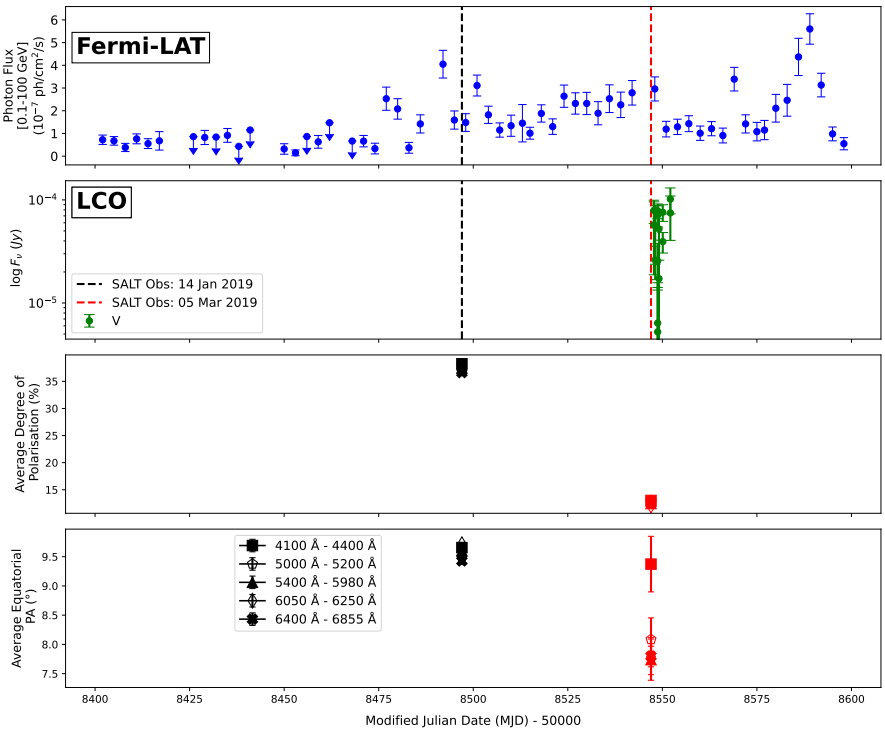

Figure 4.4: Gamma-ray (top panel) and optical (second panel) observations for the BLL, PKS 0537–441, where the black and red dashed lines indicate the dates of the SALT spectropolarimetric observations. The third and fourth panels give the averaged degree of polarisation and equatorial polarisation angle in five different wavelength bands, reported for each of the two SALT observations.

dependece of the polarisation, as well as the degree of polarisation of the comparison star was always checked to ensure that the residual polarisation was low. Since blazars are extragalactic sources, there is an expected, yet low, level of polarisation that arises from the interstellar medium (ISM) that cannot be fully accounted for during the reduction processes, and a $\sim 2\,\%$ systematic error is assumed for all of the results.

4.1.2 PKS 0537–441

PKS 0537–441 is a highly luminous and variable extragalactic source with a redshift of $z = 0.894$ and apparent visual magnitude of $V = 16.48$ (see Table 3.1), that was identified as a quasi-stellar object in 1972 as part of the Palomar survey (Peterson and Bolton, 1972). It is an LBL with a synchrotron peak frequency of $\nu_{\rm sy} = 6.24 \times 10^{12}$ Hz, as stated in the 4LAC catalogue (Table 3.1). It was known to have regular outbursts over the years, and was classified as a BLL due to its continuous optical spectrum (Cristiani, 1985). However, it was later found to have broad emission lines, which is a distinct trait of FSRQs (Wilkes et al., 1983). The presence of broad emission lines hints that PKS 0537–441 might be a transitional object between an FSRQ and a BLL (D'Ammando, 2010).

In mid-December 2018, PKS 0537–441 was observed to be steadily recovering from a low state in the γ-ray wavelength band (Nesci and Ojha, 2019), with the flux increasing by a factor of ~ 12 when compared to the average historical flux as recorded by the *Fermi* 4FGL catalogue. The γ-ray and optical behaviour of PKS 0537–441 during the reported period is shown in Figure 4.4, and the recovery from the low state in 2018 can be seen clearly in the *Fermi*-LAT γ-ray lightcurve at around MJD 58465. The optical photometric

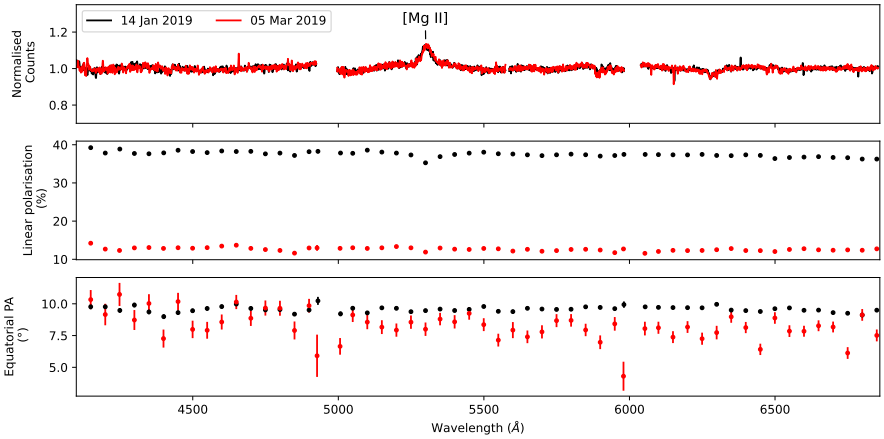

Figure 4.5: Spectropolarimetric observations for the BLL, PKS 0537–441, observed on 2019 January 14 and 2019 March 05. The top panel gives the normalised counts spectra of the two observations, where the middle and bottom panels give the degree of linear polarisation, and the equatorial polarisation angle, respectively. The gaps in the spectra in the top panel from $\lambda = 5575 - 5586$ Å, $\lambda = 4925 - 4995$ Å, and $\lambda = 5982 - 6038$ Å are due to the removal of a skyline, and the two chip gaps of the CCD detector mosaic, respectively.

data during the reported period is unfortunately sparse, and, as a result, not much can be deduced from the lightcurve.

A SALT spectropolarimetric observation was taken on 2019 January 14, revealing a high degree of linear polarisation, with an average of $\langle \Pi \rangle = 37.52 \pm 0.66\,\%$ between 4100 Å and 6855 Å (Figure 4.5). The high degree of polarisation observed indicates that the emission is dominated by the non-thermal synchrotron emission originating in the jet-component.

Approximately three months later, on 2019 March 05, the BLL was observed in a high state again with a significantly lower degree of linear polarisation of $\langle \Pi \rangle = 12.60 \pm 0.51\,\%$ (between 4100 Å and 6855 Å). During both observations, the equatorial polarisation angle remained fairly constant ($9.57 \pm 0.19°$ and $8.36 \pm 1.01°$, respectively), rotating only by $\sim 1.21°$. The optical spectra display a forbidden [Mg II] emission line at $\lambda = 5303.52 \pm 1.49$ Å. No significant change in the [Mg II] emission line strength was observed between the two spectropolarimetric observations, with the equivalent widths measured to be $|W_\lambda| = 6.39 \pm 0.17$ Å, and $|W_\lambda| = 6.48 \pm 0.24$ Å, respectively. Note that all reported equivalent widths (W_λ) of spectral features reported in this project were calculated by (as outlined in a discussion by Vollmann and Eversberg, 2006):

$$W_\lambda = \int_{\lambda_1}^{\lambda_2} \left(\frac{F_c - F_s}{F_c} \right) d\lambda, \tag{4.1}$$

with an error of:

$$\sigma(W_\lambda) = \sqrt{1 + \left(\frac{\langle F_c \rangle}{\langle F_s \rangle} \right)} \left(\frac{\Delta\lambda - W_\lambda}{S/N} \right), \tag{4.2}$$

where F_c is the continuum/background flux, F_s is the flux of the spectral line, $\Delta\lambda$ is the wavelength range over which the equivalent width is measured, and S/N is the signal-to-noise ratio of the spectrum. Here, the S/N ratio was estimated as the average of the background counts divided by the standard deviation of the background counts, i.e.

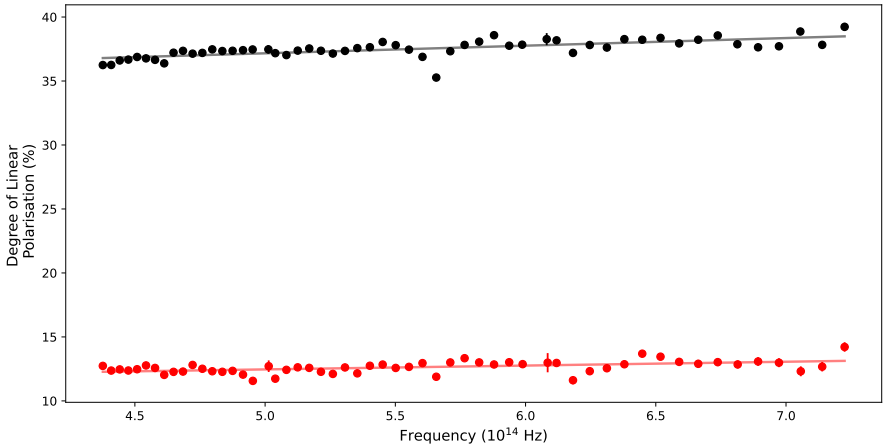

Figure 4.6: The degree of linear polarisation as a function of frequency for the BLL, PKS 0537–441, on both of the SALT observation dates. The black and red datapoints indicate the polarisation as observed on 2019 January 14 and 2019 March 05, respectively.

$\langle F_c \rangle / \sigma(F_c)$.

To investigate the activity in the jet during the reported period for PKS 0537–441, the degree of linear polarisation as a function of frequency is given in Figure 4.6. For both of the SALT observations, the degree of linear polarisation increases with decreasing wavelength (i.e. towards the optical/UV end). Since PKS 0537–441 is an LBL, the increase towards higher energies could be indicating that there is a shock travelling downstream in the jet, with the bulk of the synchrotron radiation centred at the shock. Thus, the polarisation will be highest at higher (X-ray) frequencies, and decreases towards lower frequencies. This is in agreement with the enhanced γ-ray activity, or high-state emission, as noted by Nesci and Ojha (2019).

4.1.3 AP Lib

AP Lib is a BLL that shows remarkably similar features to that of the namesake of BLLs; BL Lacertae, with a smooth optical spectrum and faint emission/absorption features (Rodgers, 1971). It was classified as the optical counterpart to the radio source, PKS 1514–241 (Bond, 1971), and was classified as a BLL-type object in 1973 by Bond (1973). AP Lib is a nearby source, with a redshift of $z = 0.049$, and apparent visual magnitude of $V = 14.00$ (see Table 3.1). The SMBH-mass has been found to be $\sim 10^{11.40 \pm 0.03}\,\mathrm{M}_\odot$ (Woo et al., 2005), and is an LBL with a synchrotron peak frequency of $\nu_{\mathrm{sy}} = 5.90 \times 10^{13}\,\mathrm{Hz}$ (as found by Hervet et al., 2015), or $\nu_{\mathrm{sy}} = 9.06 \times 10^{13}\,\mathrm{Hz}$ (as in the 4LAC catalogue, cited in Table 3.1).

The source exhibits an extremely broad high-energy component, making it difficult to model the emission with single-zone SSC or EC models (Roychowdhury et al., 2022). AP Lib was detected in the TeV energy range in 2015 by H.E.S.S., and is one of four known LBL-type blazars that emit in the VHE regime (H. E. S. S. Collaboration et al., 2015). Interestingly, AP Lib also has a resolved non-thermal X-ray jet (Kaufmann et al., 2013).

AP Lib has been monitored closely over the period between 2020 May to 2021 July as part of the long-term observing campaign. To complement the optical spectropolari-

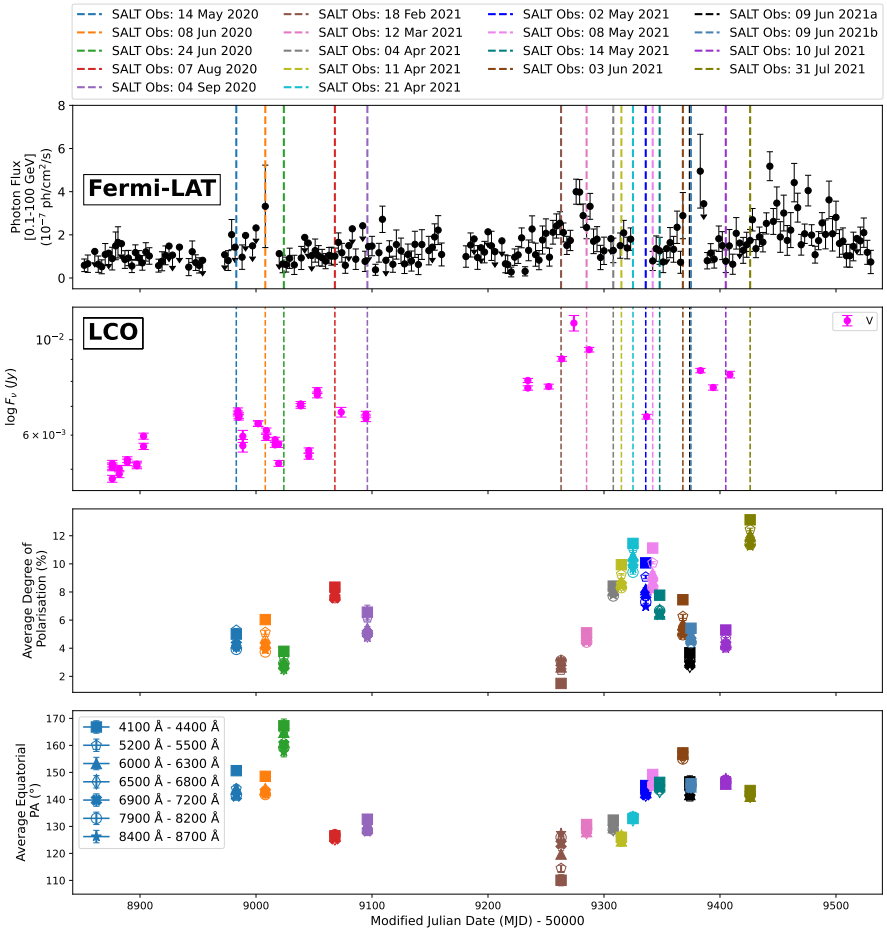

Figure 4.7: Gamma-ray (top panel) and optical (second panel) lightcurves of the BLL, AP Lib, along with the averaged degree of polarisation and equatorial polarisation angle in seven different wavelength bands, reported for each SALT observation (third and bottom panel, respectively).

Table 4.1: Equivalent widths of the [Mg I] and [N II] emission lines for each spectropolarimetric observation taken for the BLL, AP Lib.

Obs. Date	[Mg I] (Å)	[N II] (Å)	Obs. Date	[Mg I] (Å)	[N II] (Å)
2020-05-14	1.99 ± 0.49	2.01 ± 0.18	2021-04-21	0.94 ± 0.44	2.58 ± 0.16
2020-06-08	2.27 ± 0.43	1.46 ± 0.16	2021-05-02	1.46 ± 0.41	2.26 ± 0.15
2020-06-24	3.55 ± 0.54	1.18 ± 0.20	2021-05-08	0.51 ± 0.39	2.57 ± 0.14
2020-08-07	1.31 ± 0.46	2.57 ± 0.16	2021-05-14	1.42 ± 0.56	1.80 ± 0.20
2020-09-04	2.69 ± 0.61	2.60 ± 0.23	2021-06-03	0.49 ± 0.39	4.09 ± 0.14
2021-02-18	0.34 ± 0.38	3.27 ± 0.14	2021-06-09	1.32 ± 0.49	3.81 ± 0.17
2021-03-12	0.28 ± 0.34	3.17 ± 0.12	2021-06-10	1.13 ± 0.29	3.77 ± 0.10
2021-04-04	1.05 ± 0.42	1.56 ± 0.15	2021-07-10	0.14 ± 0.39	3.81 ± 0.14
2021-04-11	1.13 ± 0.36	2.22 ± 0.13	2021-07-31	1.59 ± 0.27	4.41 ± 0.10

metric data, the γ-ray and optical fluxes in the reported time period are shown in Figure 4.7. The γ-ray flux in the top panel of Figure 4.7 maintained low levels of variability, remaining fairly constant up to $\sim$ MJD 59200, after which there is a steady increase in the observed γ-ray emission lasting up to $\sim$ MJD 59400. The optical fluxes, though with less coverage, follow the same trend (as seen in the middle panel of Figure 4.7). The bottom two panels of Figure 4.7 give the average degree of polarisation and the average polarisation angle in different wavelength ranges for each SALT observation. The average degree of polarisation seems to follow the same trend of variation as the optical and γ-ray lightcurves, but appears to lag behind during the 2021 semester.

AP Lib was observed successfully with SALT 18 times (Figure 4.8), during which the average degree of polarisation fluctuated between $\langle \Pi \rangle = 12.00 \pm 0.66\,\%$ and $\langle \Pi \rangle = 2.72 \pm 0.56\,\%$ within the wavelength range of $\lambda = 3900 - 9150\,$Å. During this period, the equatorial polarisation angle rotation fluctuated within a range of $42.49 \pm 0.73°$. The optical spectra display two forbidden lines, namely [Mg I] ($\lambda = 5426.10 \pm 40.64\,$Å) and [N II] ($\lambda = 6876.16 \pm 7.33\,$Å). The Ca II H & K lines are also seen in the optical spectra. The equivalent widths of the [Mg I] and [N II] emission lines for each of the spectropolarimetric observations are tabulated in Table 4.1.

During all but one of the SALT observations, the degree of linear polarisation increases towards higher frequencies (see Figure 4.9). This indicates that (since AP Lib is an LBL) the polarisation is likely concentrated around some form of shock travelling in the jet-component, and is therefore centred around X-ray frequencies and falls off to the lower frequency range. During one observation, however, on 2021 February 18, the polarisation decreases toward the blue end, which is consistent with the non-thermal synchrotron emission being diluted by the thermal accretion disc component. However, the accretion disc component generally contributes less in BLLs than FSRQs, and a strong dilution of the polarisation is not expected. Interestingly, this negative slope in the degree of polarisation is seen for the date on which the lowest degree of polarisation is observed, as shown in Figure 4.10.

There is a general trend in the data from Figure 4.10 for this source, where the frequency dependent slope of the polarisation becomes increasingly positive towards higher degrees of polarisation. A Spearman's test was performed on the data shown in Figure

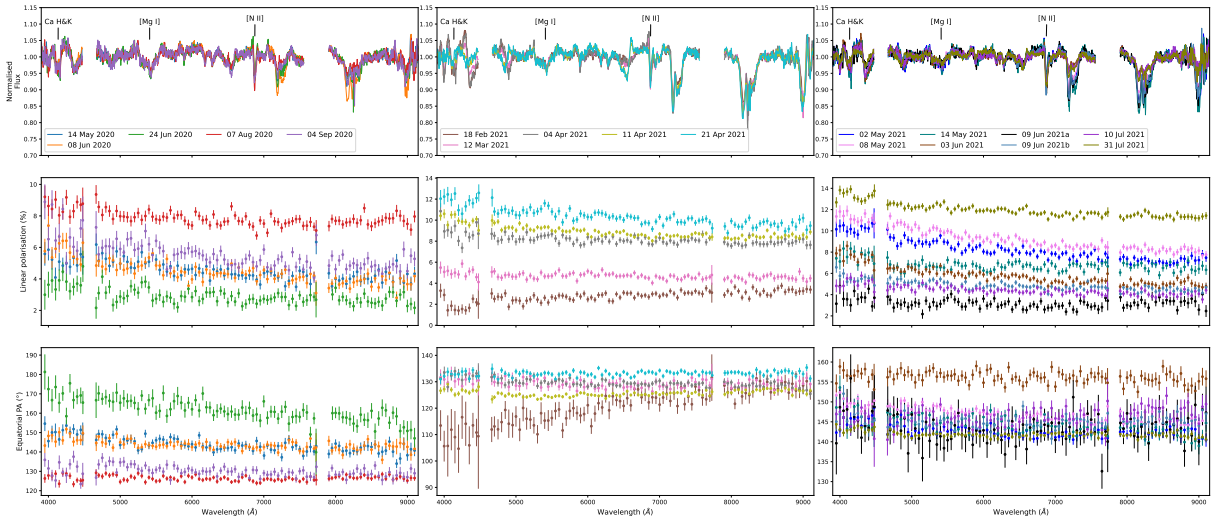

Figure 4.8: Spectropolarimetric observations for the BLL, AP Lib, observed between 2020 May 14 and 2021 July 31, separated into three different terms. The top panels give the normalised flux spectra of the two observations, where the middle and bottom panels give the degree of linear polarisation, and the equatorial polarisation angle for each observation, respectively. The gaps in the spectra in the top panels from $\lambda = 7560 - 7700$ Å, $\lambda = 4475 - 4670$ Å, and $\lambda = 7725 - 7900$ Å are due to the removal of a skyline, and the two chip gaps of the CCD detector mosaic, respectively.

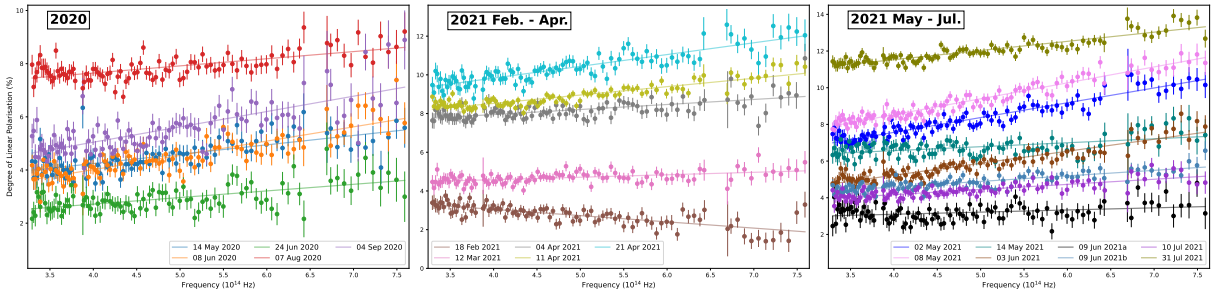

Figure 4.9: The degree of linear polarisation as a function of frequency for the BLL, AP Lib, on all eighteen of the SALT observation dates, separated into three terms: the 2020, 2021 February to April, and 2021 May to July observing periods, respectively). The different coloured datapoints represent the observation dates, as labelled in Figure 4.8.

4.10, and a correlation of $\rho = 0.618$ (p-value $= 6.251 \times 10^{-3}$) was found. The Spearman's rank correlation test measures the strength as well as the direction of a relationship between two variables as a way of estimating the monotonicity of a dataset. This correlation is given by,

$$\rho = 1 - \frac{6\Sigma d_i^2}{n(n^2-1)}, \tag{4.3}$$

where d_i is the difference between the ranks of each corresponding variable, and n is the number of points in the dataset. The quoted p-value is the probability that the observed correlation of the variables is due to randomness of the data, as opposed to it being significant and/or sufficient to support a true correlation. A significant correlation has a p-value generally defined to be < 0.05.

An interesting feature arising from the observational results outlined in Figures 4.7 to 4.10, is that the increase in the γ-ray and optical fluxes appears to occur long before there is an observed increase in the degree of linear polarisation (the regions of interest are highlighted in the first two plots of Figure 4.11). Since the optical data is sparse and unevenly sampled, a z-transformed discrete correlation function (zDCF; Alexander, 2014)

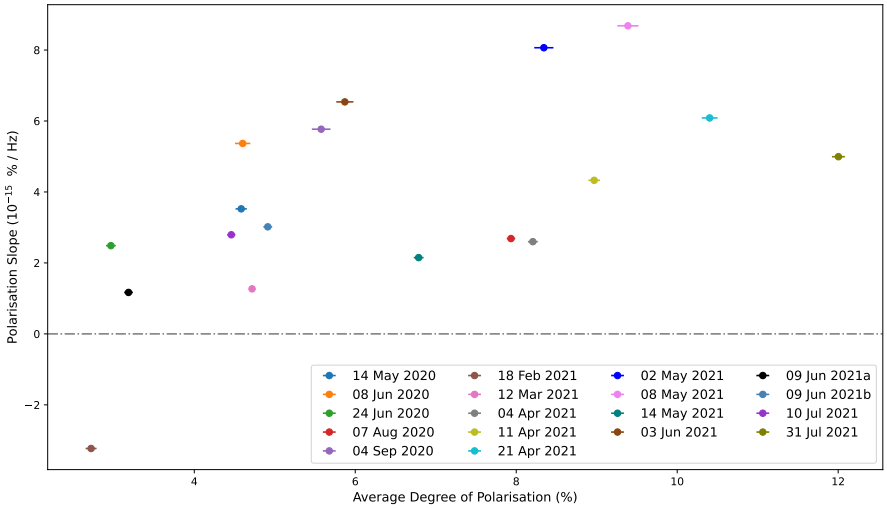

Figure 4.10: The frequency dependent slope of the degree of polarisation as a function of the averaged degree of polarisation for each of the observation dates, as observed for the BLL, AP Lib. The dashed grey line indicates where the slope is zero.

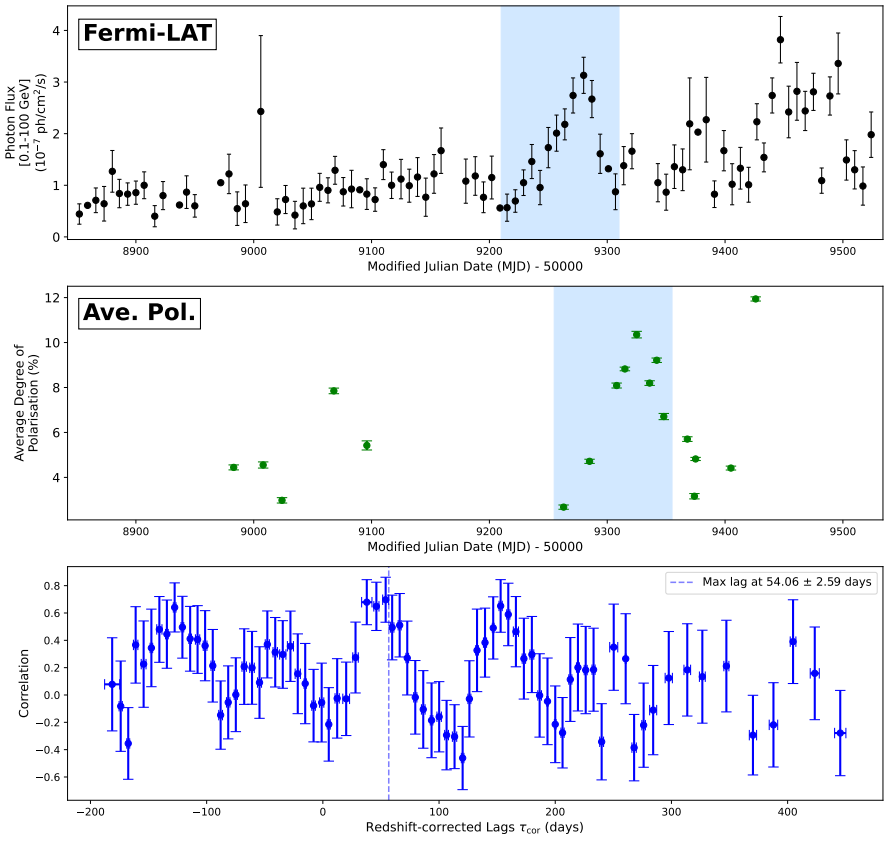

Figure 4.11: The zDCF performed between the γ-ray lightcurve and the average degree of linear polarisation for the BLL, AP Lib, to investigate the time-lag between the two events.

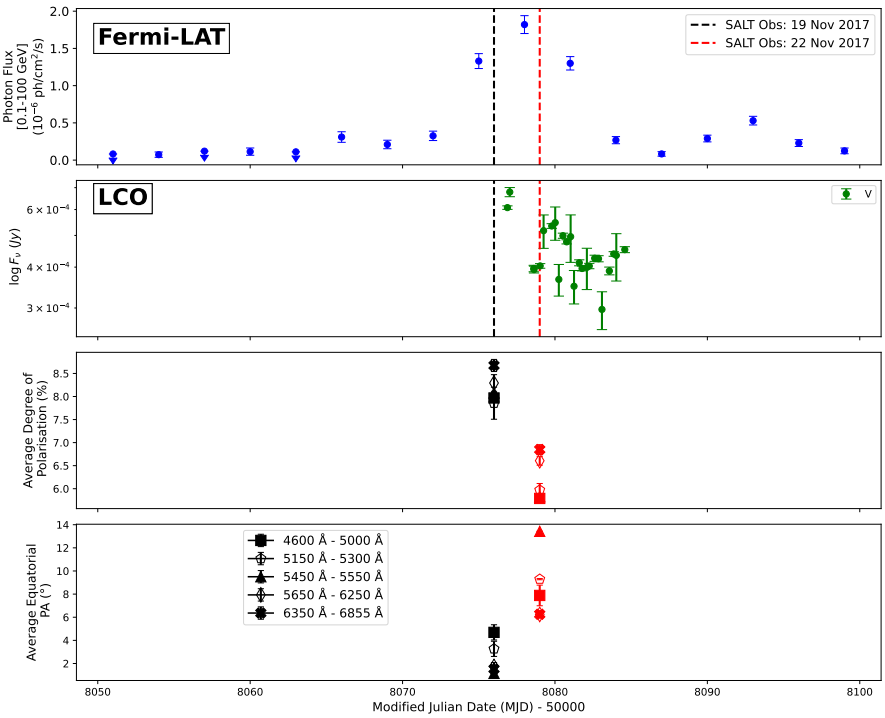

Figure 4.12: Gamma-ray (top panel) and optical (second panel) observations for the FSRQ, PKS 0131–522, where the black and red dashed lines indicate the dates of the SALT spectropolarimetric observations. The third and last panel gives the averaged degree of polarisation and equatorial polarisation angle in six different wavelength bands, reported for each of the two SALT observations.

was performed between the γ-ray lightcurve and the average degree of linear polarisation to determine the time lag between these two events. The resulting correlation function is shown in the bottom panel of Figure 4.11. The zDCF indicated that the increase in γ-ray flux occurred 54.06 ± 2.59 days before there is an observed spike in the degree of linear polarisation.

The observed time-lag, along with the fact that the polarisation slope changed between 2021 February 18 (where it decreases towards higher frequencies) and the next observation on 2021 March 12 (where the polarisation increases towards higher frequencies again), may indicate that the jet of AP Lib undergoes some sort of large-scale change. However, we caution that we are limited by the observational data, and further investigation will be required to confirm this hypothesis.

4.2 Flat-Spectrum Radio Quasars

Below, the results for six FSRQs are highlighted. Of these, five (PKS 0131–522, PKS 0208–512, 4FGL J0231.2–4745, PKS 1510–089 and PKS 2023-07) were observed under the ToO SALT transients observing campaign, and one (PKS 1034–293) was observed for the long-term programme.

4.2.1 PKS 0131–522

PKS 0131–522 has a reported redshift of $z = 0.020$, apparent visual magnitude of $V = 20.30$, and $\nu_{\rm sy} = 4.37 \times 10^{12}$ Hz (as in Table 3.1). It has only recently been identified

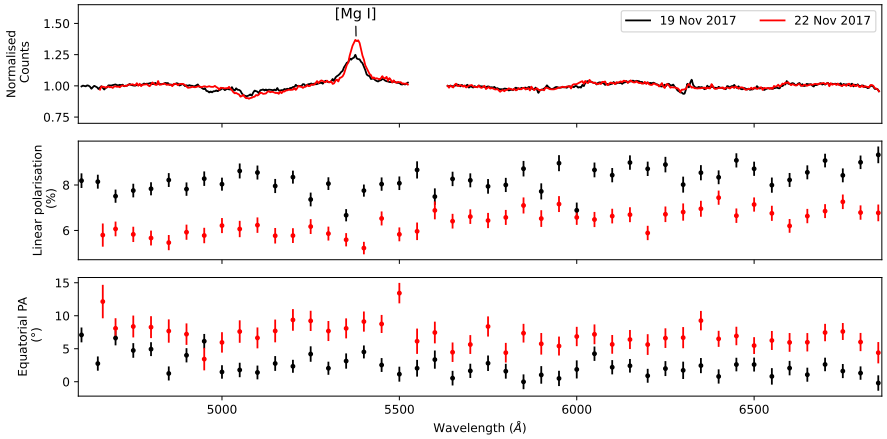

Figure 4.13: Spectropolarimetric observations for the FSRQ, PKS 0131–522, observed on 2017 November 19 and 2017 November 22. The top panel gives the normalised counts spectra of the two observations, where the middle and bottom panels give the degree of linear polarisation, and the equatorial polarisation angle, respectively. The gaps in the spectra in the top panel at $\lambda = 5525 - 5635$ Å are due to the removal of a skyline.

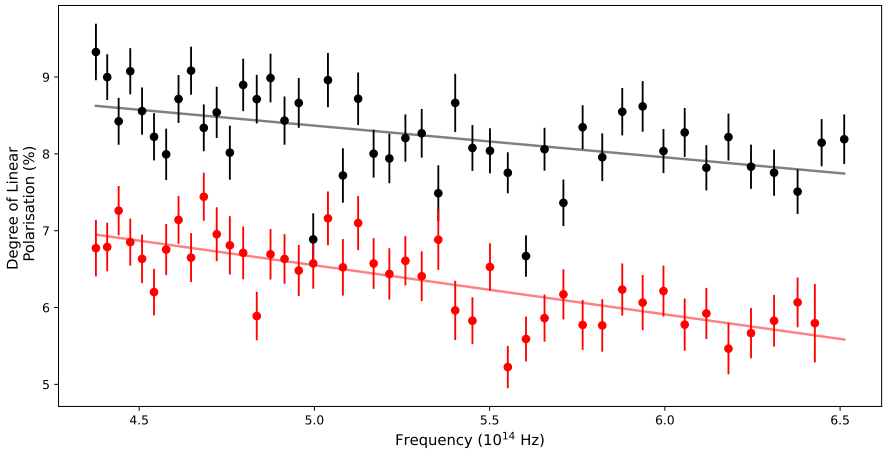

Figure 4.14: The degree of linear polarisation as a function of frequency for the FSRQ, PKS 0131–522, on both of the SALT observation dates. The black and red datapoints indicate the polarisation as observed on 2017 November 19 and 22, respectively.

as an FSRQ, and was not published in any of the *Fermi*-LAT catalogues prior to 2014 (Becerra et al., 2014). It was first detected by the LAT on 2014 June 5. Three years later, in 2017 November, it entered an extremely high flux state (detected by both AGILE and *Fermi*-LAT), increasing by a factor of 200 relative to the average γ-ray flux reported in the 3FGL *Fermi*-LAT catalogue (Ojha et al., 2017; Piano et al., 2017).

The 2017 November γ-ray flare can be seen in the top panel of Figure 4.12, and to observe this source in its flaring state, optical spectropolarimetric observations were taken on 2017 November 19 and 22, just before and just after the peak of the flare. Again, the optical lightcurve in the second panel of Figure 4.12 is sparse, but is highest during the peak of the γ-ray flare (reaching a maximum of $V = 16.89 \pm 0.04$ on MJD 58077), as expected. On November 19, the average degree of polarisation was $\langle \Pi \rangle = 8.28 \pm 0.49\,\%$ between 4600 Å and 6855 Å (as seen in Figure 4.13). On November 22, the average degree of polarisation decreased to $\langle \Pi \rangle = 6.43 \pm 0.52\,\%$. Between the two SALT observations, the equatorial polarisation angle changes from $2.44 \pm 1.65°$ to $7.05 \pm 2.04°$.

The optical spectra display a strong emission line at $\lambda = 5375.57 \pm 2.80$ Å. During the first observation, the observed emission line had an equivalent width of $|W_\lambda| = 11.99 \pm 0.27$ Å (likely diminished due to the increased jet activity), and increased to $|W_\lambda| = 15.32 \pm 0.22$ Å during the second observation as the jet contribution decreases after the flare. Using the published redshift, this emission line does not correspond to any of the typical blazar lines. The closest match would be [Mg I]. The published redshift given in Table 3.1 is taken from NED, and appears to come from Johnston et al. (1995), but no spectrum is shown. Hence, assuming the observed emission line is [Mg I], using a rest wavelength of $\lambda_0 = 5172.68$ Å, we propose a new redshift of $z = 0.039 \pm 0.001$.

The degree of linear polarisation during both observations decreased towards the higher frequency end, as shown in Figure 4.14. The comparison star observed for this source had an average degree of polarisation of $\langle \Pi \rangle = 2.50 \pm 1.45$ %, with a fairly flat, if slightly increasing towards higher frequencies, slope. This is an indication that, for PKS 0131–522, the thermal accretion disc component dilutes the polarisation/non-thermal synchrotron component at higher frequencies during the flare.

4.2.2 PKS 0208–512

PKS 0208–512 is a highly variable γ-ray blazar that was first identified as the optical counterpart of an unresolved radio source in 1976 (Savage, 1976; Stacy et al., 2003). It is a relatively bright, distant source with a redshift of $z = 1.003$, apparent visual magnitude of $V = 16.93$, and $\nu_{\rm sy} = 8.61 \times 10^{12}$ Hz. This source is highly variable, known to emit regularly at γ-ray energies, and has been in this "recurring" active state for the last couple of decades (Khatoon et al., 2022).

PKS 0208–512 was in a state of enhanced γ-ray activity from 2019 October to 2020 May 31 (MJD 58780 – 59000), and underwent a major flaring event from 2019 November to 2020 May. On 2019 November 29, the *Fermi*-LAT detected enhanced γ-ray activity from the source, with the γ-ray flux increasing by a factor of 13 when compared to the averaged daily flux in the 4FGL *Fermi*-LAT catalogue (Angioni, 2019). This flaring state is comparable to the previous highest γ-ray flare observed by the LAT for this source in 2011 May (Szostek, 2011). Two major flares occurred during this period, peaking on 2019 December 16 and 2020 March 15, respectively (Khatoon et al., 2022).

To observe the source during its 2019/2020 flare, two SALT spectropolarimetric observations were taken in 2019 December to investigate the changes in the observed polarisation signatures during the first major flaring event of this extremely high state. The optical and γ-ray fluxes of PKS 0208–512 are shown in the first two panels of Figure 4.15. There is a visible increase in the γ-ray flux from MJD 58810, with two peaks, or sub-flares during the high/flaring state in the observed emission around which the SALT spectropolarimetric observations were taken (reaching maxima in the γ-ray regime of $\mathrm{F}(0.1 - 100\,\mathrm{GeV}) = 1.16 \pm 0.10 \times 10^{-6}\,\mathrm{ph\,cm^{-2}\,s^{-1}}$ and $\mathrm{F}(0.1 - 100\,\mathrm{GeV}) = 1.39 \pm 0.09 \times 10^{-6}\,\mathrm{ph\,cm^{-2}\,s^{-1}}$, respectively). The optical lightcurve does not provide coverage around the first γ-ray peak, but indicates an increase in activity around the second γ-ray peak, decreasing from $V = 15.93 \pm 0.11$ on MJD 58826 to $V = 15.64 \pm 0.08$ on MJD 58836.

The optical spectropolarimetric observations (Figure 4.16) were taken during the first

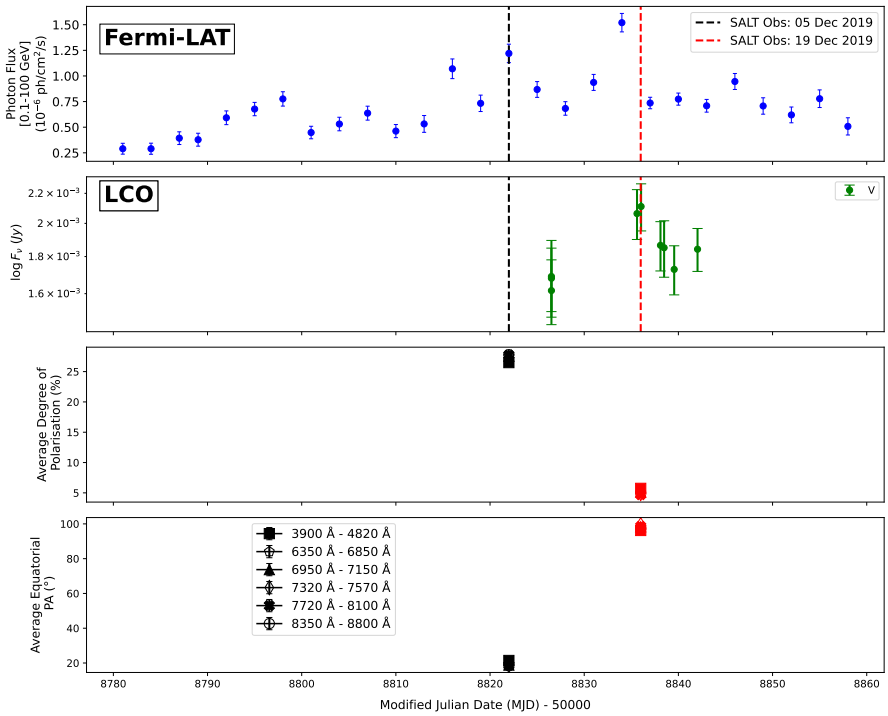

Figure 4.15: Gamma-ray (top panel) and optical (second panel) observations for the FSRQ, PKS 0208–512, where the black and red dashed lines indicate the dates of the SALT spectropolarimetric observations. The third and fourth panels give the averaged degree of polarisation and equatorial polarisation angle in six different wavelength bands, reported for each of the two SALT observations.

major flare, on 2019 December 5 and 19. During the first observation (prior to the peak of the first major flare), the average degree of polarisation from $\lambda = 3900 - 9150$ Å was observed to be $\langle \Pi \rangle = 27.30 \pm 0.54$ %. At the time of the second observation, right after the peak of the first major flare, the γ-ray and optical fluxes began to steadily decrease. Along with this, there was a decrease in the polarisation ($\langle \Pi \rangle = 5.19 \pm 0.38$ %). Between the two observations, a fairly large polarisation angle swing was observed, with a rotation from $19.56 \pm 1.03°$ to $97.65 \pm 1.49°$.

A forbidden [Mg II] emission was observed in the optical spectra at $\lambda = 5597.97 \pm 14.58$ Å. During the first observation, the [Mg II] emission line had an equivalent width of $|W_\lambda| = 10.34 \pm 0.06$ Å. At the time of the second observation, the [Mg II] emission line's equivalent width increased to $|W_\lambda| = 15.20 \pm 0.14$ Å, indicating a decrease in the non-thermal jet emission contribution in the spectrum as the flare subsided.

During the first SALT observation (before the peak of the first major flare), the degree of linear polarisation decreases towards the higher frequency end (see the black datapoints in Figure 4.17), indicating the dilution of the polarisation due to the accretion disc's contribution toward the emission. However, during the second observation shortly after the peak of the first major flare (red datapoints in Figure 4.17), the polarisation increased towards the higher frequency end. The comparison star observed for this source had an essentially flat slope, with an average degree of polarisation of $\langle \Pi \rangle = 0.99 \pm 0.39$ %. From this, it can be inferred that the observed change in the frequency dependent slope of the polarisation of PKS 0208–512 is intrinsic to the source itself. Therefore, it is possible that the jet underwent some sort of change, as such a trend is observed when there is a shock moving downstream in the jet, and the polarisation at higher (X-ray) frequencies

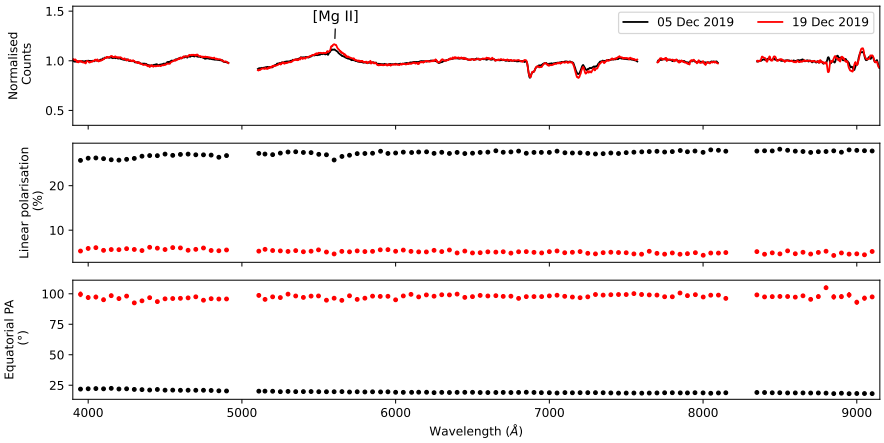

Figure 4.16: Spectropolarimetric observations for the FSRQ, PKS 0208–512, observed on 2019 December 05 and 2019 December 19. The top panel gives the normalised counts spectra of the two observations, where the middle and bottom panels give the degree of linear polarisation, and the equatorial polarisation angle, respectively. The gaps in the spectra in the top panel at $\lambda = 7575 - 7700$ Å, $\lambda = 4915 - 5100$ Å, and $\lambda = 8100 - 8350$ Å are due to the removal of a skyline, and the two chip gaps of the CCD detector mosaic, respectively.

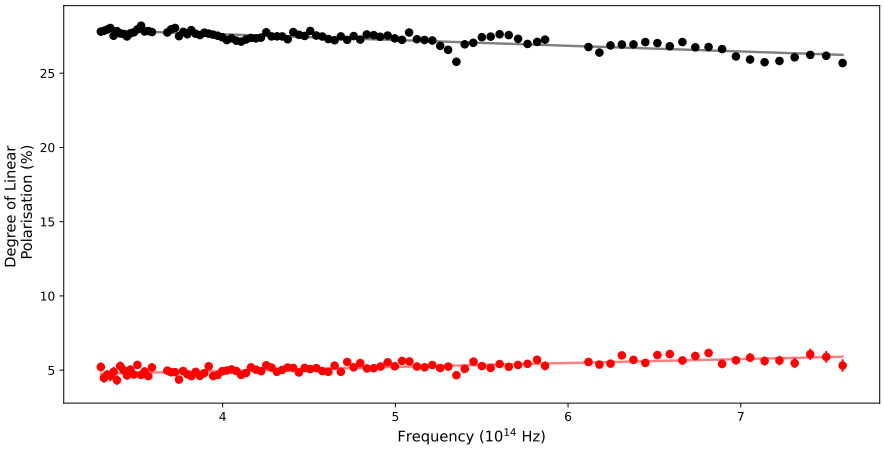

Figure 4.17: The degree of linear polarisation as a function of frequency for the FSRQ, PKS 0208–512, on both of the SALT observation dates. The black and red datapoints indicate the polarisation as observed on 2019 December 5 and 19, respectively.

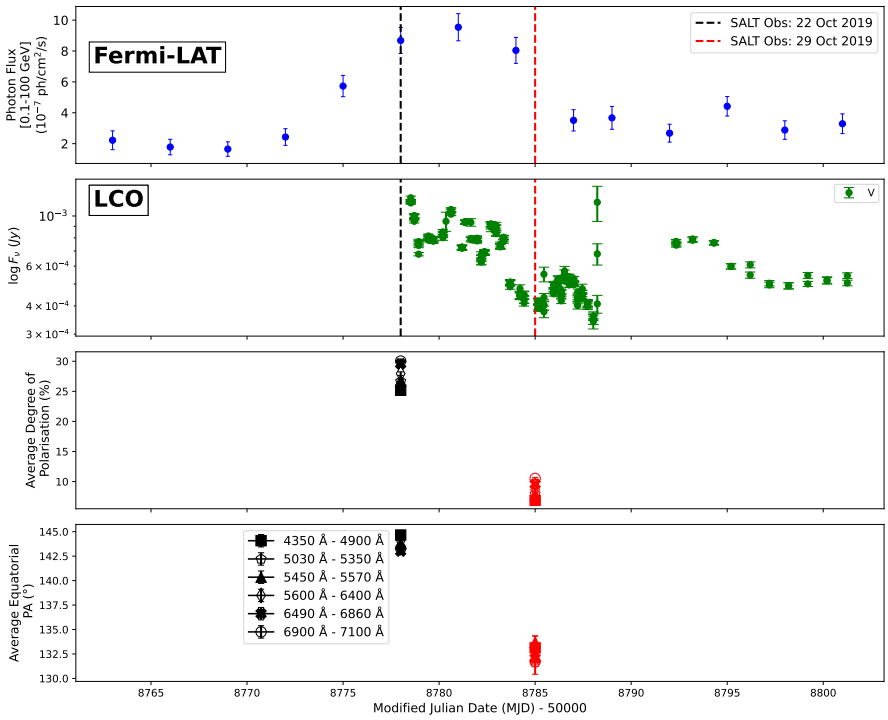

Figure 4.18: Gamma-ray (top panel) and optical (second panel) observations for the FSRQ, 4FGL J0231.2–4745, where the black and red dashed lines indicate the dates of the SALT spectropolarimetric observations. The third and fourth panels give the averaged degree of polarisation and equatorial polarisation angle in six different wavelength bands, reported for each of the two SALT observations.

are higher than at lower(optical/IR) frequencies.

4.2.3 4FGL J0231.2–4745

4FGL J0231.2–4745, or PMN J0231–4746, is a fainter FSRQ, with an apparent visual magnitude of $V = 17.87$, a redshift of $z = 0.765$, and $\nu_{\rm sy} = 1.31 \times 10^{12}$ Hz (from Table 3.1). The *Fermi*-LAT detected enhanced γ-ray activity from this source in 2019 October, starting from October 17 (Principe and Angioni, 2019). On October 19, this source reached its highest ever average daily flux, increased by a factor of 60 when compared to the average flux from the 4FGL *Fermi*-LAT catalogue (Principe and Angioni, 2019). The *Fermi*-LAT detection of the flare led to contemporaneous follow-up observations with the Swift-XRT and Swift-UVOT, and La Palma observatory, confirming enhanced flaring activity in X-ray, UV, and optical as well (D'Ammando et al., 2019; Pursimo et al., 2019).

The flare, extending from MJD 58770 to MJD 58790 in both the optical and γ-ray regimes, can be seen in Figure 4.18. During this time, the optical LCO observations show a maximum of $V = 16.24 \pm 0.02$ on MJD 58778, while the γ-ray fluxes were still on the rise (increasing from $\mathrm{F}(0.1 - 100\,\mathrm{GeV}) = 7.26 \pm 0.78 \times 10^{-7}\,\mathrm{ph\,cm^{-2}\,s^{-1}}$ on MJD 58778 to a maximum of $\mathrm{F}(0.1 - 100\,\mathrm{GeV}) = 7.66 \pm 0.79 \times 10^{-7}\,\mathrm{ph\,cm^{-2}\,s^{-1}}$ on MJD 58781). After the peak of the γ-ray flare, the optical fluxes decreased dramatically, reaching an apparent visual magnitude of $V = 17.50 \pm 0.06$ on MJD 58785.

Optical spectropolarimetric observations were taken on 2019 October 22 and 2019 October 29, and are shown in Figure 4.19. The first SALT observation, taken prior to the peak of the flare, had an average degree of polarisation of $\langle \Pi \rangle = 27.47 \pm 1.93\,\%$

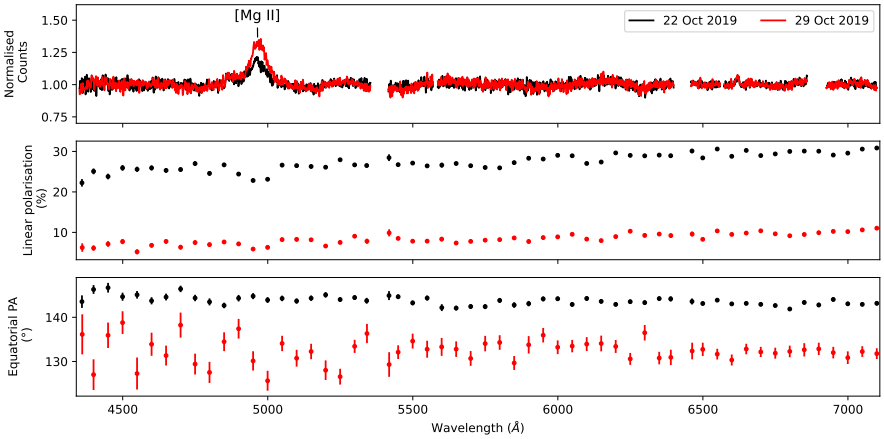

Figure 4.19: Spectropolarimetric observations for the FSRQ, 4FGL J0231.2–4745, observed on 2019 October 22 and 2019 October 29. The top panel gives the normalised counts spectra of the two observations, where the middle and bottom panels give the degree of linear polarisation, and the equatorial polarisation angle, respectively. The gaps in the spectra in the top panel at $\lambda = 5570 - 5585$ Å and $\lambda = 6560 - 6572$ Å are due to the removal of a skyline, where the gaps at $\lambda = 5355 - 5415$ Å and $\lambda = 6400 - 6458$ Å are due to the chip gaps in the CCD detector mosaic. Lastly the gap at $\lambda = 6560 - 6572$ Å is due to the removal of a cosmic ray.

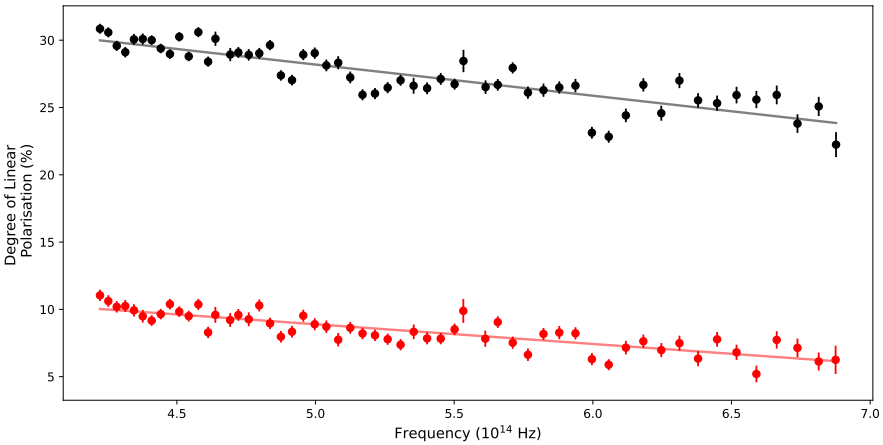

Figure 4.20: The degree of linear polarisation as a function of frequency for the FSRQ, 4FGL J0231.2–4745, on both of the SALT observation dates. The black and red datapoints indicate the polarisation as observed on 2019 October 22 and 29, respectively.

($\lambda = 4350 - 7100$ Å). During the second observation (after the peak of the flare, with significantly lower fluxes in both the optical and γ-ray bands), the observed degree of polarisation decreased to $\langle \Pi \rangle = 8.39 \pm 1.30\,\%$. The low optical and γ-ray fluxes, along with the low degree of polarisation, indicate that the non-thermal contribution to the emission was significantly lower during the second SALT observation than during the first. The polarisation angle at the time of the two observations changed from $143.76 \pm 1.01°$ to $132.61 \pm 2.76°$.

The optical spectra in Figure 4.19 also exhibit a [Mg II] emission line at $\lambda = 4966.10 \pm 6.67$ Å, with equivalent widths increasing from $|W_\lambda| = 11.79 \pm 0.98$ Å on October 22, to $|W_\lambda| = 21.27 \pm 1.20$ Å on October 29, indicating that the strength of the non-thermal emission contribution had diminished greatly between the two spectropolarimetric observations. This is in agreement with the behaviour observed in the optical and γ-ray lightcurves as shown in Figure 4.18.

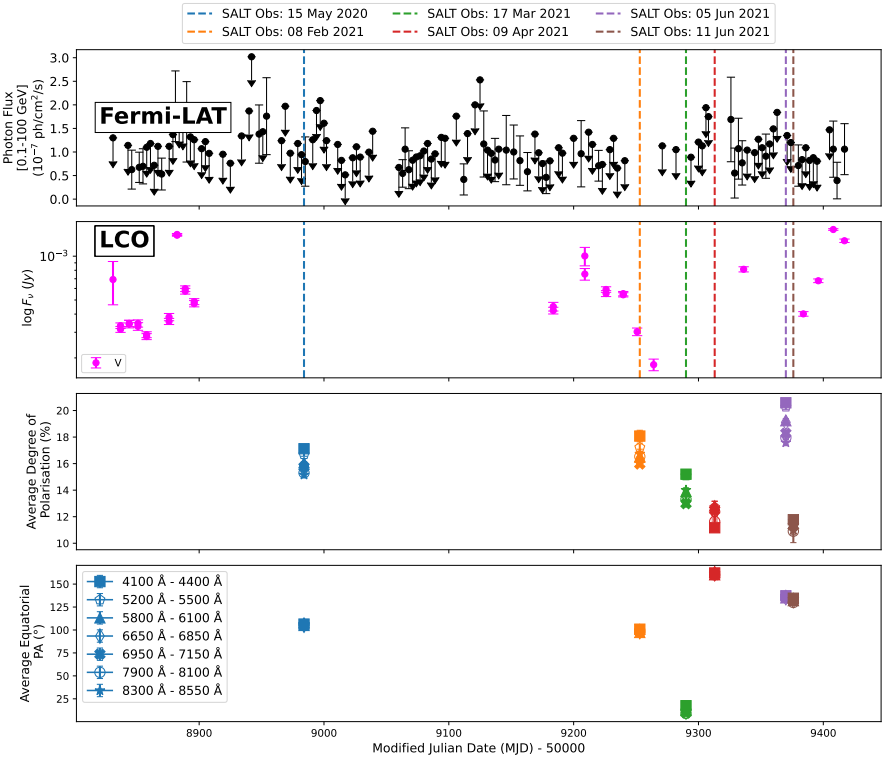

Figure 4.21: Gamma-ray (top panel) and optical (second panel) observations for the FSRQ, PKS 1034–293, along with the averaged degree of polarisation and equatorial polarisation angle in seven different wavelength bands, reported for each SALT observation (third and bottom panel, respectively).

For both of the SALT spectropolarimetric observations, the polarisation levels decreased to the blue end of the spectrum, suggesting that the non-thermal emission is diluted by the accretion disc's contribution during the flare (Figure 4.20). The comparison star observed for this source had an average degree of polarisation of $\langle \Pi \rangle = 2.50 \pm 1.45\,\%$, with an essentially flat slope, indicating that the observed negative slopes for the two observations shown in Figure 4.20 are intrinsic to the source itself.

4.2.4 PKS 1034–293

PKS 1034–293 is the selected FSRQ observed for the long-term observing campaign, and has been monitored between 2020 May and 2021 July (Figure 4.21). It is a bright, relatively nearby galaxy with a redshift of $z = 0.310$, and apparent visual magnitude of $V = 16.46$. The low-energy component of this blazar has a synchrotron peak frequency of $\nu_{\rm sy} = 8.3 \times 10^{13}$ Hz (as found by Lin et al., 2017), or $\nu_{\rm sy} = 6.92 \times 10^{12}$ Hz (as in the 4LAC catalogue, cited in Table 3.1).

The γ-ray and optical lightcurves are shown in Figure 4.21. The γ-ray fluxes fluctuate somewhat, but remain fairly low throughout the reported period, with the majority of LAT datapoints being upper limits. The bottom two panels of Figure 4.21 give the average degree of polarisation in different wavelength bands for each SALT observation.

During the reported period of observation (2020 May to 2021 June), six successful SALT spectropolarimetric observations were taken, and are shown in Figure 4.22. The average degree of polarisation reached a maximum of $\langle \Pi \rangle = 19.13 \pm 1.31\,\%$, and a minimum

Table 4.2: Equivalent widths of the two forbidden [O III] emission lines for each spectropolarimetric observation taken for the FSRQ, PKS 1034–293.

Obs. Date	$[\text{O III}]_1$ (Å)	$[\text{O III}]_2$ (Å)
2020-05-15	0.71 ± 0.04	2.71 ± 0.05
2021-02-08	2.08 ± 0.08	6.39 ± 0.09
2021-03-17	2.24 ± 0.09	6.07 ± 0.09
2021-04-09	1.71 ± 0.08	4.86 ± 0.09
2021-06-05	1.91 ± 0.06	4.83 ± 0.07
2021-06-11	1.08 ± 0.07	3.39 ± 0.07

of $\langle \Pi \rangle = 11.45 \pm 0.11\,\%$ (in the wavelength range of $\lambda = 3900 - 9150\,\text{Å}$). The equatorial polarisation angle exhibited high variability, rotating through a range of $\approx 150°$ during the observation period (from $160.72 \pm 1.91°$ to $12.03 \pm 3.12°$). An interesting feature in the behaviour of the polarisation of this source occurs in 2021 June, where the average degree of polarisation changed rapidly between the observations taken on June 05 (MJD 59370) and June 11 (MJD 59376). The polarisation changed from $\langle \Pi \rangle = 19.13 \pm 1.31\,\%$ to $\langle \Pi \rangle = 11.45 \pm 0.86\,\%$, where the polarisation angle remained effectively unchanged, observed to be $135.56 \pm 1.07°$ and $132.21 \pm 1.83°$ on the two respective dates. Two forbidden [O III] lines are observed in the optical spectra at $\lambda = 6500.02 \pm 9.20\,\text{Å}$ and $\lambda = 6561.93 \pm 5.09\,\text{Å}$. The equivalent widths of these emission lines for each of the spectropolarimetric observations are given in Table 4.2.

During all of the SALT observations, the degree of linear polarisation increased towards higher frequencies, as shown in Figure 4.23, possibly indicating that a shock is travelling in the jet. Interestingly, the γ-ray and optical lightcurves remain fairly constant at low values. This is also represented in Figure 4.24, where the trend of an increasingly positive polarisation slope of frequency dependence towards higher degrees of polarisation is again observed, similarly to what was observed for AP Lib in Section 4.1.3. However, the correlation is not significant, as a Spearman's test gives $\rho = 0.714$ (p-value = 0.111). Therefore, more data is required to fully investigate these results.

Maraschi et al. (1995) found that the X-ray spectrum is inverted in the νF_ν representation, and that the observed X-ray fluxes are in excess of the extrapolation of the optical spectrum. The authors put forth two possible interpretations for this. The first is that the observed X-ray emission is due to a different (likely IC processes) emission mechanism than the IR/optical emission (which is produced by synchrotron radiation). The second alternative is that the observed X-ray emission is the high-energy extension of the lower-energy synchrotron radiation. The latter result from Maraschi et al. (1995) could possibly provide an explanation for the increased degree of polarisation towards higher frequencies as shown in Figure 4.23, as the polarisation might be concentrated in the X-ray regime rather than the optical.

4.2.5 PKS 1510–089

PKS 1510–089 is a famous, highly polarised blazar situated at a redshift of $z = 0.36$ with an apparent visual magnitude of $V = 16.54$ and synchrotron peak frequency of

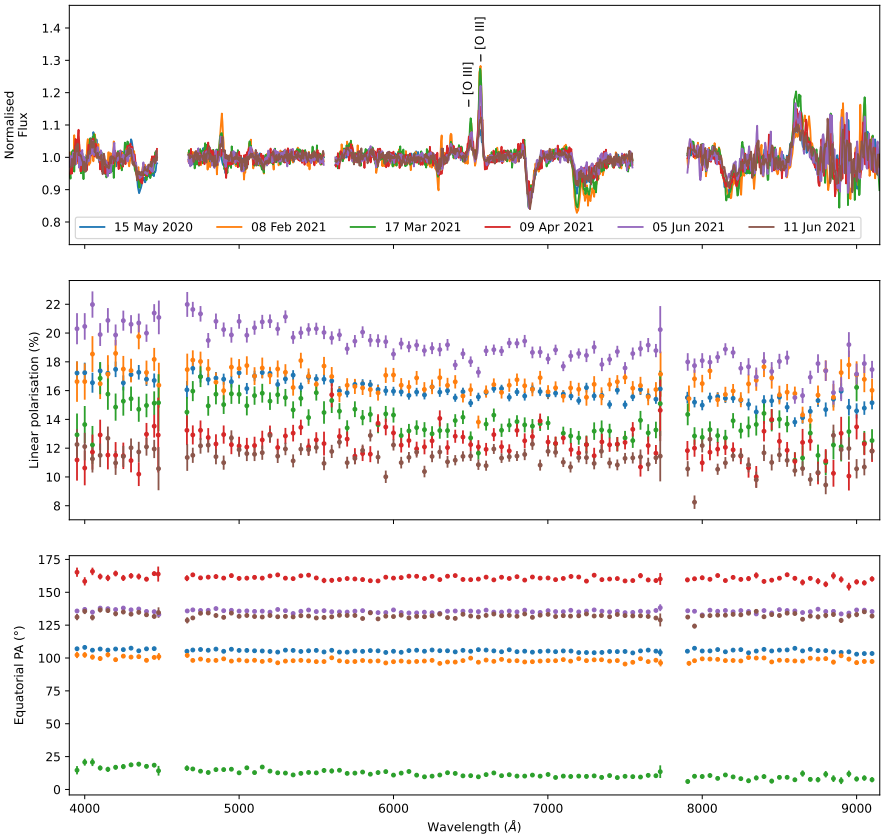

Figure 4.22: Spectropolarimetric observations for the FSRQ, PKS 1034–293, observed between 2020 May 15 and 2021 June 11. The top panel gives the normalised counts spectra of the two observations, where the middle and bottom panels give the degree of linear polarisation, and the equatorial polarisation angle, respectively. The gaps in the spectra in the top panel at $\lambda = 5550 - 5620$ Å and $\lambda = 7550 - 7700$ Å are due to the removal of a skyline, where the gaps at $\lambda = 4470 - 4670$ Å and $\lambda = 7700 - 7900$ Å are due to the chip gaps in the CCD detector mosaic.

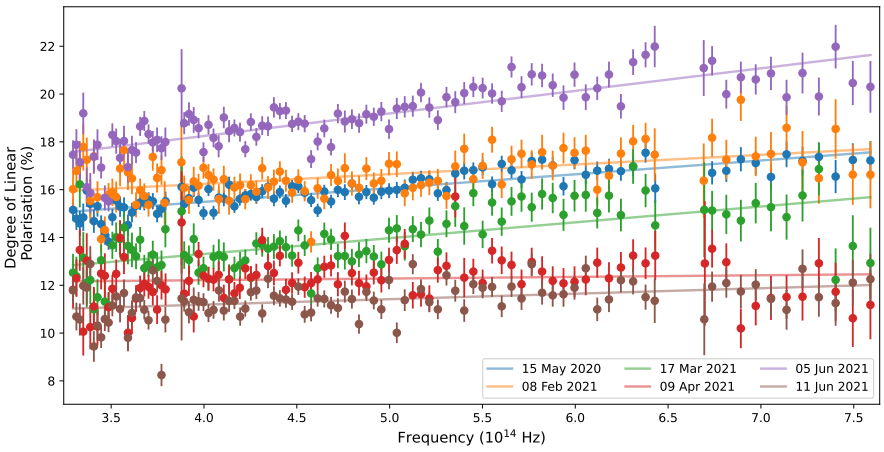

Figure 4.23: The degree of linear polarisation as a function of frequency for the FSRQ, PKS 1034–293, on all six of the SALT observation dates. The different coloured datapoints represent the observation dates, as labelled in Figure 4.22.

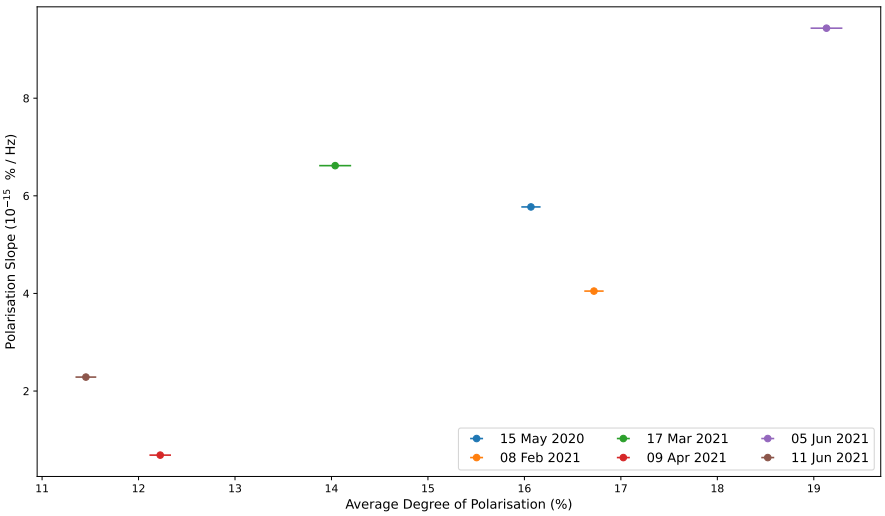

Figure 4.24: The frequency dependent slope of the degree of polarisation as a function of the averaged degree of polarisation for each of the observation dates, as observed for the FSRQ, PKS 1034–293.

$\nu_{\rm sy} = 1.10 \times 10^{13}$ Hz (as given in Table 3.1). It was classified as a flat-spectrum radio source in 1996 by Tanner et al. (1996). The source displayed highly variable emission in the γ-ray regime during the first eight years of *Fermi*-LAT monitoring, but has since been less active. During low states, strong VHE emission was still observed with MAGIC, establishing it as the first FSRQ to be a continuous or persistent VHE γ-ray emitter, possibly explained by hadronic processes (Dzhatdoev et al., 2022; Zacharias, 2018).

PKS 1510–089 is characterised as one of the most variable FSRQs, emitting very high γ-ray fluxes during outbursts. The jet-component shows superluminal motion of up to $20c$, and is one of the most highly aligned radio galaxies known (177°), i.e. the jet is in a near-perfect alignment with the observer's line of sight (D'Ammando et al., 2010; Homan et al., 2002; Wardle et al., 2005). To explain some of this source's behavioural traits, it has been proposed that the central engine might be a binary black hole system (Li et al., 2007; Wu et al., 2005).

However, from the full *Fermi*-LAT lightcurve in Figure 4.25, it is clear that the strength and regularity of the variability of PKS 1510–089 in the γ-ray regime has been gradually decreasing over time, reaching a near constant low-state in 2021 July. This source, for all its interesting traits, has been observed as part of the SALT transients spectropolarimetric monitoring campaign from 2021 April to 2022 July, and the γ-ray lightcurve around the SALT spectropolarimetry observations (2021 April to 2022 July) is given in the top panel of Figure 4.26. Since the LCO data for this source only spans the time period from 2018 August to 2020 June, no optical lightcurves were plotted for this source.

Spectropolarimetric observations with SALT were taken nineteen times between 2021 April and 2022 July, as shown in Figure 4.28. During the 2021 semester, the source was observed eight times, and exhibited some activity in the γ-ray regime (as shown in the top left panel of Figure 4.27), with the average degree of polarisation reaching a maximum of $\langle \Pi \rangle = 12.45 \pm 1.14\,\%$ and a minimum of $\langle \Pi \rangle = 2.18 \pm 0.54\,\%$ (taken from $\lambda = 4100 - 6200$Å). During this time, the polarisation angle varied substantially, ranging from $4.73 \pm 2.69°$ to $178.93 \pm 4.82°$.

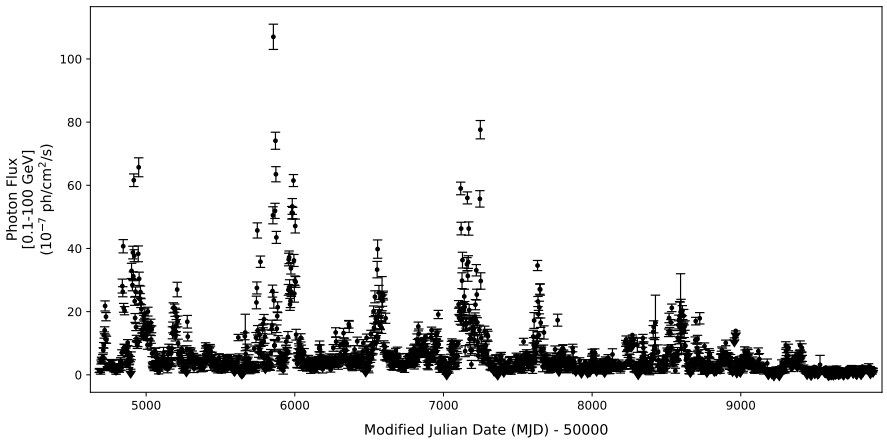

Figure 4.25: The full *Fermi*-LAT lightcurve of the FSRQ, PKS 1510–089.

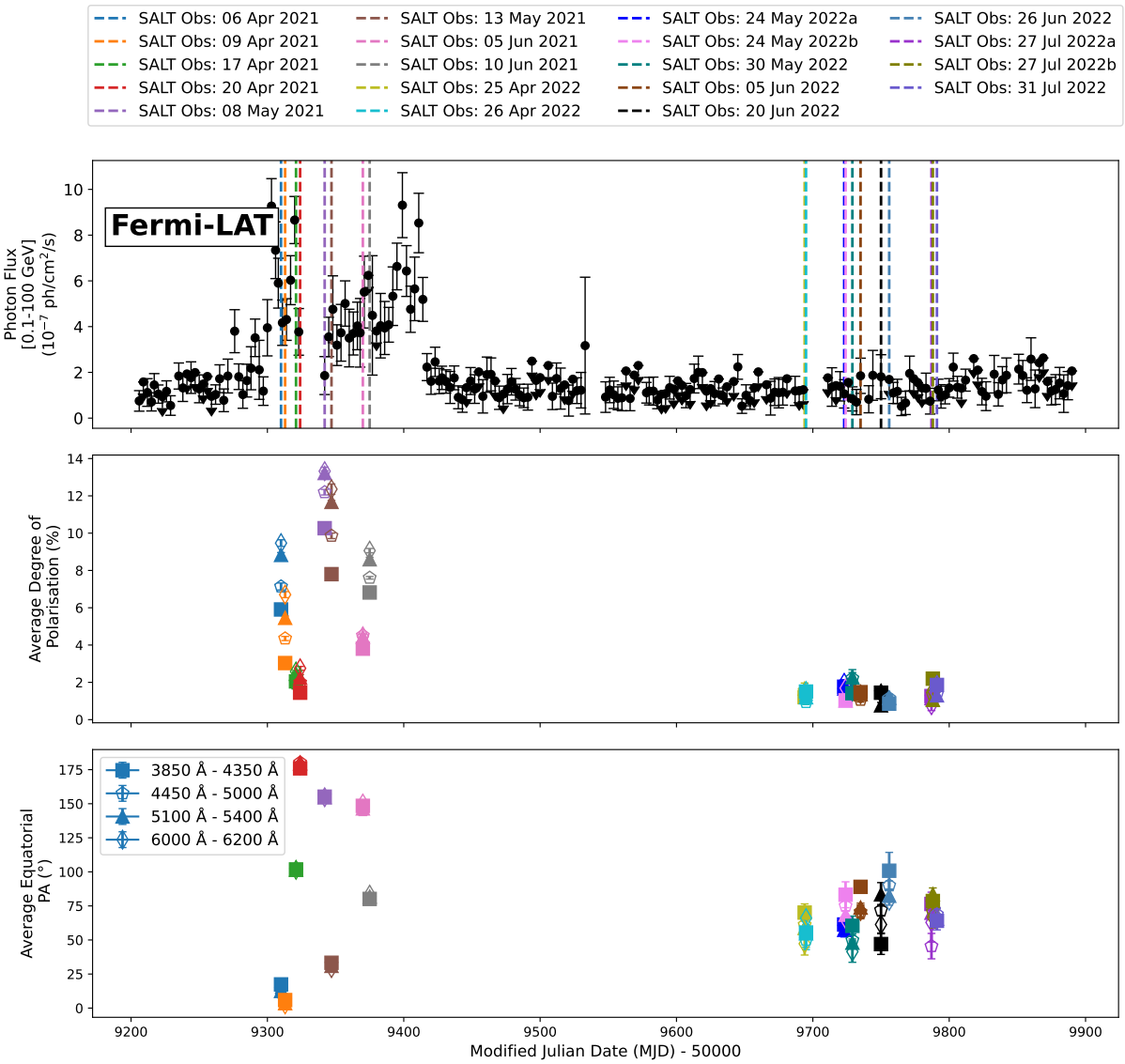

Figure 4.26: Gamma-ray (top panel) observations for the FSRQ, PKS 1510–089, along with the averaged degree of polarisation and equatorial polarisation angle in four different wavelength bands, reported for each SALT observation (middle and bottom panel, respectively).

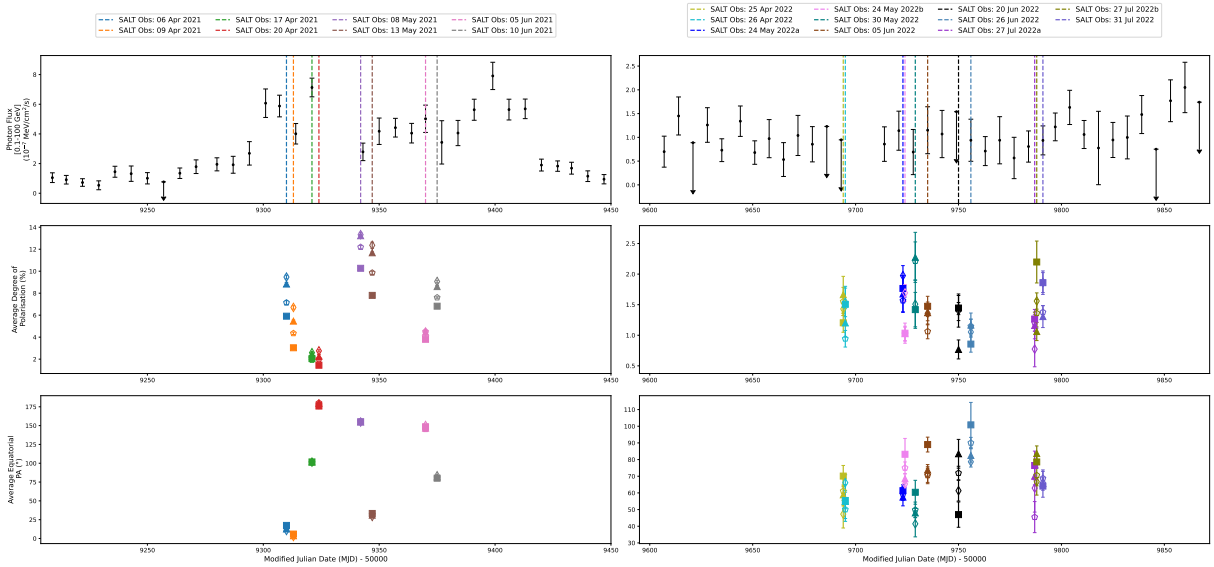

Figure 4.27: Gamma-ray observations for the FSRQ, PKS 1510–089 during the two different observing periods (top left and top right panels, respectively), along with the averaged degree of polarisation and equatorial polarisation angle in four different wavelength bands, reported for each SALT observation during the two observing periods (middle and bottom panels, respectively).

During the 2022 semester, the source was observed eleven times, and exhibited little to no activity in the γ-ray regime (see the top right panel of Figure 4.27). This "quiet" state is mirrored in the behaviour in the optical regime, with the strength and width of the emission features remaining constant, and the degree of linear polarisation remaining below 2 % for the entire observing period, reaching a maximum of only $\langle \Pi \rangle = 1.99 \pm 0.99$ %.

Throughout both the 2021 and 2022 observing periods, a comparison star was observed on the slit alongside the target. The comparison star exhibited polarisation levels consistently below 2 %, averaging around $\langle \Pi \rangle = 1.26 \pm 0.69$ %. The average degree of polarisation observed for PKS 1510–089 during the 2022 semester was comparable to that of the comparison star. Thus, the observed polarisation levels of PKS 1510–089 in 2022 can be attributed to some intergalactic effect in that region of the sky, rather than intrinsic polarisation in the jet-component of the target itself.

The polarisation angle remained more constant during the 2022 observing period, ranging from $83.88 \pm 22.87°$ to $48.96 \pm 13.93°$. The optical spectra show three emission lines: [Mg II] at $\lambda = 3804.38 \pm 1.50$ Å, H_δ at $\lambda = 5578.83 \pm 1.59$ Å, and H_γ at $\lambda = 5904.46 \pm 0.85$ Å. The equivalent widths for each of these emission lines, for each of the spectropolarimetric observations, are given in Table 4.3. Note the increase in equivalent widths of the emission lines during the 2022 semester when compared to those of the 2021 semester. This gives further indication that the non-thermal jet emission contribution has decreased significantly from 2021 to 2022.

There is a definite change in the slope of the frequency dependence of the degree of linear polarisation between the 2021 and 2022 observing semesters, and this is shown in Figure 4.29. For the SALT observations taken during the 2021 observing period, the degree of linear polarisation was observed to decrease towards the higher frequencies in the optical regime, indicating the dilution of the non-thermal synchrotron contribution

Table 4.3: Equivalent widths of the [Mg II], H_δ, and H_γ emission lines for each spectropolarimetric observation taken for the FSRQ, PKS 1510-089.

Obs. Date	[Mg II] (Å)	H_δ (Å)	H_γ (Å)
2021-04-06	25.62 ± 0.16	3.42 ± 0.18	23.40 ± 0.52
2021-04-09	29.11 ± 0.13	5.17 ± 0.16	30.71 ± 0.43
2021-04-17	29.06 ± 0.14	5.03 ± 0.17	30.11 ± 0.48
2021-04-20	28.73 ± 0.13	5.17 ± 0.15	29.58 ± 0.42
2021-05-08	20.41 ± 0.08	2.36 ± 0.08	15.53 ± 0.24
2021-05-13	25.75 ± 0.10	3.65 ± 0.11	22.76 ± 0.33
2021-06-05	13.75 ± 0.10	1.50 ± 0.10	13.04 ± 0.29
2021-06-10	12.85 ± 0.06	1.29 ± 0.06	10.26 ± 0.18
2022-04-25	33.07 ± 0.41	6.27 ± 0.48	41.02 ± 1.24
2022-04-26	31.54 ± 0.31	5.29 ± 0.39	39.87 ± 0.97
2022-05-24	31.92 ± 0.30	5.22 ± 0.38	38.88 ± 0.96
2022-05-25	33.22 ± 0.27	5.27 ± 0.35	38.52 ± 0.89
2022-05-30	30.92 ± 0.63	4.87 ± 0.77	40.27 ± 1.90
2022-06-05	31.46 ± 0.30	5.55 ± 0.36	38.24 ± 0.94
2022-06-20	32.18 ± 0.32	4.80 ± 0.41	36.96 ± 1.04
2022-06-26	31.31 ± 0.26	4.70 ± 0.33	34.02 ± 0.87
2022-07-27	32.03 ± 0.41	4.44 ± 0.55	36.48 ± 1.41
2022-07-28	30.58 ± 0.52	4.40 ± 0.71	33.38 ± 1.88
2022-07-31	31.88 ± 0.27	4.77 ± 0.36	35.99 ± 0.94

by the thermal accretion disc component. However, the picture changes during the 2022 observing period, in which the polarisation decreased to less than 2 %, with a flattened slope in the degree of polarisation – barring the two observations taken on 2022 May 24, the degree of linear polarisation is observed to increase towards the higher optical frequencies. The comparison star exhibited flat slopes in the degree of polarisation (comparable to that of the target in 2022), thus providing further evidence that the observed polarisation is an intergalactic or interstellar effect.

The slope in the frequency dependence of the degree of polarisation versus the averaged degree of polarisation for each observation during the 2021 semester is given in Figure 4.30. In this plot, the increasingly negative slopes are associated with the higher average degree of polarisation. The days on which a positive/flattened slope in the polarisation is observed, the degree of polarisation remained low and comparable to the polarisation levels of the comparison star (i.e. the 2022 observing term), and is therefore not shown in the figure. A Spearman's test on the data from the 2021 semester resulted in a strong anti-correlation of $\rho = -0.782$ (p-value $= 7.519 \times 10^{-5}$). However, since polarisation levels of $\langle \Pi \rangle < 2\,\%$ are comparable to that of the comparison star, a Spearman's test was conducted on the data from the 2021 semester excluding all points with polarisation levels below 3 %. This resulted in a slightly weaker, less significant anti-correlation of $\rho = -0.314$ (p-value $= 0.544$). This anti-correlation is the opposite of what has been observed for the BLL, AP Lib, and the FSRQ, PKS 1034–293 as discussed in Sections 4.1.3 and 4.2.4, respectively.

The change in the slopes of the degree of polarisation between 2021 and 2022, together with the "switched off" high-energy emission observed (Figures 4.25 and 4.26), and the

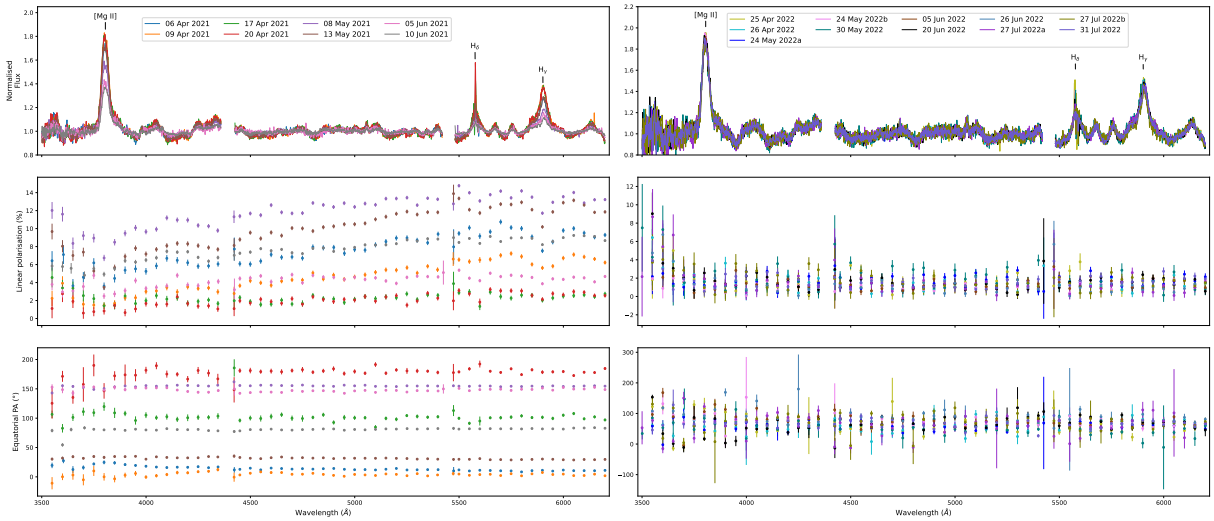

Figure 4.28: Spectropolarimetric observations for the FSRQ, PKS 1510–089, observed between 2021 April 06 and 2022 July 31, separated into two different terms (2021 and 2022, respectively). The top panels gives the normalised counts spectra of the observations, where the middle and bottom panels give the degree of linear polarisation, and the equatorial polarisation angle, respectively.

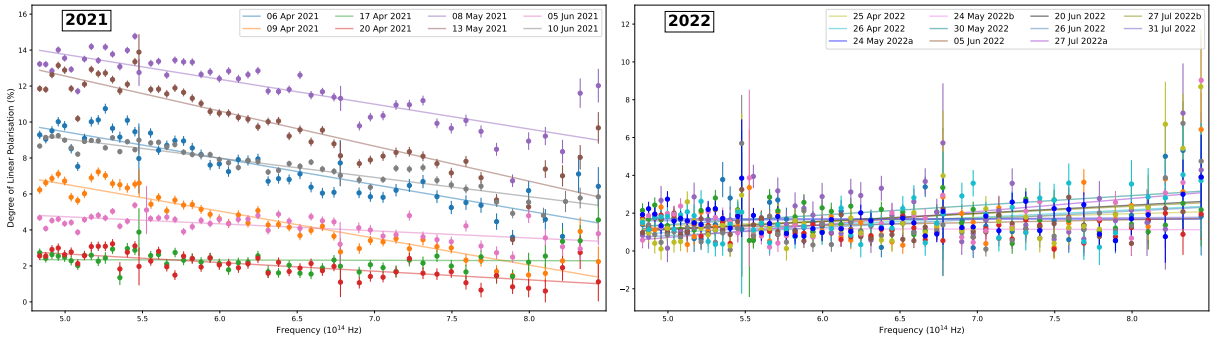

Figure 4.29: The degree of linear polarisation as a function of frequency for the FSRQ, PKS 1510–089, on all nineteen of the SALT observation dates. The different coloured datapoints represent the observation dates, as labelled in Figure 4.28. The left panel gives the data for the 2021 observing period while the source was still fairly active, and the panel on the right gives the data for the 2022 observing period, after it went quiet.

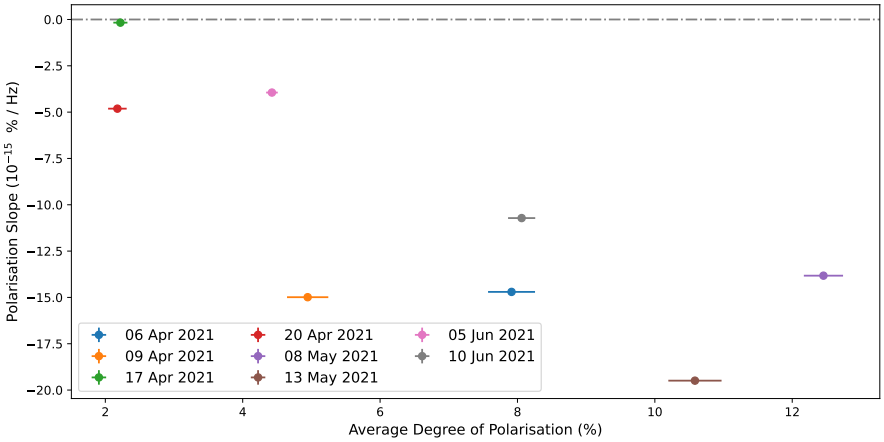

Figure 4.30: The frequency dependent slope of the degree of polarisation as a function of the averaged degree of polarisation for each of the observation dates, as observed for the FSRQ, PKS 15150–089 during the 2021 semester. The dashed grey line indicates where the slope is zero.

near-zero polarisation levels in the optical regime during the 2022 period, indicate that the source is in an unprecedented low-state, with little (if any) non-thermal contribution to the observed emission. The historically active and superluminal jet-component seems to have been completely diminished. The mysterious behaviour of this source requires much more observation and modeling in future work.

4.2.6 PKS 2023–07

PKS 2023–07 is a faint, distant FSRQ with apparent visual magnitude of $V = 18.23$, a redshift of $z = 1.388$, and a synchrotron peak frequency of $\nu_{\rm sy} = 4.16 \times 10^{12}$ Hz (Table 3.1). It has been identified as a persistent weak γ-ray emitter (Piano et al., 2016, 2018), with outbursts or flares sometimes occurring.

PKS 2023–07 was in a quiescent state for ~ 5.5 years before enhanced activity was detected by the *Fermi*-LAT in 2015 July (Ciprini and Fermi Large Area Telescope Collaboration, 2016). In 2016 April, the blazar reached a high/flaring state, and was detected by AGILE, Swift and the *Fermi*-LAT, with average daily fluxes ~ 16 times greater than that of a four-year averaged flux as given in the 3FGL *Fermi*-LAT catalogue (see the γ-ray lightcurve as shown in the top panel of Figure 4.31; Ciprini and Fermi Large Area Telescope Collaboration, 2016; Piano et al., 2018). Since the LCO data for this source spans only about three days in 2017, no optical lightcurves were plotted for this source.

An optical SALT spectropolarimetric observation for PKS 2023–07 was taken once during the 2016 flare (Figure 4.32). The spectrum was featureless with an average degree of polarisation of $\langle \Pi \rangle = 26.43 \pm 0.82\,\%$ and a polarisation angle of $167.14 \pm 0.70^\circ$ (between $\lambda = 3900 - 9150\,$Å). The γ-ray flux during the 2016 SALT observation was $\mathrm{F}(0.1 - 100\,\mathrm{GeV}) = 2.77 \pm 0.16 \times 10^{-6}\,\mathrm{ph\,cm^{-2}\,s^{-1}}$ (Figure 4.31). The degree of linear polarisation was observed to be decreasing slightly towards higher frequencies, indicating that the synchrotron emission is diluted by the accretion disc component (see Figure 4.33).

After the initial spectropolarimetric obserations in 2016, a follow-up observation was taken on 2018 October 04 during a low state (see Figure 4.32). During this observation, the observed degree of polarisation was found to be $\langle \Pi \rangle = 10.63 \pm 2.00\,\%$, with a polarisation

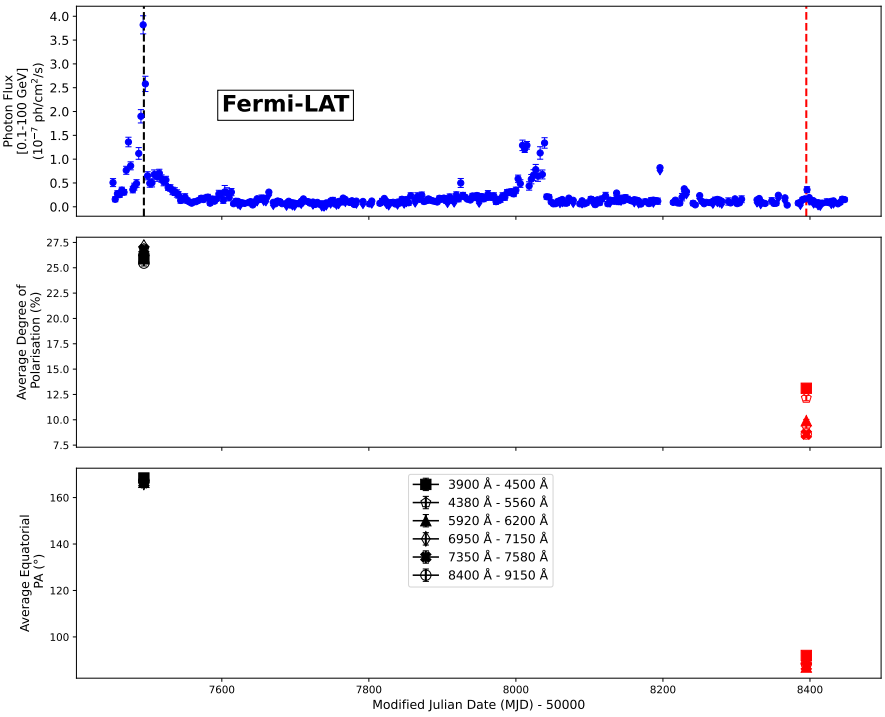

Figure 4.31: Gamma-ray (top panel) and optical (second panel) observations for the FSRQ, PKS 2023–07, where the black and red dashed lines indicate the dates of the SALT spectropolarimetric observations. The third and fourth panels give the averaged degree of polarisation and equatorial polarisation angle in six different wavelength bands, reported for each of the two SALT observations.

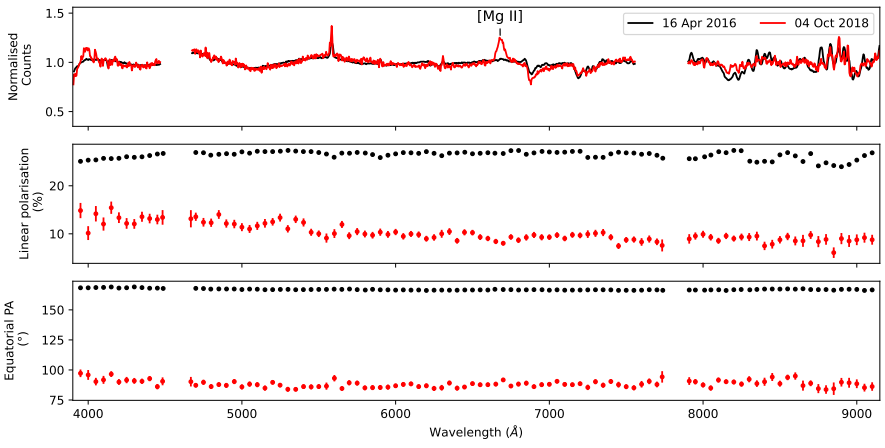

Figure 4.32: Spectropolarimetric observations for the FSRQ, PKS 2023–07, observed on 2016 April 16 and 2018 October 04. The top panel gives the normalised counts spectra of the two observations, where the middle and bottom panels give the degree of linear polarisation, and the equatorial polarisation angle, respectively. The gaps in the spectra in the top panel at $\lambda = 5540 - 5645$ Å and $\lambda = 6200 - 6320$ Å are due to the removal of a skyline.

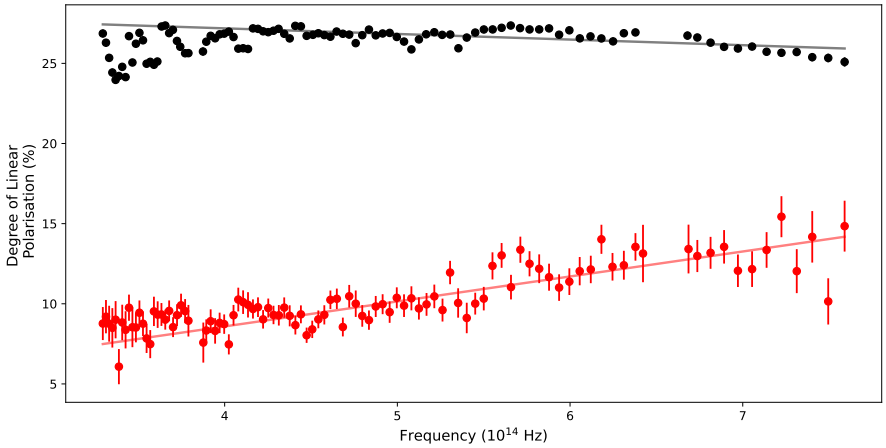

Figure 4.33: The degree of linear polarisation as a function of frequency for the FSRQ, PKS 2023–07, on both of the SALT observation dates. The black and red datapoints indicate the polarisation as observed on 2016 April 16 and 2018 October 4, respectively.

angle of $88.47 \pm 3.03°$. The optical spectrum taken on 2018 October 04 displayed a forbidden [Mg II] line at $\lambda = 6684.67 \pm 9.12$ Å (with equivalent width $|W_\lambda| = 14.59 \pm 0.52$ Å), whereas the earlier spectrum taken on 2016 April 16 displays no such feature. This indicates how the non-thermal synchrotron emission was dominant during the flare, and diluted the thermal spectral features. The γ-ray flux during the 2018 observation was $\mathrm{F}(0.1 - 100\,\mathrm{GeV}) = 2.40 \pm 0.54 \times 10^{-7}\,\mathrm{ph\,cm^{-2}\,s^{-1}}$. During the 2018 observation, the degree of polarisation was observed to increase towards higher frequencies, as shown by the red datapoints in Figure 4.33.

The next chapter will present a summary of all the findings from the observational data, along with some statistical analyses performed on the sample as a whole in a search for trends in the overall behaviour of the sample of blazars presented in this project.

Chapter 5

Discussion

This chapter will provide a discussion of all the results from the observational data, as well as provide some comments on the behaviour of the sample of blazars investigated as a whole. A summary of all the observational results for the entire sample will be given in Section 5.1, while Section 5.2 to Section 5.7 will discuss the behaviour of the polarisation for the blazar population, and how it relates to the slope of the frequency dependence of the polarisation, the γ-ray flux and luminosity, synchrotron peak frequency, and redshift of all of the sources.

Throughout this project, a cosmology was adopted with the following parameters: the Hubble constant defined as $H_0 = 70\,\mathrm{km\,s^{-1}\,Mpc^{-1}}$, and $\Omega_m = 0.3$.

5.1 Summary of Observational Results

Table 5.1 provides a summary of all the observational results obtained for all of the sources investigated in this project. This includes the γ-ray state, whether the fluxes were rising or falling (as seen in the γ-ray lightcurves given in Chapter 4 and Appendix A), the average degree of polarisation and polarisation angle, the slope of the frequency dependence of the polarisation – where a positive (+) slope indicates an increase in polarisation towards higher frequencies, and a negative (−) slope indicates a decrease in polarisation towards higher frequencies – and the isotropic-equivalent γ-ray luminosity on the respective dates of observation. The γ-ray states were defined as active/high based on what has been reported in literature, and/or when the observed fluxes were greater than the daily averaged flux in the *Fermi* 4FGL catalogue by a factor of ~ 10.

In total, six BLLs and twelve FSRQs were investigated in this project. Of the six BLLs, three were LBLs ($\nu_{\mathrm{sy}} < 10^{14}\,\mathrm{Hz}$), two were IBLs ($10^{14} < \nu_{\mathrm{sy}} < 10^{15}\,\mathrm{Hz}$), and one was an HBL ($\nu_{\mathrm{sy}} > 10^{15}\,\mathrm{Hz}$). All twelve FSRQs observed were LSPs, with $\nu_{\mathrm{sy}} < 10^{14}\,\mathrm{Hz}$, as shown in Figure 5.1. The distribution of γ-ray luminosities of the BLL and FSRQ samples at the time of the SALT observations is shown in Figure 5.2. During low states of activity, the FSRQs had a wider range of observed γ-ray luminosities than BLLs. During high states, the ranges of luminosities were similar, but the FSRQs reached higher luminosities ($L_\gamma > 10^{47}\mathrm{ergs}^{-1}$) than the BLLs.

A noteworthy remark is that more observations were taken during γ-ray active states than during quiescent states due to the nature of the observing campaigns as outlined in

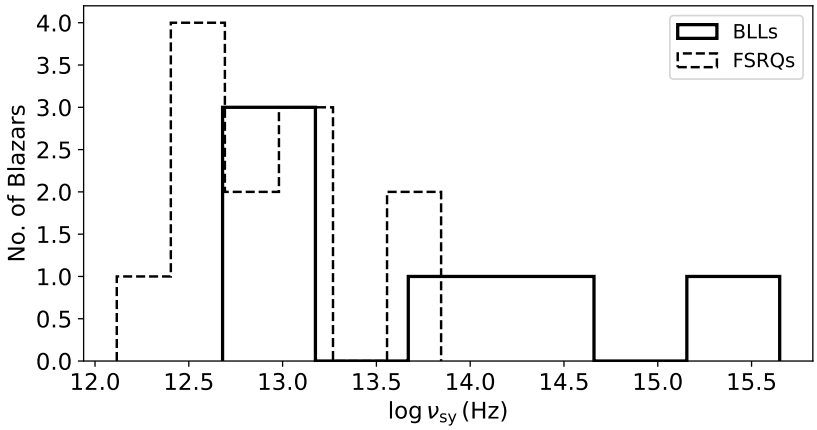

Figure 5.1: The location of the synchrotron peak frequencies (ν_{sy}) of the entire blazar sample investigated in this project. The synchrotron peaks for BLLs are indicated by the solid black line, whereas for the FSRQs, it is indicated by the dashed black line.

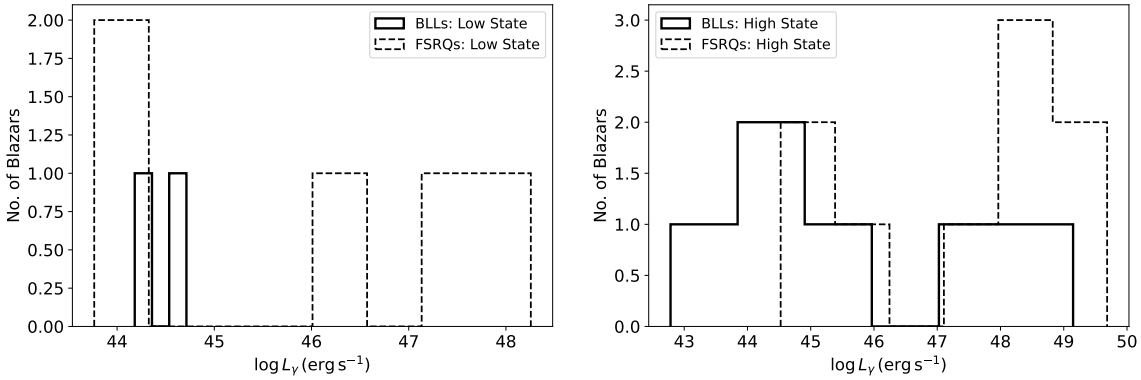

Figure 5.2: The behaviour of the γ-ray luminosities of BLLs and FSRQs during low states (left panel) and high states (right panel) of the entire blazar sample. The γ-ray luminosities for BLLs are indicated by a solid black line, whereas for the FSRQs, it is indicated by a dashed black line.

Chapter 3. Since the bulk of this project aimed at investigating the spectropolarimetric behaviour of flaring/active blazars, having a sample containing more FSRQs than BLLs was to be expected, as FSRQs tend to be more variable with more regular outbursts than BLLs. It was also expected to see larger changes in the degree of polarisation in FSRQs than in BLLs, and flaring FSRQs were observed more frequently, due to the stronger and more variable non-thermal emission component at optical wavelengths. Hence, any interpretation discussed here may be biased towards high/active, or flaring, states of largely FSRQs.

It is also of interest to note that, for the majority of the sources that were observed multiple times during γ-ray high states, the average degree of polarisation, $\langle \Pi \rangle$, was higher while the γ-ray fluxes were still on the rise, and lower while the γ-ray fluxes were falling, even if the level of flux was similar. This effect is seen in, for example, PKS 0131–522 (see Section 4.2.1, p. 57) and 4FGL J0231.2–4745 (see Section 4.2.3, p. 62), as discussed in Chapter 4.

From the observational results summarised in Table 5.1, it is also interesting to see that an active or high γ-ray state does not necessarily imply a high degree of polarisation, as is seen for e.g. PKS 1454–354 and PKS 0035–252 (see Sections A.1.3 on p. 121, and

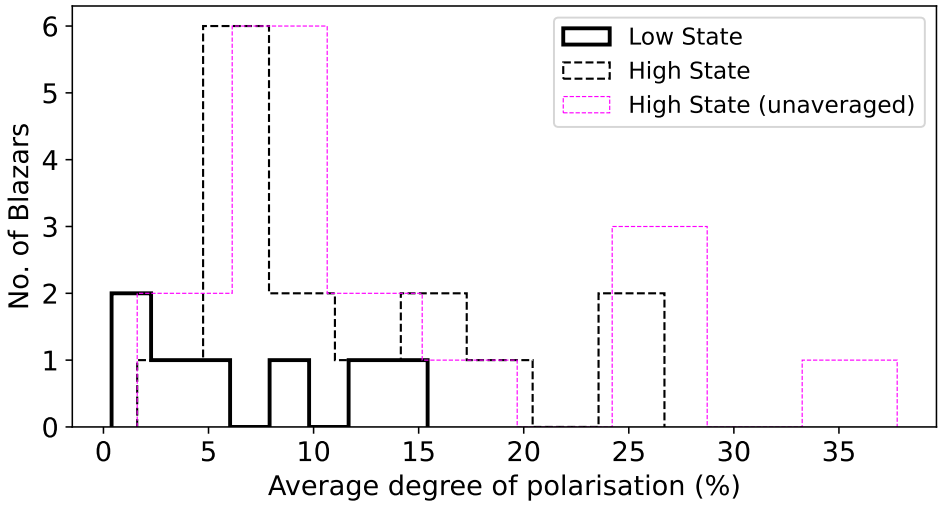

Figure 5.3: The averaged degree of polarisation of the entire blazar sample. The polarisation levels during low/quiescent states are indicated by the solid black line, whereas the high/active states are indicated by the dashed black line. The dashed magenta line indicates the distribution when only the maximum degree of polarisation is considered for PKS 0537–441, PKS 0208–512, and 4FGL J0231.2–4745.

A.2.1 on p. 123 in Appendix A, for the observational data for these two sources). However, there does seem to be a general trend in the optical polarisation levels to increase with increased γ-ray activity. This finding is in agreement with the findings from the RoboPol collaboration (see Angelakis et al., 2016). Since optical photometric coverage for most of the sources observed was limited, the nature of the enhanced state of activity cannot be constrained from this data alone. Below, the behaviour of the optical polarisation of the eighteen selected blazars will be discussed.

5.2 Polarisation Levels of the Blazar Population

Of the eighteen blazars investigated, three were observed only during low states, eleven were observed only during high states, and four were observed during both high and low states. The distribution of the average degree of polarisation (between $\lambda = 4100 - 6200$ Å) for the entire sample during low and high states is shown in Figure 5.3. Here, it is important to note three things. First, where multiple observations were taken during the same (high or low) state, the average was found over the whole of that specific state. Second, for the FSRQ PKS 0346–279, where observations were taken during two different periods of enhanced γ-ray activity (i.e. two different high states, one in 2018 February, and one in 2021 November), only the period with the highest average degree of polarisation was used. Last, for three sources (PKS 0537–441, PKS 0208–512, and 4FGL J0231.2–4745), the degree of polarisation changed by more than 15% during the same high state, being higher at the rise of the flare. The dashed magenta line in Figure 5.3 shows the distribution if only the higher degree of polarisation is included for these sources. However, for consistency, all the results discussed below will be given with respect to the averaged degree of polarisation for all of the sources.

Table 5.1: A summary of the SALT observational results, with the γ-ray state, and whether it was rising or falling, the average degree of polarisation ($\langle\Pi\rangle$) and average polarisation angle ($\langle\mathrm{PA}\rangle$), taken between $\lambda = 4100\,\text{Å}$ and $\lambda = 6200\,\text{Å}$ to obtain a consistent result for all of the sources across the various instrumental setups used. The luminosity distance D_L was calculated from the redshifts of each target, and the γ-ray luminosity is obtained from the average flux values for each source on the dates of observation. The slope of the frequency dependence of the degree of polarisation (m_Π) is indicated by either a + or −, indicating whether the degree of polarisation increases or decreases towards higher frequencies, respectively. Note that, where empty, the slope of the degree of polarisation was flat and/or comparable to that of the comparison star.

Target	Obs. Date	Gamma-ray State	Rise/Fall	$\langle\Pi\rangle$ (%)	$\langle\mathrm{PA}\rangle$ (°)	m_Π	D_L (Mpc)	L_γ (erg s^{-1})
PKS 0426–380	2017-01-21	Active	Fall	10.92 ± 0.34	11.04 ± 1.03	+	7525.73	$5.48 \pm 0.78 \times 10^{45}$
	2017-02-20	Active	Fall	11.28 ± 0.38	50.21 ± 0.94	+		$3.27 \pm 0.73 \times 10^{45}$
PKS 0447–439	2017-02-21	Active	Fall	1.61 ± 1.72	151.06 ± 45.48	+	494.82	$6.08 \pm 2.06 \times 10^{42}$
TXS 0506+056	2017-10-15	Active	Fall	10.74 ± 0.33	29.76 ± 0.79	+	1776.71	$1.60 \pm 0.26 \times 10^{44}$
	2017-10-21	Quiescent		8.65 ± 0.38	52.64 ± 1.02	−		$1.52 \pm 0.33 \times 10^{44}$
PKS 0537–441	2019-01-14	Active	Rise	37.77 ± 0.50	9.60 ± 0.18	+	5737.33	$6.16 \pm 1.56 \times 10^{47}$
	2019-03-05	Active	Fall	12.65 ± 0.56	8.51 ± 0.98	+		$5.53 \pm 1.34 \times 10^{47}$
PKS 1454–354	2021-06-13	Active	Fall	6.62 ± 0.39	123.21 ± 1.38		10229.91	$1.41 \pm 0.25 \times 10^{49}$
AP Lib	2020-05-14	Quiescent		5.04 ± 0.37	147.00 ± 3.06	+	217.69	$6.57 \pm 5.32 \times 10^{44}$
	2020-06-08	Quiescent		5.07 ± 0.60	145.15 ± 2.58	+		$6.07 \pm 4.54 \times 10^{44}$
	2020-06-24	Quiescent		3.20 ± 0.55	165.87 ± 3.84	+		$3.98 \pm 3.06 \times 10^{44}$
	2020-08-07	Quiescent		8.10 ± 0.32	126.74 ± 1.64	+		$4.88 \pm 2.36 \times 10^{44}$
	2020-09-04	Quiescent		6.07 ± 0.74	132.31 ± 2.77	+		$4.33 \pm 2.32 \times 10^{44}$
	2021-02-18	Active	Rise	2.30 ± 0.49	114.55 ± 3.90	−		$6.20 \pm 1.94 \times 10^{44}$
	2021-03-12	Active	Rise	4.79 ± 0.30	129.98 ± 1.52	+		$6.65 \pm 2.25 \times 10^{44}$
	2021-04-04	Active	Fall	8.34 ± 0.41	130.54 ± 1.34	+		$6.16 \pm 3.31 \times 10^{44}$
	2021-04-11	Active	Fall	9.36 ± 0.39	124.89 ± 0.82	+		$6.85 \pm 3.65 \times 10^{44}$
	2021-04-21	Active	Fall	10.93 ± 0.52	132.88 ± 0.91	+		$6.51 \pm 3.20 \times 10^{44}$
	2021-05-02	Active	Fall	9.06 ± 0.62	143.51 ± 1.35	+		$7.25 \pm 3.62 \times 10^{44}$
	2021-05-08	Active	Fall	10.26 ± 0.58	148.54 ± 1.07	+		$6.33 \pm 4.13 \times 10^{44}$
	2021-05-14	Active	Fall	6.88 ± 0.56	145.44 ± 1.71	+		$6.69 \pm 4.10 \times 10^{44}$
	2021-06-03	Active	Rise	6.43 ± 0.58	156.80 ± 0.90	+		$7.37 \pm 4.27 \times 10^{44}$
	2021-06-09	Active	Rise	3.25 ± 0.44	143.22 ± 4.01	+		$5.68 \pm 3.67 \times 10^{44}$
	2021-06-10	Active	Rise	5.17 ± 0.28	145.06 ± 1.12	+		$6.23 \pm 4.43 \times 10^{44}$
	2021-07-10	Active	Fall	4.79 ± 0.36	145.99 ± 1.77	+		$6.02 \pm 3.56 \times 10^{44}$
	2021-07-31	Active	Rise	12.42 ± 0.45	142.04 ± 0.73	+		$7.00 \pm 2.79 \times 10^{44}$
PKS 0035–252	2018-07-21	Active	Fall	7.79 ± 0.31	78.66 ± 1.26	−	2819.22	$4.79 \pm 0.98 \times 10^{47}$

Table 5.1 – *Continued*

Target	Obs. Date	Gamma-ray State	Rise/Fall	$\langle \Pi \rangle$ (%)	$\langle \mathrm{PA} \rangle$ (°)	m_Π	D_L (Mpc)	L_γ (erg s^{-1})
PKS 0131–522	2017-11-19	Active	Rise	8.08 ± 0.44	2.77 ± 1.91	–	86.97	$9.28 \pm 1.29 \times 10^{44}$
	2017-11-22	Active	Fall	6.25 ± 0.47	7.51 ± 2.32	–		$1.24 \pm 0.15 \times 10^{45}$
PKS 0208–512	2019-12-05	Active	Rise	26.99 ± 0.53	20.29 ± 0.90	–	6631.56	$3.16 \pm 0.38 \times 10^{48}$
	2019-12-19	Active	Fall	5.47 ± 0.25	96.96 ± 1.66	+		$3.51 \pm 0.34 \times 10^{48}$
4FGL J0231.2–4745	2019-10-23	Active	Rise	26.47 ± 1.49	143.99 ± 1.09	–	4749.09	$2.84 \pm 0.32 \times 10^{45}$
	2019-10-29	Active	Fall	7.70 ± 0.92	132.89 ± 3.18	–		$2.29 \pm 0.33 \times 10^{45}$
PKS 0346–279	2018-02-09	Active	Rise	17.85 ± 0.59	116.33 ± 0.95	–	6533.63	$1.03 \pm 0.51 \times 10^{48}$
	2021-11-05	Active	Rise	6.11 ± 0.75	79.15 ± 2.71	+		$3.25 \pm 0.43 \times 10^{48}$
PKS 0837+012	2021-03-16	Active	Fall	10.00 ± 1.15	132.48 ± 3.14	–	7626.43	$1.30 \pm 0.27 \times 10^{48}$
PKS 0907-023	2017-01-19	Quiescent		2.58 ± 1.62	58.75 ± 26.00	–	6257.77	$3.11 \pm 1.42 \times 10^{47}$
PKS 1034–293	2020-05-15	Quiescent		16.57 ± 0.50	105.53 ± 0.70	+	1612.60	$5.84 \pm 2.51 \times 10^{43}$
	2021-02-08	Quiescent		16.95 ± 0.72	98.07 ± 1.24	+		$4.06 \pm 2.49 \times 10^{43}$
	2021-03-17	Quiescent		14.87 ± 0.94	13.58 ± 1.78	+		$5.23 \pm 2.49 \times 10^{43}$
	2021-04-09	Quiescent		12.43 ± 0.63	161.20 ± 1.24	+		$8.01 \pm 2.49 \times 10^{43}$
	2021-06-05	Quiescent		20.01 ± 0.70	135.73 ± 1.02	+		$6.57 \pm 2.43 \times 10^{43}$
	2021-06-11	Quiescent		11.73 ± 0.64	132.27 ± 1.46	+		$5.17 \pm 2.43 \times 10^{43}$
3C 273	2017-06-13	Quiescent		0.40 ± 0.16	27.17 ± 22.15		754.94	$9.94 \pm 2.17 \times 10^{45}$
	2017-06-14	Quiescent		0.38 ± 0.16	43.25 ± 19.31			$1.08 \pm 0.24 \times 10^{46}$
PKS 1424–418	2022-07-26	Active	Rise	7.07 ± 0.27	160.43 ± 3.04		11105.97	$4.89 \pm 0.46 \times 10^{49}$
	2022-08-15	Active	Fall	3.10 ± 0.51	141.10 ± 3.68	+		$4.82 \pm 0.34 \times 10^{49}$
PKS 1510–089	2021-04-06	Active	Fall	7.91 ± 1.37	13.03 ± 2.17	–	1919.07	$1.22 \pm 0.25 \times 10^{47}$
	2021-04-09	Active	Fall	4.95 ± 1.20	4.73 ± 2.69	–		$1.11 \pm 0.23 \times 10^{47}$
	2021-04-17	Active	Fall	2.22 ± 0.41	100.32 ± 4.45	–		$1.44 \pm 0.25 \times 10^{47}$
	2021-04-20	Active	Fall	2.18 ± 0.54	178.93 ± 4.82	–		$1.40 \pm 0.24 \times 10^{47}$
	2021-05-08	Active	Rise	12.45 ± 1.14	155.16 ± 0.75	–		$6.27 \pm 1.96 \times 10^{46}$
	2021-05-13	Active	Rise	10.58 ± 1.55	31.41 ± 1.46	–		$9.30 \pm 2.56 \times 10^{46}$
	2021-06-05	Active	Fall	4.43 ± 0.34	146.56 ± 2.19	–		$1.13 \pm 0.30 \times 10^{47}$
	2021-06-10	Active	Fall	8.06 ± 0.79	81.21 ± 1.26	–		$1.26 \pm 0.45 \times 10^{47}$
	2022-04-25	Quiescent		1.51 ± 0.69	56.99 ± 22.50			$2.87 \pm 3.53 \times 10^{46}$
	2022-04-26	Quiescent		1.17 ± 0.55	57.62 ± 23.75			$2.92 \pm 3.53 \times 10^{46}$

Table 5.1 – *Continued*

Target	Obs. Date	Gamma-ray State	Rise/Fall	$\langle \Pi \rangle$ (%)	$\langle \mathrm{PA} \rangle$ (°)	m_Π	D_L (Mpc)	L_γ ($\mathrm{erg\,s^{-1}}$)
PKS 1510–089	2022-05-24	Quiescent		1.69 ± 0.65	58.87 ± 11.91			$3.67 \pm 2.73 \times 10^{46}$
(cont.)	2022-05-25	Quiescent		1.12 ± 0.40	74.51 ± 11.44			$3.67 \pm 2.73 \times 10^{46}$
	2022-05-30	Quiescent		1.99 ± 0.99	48.96 ± 13.93			$3.59 \pm 3.56 \times 10^{46}$
	2022-06-05	Quiescent		1.24 ± 0.43	71.56 ± 11.67			$4.31 \pm 3.19 \times 10^{46}$
	2022-06-20	Quiescent		1.24 ± 0.48	71.26 ± 18.25			$3.26 \pm 3.14 \times 10^{46}$
	2022-06-26	Quiescent		1.00 ± 0.53	83.88 ± 22.87			$3.33 \pm 3.19 \times 10^{46}$
	2022-07-27	Quiescent		1.16 ± 0.53	63.39 ± 27.55			$2.73 \pm 2.41 \times 10^{46}$
	2022-07-28	Quiescent		1.49 ± 0.75	77.57 ± 21.42			$3.56 \pm 3.13 \times 10^{46}$
	2022-07-31	Quiescent		1.44 ± 0.46	63.66 ± 14.41			$3.76 \pm 3.21 \times 10^{46}$
PKS 2023–07	2016-04-16	Active	Rise	26.70 ± 0.42	167.33 ± 0.70	–	9911.33	$3.30 \pm 0.31 \times 10^{49}$
	2018-10-04	Quiescent		11.90 ± 1.45	88.00 ± 2.70	+		$1.80 \pm 0.41 \times 10^{48}$

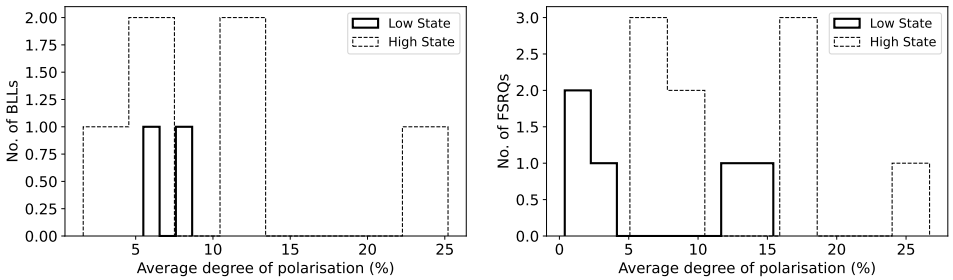

Figure 5.4: The averaged degree of polarisation of the BLLs (left) and FSRQs (right) for the sample of blazars investigated. The polarisation levels during low/quiescent states are indicated by the solid black line, whereas the high/active states are indicated by the dashed black line.

For all but one blazar (PKS 0537–441), the average degree of polarisation remained below 30% during high states. During low states, the average degree of polarisation remained below $\sim$ 15% for both BLLs and FSRQs. During low states, the degree of linear polarisation ranged from a minimum of $\langle\Pi\rangle = 0.39 \pm 0.16\,\%$ to a maximum of $\langle\Pi\rangle = 15.43 \pm 2.82\,\%$. The spread/standard deviation in the degree of polarisation during low states over all of the sources was $\sigma \approx 5.26\,\%$. During high states, the degree of linear polarisation ranged from $\langle\Pi\rangle = 1.61 \pm 1.12\,\%$ to $\langle\Pi\rangle = 26.70 \pm 0.42\,\%$, with a significantly larger spread in the data, with a standard deviation of $\sigma \approx 7.08\,\%$.

The distributions for BLLs and FSRQs are shown separately in Figure 5.4. Of the six BLLs in the sample, two were observed in low states, and all six were observed during a high state. During a low state of activity, the average degree of polarisation remained below 15% for all of the BLLs, reaching a maximum of $\Pi = 8.65 \pm 0.38\,\%$. During high states, the average degree of polarisation remained below 15% for all but one BLL, for which an average degree of polarisation was found to be $\Pi = 25.02 \pm 0.53\,\%$.

Of the twelve FSRQs studied, five were observed during a low state of activity, and nine were observed during a high state, as shown in the right panel of Figure 5.4. The average degree of polarisation reached a maximum of $\Pi = 15.43 \pm 2.82\%$ during low states, and $\Pi = 26.69 \pm 0.42\%$ during high states. From the results shown in Figure 5.3 and 5.4, it can be seen that, on average, the degree of polarisation during high states are higher for FSRQs than for BLLs.

5.3 Nature of the Polarisation Slopes

The nature of the observed polarisation of blazars can be investigated by both its degree or level of polarisation, and the frequency dependent slope in the observed degree of polarisation. However, from the results discussed in this project, it is clear that the nature of the polarisation does not depend only on the state of activity of the blazar, or the observed flux alone. Therefore, further investigation is required.

The analysis of three individual sources with multiple observations (AP Lib, PKS 1034–293 and PKS 1510–089) indicated a trend between the frequency dependent slope of polarisation and the average degree of polarisation. To investigate this further, the analysis is extended to all sources in Figure 5.5. There does not seem to be a general trend for the entire sample (both BLLs and FSRQs), as a Spearman's test resulted in

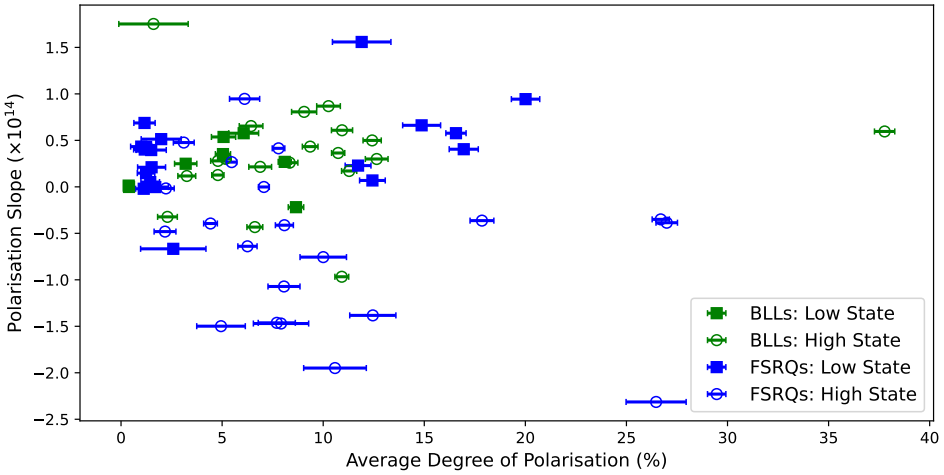

Figure 5.5: The relation between the degree of polarisation and its frequency dependent slope for all of the sources in the sample. The open circles indicate the averaged degree of linear polarisation of blazars during high/active states, and the filled squares indicate the averaged degree of linear polarisation of blazars during low/quiescent states. Green datapoints indicate values associated with BLLs, and blue datapoints indicate the values associated with FSRQs.

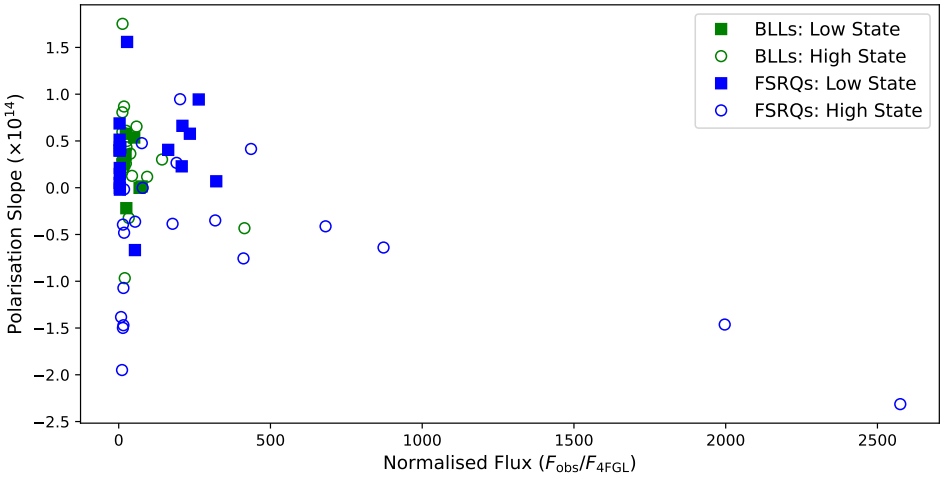

Figure 5.6: The relation between the frequency dependent slope in degree of polarisation and the normalised γ-ray flux for all of the sources in the sample. The open circles indicate the normalised flux of blazars during high/active states, and the filled squares indicate the normalised flux of blazars during low/quiescent states. Green datapoints indicate values associated with BLLs, and blue datapoints indicate the values associated with FSRQs.

$\rho = -0.080$ (p-value = 0.621) during high states. However, during low states, a Spearman's test showed a slightly more significant correlation of $\rho = 0.375$ (p-value = 0.054). No strong correlation is observed when investigating the BLLs and FSRQs separately. BLLs show $\rho = 0.167$ (p-value = 0.693) during low states, and $\rho = 0.189$ (p-value = 0.424) during high states, while FSRQs show $\rho = 0.289$ (p-value = 0.229) during low states, and $\rho = -0.319$ (p-value = 0.158) during high states. Thus, there is no strong monotonic relationship between the observed degree of polarisation and the slope of that polarisation.

As the slope in the degree of polarisation can be either positive (increasing towards higher frequencies) or negative (decreasing towards higher frequencies), and therefore be indicative of different scenarios surrounding the high-energy jet-emission, a correlation may occur between the slope and the observed γ-ray flux. In order to investigate this, we compared the slope of the frequency dependence of the polarisation against a normalised

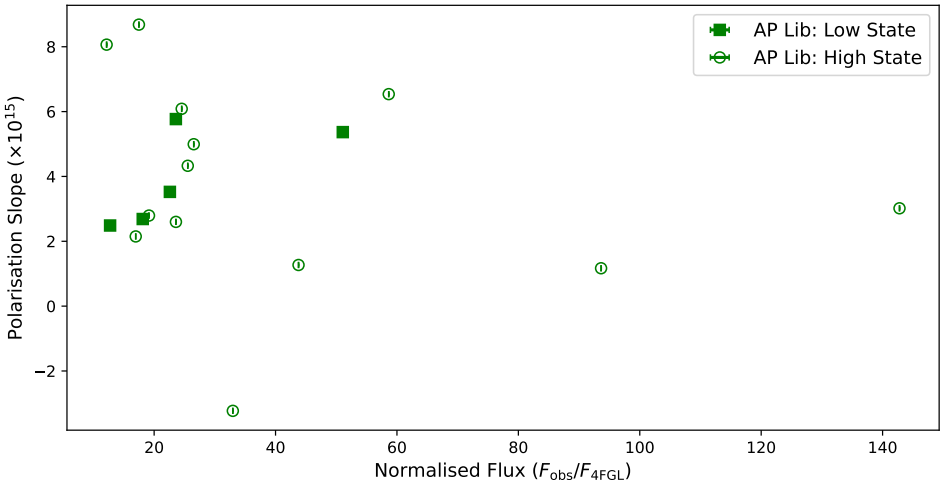

Figure 5.7: The relation between the frequency dependent slope in degree of polarisation and the normalised γ-ray flux for the BLL, AP Lib. The open circles indicate the normalised flux of blazars during high/active states, and the filled squares indicate the normalised flux of blazars during low/quiescent states.

flux or *flare parameter* (Figure 5.6). The flare parameter is the observed γ-ray flux divided by the flux given in the *Fermi* 4FGL catalogue (or $F_{\rm obs}/F_{\rm 4FGL}$). This is done so that the flare-parameter indicates the strength of the flare, rather than just the level of observed flux.

For the entire sample (both BLLs and FSRQs), a Spearman's test resulted in $\rho = 0.085$ (p-value = 0.672) during low states, and $\rho = -0.096$ (p-value = 0.550) during high states, indicating no correlation. For the BLL sample, $\rho = -0.310$ (p-value = 0.456) during low states, and $\rho = -0.320$ (p-value = 0.169) during high states, was found. The FSRQ sample gave $\rho = 0.153$ (p-value = 0.533) during low states, and $\rho = 0.182$ (p-value = 0.430) during high states. These values all indicate that there was no observed correlation between the slope in the degree of polarisation and the strength of the flare in the γ-ray regime.

These results may be skewed due to both the quantity of observational data, as well as the observed behaviour of AP Lib, PKS 1034–293, and PKS 1510–089. For AP Lib, a time lag was observed between the optical polarisation and γ-ray fluxes. As such, the behaviour of the slope and degree of polarisation with γ-ray flux during high states is skewed, and a stronger correlation could arise if this effect is corrected for. The slope of polarisation against the normalised flux is shown for AP Lib alone in Figure 5.7. A Spearman's test for this source resulted in a stronger correlation of $\rho = 0.900$ (p-value = 0.037) during low states, and a less significant anti-correlation of $\rho = -0.363$ (p-value = 0.223) during high states. Although these results are constrained by the limited observational data, it seems as if the slope of the polarisation increases (i.e. becomes more positive) with increasing γ-ray flux during low states, and decreases (becomes more negative) with increasing γ-ray flux during high states.

PKS 1034-293 was observed in a persistent low state with varying levels of polarisation and γ-ray fluxes, always exhibiting an increase in polarisation towards higher frequencies (see Figure 5.8). For this source, a Spearman's test resulted in $\rho = 0.029$ (p-value = 0.957), and showed no correlation in the data. However, the observational data is severely lim-

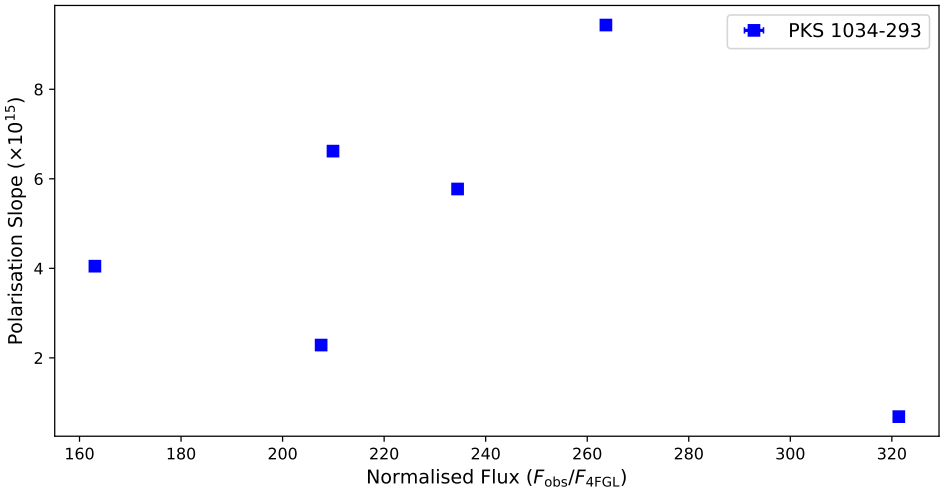

Figure 5.8: The relation between the frequency dependent slope in degree of polarisation and the normalised γ-ray flux for the FSRQ, PKS 1034–293.

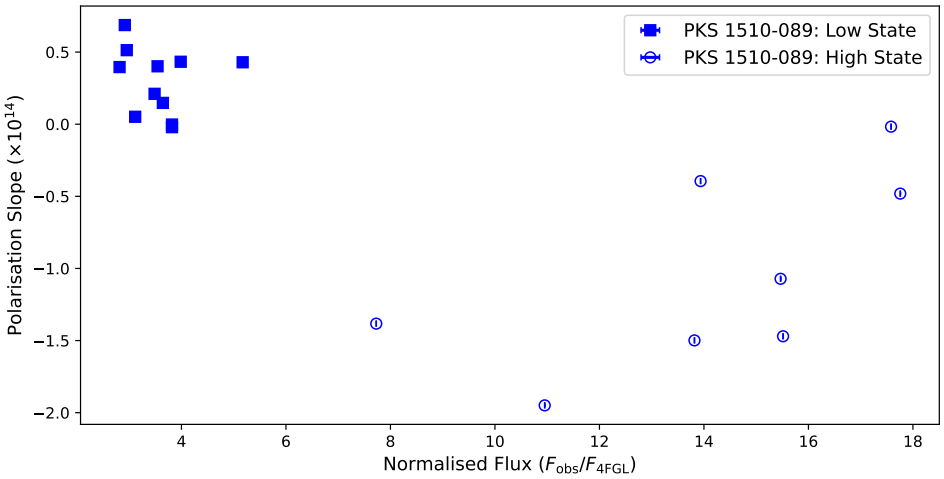

Figure 5.9: The relation between the frequency dependent slope in degree of polarisation and the normalised γ-ray flux for the FSRQ, PKS 1510–089. The open circles indicate the normalised flux of blazars during high/active states, and the filled squares indicate the normalised flux of blazars during low/quiescent states.

ited, and, since the source was not observed during a high state of activity, the possibility of correlation cannot be excluded.

The behaviour of PKS 1510–089 completely changed from 2021 to 2022, entering an unprecedented low state in 2022. The behaviour of the slope of the frequency dependence of the polarisation with γ-ray flux mirrors this low/high state change in Figure 5.9. During high states, the data shows a correlation of $\rho = 0.595$ (p-value = 0.120), where the degree of polarisation decreased with increasing γ-ray flux, and the slope remained negative. During low states, there is also no significant correlation, with $\rho = -0.255$ (p-value = 0.450). This is as expected, as the observed polarisation levels during the 2022 semester are comparable to that of the comparison star, and are due to intergalactic effects. By including the observational data from the 2022 observing period, the overall results for the sample may be more random than it truly is, as the polarisation effects are not intrinsic to the source itself.

Table 5.2: The parameters used to initialise the emission region, its magnetic field, the electron population, as well as some properties of the blazar's accretion disc and SMBH. These were used to model how the SED and the slope of the frequency dependence of the polarisation changes with varying flux and ordering of the magnetic field.

Property	Value
Magnetic field strength B [G]	0.82
Bulk Lorentz factor Γ	15
Blob radius $R_{\rm blob}$ [cm]	3×10^{17}
Minimum energy $\gamma_{\rm min}$	54.8
Break energy $\gamma_{\rm break}$	7.27×10^{2}
Maximum energy $\gamma_{\rm max}$	4×10^{3}
Electron spectral index p_1	2.62
Electron spectral index p_2	3.00
Normalisation of electron spectrum k [cm^{-3}]	0.5×10^{-5}
Black hole mass $M_{\rm SMBH}$ [$M_\odot$]	3×10^{9}
Disk luminosity $L_{\rm AD}$ [erg/s]	4.5×10^{46}
Redshift z	0.35

As already mentioned, the frequency dependent slope and degree of the observed polarisation for blazars depend on a multitude of factors. These include, for example, the observed flux F (across the electromagnetic spectrum), the redshift (z) of the source, the location of the synchrotron peak frequency ($\nu_{\rm sy}$), and the ordering of the magnetic field ($F_{\rm B}$). The nature of the polarisation will also differ between BLLs and FSRQs, as FSRQs generally exhibit a stronger accretion disc component than BLLs, which plays a role in the dilution of the non-thermal synchrotron radiation at higher (optical/UV) frequencies.

To investigate how the SED and the slope of the frequency dependence of the polarisation might be predicted to vary with the γ-ray flux and the ordering of the magnetic field, an illustrative, or toy model, was constructed. The SEDs were modelled using AGNPY (Nigro et al., 2022). Here, a one-zone model is assumed, with a single blob producing the synchrotron emission component. To set up the model, the parameters were based off of what was found by Schutte et al. (2022), and are summarised in Table 5.2. Note that these parameters are not representative of all blazars, specifically not for BLLs, but used just as a demonstration of the idea. The thermal accretion disc component was modelled using a Shakura and Sunyaev accretion disc (Shakura and Sunyaev, 1973), and the synchrotron emission was calculated for a broken power-law energy distribution of relativistic electrons. The total observed degree of polarisation is calculated from (see e.g. Schutte et al., 2022),

$$\Pi_{\omega}^{\rm sy} = F_{\rm B} \cdot \frac{\int N_e(\gamma) x(\gamma) K_{2/3}\left(x(\gamma)\right) d\gamma}{\int N_e(\gamma) x(\gamma) \int_{x(\gamma)}^{\infty} K_{5/3}\left(x(\xi)\right) d\xi d\gamma}, \tag{5.1}$$

where N_e is the electron distribution, $K_{2/3}$ and $K_{5/3}$ are Bessel functions of the second kind of order 2/3 and 5/3, respectively, and $F_{\rm B}$ is introduced to indicate the level of ordering of the magnetic field.

First, to see how an increase in the non-thermal flux will change the slope of the polarisation, the ordering of the magnetic field was kept constant and the normalisation constant (n_0) of the electron distribution was increased by a factor of 500. In Figure 5.10, the top panel shows the low-energy component of the SED at varying flux levels,

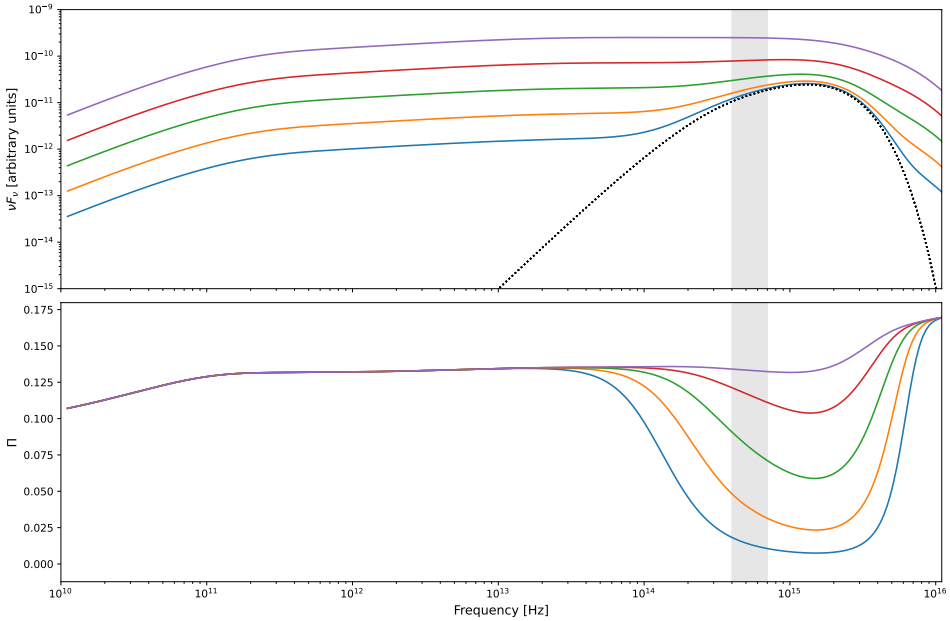

Figure 5.10: An illustration of the low-energy component of a blazar SED (top panel) at varying flux levels, with the corresponding expected degree of polarisation (bottom panel). The solid coloured lines give the combined synchrotron and thermal emission contributions at different flux levels, whereas the dashed black line gives the accretion disc (thermal) component. From bottom to top, the coloured lines indicate the flux as increased by an arbitrary factor of 3.5, 12.3, 43.2, and 151.7, from the lowest flux level considered (solid blue line). The grey shaded region indicates the optical frequency range.

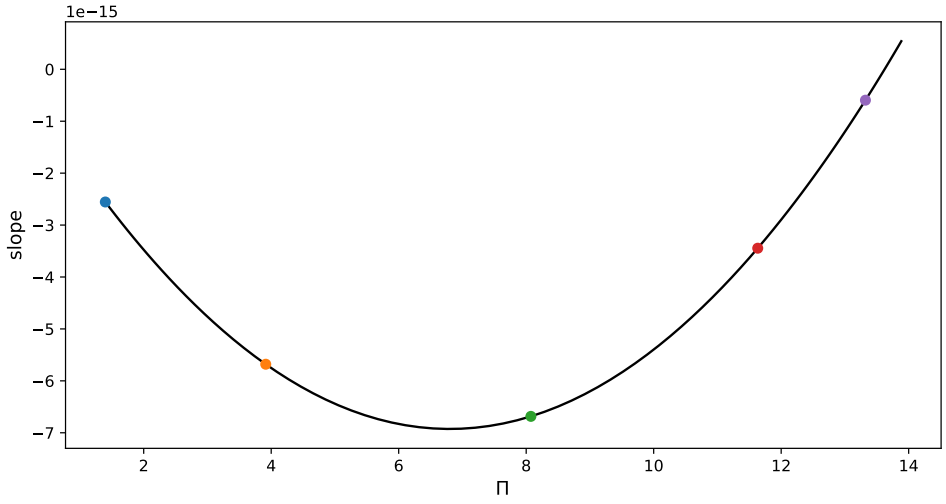

Figure 5.11: An illustration of how the slope of the frequency dependence of the polarisation will change with the degree of polarisation at optical frequencies as the flux levels vary. The coloured marked circles correspond to the model illustrated in Figure 5.10.

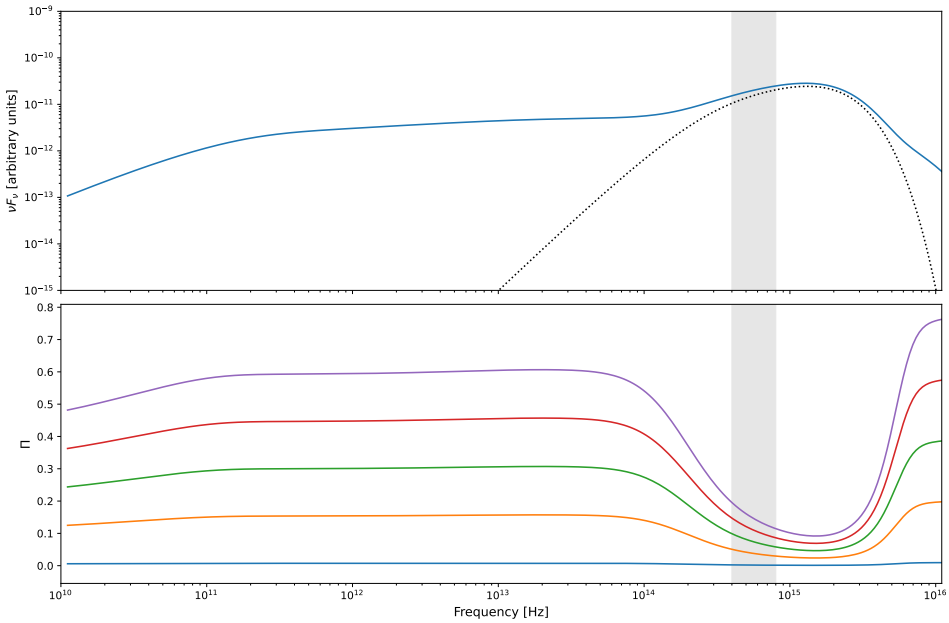

Figure 5.12: An illustration of the low-energy component of a blazar SED (top panel) with varying ordering of the magnetic field ($F_{\rm B}$, with the corresponding expected degree of polarisation (bottom panel). The solid coloured lines give the combined synchrotron and thermal emission contributions with different $F_{\rm B}$-values, whereas the dashed black line gives the accretion disc (thermal) component. From bottom to top, the coloured lines correspond to $F_{\rm B}$ = 0.01, 0.21, 0.41, 0.61, and 0.81. The grey shaded region indicates the optical frequency range.

whereas the bottom panel shows the degree of polarisation, with the vertical grey strip indicating the optical regime ($\nu = 4 - 7 \times 10^{14}$ Hz). Figure 5.11 shows how the slope of the polarisation in the optical regime will change with increasing flux levels. First, the slope becomes increasingly negative; then the slope becomes less negative with increasing polarisation as the optical region becomes dominated by the synchrotron emission.

Second, the synchrotron flux was kept constant, and only the ordering of the magnetic field ($F_{\rm B}$) was increased, ranging from $F_{\rm B} = 0.01 - 1.00$. This effectively increases the degree of polarisation. The top panel of Figure 5.12 shows the low-energy component of the SED at a constant flux level, whereas the bottom panel shows the varying levels of polarisation as the ordering of the magnetic field ($F_{\rm B}$) changes. This predicts that, as the average polarisation increases, the slope of the polarisation will become increasingly negative in the optical regime (as shown in Figure 5.13).

While the relation of increasingly negative slopes as the degree of polarisation increases, is found for some individual sources (for example, 4FGL J 0231.2-4745, PKS 1510–089, and PKS 0346–279), the effect is not seen for the population as a whole (see Figure 5.5). This is likely due to the fact that many sources were only sampled once or twice, and not necessarily during two different states of activity. In order to further test the hypotheses outlined by this model, higher cadence observations are required during both high and low states of activity.

However, this simple, first-approximation model shows that the most simplistic idea that increased non-thermal flux results in higher degrees of polarisation and polarisation slopes, is not necessarily true. The ordering of the magnetic field within the region where the emission is produced, also plays a critical role. The redshift of the source, as well as the assumed electron spectrum, is also important, as this will change the slope of the

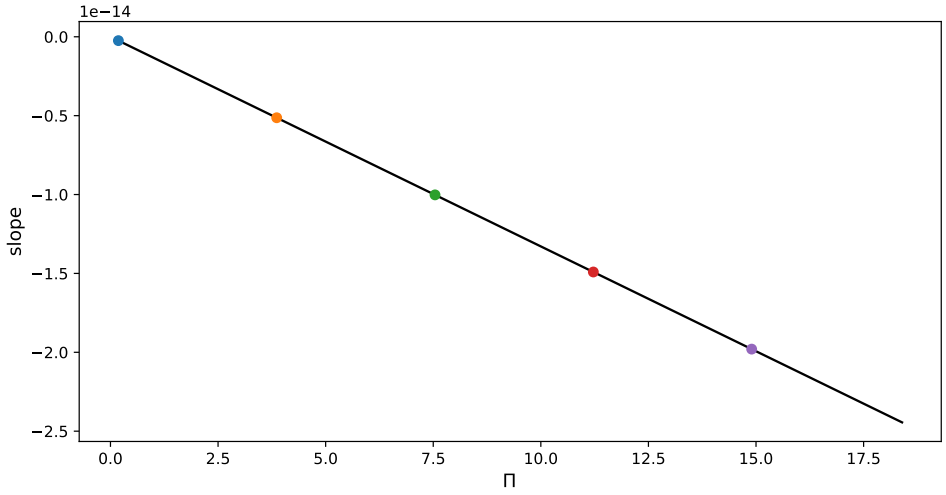

Figure 5.13: An illustration of how the frequency dependent slope of the polarisation will change with the degree of polarisation at optical frequencies as the ordering of the magnetic field varies. The coloured marked circles, correspond to the model illustrated in Figure 5.12.

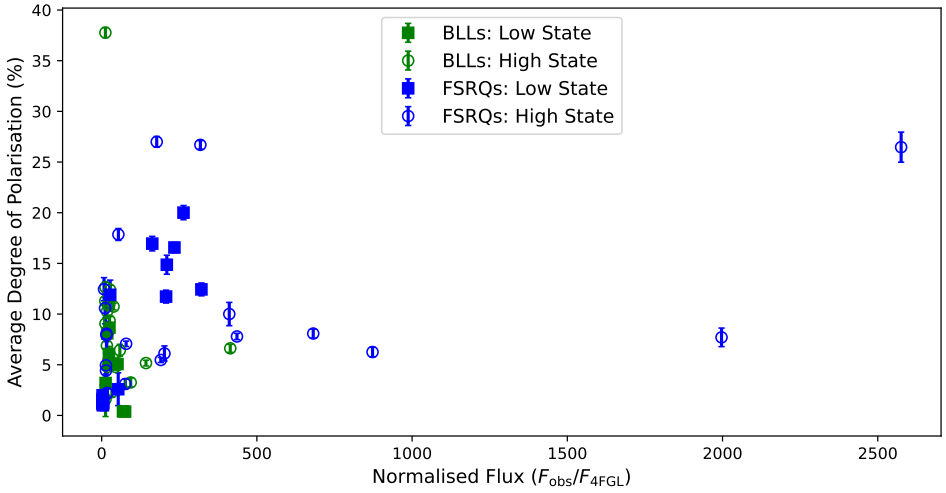

Figure 5.14: The relation between the frequency dependent slope in degree of polarisation and the normalised γ-ray flux for all of the sources in the sample. The open circles indicate the normalised flux of blazars during high/active states, and the filled squares indicate the normalised flux of blazars during low/quiescent states. Green datapoints indicate values associated with BLLs, and blue datapoints indicate the values associated with FSRQs.

polarisation in the narrow optical regime.

5.4 Polarisation vs. γ-ray Flux

The average degree of polarisation as a function of the normalised flux ($F_{\rm obs}/F_{\rm 4FGL}$) for the entire sample, is shown in Figure 5.14. For the entire sample, a Spearman's test resulted in a significant correlation of $\rho = 0.623$ (p-value $= 5.223 \times 10^{-3}$) during low states. This indicates that, during low states, the average degree of polarisation increases with increasing γ-ray flux. During high states, $\rho = -0.068$ (p-value $= 0.671$), no correlation is found. For the BLL sample, no significant correlations were found, with $\rho = -0.405$ (p-value $= 0.320$) and $\rho = -0.468$ (p-value $= 0.038$) during low and high states, respectively. For the FSRQ sample, a strong correlation of $\rho = 0.695$ (p-value $= 9.630 \times 10^{-3}$) was found during low states. However, during high states, there was no clear correlation,

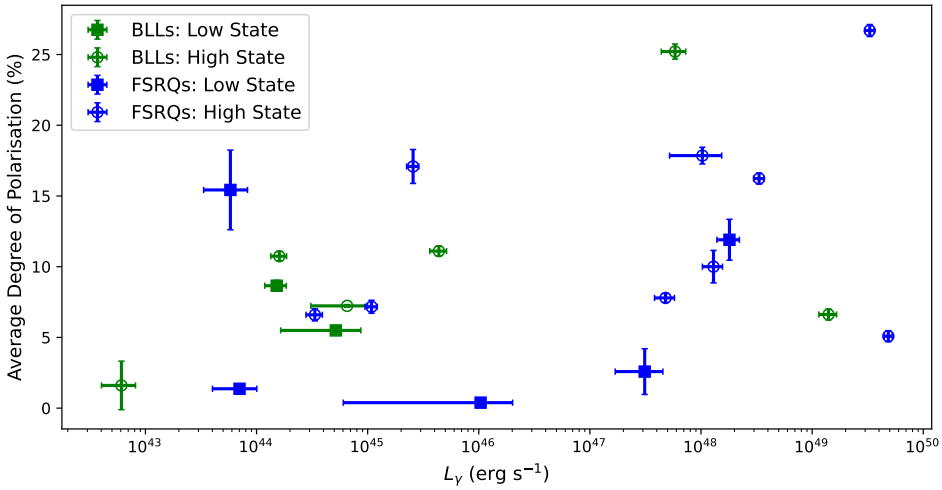

Figure 5.15: The averaged degree of polarisation of the entire blazar sample vs. the γ-ray luminosity (L_γ) of each source. The open circles indicate the averaged degree of linear polarisation of blazars during high/active states, and the filled squares indicate the averaged degree of linear polarisation of blazars during low/quiescent states. Green datapoints indicate values associated with BLLs, and blue datapoints indicate the values associated with FSRQs.

with $\rho = 0.191$ (p-value = 0.407).

5.5 Polarisation vs. γ-ray Luminosity

The average degree of polarisation as a function of the γ-ray luminosity is shown in Figure 5.15. There does not seem to be any clear trend or correlation in the data, as various levels of polarisation are detected for the same range of γ-ray luminosities for both FSRQs and BLLs. A Spearman's rank order correlation test between the average degree of polarisation and γ-ray luminosity during a low state yields a correlation coefficient of $\rho = -0.179$ (p-value = 0.702). During a high state, a correlation of $\rho = 0.296$ (p-value = 0.283) was found. This erratic behaviour of the polarisation with γ-ray luminosity is in agreement with findings from the RoboPol programme (Angelakis et al., 2016), as shown in Figure 2.11 in Chapter 2, p. 25. This indicates that there is no discernable trend with which an increasing γ-ray luminosity correlates or anti-correlates with the observed degree of polarisation in the optical regime.

For the polarisation angle and γ-ray luminosity during low states, the correlation was $\rho = -0.214$ (p-value = 0.645). During high states, the correlation was $\rho = 0.236$ (p-value = 0.398), showing no clear correlation or trend. The erratic behaviour of the polarisation angle with γ-ray luminosity as shown in Figure 5.16 is, therefore, also in agreement with observational findings by, for example, Angelakis et al. (2016) and Blinov et al. (2016).

5.6 Polarisation vs. Synchrotron Peak Frequency

For both FSRQs and BLLs, during both high and low states of γ-ray activity, the average degree of polarisation appears to anti-correlate with the location of the synchrotron peak frequency ($\nu_{\rm sy}$) as shown in Figure 5.17. Here, higher degrees of polarisation are observed for sources with lower synchrotron peak frequencies during both active and qui-

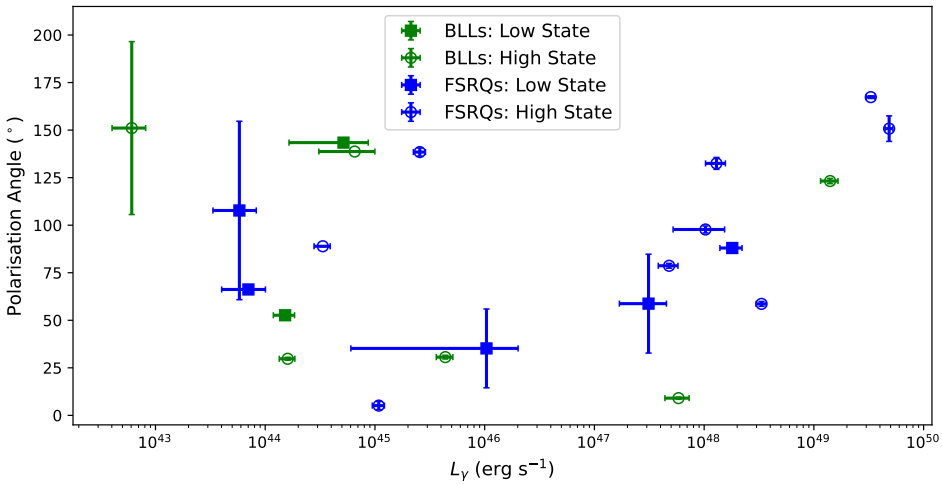

Figure 5.16: The averaged polarisation angle of the entire blazar sample vs. the γ-ray luminosity (L_γ) of each source. The open circles indicate the averaged polarisation angle of blazars during high/active states, and the filled squares indicate the averaged polarisation angle of blazars during low/quiescent states. Green datapoints indicate values associated with BLLs, and blue datapoints indicate the values associated with FSRQs.

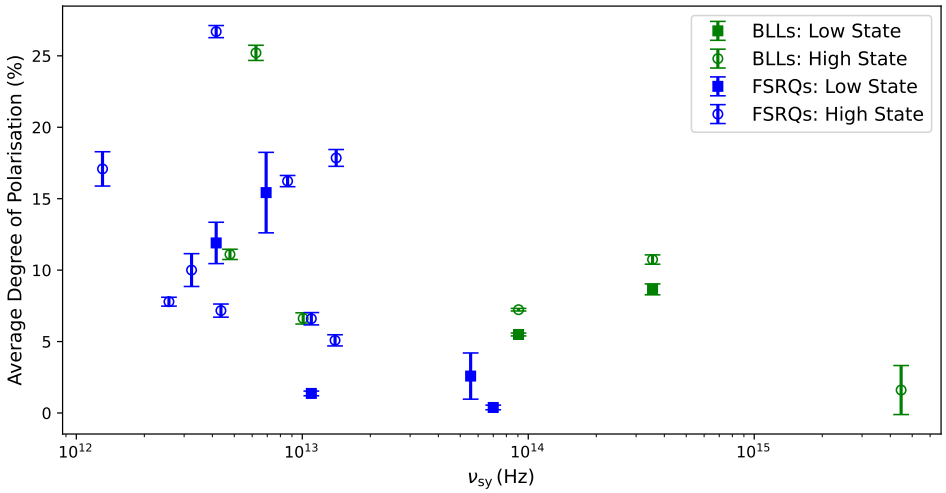

Figure 5.17: The averaged degree of polarisation of the entire blazar sample vs. the synchrotron peak frequencies (ν_{sy}) of each source. The open circles indicate the averaged degree of linear polarisation of blazars during high/active states, and the filled squares indicate the averaged degree of linear polarisation of blazars during low/quiescent states. Green datapoints indicate values associated with BLLs, and blue datapoints indicate the values associated with FSRQs.

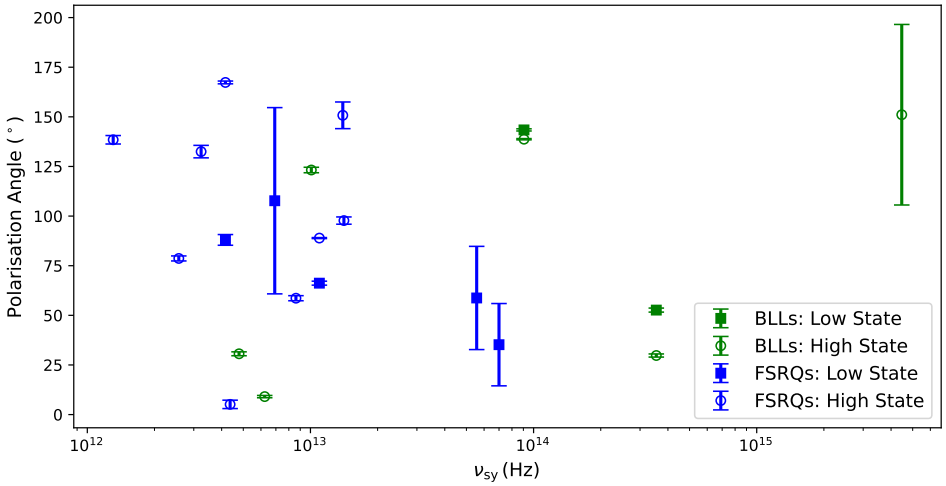

Figure 5.18: The averaged polarisation angle of the entire blazar sample vs. the synchrotron peak frequencies (ν_{sy}) of each source. The open circles indicate the averaged polarisation angle of blazars during high/active states, and the filled squares indicate the averaged polarisation angle of blazars during low/quiescent states. Green datapoints indicate values associated with BLLs, and blue datapoints indicate the values associated with FSRQs.

escent states. For this sample of blazars, a Spearman's test yielded $\rho = -0.357$ (p-value = 0.432) during low states, and $\rho = -0.414$ (p-value = 0.125) during high states. The correlation agrees well with what has been found by Angelakis et al. (2016), who found $\rho = -0.300$ (p-value = 2×10^{-3}) for their sample. The significance of the correlation for this sample is not as strong as that of the sample used by Angelakis et al. (2016), which is likely due to a lack of sufficient data. Thus, the anti-correlation between the polarisation and synchrotron peak frequency (as found by Angelakis et al., 2016, 2017) shows that LSP blazars are, as a whole, more polarised than HSPs. This result is shown in Figure 2.11 of Chapter 2, p. 25.

The polarisation angle as a function of ν_{sy} for both FSRQs and BLLs, during both high and low states, are shown in Figure 5.18. During low states, a correlation coefficient of $\rho = -0.357$ (p-value = 0.432) was found between the polarisation angle and location of the synchrotron peak frequency. During high states, these values were found to be $\rho = 0.121$ (p-value = 0.666). From the Spearman's test, there does not seem to be a clear monotonic relation between the observed polarisation angle and ν_{sy}. However, it was suggested by Angelakis et al. (2016) that – from additional statistical tests – the randomness of the polarisation angle does indeed depend on the location of the source's synchrotron peak frequency, with $\rho = 0.340$ (p-value = 0.044). Specifically, the authors showed that LSP sources will be less likely to have a preferred direction of polarisation than HSP sources.

The dependence of the degree of polarisation and the randomness of the polarisation angle on the location of the synchrotron peak frequency (ν_{sy}) hint towards a helical magnetic field structure downstream of a shock, as in the shock-in-jet model explained in Chapter 2 (see, for example, Figures 2.14 and 2.15 on pages 29 and 29). For a more detailed discussion, see e.g. Angelakis et al. (2016) and Tavecchio et al. (2018).

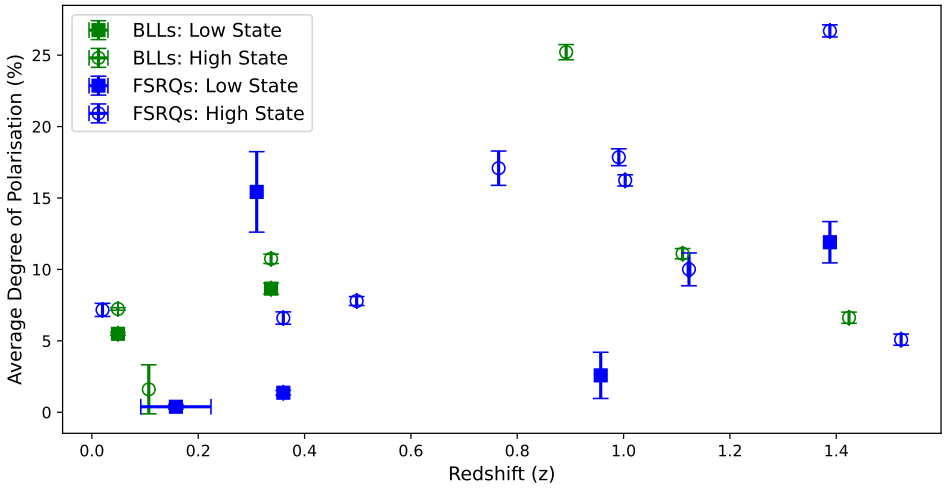

Figure 5.19: The averaged degree of polarisation of the entire blazar sample vs. the redshifts (z) of each source. The open circles indicate the averaged polarisation angle of blazars during high/active states, and the filled squares indicate the averaged polarisation angle of blazars during low/quiescent states. Green datapoints indicate values associated with BLLs, and blue datapoints indicate the values associated with FSRQs.

5.7 Polarisation vs. Redshift

We found no correlation between the observed degree of polarisation and the redshift of the blazars (see Figure 5.19), which is in agreement with what was found by the RoboPol monitoring campaign. During low states, the correlation between the degree of polarisation and redshifts was found to be $\rho = 0.179$ (p-value $= 0.702$). During high states, a similar result was obtained, with $\rho = 0.225$ (p-value $= 0.420$).

From the discussion above, it is clear that the observational findings in this project correlate well with what was found by the RoboPol monitoring campaign. In the following chapter, some concluding remarks will be given on the overall and noteworthy results from this project, along with a brief discussion of the intrinsic caveats and biases in this study, as well as how to improve upon it in future work.

Chapter 6

Conclusion

Blazars are some of the most numerous, brightest, and extreme sources in the γ-ray sky. The observed emission from blazars is jet-dominated and, therefore, highly Doppler boosted, emitted across the entire electromagnetic spectrum (radio to γ-ray bands). These sources are characterised by highly variable emission, with rapid outbursts/flares occurring on short timescales. At optical/UV wavelengths, blazar emission is a superposition of the non-thermal (polarised) synchrotron emission originating within the relativistic jet, and thermal (unpolarised) emission from the accretion disc, host galaxy, and other components of the AGN structure. However, their jet-dominated, multi-wavelength, variable and polarised emission has proven to be exceptionally difficult to explain and/or model, as the precise nature of the particle populations and resulting emission is still unclear.

Spectropolarimetry, then, is a powerful diagnostic tool in the study of blazar emission, as it allows for the thermal (unpolarised) and non-thermal (polarised) emission components to the emission at optical/UV wavelengths to be disentangled. This, in turn, can constrain the accretion disc component of the observed emission, and provide an insight into the particle population that produces the non-thermal emission, the magnetic field in the jet, and mass of the central SMBH.

To investigate the spectropolarimetric behaviour of the blazar population as a whole is a critical step towards a better understanding of blazars. To this end, both low-energy (i.e. optical/UV) and high-energy (X-ray, γ-ray) polarimetric monitoring campaigns have been launched/are to be launched in the near future, like, for example, the RoboPol optical monitoring campaign at optical wavelengths, and the IXPE mission in the X-ray regime. The information resulting from these campaigns will provide critical information on the nature and origin of blazar emission, and will lead to a clearer understanding of these highly energetic, extragalactic sources.

To this end, an optical spectropolarimetric observation campaign of a number of high-energy blazars was undertaken to investigate their polarimetric behaviour. The aims of this project were to a) investigate the change in the degree of polarisation as the blazars transition from high/flaring states to low/quiescent states, b) monitor the evolution of polarisation in different types of blazars over a longer period of time, and c) determine the overall trends in the behaviour of the selected blazars. Such a project is of importance, not only to constrain the parameters in combined SED and polarimetry modelling, but also to serve as a complement to the upcoming results from high-energy polarimetry

missions, such as the IXPE. Combined, the polarimetry information might lead to a clear understanding of the various contributions to the observed blazar emission.

This study looked at the optical spectropolarimetric behaviour of eighteen different blazars (of which six were BLLs and twelve were FSRQs), spanning the period from 2016 to 2022. A total of 68 optical spectropolarimetric observations were obtained using SALT, all of which where reduced and analysed in this investigation. This was complemented by optical photometry obtained with the LCO Telescope Network, and the publicly available γ-ray light curves from the Fermi LCR. The observations showed how the polarisation changed for each blazar during different stages of activity, including how the slope of polarisation changed. The behaviour of all the sources was considered, showing results consistent with, for example, the RoboPol analyses. From the observations, the most noteworthy results are summarised in Section 6.1, while in Section 6.2, we discussed how this study could be improved and expanded on in future work.

6.1 Noteworthy Results

Two blazars with interesting, out of the ordinary results were observed. The first is the LBL AP Librae, where the γ-ray and optical emission underwent some large-scale, long-term variability during the first half of 2021. The observed degree of linear polarisation followed the same trend, but lagged behind the behaviour of the lightcurves by ~ 56 days. The optical and γ-ray behaviour of this source indicates some large-scale change in the structure of the jet, but this hypothesis is constrained by the limited observational data available.

The second source exhibiting interesting behaviour is the FSRQ PKS 1510–089. This source was in an active state during the 2021 observing period, but diminished greatly in the γ-ray and optical regimes during the 2022 semester. The observed degree of polarisation also decreased from $\langle \Pi \rangle \approx 6.60\%$ in 2021 to consistently $< 2\%$ in 2022. All the observational results seem to indicate that the jet-component of the emission has "switched off".

The overall behaviour of the observed BLLs and FSRQs were consistent with what is expected from literature, with FSRQs displaying higher degrees of polarisation, and a wider spread in the degrees of polarisation, accompanied by more regular outbursts/flares than BLLs. During quiescence, the average degree of polarisation remained below $\sim 15\%$ for both the FSRQ and BLL samples, with an average of $\Pi \approx 5.99\%$ and $\Pi \approx 8.93\%$, respectively. This increased to an average of $\Pi \approx 14.56\%$ for FSRQs, and $\Pi \approx 11.57\%$ for BLLs during high states.

An interesting result that arose from this project is that, for the sources that were observed twice during the same high/active γ-ray state, the degree of polarisation observed while the flux values were still on the rise was significantly higher than what was observed after the peak of the enhanced state, while the fluxes were decreasing. This is especially clear for three sources, namely PKS 0537–441, PKS 0208–512, and 4FGL J0231.2–4745, where the degree of polarisation changed by more than 15% in all three cases.

There does not seem to be a significant correlation between the slope of the polarisation and the degree of the polarisation, nor between the slope of the polarisation and the normalised γ-ray flux ($F_{\rm obs}/F_{\rm 4FGL}$). For both BLLs and FSRQs, the slope and the degree of polarisation, a correlation of $\rho = 0.375$ (p-value = 0.054) and $\rho = -0.080$ (p-value = 0.621) during low and high states, respectively, was found. For the slope and the γ-ray flux, a correlation of $\rho = 0.085$ (p-value = 0.672) was found during low states, and $\rho = -0.096$ (p-value = 0.550) during high states. However, the lack of a strong correlation/anti-correlation may be due to the uneven sampling of sources, since most sources are only sampled once or twice during one state of activity. Stronger correlations were found when considering individual sources, and further investigation is warranted. It would be expected that combined changes in the level of the non-thermal flux, as well as the ordering of the magnetic field would introduce changing slopes in the polarisation (as discussed in Section 5.3 of Chapter 5, p. 81).

There appears to be a trend between the average degree of polarisation and γ-ray flux. A Spearman's test (for both BLLs and FSRQs) resulted in a strong correlation of $\rho = 0.623$ (p-value $= 5.223 \times 10^{-3}$) during low states. However, no correlation during high states, with $\rho = -0.068$ (p-value = 0.671), was found. For both BLLs and FSRQs, we found no correlation between the average degree of polarisation and γ-ray luminosity. A Spearman's test resulted in $\rho = -0.179$ (p-value = 0.702) during low states, and $\rho = 0.296$ (p-value = 0.283) during high states.

The average degree of polarisation does, however, by eye appear to be anti-correlated with the location of the synchrotron peak frequency. This is similar to what has previously been found by the RoboPol studies, where higher degrees of polarisation are observed for LSP blazars than for HSPs. However, from our small sample, no significant correlation could be found, with $\rho = -0.357$ (p-value = 0.432) and $\rho = -0.414$ (p-value = 0.125) during low and high states, respectively. This anti-correlation has been suggested to be linked to a helically structured magnetic field in the downstream direction of a shock in the blazar-jet.

There is no clear correlation between the average degree of polarisation of blazars and its corresponding redshift, with $\rho = 0.179$ (p-value = 0.702) during low states, and $\rho = 0.225$ (p-value = 0.420) during high states. This is also in agreement with what has been found by the RoboPol collaboration, where the modulation index of the polarisation, rather than the polarisation itself, depends on the redshift of the source.

6.2 Future Work

The overall results from this spectropolarimetric study are in general agreement with the findings from, for example, the RoboPol monitoring campaign, despite the smaller sample of sources and the bias towards flaring activity. This study, however, adds the additional element of the slope of polarisation, which showed varying behaviour during different flaring states, as well as trends with the level of polarisation for a few sources.

This highlights that a larger, more systematic, multi-wavelength survey of blazars is required. This will require an unbiased, high-cadence investigation that does not focus

only on blazars in an enhanced state of activity, but investigates BLLs and FSRQs with equal weight. Additional observational data in other wavelength bands (specifically in the radio and X-ray regimes) is required to investigate the radio signatures of the jet, as well as the high-energy polarisation of the jet. Further, modelling of the nature of polarisation as it varies with flux, ordering of the magnetic field, redshifts, etc., is required to fully understand these highly energetic sources.

Future work would involve more detailed modelling of the individual sources observed, considering any available multiwavelenth observations. But, more importantly, a more systematic spectropolarimetry survey is required of a selected number of blazars. This will provide a more objective study of the optical spectropolarimetric behaviour of blazars, and will serve as an excellent complement to the behaviour of the polarisation in the X-ray regime (as will be detected by the IXPE in the near future), and it is left as a future work to perform such a survey.

Bibliography

A. A. Abdo, M. Ackermann, M. Ajello, W. B. Atwood, M. Axelsson, L. Baldini, J. Ballet, D. L. Band, G. Barbiellini, D. Bastieri, M. Battelino, B. M. Baughman, K. Bechtol, R. Bellazzini, B. Berenji, G. F. Bignami, R. D. Blandford, E. D. Bloom, E. Bonamente, A. W. Borgland, A. Bouvier, J. Bregeon, A. Brez, M. Brigida, P. Bruel, T. H. Burnett, G. A. Caliandro, R. A. Cameron, P. A. Caraveo, J. M. Casandjian, E. Cavazzuti, C. Cecchi, E. Charles, A. Chekhtman, C. C. Cheung, J. Chiang, S. Ciprini, R. Claus, J. Cohen-Tanugi, L. R. Cominsky, J. Conrad, R. Corbet, L. Costamante, S. Cutini, D. S. Davis, C. D. Dermer, A. de Angelis, A. de Luca, F. de Palma, S. W. Digel, M. Dormody, E. do Couto e Silva, P. S. Drell, R. Dubois, D. Dumora, C. Farnier, C. Favuzzi, S. J. Fegan, E. C. Ferrara, W. B. Focke, M. Frailis, Y. Fukazawa, S. Funk, P. Fusco, F. Gargano, D. Gasparrini, N. Gehrels, S. Germani, B. Giebels, N. Giglietto, P. Giommi, F. Giordano, T. Glanzman, G. Godfrey, I. A. Grenier, M. H. Grondin, J. E. Grove, L. Guillemot, S. Guiriec, Y. Hanabata, A. K. Harding, R. C. Hartman, M. Hayashida, E. Hays, S. E. Healey, D. Horan, R. E. Hughes, G. Jóhannesson, A. S. Johnson, R. P. Johnson, T. J. Johnson, W. N. Johnson, T. Kamae, H. Katagiri, J. Kataoka, N. Kawai, M. Kerr, J. Knödlseder, D. Kocevski, M. L. Kocian, N. Komin, F. Kuehn, M. Kuss, J. Lande, L. Latronico, S. H. Lee, M. Lemoine-Goumard, F. Longo, F. Loparco, B. Lott, M. N. Lovellette, P. Lubrano, G. M. Madejski, A. Makeev, M. Marelli, M. N. Mazziotta, W. McConville, J. E. McEnery, S. McGlynn, C. Meurer, P. F. Michelson, W. Mitthumsiri, T. Mizuno, A. A. Moiseev, C. Monte, M. E. Monzani, E. Moretti, A. Morselli, I. V. Moskalenko, S. Murgia, T. Nakamori, P. L. Nolan, J. P. Norris, E. Nuss, M. Ohno, T. Ohsugi, N. Omodei, E. Orlando, J. F. Ormes, M. Ozaki, D. Paneque, J. H. Panetta, D. Parent, V. Pelassa, M. Pepe, M. Pesce-Rollins, F. Piron, T. A. Porter, L. Poupard, S. Rainò, R. Rando, P. S. Ray, M. Razzano, N. Rea, A. Reimer, O. Reimer, T. Reposeur, S. Ritz, L. S. Rochester, A. Y. Rodriguez, R. W. Romani, M. Roth, F. Ryde, H. F. W. Sadrozinski, D. Sanchez, A. Sander, P. M. Saz Parkinson, J. D. Scargle, T. L. Schalk, A. Sellerholm, C. Sgrò, M. S. Shaw, C. Shrader, A. Sierpowska-Bartosik, E. J. Siskind, D. A. Smith, P. D. Smith, G. Spandre, P. Spinelli, J. L. Starck, T. E. Stephens, M. S. Strickman, A. W. Strong, D. J. Suson, H. Tajima, H. Takahashi, T. Takahashi, T. Tanaka, J. B. Thayer, J. G. Thayer, D. J. Thompson, L. Tibaldo, O. Tibolla, D. F. Torres, G. Tosti, A. Tramacere, Y. Uchiyama, T. L. Usher, A. Van Etten, N. Vilchez, V. Vitale, A. P. Waite, E. Wallace, P. Wang, K. Watters, B. L. Winer, K. S. Wood, T. Ylinen, M. Ziegler, and Fermi/LAT Collaboration. Fermi/Large Area Telescope Bright Gamma-Ray Source List. ApJS, 183(1):46–66, July 2009. doi: 10.1088/0067-0049/183/1/46.

A. A. Abdo, M. Ackermann, I. Agudo, M. Ajello, H. D. Aller, M. F. Aller, E. Angelakis, A. A. Arkharov, M. Axelsson, U. Bach, L. Baldini, J. Ballet, G. Barbiellini, D. Bastieri, B. M. Baughman, K. Bechtol, R. Bellazzini, E. Benitez, A. Berdyugin, B. Berenji, R. D.

Blandford, E. D. Bloom, M. Boettcher, E. Bonamente, A. W. Borgland, J. Bregeon, A. Brez, M. Brigida, P. Bruel, T. H. Burnett, D. Burrows, S. Buson, G. A. Caliandro, L. Calzoletti, R. A. Cameron, M. Capalbi, P. A. Caraveo, D. Carosati, J. M. Casandjian, E. Cavazzuti, C. Cecchi, Ö. Çelik, E. Charles, S. Chaty, A. Chekhtman, W. P. Chen, J. Chiang, G. Chincarini, S. Ciprini, R. Claus, J. Cohen-Tanugi, S. Colafrancesco, L. R. Cominsky, J. Conrad, L. Costamante, S. Cutini, F. D'ammando, R. Deitrick, V. D'Elia, C. D. Dermer, A. de Angelis, F. de Palma, S. W. Digel, I. Donnarumma, E. do Couto e. Silva, P. S. Drell, R. Dubois, D. Dultzin, D. Dumora, A. Falcone, C. Farnier, C. Favuzzi, S. J. Fegan, W. B. Focke, E. Forné, P. Fortin, M. Frailis, L. Fuhrmann, Y. Fukazawa, S. Funk, P. Fusco, J. L. Gómez, F. Gargano, D. Gasparrini, N. Gehrels, S. Germani, B. Giebels, N. Giglietto, P. Giommi, F. Giordano, A. Giuliani, T. Glanzman, G. Godfrey, I. A. Grenier, C. Gronwall, J. E. Grove, L. Guillemot, S. Guiriec, M. A. Gurwell, D. Hadasch, Y. Hanabata, A. K. Harding, M. Hayashida, E. Hays, S. E. Healey, J. Heidt, D. Hiriart, D. Horan, E. A. Hoversten, R. E. Hughes, R. Itoh, M. S. Jackson, G. Jóhannesson, A. S. Johnson, W. N. Johnson, S. G. Jorstad, M. Kadler, T. Kamae, H. Katagiri, J. Kataoka, N. Kawai, J. Kennea, M. Kerr, G. Kimeridze, J. Knödlseder, M. L. Kocian, E. N. Kopatskaya, E. Koptelova, T. S. Konstantinova, Y. Y. Kovalev, Yu. A. Kovalev, O. M. Kurtanidze, M. Kuss, J. Lande, V. M. Larionov, L. Latronico, P. Leto, E. Lindfors, F. Longo, F. Loparco, B. Lott, M. N. Lovellette, P. Lubrano, G. M. Madejski, A. Makeev, P. Marchegiani, A. P. Marscher, F. Marshall, W. Max-Moerbeck, M. N. Mazziotta, W. McConville, J. E. McEnery, C. Meurer, P. F. Michelson, W. Mitthumsiri, T. Mizuno, A. A. Moiseev, C. Monte, M. E. Monzani, A. Morselli, I. V. Moskalenko, S. Murgia, I. Nestoras, K. Nilsson, N. A. Nizhelsky, P. L. Nolan, J. P. Norris, E. Nuss, T. Ohsugi, R. Ojha, N. Omodei, E. Orlando, J. F. Ormes, J. Osborne, M. Ozaki, L. Pacciani, P. Padovani, C. Pagani, K. Page, D. Paneque, J. H. Panetta, D. Parent, M. Pasanen, V. Pavlidou, V. Pelassa, M. Pepe, M. Perri, M. Pesce-Rollins, S. Piranomonte, F. Piron, C. Pittori, T. A. Porter, S. Puccetti, F. Rahoui, S. Rainò, C. Raiteri, R. Rando, M. Razzano, A. Reimer, O. Reimer, T. Reposeur, J. L. Richards, S. Ritz, L. S. Rochester, A. Y. Rodriguez, R. W. Romani, J. A. Ros, M. Roth, P. Roustazadeh, F. Ryde, H. F. W. Sadrozinski, A. Sadun, D. Sanchez, A. Sander, P. M. Saz Parkinson, J. D. Scargle, A. Sellerholm, C. Sgrò, M. S. Shaw, L. A. Sigua, E. J. Siskind, D. A. Smith, P. D. Smith, G. Spandre, P. Spinelli, J. L. Starck, M. Stevenson, G. Stratta, M. S. Strickman, D. J. Suson, H. Tajima, H. Takahashi, T. Takahashi, L. O. Takalo, T. Tanaka, J. B. Thayer, J. G. Thayer, D. J. Thompson, L. Tibaldo, D. F. Torres, G. Tosti, A. Tramacere, Y. Uchiyama, T. L. Usher, V. Vasileiou, F. Verrecchia, N. Vilchez, M. Villata, V. Vitale, A. P. Waite, P. Wang, B. L. Winer, K. S. Wood, T. Ylinen, J. A. Zensus, G. V. Zhekanis, and M. Ziegler. The Spectral Energy Distribution of Fermi Bright Blazars. ApJ, 716(1):30–70, June 2010a. doi: 10.1088/0004-637X/716/1/30.

A. A. Abdo, M. Ackermann, M. Ajello, W. B. Atwood, M. Axelsson, L. Baldini, J. Ballet, G. Barbiellini, D. Bastieri, K. Bechtol, R. Bellazzini, B. Berenji, R. D. Blandford, E. D. Bloom, E. Bonamente, A. W. Borgland, A. Bouvier, J. Bregeon, A. Brez, M. Brigida, P. Bruel, T. H. Burnett, S. Buson, G. A. Caliandro, R. A. Cameron, P. A. Caraveo, S. Carrigan, J. M. Casandjian, E. Cavazzuti, C. Cecchi, Ö. Çelik, E. Charles, A. Chekhtman, C. C. Cheung, J. Chiang, S. Ciprini, R. Claus, J. Cohen-Tanugi, J. Conrad, S. Cutini, C. D. Dermer, A. de Angelis, F. de Palma, S. W. Digel, E. do Couto e. Silva, P. S. Drell, R. Dubois, D. Dumora, C. Farnier, C. Favuzzi, S. J. Fegan, W. B. Focke, P. Fortin, M. Frailis, Y. Fukazawa, S. Funk, P. Fusco, F. Gargano, D. Gas-

parrini, N. Gehrels, S. Germani, B. Giebels, N. Giglietto, P. Giommi, F. Giordano, T. Glanzman, G. Godfrey, I. A. Grenier, M. H. Grondin, J. E. Grove, L. Guillemot, S. Guiriec, A. K. Harding, R. C. Hartman, M. Hayashida, E. Hays, S. E. Healey, D. Horan, R. E. Hughes, M. S. Jackson, G. Jóhannesson, A. S. Johnson, W. N. Johnson, T. Kamae, H. Katagiri, J. Kataoka, N. Kawai, M. Kerr, J. Knödlseder, M. Kuss, J. Lande, L. Latronico, M. Lemoine-Goumard, F. Longo, F. Loparco, B. Lott, M. N. Lovellette, P. Lubrano, G. M. Madejski, A. Makeev, M. N. Mazziotta, W. McConville, J. E. McEnery, C. Meurer, P. F. Michelson, W. Mitthumsiri, T. Mizuno, A. A. Moiseev, C. Monte, M. E. Monzani, A. Morselli, I. V. Moskalenko, S. Murgia, P. L. Nolan, J. P. Norris, E. Nuss, T. Ohsugi, N. Omodei, E. Orlando, J. F. Ormes, D. Paneque, J. H. Panetta, D. Parent, V. Pelassa, M. Pepe, M. Persic, M. Pesce-Rollins, F. Piron, T. A. Porter, S. Rainò, R. Rando, M. Razzano, A. Reimer, O. Reimer, T. Reposeur, S. Ritz, L. S. Rochester, A. Y. Rodriguez, R. W. Romani, M. Roth, F. Ryde, H. F. W. Sadrozinski, D. Sanchez, A. Sander, P. M. Saz Parkinson, J. D. Scargle, C. Sgrò, E. J. Siskind, D. A. Smith, P. D. Smith, G. Spandre, P. Spinelli, M. S. Strickman, D. J. Suson, H. Tajima, H. Takahashi, T. Takahashi, T. Tanaka, J. B. Thayer, J. G. Thayer, D. J. Thompson, L. Tibaldo, D. F. Torres, G. Tosti, A. Tramacere, Y. Uchiyama, T. L. Usher, V. Vasileiou, N. Vilchez, M. Villata, V. Vitale, A. P. Waite, P. Wang, B. L. Winer, K. S. Wood, T. Ylinen, and M. Ziegler. Spectral Properties of Bright Fermi-Detected Blazars in the Gamma-Ray Band. ApJ, 710(2):1271–1285, February 2010b. doi: 10.1088/0004-637X/710/2/1271.

M. Ackermann, M. Ajello, W. B. Atwood, L. Baldini, J. Ballet, G. Barbiellini, D. Bastieri, J. Becerra Gonzalez, R. Bellazzini, E. Bissaldi, R. D. Blandford, E. D. Bloom, R. Bonino, E. Bottacini, T. J. Brandt, J. Bregeon, R. J. Britto, P. Bruel, R. Buehler, S. Buson, G. A. Caliandro, R. A. Cameron, M. Caragiulo, P. A. Caraveo, B. Carpenter, J. M. Casandjian, E. Cavazzuti, C. Cecchi, E. Charles, A. Chekhtman, C. C. Cheung, J. Chiang, G. Chiaro, S. Ciprini, R. Claus, J. Cohen-Tanugi, L. R. Cominsky, J. Conrad, S. Cutini, R. D'Abrusco, F. D'Ammando, A. de Angelis, R. Desiante, S. W. Digel, L. Di Venere, P. S. Drell, C. Favuzzi, S. J. Fegan, E. C. Ferrara, J. Finke, W. B. Focke, A. Franckowiak, L. Fuhrmann, Y. Fukazawa, A. K. Furniss, P. Fusco, F. Gargano, D. Gasparrini, N. Giglietto, P. Giommi, F. Giordano, M. Giroletti, T. Glanzman, G. Godfrey, I. A. Grenier, J. E. Grove, S. Guiriec, J. W. Hewitt, A. B. Hill, D. Horan, R. Itoh, G. Jóhannesson, A. S. Johnson, W. N. Johnson, J. Kataoka, T. Kawano, F. Krauss, M. Kuss, G. La Mura, S. Larsson, L. Latronico, C. Leto, J. Li, L. Li, F. Longo, F. Loparco, B. Lott, M. N. Lovellette, P. Lubrano, G. M. Madejski, M. Mayer, M. N. Mazziotta, J. E. McEnery, P. F. Michelson, T. Mizuno, A. A. Moiseev, M. E. Monzani, A. Morselli, I. V. Moskalenko, S. Murgia, E. Nuss, M. Ohno, T. Ohsugi, R. Ojha, N. Omodei, M. Orienti, E. Orlando, A. Paggi, D. Paneque, J. S. Perkins, M. Pesce-Rollins, F. Piron, G. Pivato, T. A. Porter, S. Rainò, R. Rando, M. Razzano, S. Razzaque, A. Reimer, O. Reimer, R. W. Romani, D. Salvetti, M. Schaal, F. K. Schinzel, A. Schulz, C. Sgrò, E. J. Siskind, K. V. Sokolovsky, F. Spada, G. Spandre, P. Spinelli, L. Stawarz, D. J. Suson, H. Takahashi, T. Takahashi, Y. Tanaka, J. G. Thayer, J. B. Thayer, L. Tibaldo, D. F. Torres, E. Torresi, G. Tosti, E. Troja, Y. Uchiyama, G. Vianello, B. L. Winer, K. S. Wood, and S. Zimmer. The Third Catalog of Active Galactic Nuclei Detected by the Fermi Large Area Telescope. ApJ, 810 (1):14, September 2015. doi: 10.1088/0004-637X/810/1/14.

F. Aharonian, A. G. Akhperjanian, A. R. Bazer-Bachi, B. Behera, M. Beilicke, W. Ben-

bow, D. Berge, K. Bernlöhr, C. Boisson, O. Bolz, V. Borrel, T. Boutelier, I. Braun, E. Brion, A. M. Brown, R. Bühler, I. Büsching, T. Bulik, S. Carrigan, P. M. Chadwick, A. C. Clapson, L. M. Chounet, G. Coignet, R. Cornils, L. Costamante, B. Degrange, H. J. Dickinson, A. Djannati-Ataï, W. Domainko, L. O'C. Drury, G. Dubus, J. Dyks, K. Egberts, D. Emmanoulopoulos, P. Espigat, C. Farnier, F. Feinstein, A. Fiasson, A. Förster, G. Fontaine, Seb. Funk, S. Funk, M. Füßling, Y. A. Gallant, B. Giebels, J. F. Glicenstein, B. Glück, P. Goret, C. Hadjichristidis, D. Hauser, M. Hauser, G. Heinzelmann, G. Henri, G. Hermann, J. A. Hinton, A. Hoffmann, W. Hofmann, M. Holleran, S. Hoppe, D. Horns, A. Jacholkowska, O. C. de Jager, E. Kendziorra, M. Kerschhaggl, B. Khélifi, Nu. Komin, K. Kosack, G. Lamanna, I. J. Latham, R. Le Gallou, A. Lemière, M. Lemoine-Goumard, J. P. Lenain, T. Lohse, J. M. Martin, O. Martineau-Huynh, A. Marcowith, C. Masterson, G. Maurin, T. J. L. McComb, R. Moderski, E. Moulin, M. de Naurois, D. Nedbal, S. J. Nolan, J. P. Olive, K. J. Orford, J. L. Osborne, M. Ostrowski, M. Panter, G. Pedaletti, G. Pelletier, P. O. Petrucci, S. Pita, G. Pühlhofer, M. Punch, S. Ranchon, B. C. Raubenheimer, M. Raue, S. M. Rayner, M. Renaud, J. Ripken, L. Rob, L. Rolland, S. Rosier-Lees, G. Rowell, B. Rudak, J. Ruppel, V. Sahakian, A. Santangelo, L. Saugé, S. Schlenker, R. Schlickeiser, R. Schröder, U. Schwanke, S. Schwarzburg, S. Schwemmer, A. Shalchi, H. Sol, D. Spangler, Ł. Stawarz, R. Steenkamp, C. Stegmann, G. Superina, P. H. Tam, J. P. Tavernet, R. Terrier, C. van Eldik, G. Vasileiadis, C. Venter, J. P. Vialle, P. Vincent, M. Vivier, H. J. Völk, F. Volpe, S. J. Wagner, M. Ward, and A. A. Zdziarski. An Exceptional Very High Energy Gamma-Ray Flare of PKS 2155-304. ApJ, 664(2):L71–L74, August 2007. doi: 10.1086/520635.

F. Ait Benkhali, W. Hofmann, F. M. Rieger, and N. Chakraborty. Evaluating quasi-periodic variations in the γ-ray light curves of Fermi-LAT blazars. A&A, 634:A120, February 2020. doi: 10.1051/0004-6361/201935117.

M. Ajello, R. Angioni, M. Axelsson, J. Ballet, G. Barbiellini, D. Bastieri, J. Becerra Gonzalez, R. Bellazzini, E. Bissaldi, E. D. Bloom, R. Bonino, E. Bottacini, P. Bruel, S. Buson, F. Cafardo, R. A. Cameron, E. Cavazzuti, S. Chen, C. C. Cheung, S. Ciprini, D. Costantin, S. Cutini, F. D'Ammando, P. de la Torre Luque, R. de Menezes, F. de Palma, A. Desai, N. Di Lalla, L. Di Venere, A. Domínguez, F. Fana Dirirsa, E. C. Ferrara, J. Finke, A. Franckowiak, Y. Fukazawa, S. Funk, P. Fusco, F. Gargano, S. Garrappa, D. Gasparrini, N. Giglietto, F. Giordano, M. Giroletti, D. Green, I. A. Grenier, S. Guiriec, S. Harita, E. Hays, D. Horan, R. Itoh, G. Jóhannesson, M. Kovac'evic', F. Krauss, M. Kreter, M. Kuss, S. Larsson, C. Leto, J. Li, I. Liodakis, F. Longo, F. Loparco, B. Lott, M. N. Lovellette, P. Lubrano, G. M. Madejski, S. Maldera, A. Manfreda, G. Martí-Devesa, F. Massaro, M. N. Mazziotta, I. Mereu, M. Meyer, G. Migliori, N. Mirabal, T. Mizuno, M. E. Monzani, A. Morselli, I. V. Moskalenko, M. Negro, R. Nemmen, E. Nuss, L. S. Ojha, R. Ojha, N. Omodei, M. Orienti, E. Orlando, J. F. Ormes, V. S. Paliya, Z. Pei, H. Peña-Herazo, M. Persic, M. Pesce-Rollins, L. Petrov, F. Piron, H. Poon, G. Principe, S. Rainò, R. Rando, B. Rani, M. Razzano, S. Razzaque, A. Reimer, O. Reimer, F. K. Schinzel, D. Serini, C. Sgrò, E. J. Siskind, G. Spandre, P. Spinelli, D. J. Suson, Y. Tachibana, D. J. Thompson, D. F. Torres, E. Torresi, E. Troja, J. Valverde, P. van Zyl, and M. Yassine. The Fourth Catalog of Active Galactic Nuclei Detected by the Fermi Large Area Telescope. ApJ, 892(2):105, April 2020. doi: 10.3847/1538-4357/ab791e.

J. Albert, E. Aliu, H. Anderhub, P. Antoranz, A. Armada, C. Baixeras, J. A. Barrio, H. Bartko, D. Bastieri, J. K. Becker, W. Bednarek, K. Berger, C. Bigongiari, A. Biland, R. K. Bock, P. Bordas, V. Bosch-Ramon, T. Bretz, I. Britvitch, M. Camara, E. Carmona, A. Chilingarian, J. A. Coarasa, S. Commichau, J. L. Contreras, J. Cortina, M. T. Costado, V. Curtef, V. Danielyan, F. Dazzi, A. De Angelis, C. Delgado, R. de los Reyes, B. De Lotto, E. Domingo-Santamaría, D. Dorner, M. Doro, M. Errando, M. Fagiolini, D. Ferenc, E. Fernández, R. Firpo, J. Flix, M. V. Fonseca, L. Font, M. Fuchs, N. Galante, R. J. García-López, M. Garczarczyk, M. Gaug, M. Giller, F. Goebel, D. Hakobyan, M. Hayashida, T. Hengstebeck, A. Herrero, D. Höhne, J. Hose, D. Hrupec, C. C. Hsu, P. Jacon, T. Jogler, R. Kosyra, D. Kranich, R. Kritzer, A. Laille, E. Lindfors, S. Lombardi, F. Longo, J. López, M. López, E. Lorenz, P. Majumdar, G. Maneva, K. Mannheim, O. Mansutti, M. Mariotti, M. Martínez, D. Mazin, C. Merck, M. Meucci, M. Meyer, J. M. Miranda, R. Mirzoyan, S. Mizobuchi, A. Moralejo, D. Nieto, K. Nilsson, J. Ninkovic, E. Oña-Wilhelmi, N. Otte, I. Oya, D. Paneque, M. Panniello, R. Paoletti, J. M. Paredes, M. Pasanen, D. Pascoli, F. Pauss, R. Pegna, M. Persic, L. Peruzzo, A. Piccioli, E. Prandini, N. Puchades, A. Raymers, W. Rhode, M. Ribó, J. Rico, M. Rissi, A. Robert, S. Rügamer, A. Saggion, T. Saito, A. Sánchez, P. Sartori, V. Scalzotto, V. Scapin, R. Schmitt, T. Schweizer, M. Shayduk, K. Shinozaki, S. N. Shore, N. Sidro, A. Sillanpää, D. Sobczynska, A. Stamerra, L. S. Stark, L. Takalo, F. Tavecchio, P. Temnikov, D. Tescaro, M. Teshima, D. F. Torres, N. Turini, H. Vankov, V. Vitale, R. M. Wagner, T. Wibig, W. Wittek, F. Zandanel, R. Zanin, and J. Zapatero. Variable Very High Energy γ-Ray Emission from Markarian 501. ApJ, 669(2):862–883, November 2007. doi: 10.1086/521382.

Tal Alexander. ZDCF: Z-Transformed Discrete Correlation Function. Astrophysics Source Code Library, record ascl:1404.002, April 2014.

E. Angelakis, T. Hovatta, D. Blinov, V. Pavlidou, S. Kiehlmann, I. Myserlis, M. Böttcher, P. Mao, G. V. Panopoulou, I. Liodakis, O. G. King, M. Baloković, A. Kus, N. Kylafis, A. Mahabal, A. Marecki, E. Paleologou, I. Papadakis, I. Papamastorakis, E. Pazderski, T. J. Pearson, S. Prabhudesai, A. N. Ramaprakash, A. C. S. Readhead, P. Reig, K. Tassis, M. Urry, and J. A. Zensus. RoboPol: the optical polarization of gamma-ray-loud and gamma-ray-quiet blazars. MNRAS, 463(3):3365–3380, December 2016. doi: 10.1093/mnras/stw2217.

E. Angelakis, RoboPol Collaboration, D. A. Blinov, M. Böttcher, T. Hovatta, S. Kiehlmann, I. Myserlis, V. Pavlidou, and J. Anton Zensus. The dependence of optical polarisation of blazars on the synchrotron peak frequency. In *Proceedings of the 7th International Fermi Symposium*, page 19, October 2017. doi: 10.22323/1.312.0019.

R. Angioni. Fermi-LAT detection of strong gamma-ray activity from the FSRQ PKS 0346-27. *The Astronomer's Telegram*, 11251:1, February 2018.

R. Angioni. Fermi-LAT detection of enhanced gamma-ray activity from the FSRQ PKS 0208-512. *The Astronomer's Telegram*, 13320:1, December 2019.

R. Angioni. Fermi-LAT detection of enhanced gamma-ray activity from the FSRQs PKS 0837+012 and PKS 1127-14. *The Astronomer's Telegram*, 14260:1, December 2020.

R. Angioni, Janeth Valverde, and Roopesh Ojha. Fermi-LAT detection of renewed gamma-ray activity from the FSRQ PKS 0035-252. *The Astronomer's Telegram*, 11854:1, July 2018.

R. R. J. Antonucci and J. S. Miller. Spectropolarimetry and the nature of NGC 1068. ApJ, 297:621–632, October 1985. doi: 10.1086/163559.

Robert Antonucci. Unified models for active galactic nuclei and quasars. ARA&A, 31: 473–521, January 1993. doi: 10.1146/annurev.aa.31.090193.002353.

F. Arago and J. A. Barral. *Astronomie populaire*. 1854.

W. B. Atwood, A. A. Abdo, M. Ackermann, W. Althouse, B. Anderson, M. Axelsson, L. Baldini, J. Ballet, D. L. Band, G. Barbiellini, J. Bartelt, D. Bastieri, B. M. Baughman, K. Bechtol, D. Bédérède, F. Bellardi, R. Bellazzini, B. Berenji, G. F. Bignami, D. Bisello, E. Bissaldi, R. D. Blandford, E. D. Bloom, J. R. Bogart, E. Bonamente, J. Bonnell, A. W. Borgland, A. Bouvier, J. Bregeon, A. Brez, M. Brigida, P. Bruel, T. H. Burnett, G. Busetto, G. A. Caliandro, R. A. Cameron, P. A. Caraveo, S. Carius, P. Carlson, J. M. Casandjian, E. Cavazzuti, M. Ceccanti, C. Cecchi, E. Charles, A. Chekhtman, C. C. Cheung, J. Chiang, R. Chipaux, A. N. Cillis, S. Ciprini, R. Claus, J. Cohen-Tanugi, S. Condamoor, J. Conrad, R. Corbet, L. Corucci, L. Costamante, S. Cutini, D. S. Davis, D. Decotigny, M. DeKlotz, C. D. Dermer, A. de Angelis, S. W. Digel, E. do Couto e Silva, P. S. Drell, R. Dubois, D. Dumora, Y. Edmonds, D. Fabiani, C. Farnier, C. Favuzzi, D. L. Flath, P. Fleury, W. B. Focke, S. Funk, P. Fusco, F. Gargano, D. Gasparrini, N. Gehrels, F. X. Gentit, S. Germani, B. Giebels, N. Giglietto, P. Giommi, F. Giordano, T. Glanzman, G. Godfrey, I. A. Grenier, M. H. Grondin, J. E. Grove, L. Guillemot, S. Guiriec, G. Haller, A. K. Harding, P. A. Hart, E. Hays, S. E. Healey, M. Hirayama, L. Hjalmarsdotter, R. Horn, R. E. Hughes, G. Jóhannesson, G. Johansson, A. S. Johnson, R. P. Johnson, T. J. Johnson, W. N. Johnson, T. Kamae, H. Katagiri, J. Kataoka, A. Kavelaars, N. Kawai, H. Kelly, M. Kerr, W. Klamra, J. Knödlseder, M. L. Kocian, N. Komin, F. Kuehn, M. Kuss, D. Landriu, L. Latronico, B. Lee, S. H. Lee, M. Lemoine-Goumard, A. M. Lionetto, F. Longo, F. Loparco, B. Lott, M. N. Lovellette, P. Lubrano, G. M. Madejski, A. Makeev, B. Marangelli, M. M. Massai, M. N. Mazziotta, J. E. McEnery, N. Menon, C. Meurer, P. F. Michelson, M. Minuti, N. Mirizzi, W. Mitthumsiri, T. Mizuno, A. A. Moiseev, C. Monte, M. E. Monzani, E. Moretti, A. Morselli, I. V. Moskalenko, S. Murgia, T. Nakamori, S. Nishino, P. L. Nolan, J. P. Norris, E. Nuss, M. Ohno, T. Ohsugi, N. Omodei, E. Orlando, J. F. Ormes, A. Paccagnella, D. Paneque, J. H. Panetta, D. Parent, M. Pearce, M. Pepe, A. Perazzo, M. Pesce-Rollins, P. Picozza, L. Pieri, M. Pinchera, F. Piron, T. A. Porter, L. Poupard, S. Rainò, R. Rando, E. Rapposelli, M. Razzano, A. Reimer, O. Reimer, T. Reposeur, L. C. Reyes, S. Ritz, L. S. Rochester, A. Y. Rodriguez, R. W. Romani, M. Roth, J. J. Russell, F. Ryde, S. Sabatini, H. F. W. Sadrozinski, D. Sanchez, A. Sander, L. Sapozhnikov, P. M. Saz Parkinson, J. D. Scargle, T. L. Schalk, G. Scolieri, C. Sgrò, G. H. Share, M. Shaw, T. Shimokawabe, C. Shrader, A. Sierpowska-Bartosik, E. J. Siskind, D. A. Smith, P. D. Smith, G. Spandre, P. Spinelli, J. L. Starck, T. E. Stephens, M. S. Strickman, A. W. Strong, D. J. Suson, H. Tajima, H. Takahashi, T. Takahashi, T. Tanaka, A. Tenze, S. Tether, J. B. Thayer, J. G. Thayer, D. J. Thompson, L. Tibaldo, O. Tibolla, D. F. Torres, G. Tosti, A. Tramacere, M. Turri, T. L. Usher, N. Vilchez, V. Vitale, P. Wang, K. Watters, B. L. Winer, K. S. Wood, T. Ylinen, and M. Ziegler. The Large

Area Telescope on the Fermi Gamma-Ray Space Telescope Mission. ApJ, 697(2):1071–1102, June 2009. doi: 10.1088/0004-637X/697/2/1071.

L. Bassani and A. J. Dean. Extragalactic γ-ray astronomy. Space Sci. Rev., 35(4):367–398, August 1983. doi: 10.1007/BF00169232.

J. Becerra, R. Ojha, Marco Ajello, D. Kocevski, and R. Buehl. Fermi LAT Detection of a New Gamma-ray Source PKS 0131-522. *The Astronomer's Telegram*, 6223:1, June 2014.

V. Beckmann and C. Shrader. The AGN phenomenon: open issues. In *Proceedings of "An INTEGRAL view of the high-energy sky (the first 10 years)" - 9th INTEGRAL Workshop and celebration of the 10th anniversary of the launch (INTEGRAL 2012). 15-19 October 2012. Bibliotheque Nationale de France*, page 69, January 2012a.

Volker Beckmann and Chris R. Shrader. *Active Galactic Nuclei*. 2012b.

Nicola Bennert, Heino Falcke, Hartmut Schulz, Andrew S. Wilson, and Beverley J. Wills. Size and Structure of the Narrow-Line Region of Quasars. ApJ, 574(2):L105–L109, August 2002. doi: 10.1086/342420.

P. N. Best, G. Kauffmann, T. M. Heckman, J. Brinchmann, S. Charlot, Ž. Ivezić, and S. D. M. White. The host galaxies of radio-loud active galactic nuclei: mass dependences, gas cooling and active galactic nuclei feedback. MNRAS, 362(1):25–40, September 2005. doi: 10.1111/j.1365-2966.2005.09192.x.

M. Błażejowski, M. Sikora, R. Moderski, and G. M. Madejski. Comptonization of Infrared Radiation from Hot Dust by Relativistic Jets in Quasars. ApJ, 545(1):107–116, December 2000. doi: 10.1086/317791.

M. Błażejowski, G. Blaylock, I. H. Bond, S. M. Bradbury, J. H. Buckley, D. A. Carter-Lewis, O. Celik, P. Cogan, W. Cui, M. Daniel, C. Duke, A. Falcone, D. J. Fegan, S. J. Fegan, J. P. Finley, L. Fortson, S. Gammell, K. Gibbs, G. G. Gillanders, J. Grube, K. Gutierrez, J. Hall, D. Hanna, J. Holder, D. Horan, B. Humensky, G. Kenny, M. Kertzman, D. Kieda, J. Kildea, J. Knapp, K. Kosack, H. Krawczynski, F. Krennrich, M. Lang, S. LeBohec, E. Linton, J. Lloyd-Evans, G. Maier, D. Mendoza, A. Milovanovic, P. Moriarty, T. N. Nagai, R. A. Ong, B. Power-Mooney, J. Quinn, M. Quinn, K. Ragan, P. T. Reynolds, P. Rebillot, H. J. Rose, M. Schroedter, G. H. Sembroski, S. P. Swordy, A. Syson, L. Valcarel, V. V. Vassiliev, S. P. Wakely, G. Walker, T. C. Weekes, R. White, J. Zweerink, VERITAS Collaboration, B. Mochejska, B. Smith, M. Aller, H. Aller, H. Teräsranta, P. Boltwood, A. Sadun, K. Stanek, E. Adams, J. Foster, J. Hartman, K. Lai, M. Böttcher, A. Reimer, and I. Jung. A Multiwavelength View of the TeV Blazar Markarian 421: Correlated Variability, Flaring, and Spectral Evolution. ApJ, 630(1):130–141, September 2005. doi: 10.1086/431925.

D. Blinov, V. Pavlidou, I. E. Papadakis, T. Hovatta, T. J. Pearson, I. Liodakis, G. V. Panopoulou, E. Angelakis, M. Baloković, H. Das, P. Khodade, S. Kiehlmann, O. G. King, A. Kus, N. Kylafis, A. Mahabal, A. Marecki, D. Modi, I. Myserlis, E. Paleologou, I. Papamastorakis, B. Pazderska, E. Pazderski, C. Rajarshi, A. Ramaprakash, A. C. S. Readhead, P. Reig, K. Tassis, and J. A. Zensus. RoboPol: optical polarization-plane rotations and flaring activity in blazars. MNRAS, 457(2):2252–2262, April 2016. doi: 10.1093/mnras/stw158.

D. Blinov, V. Pavlidou, I. Papadakis, S. Kiehlmann, I. Liodakis, G. V. Panopoulou, E. Angelakis, M. Baloković, T. Hovatta, O. G. King, A. Kus, N. Kylafis, A. Mahabal, S. Maharana, I. Myserlis, E. Paleologou, I. Papamastorakis, E. Pazderski, T. J. Pearson, A. Ramaprakash, A. C. S. Readhead, P. Reig, K. Tassis, and J. A. Zensus. RoboPol: connection between optical polarization plane rotations and gamma-ray flares in blazars. MNRAS, 474(1):1296–1306, February 2018. doi: 10.1093/mnras/stx2786.

Steven D. Bloom and Alan P. Marscher. An Analysis of the Synchrotron Self-Compton Model for the Multi–Wave Band Spectra of Blazars. ApJ, 461:657, April 1996. doi: 10.1086/177092.

Markus Boettcher. Models for the Spectral Energy Distributions and Variability of Blazars. *arXiv e-prints*, art. arXiv:1006.5048, June 2010.

Markus Boettcher. Modeling the Spectral Energy Distributions and Variability of Blazars. *arXiv e-prints*, art. arXiv:1205.0539, May 2012.

Markus Boettcher, Daniel E. Harris, and Henric Krawczynski. *Relativistic Jets from Active Galactic Nuclei*. 2012.

Howard E. Bond. The Optically Variable Radio Source PKS 1514-24 = AP Librae. ApJ, 167:L79, July 1971. doi: 10.1086/180764.

Howard E. Bond. A Search for Extragalactic Objects in the General Catalog of Variable Stars. ApJ, 181:L23, April 1973. doi: 10.1086/181176.

M. Böttcher and C. D. Dermer. An Evolutionary Scenario for Blazar Unification. ApJ, 564(1):86–91, January 2002. doi: 10.1086/324134.

M. Böttcher, A. Reimer, K. Sweeney, and A. Prakash. Leptonic and Hadronic Modeling of Fermi-detected Blazars. ApJ, 768(1):54, May 2013. doi: 10.1088/0004-637X/768/1/54.

Markus Böttcher. Progress in Multi-wavelength and Multi-Messenger Observations of Blazars and Theoretical Challenges. *Galaxies*, 7(1):20, January 2019. doi: 10.3390/galaxies7010020.

Markus Böttcher, Brian van Soelen, Richard Britto, David Buckley, Johannes Marais, and Hester Schutte. SALT Spectropolarimetry and Self-Consistent SED and Polarization Modeling of Blazars. *Galaxies*, 5(3):52, September 2017. doi: 10.3390/galaxies5030052.

D. A. H. Buckley, D. O'Donoghue, S. B. Potter, and K. H. Nordsieck. Time Resolved Spectropolarimetric Studies of Magnetic Cataclysmic Variables with the SALT. In A. Adamson, C. Aspin, C. Davis, and T. Fujiyoshi, editors, *Astronomical Polarimetry: Current Status and Future Directions*, volume 343 of *Astronomical Society of the Pacific Conference Series*, page 415, December 2005.

David Buckley, Gerhard Swart, and Jacobus Meiring. Completion and commissioning of the southern african large telescope - art. no. 62670z. *Proceedings of SPIE - The International Society for Optical Engineering*, 6267, 06 2006. doi: 10.1117/12.673750.

Eric B. Burgh, Kenneth H. Nordsieck, Henry A. Kobulnicky, Ted B. Williams, Darragh O'Donoghue, Michael P. Smith, and Jeffrey W. Percival. Prime Focus Imaging Spectrograph for the Southern African Large Telescope: optical design. In Masanori Iye

and Alan F. M. Moorwood, editors, *Instrument Design and Performance for Optical/Infrared Ground-based Telescopes*, volume 4841 of *Society of Photo-Optical Instrumentation Engineers (SPIE) Conference Series*, pages 1463–1471, March 2003. doi: 10.1117/12.460312.

Bradley W. Carroll and Dale A. Ostlie. *An Introduction to Modern Astrophysics*. 1996.

N. Castelló-Mor, H. Netzer, and S. Kaspi. Super- and sub-Eddington accreting massive black holes: a comparison of slim and thin accretion discs through study of the spectral energy distribution. MNRAS, 458(2):1839–1858, May 2016. doi: 10.1093/mnras/stw445.

Annalisa Celotti and Gabriele Ghisellini. The power of blazar jets. MNRAS, 385(1): 283–300, March 2008. doi: 10.1111/j.1365-2966.2007.12758.x.

Stefano Ciprini and Fermi Large Area Telescope Collaboration. Fermi-LAT detection of a GeV gamma-ray flare from the blazar PKS 2023-07. *The Astronomer's Telegram*, 8932: 1, April 2016.

J. Cooper, B. van Soelen, and R. Britto. Development of tools for SALT/RSS spectropolarimetry reductions: application to the blazar 3C279. In *High Energy Astrophysics in Southern Africa 2021*, page 56, May 2022.

S. Covino, A. Sandrinelli, and A. Treves. Gamma-ray quasi-periodicities of blazars. A cautious approach. MNRAS, 482(1):1270–1274, January 2019. doi: 10.1093/mnras/sty2720.

Steven M. Crawford, Martin Still, Pim Schellart, Luis Balona, David A. H. Buckley, Garith Dugmore, Amanda A. S. Gulbis, Alexei Kniazev, Marissa Kotze, Nicola Loaring, Kenneth H. Nordsieck, Timothy E. Pickering, Stephen Potter, Encarni Romero Colmenero, Petri Vaisanen, Theodore Williams, and Ewald Zietsman. PySALT: the SALT science pipeline. In David R. Silva, Alison B. Peck, and B. Thomas Soifer, editors, *Observatory Operations: Strategies, Processes, and Systems III*, volume 7737 of *Society of Photo-Optical Instrumentation Engineers (SPIE) Conference Series*, page 773725, July 2010. doi: 10.1117/12.857000.

S. Cristiani. PKS 0537-441. IAU Circ., 4027:3, January 1985.

F. D'Ammando and S. Garrappa. Swift follow-up observations of the gamma-ray flaring blazar PKS 1454-354. *The Astronomer's Telegram*, 14712:1, June 2021.

F. D'Ammando, C. M. Raiteri, M. Villata, P. Romano, S. Covino, H. Krimm, and M. Tavani. Not Only Once: The Amazing γ-ray Activity of the Blazar PKS 1510-089. In L. Maraschi, G. Ghisellini, R. Della Ceca, and F. Tavecchio, editors, *Accretion and Ejection in AGN: a Global View*, volume 427 of *Astronomical Society of the Pacific Conference Series*, page 271, October 2010.

F. D'Ammando, G. Principe, and R. Angioni. Swift follow-up of the flaring FSRQ PMN J0231-4746. *The Astronomer's Telegram*, 13212:1, October 2019.

Filippo D'Ammando. PKS 0537-441: a transitional object between BL Lacs and FSRQs? In *Active Galactic Nuclei 9: Black Holes and Revelations*, page 7, May 2010.

Mathieu de Naurois and H. E. S. S. Collaboration. H.E.S.S. follow-up of IceCube-170922A. *The Astronomer's Telegram*, 10787:1, September 2017.

Bernard Degrange and Gérard Fontaine. Introduction to high-energy gamma-ray astronomy. *Comptes Rendus Physique*, 16(6-7):587–599, August 2015. doi: 10.1016/j.crhy.2015.07.003.

Charles D. Dermer and Reinhard Schlickeiser. Model for the High-Energy Emission from Blazars. ApJ, 416:458, October 1993. doi: 10.1086/173251.

Charles D. Dermer, Steven J. Sturner, and Reinhard Schlickeiser. Nonthermal Compton and Synchrotron Processes in the Jets of Active Galactic Nuclei. ApJS, 109(1):103–137, March 1997. doi: 10.1086/312972.

Charles Dennison Dermer and Berrie Giebels. Active galactic nuclei at gamma-ray energies. *Comptes Rendus Physique*, 17(6):594–616, June 2016. doi: 10.1016/j.crhy.2016.04.004.

D. Dornic and A. Coleiro. Search for counterpart to IceCube-170922A with ANTARES. *The Astronomer's Telegram*, 10773:1, September 2017.

J. L. E. Dreyer. A New General Catalogue of Nebulæ and Clusters of Stars, being the Catalogue of the late Sir John F. W. Herschel, Bart, revised, corrected, and enlarged. MmRAS, 49:1, January 1888.

T. A. Dzhatdoev, E. V. Khalikov, V. S. Latypova, E. I. Podlesnyi, and I. A. Vaiman. Modelling the persistent low-state γ-ray emission of the PKS 1510-089 blazar with electromagnetic cascades initiated in hadronuclear interactions. MNRAS, 515(4):5242–5250, October 2022. doi: 10.1093/mnras/stac2094.

P. A. Evans, A. Keivani, J. A. Kennea, D. B. Fox, D. F. Cowen, J. P. Osborne, F. E. Marshall, and Swift-IceCube Collaboration. Further Swift-XRT observations of IceCube 170922A. *The Astronomer's Telegram*, 10792:1, September 2017.

B. L. Fanaroff and J. M. Riley. The morphology of extragalactic radio sources of high and low luminosity. MNRAS, 167:31P–36P, May 1974. doi: 10.1093/mnras/167.1.31P.

Fermi Large Area Telescope Collaboration. 10-year Fermi LAT point source catalog. *The Astronomer's Telegram*, 15110:1, December 2021.

G. Fossati, L. Maraschi, A. Celotti, A. Comastri, and G. Ghisellini. A unifying view of the spectral energy distributions of blazars. MNRAS, 299(2):433–448, September 1998. doi: 10.1046/j.1365-8711.1998.01828.x.

A. Franckowiak, K. Z. Stanek, C. S. Kochanek, T. A. Thompson, T. W. S. Holoien, B. J. Shappee, J. L. Prieto, and Subo Dong. ASAS-SN optical light-curve of blazar TXS 0506+056, located inside the IceCube-170922A error region, shows increased optical activity. *The Astronomer's Telegram*, 10794:1, September 2017.

S. Garrappa. Fermi-LAT detection of renewed gamma-ray activity from the FSRQ PKS 1454-354. *The Astronomer's Telegram*, 14700:1, June 2021.

C. Martin Gaskell. What broad emission lines tell us about how active galactic nuclei work. New A Rev., 53(7-10):140–148, July 2009. doi: 10.1016/j.newar.2009.09.006.

G. Ghisellini, A. Celotti, G. Fossati, L. Maraschi, and A. Comastri. A theoretical unifying scheme for gamma-ray bright blazars. MNRAS, 301(2):451–468, December 1998. doi: 10.1046/j.1365-8711.1998.02032.x.

G. Ghisellini, F. Tavecchio, L. Foschini, and G. Ghirlanda. The transition between BL Lac objects and flat spectrum radio quasars. MNRAS, 414(3):2674–2689, July 2011. doi: 10.1111/j.1365-2966.2011.18578.x.

A. Gokus and R. Angioni. Fermi-LAT detection of renewed gamma-ray activity from the blazars PKS 0346-27 and PKS 2246+208. *The Astronomer's Telegram*, 12693:1, April 2019.

David J Griffiths. *Introduction to electrodynamics; 4th ed.* Pearson, Boston, MA, 2013. doi: 1108420419. URL `https://cds.cern.ch/record/1492149`. Re-published by Cambridge University Press in 2017.

H. E. S. S. Collaboration, A. Abramowski, F. Aharonian, F. Ait Benkhali, A. G. Akhperjanian, E. Angüner, G. Anton, M. Backes, S. Balenderan, A. Balzer, A. Barnacka, Y. Becherini, J. Becker Tjus, K. Bernlöhr, E. Birsin, E. Bissaldi, J. Biteau, M. Böttcher, C. Boisson, J. Bolmont, P. Bordas, J. Brucker, F. Brun, P. Brun, T. Bulik, S. Carrigan, S. Casanova, P. M. Chadwick, R. Chalme-Calvet, R. C. G. Chaves, A. Cheesebrough, M. Chrétien, S. Colafrancesco, G. Cologna, J. Conrad, C. Couturier, Y. Cui, M. Dalton, M. K. Daniel, I. D. Davids, B. Degrange, C. Deil, P. deWilt, H. J. Dickinson, A. Djannati-Ataï, W. Domainko, L. O'C. Drury, G. Dubus, K. Dutson, J. Dyks, M. Dyrda, T. Edwards, K. Egberts, P. Eger, P. Espigat, C. Farnier, S. Fegan, F. Feinstein, M. V. Fernandes, D. Fernandez, A. Fiasson, G. Fontaine, A. Förster, M. Füßling, M. Gajdus, Y. A. Gallant, T. Garrigoux, G. Giavitto, B. Giebels, J. F. Glicenstein, M. H. Grondin, M. Grudzińska, S. Häffner, J. Hahn, J. Harris, G. Heinzelmann, G. Henri, G. Hermann, O. Hervet, A. Hillert, J. A. Hinton, W. Hofmann, P. Hofverberg, M. Holler, D. Horns, A. Jacholkowska, C. Jahn, M. Jamrozy, M. Janiak, F. Jankowsky, I. Jung, M. A. Kastendieck, K. Katarzyński, U. Katz, S. Kaufmann, B. Khélifi, M. Kieffer, S. Klepser, D. Klochkov, W. Kluźniak, T. Kneiske, D. Kolitzus, Nu. Komin, K. Kosack, S. Krakau, F. Krayzel, P. P. Krüger, H. Laffon, G. Lamanna, J. Lefaucheur, A. Lemière, M. Lemoine-Goumard, J. P. Lenain, T. Lohse, A. Lopatin, C. C. Lu, V. Marandon, A. Marcowith, R. Marx, G. Maurin, N. Maxted, M. Mayer, T. J. L. McComb, J. Méhault, P. J. Meintjes, U. Menzler, M. Meyer, R. Moderski, M. Mohamed, E. Moulin, T. Murach, C. L. Naumann, M. de Naurois, J. Niemiec, S. J. Nolan, L. Oakes, H. Odaka, S. Ohm, E. de Oña Wilhelmi, B. Opitz, M. Ostrowski, I. Oya, M. Panter, R. D. Parsons, M. Paz Arribas, N. W. Pekeur, G. Pelletier, J. Perez, P. O. Petrucci, B. Peyaud, S. Pita, H. Poon, G. Pühlhofer, M. Punch, A. Quirrenbach, S. Raab, M. Raue, I. Reichardt, A. Reimer, O. Reimer, M. Renaud, R. de los Reyes, F. Rieger, L. Rob, C. Romoli, S. Rosier-Lees, G. Rowell, B. Rudak, C. B. Rulten, V. Sahakian, D. A. Sanchez, A. Santangelo, R. Schlickeiser, F. Schüssler, A. Schulz, U. Schwanke, S. Schwarzburg, S. Schwemmer, H. Sol, G. Spengler, F. Spies, Ł. Stawarz, R. Steenkamp, C. Stegmann, F. Stinzing, K. Stycz, I. Sushch, J. P. Tavernet, T. Tavernier, A. M. Taylor, R. Terrier, M. Tluczykont, C. Trichard, K. Valerius, C. van Eldik, B. van Soelen, G. Vasileiadis, C. Venter, A. Viana, P. Vincent, H. J. Völk, F. Volpe,

M. Vorster, T. Vuillaume, S. J. Wagner, P. Wagner, R. M. Wagner, M. Ward, M. Weidinger, Q. Weitzel, R. White, A. Wierzcholska, P. Willmann, A. Wörnlein, D. Wouters, R. Yang, V. Zabalza, M. Zacharias, A. A. Zdziarski, A. Zech, H. S. Zechlin, J. Finke, P. Fortin, and D. Horan. The high-energy γ-ray emission of AP Librae. A&A, 573:A31, January 2015. doi: 10.1051/0004-6361/201321436.

Timothy M. Heckman and Philip N. Best. The Coevolution of Galaxies and Supermassive Black Holes: Insights from Surveys of the Contemporary Universe. ARA&A, 52:589–660, August 2014. doi: 10.1146/annurev-astro-081913-035722.

J. Heidt, M. Tröller, K. Nilsson, K. Jäger, L. Takalo, R. Rekola, and A. Sillanpää. Evolution of BL Lacertae host galaxies. A&A, 418:813–825, May 2004. doi: 10.1051/0004-6361:20034467.

A. A. Henden, M. Templeton, D. Terrell, T. C. Smith, S. Levine, and D. Welch. VizieR Online Data Catalog: AAVSO Photometric All Sky Survey (APASS) DR9 (Henden+, 2016). *VizieR Online Data Catalog*, art. II/336, January 2016.

Arne A. Henden, Stephen Levine, Dirk Terrell, Douglas L. Welch, Ulisse Munari, and Brian K. Kloppenborg. APASS Data Release 10. In *American Astronomical Society Meeting Abstracts #232*, volume 232 of *American Astronomical Society Meeting Abstracts*, page 223.06, June 2018.

John Frederick William Herschel. A General Catalogue of Nebulae and Clusters of Stars. *Philosophical Transactions of the Royal Society of London Series I*, 154:1–137, January 1864.

William Herschel. On the Construction of the Heavens. *Philosophical Transactions of the Royal Society of London Series I*, 75:213–266, January 1785.

O. Hervet, C. Boisson, and H. Sol. Linking radio and gamma-ray emission in Ap Librae. A&A, 578:A69, June 2015. doi: 10.1051/0004-6361/201425330.

L. C. Ho. Nuclear activity in nearby galaxies. ARA&A, 46:475–539, September 2008. doi: 10.1146/annurev.astro.45.051806.110546.

Daniel C. Homan, John F. C. Wardle, Chi C. Cheung, David H. Roberts, and Joanne M. Attridge. PKS 1510-089: A Head-on View of a Relativistic Jet. ApJ, 580(2):742–748, December 2002. doi: 10.1086/343894.

T. Hovatta, E. Lindfors, D. Blinov, V. Pavlidou, K. Nilsson, S. Kiehlmann, E. Angelakis, V. Fallah Ramazani, I. Liodakis, I. Myserlis, G. V. Panopoulou, and T. Pursimo. Optical polarization of high-energy BL Lacertae objects. A&A, 596:A78, December 2016. doi: 10.1051/0004-6361/201628974.

F. Hoyle and W. A. Fowler. On the nature of strong radio sources. MNRAS, 125:169, January 1963. doi: 10.1093/mnras/125.2.169.

Edwin. Hubble. No. 310. A spiral nebula as a stellar system. Messier 33. *Contributions from the Mount Wilson Observatory / Carnegie Institution of Washington*, 310:1–39, January 1926.

John David Jackson. *Classical electrodynamics*. 1975.

F. Jankowsky, S. J. Wagner, and F. Ait-Benkhali. Bright optical/GeV-ray flares in Blazars PKS 1424-418 and PKS 1406-076. *The Astronomer's Telegram*, 15525:1, July 2022.

K. J. Johnston, A. L. Fey, N. Zacharias, J. L. Russell, C. Ma, C. de Vegt, J. E. Reynolds, D. L. Jauncey, B. A. Archinal, M. S. Carter, T. E. Corbin, T. M. Eubanks, D. R. Florkowski, D. M. Hall, D. D. McCarthy, P. M. McCulloch, E. A. King, G. Nicolson, and D. B. Shaffer. A Radio Reference Frame. AJ, 110:880, August 1995. doi: 10.1086/117571.

Immanuel Kant. *Allgemeine Naturgeschichte und Theorie des Himmels*. 1755.

S. Kaufmann, S. J. Wagner, and O. Tibolla. Discovery of an Extended X-Ray Jet in AP Librae. ApJ, 776(2):68, October 2013. doi: 10.1088/0004-637X/776/2/68.

K. I. Kellermann. The road to quasars. In F. Massaro, C. C. Cheung, E. Lopez, and A. Siemiginowska, editors, *Extragalactic Jets from Every Angle*, volume 313, pages 190–195, March 2015. doi: 10.1017/S1743921315002185.

Rukaiya Khatoon, Raj Prince, Zahir Shah, Sunder Sahayanathan, and Rupjyoti Gogoi. Temporal and spectral study of PKS 0208-512 during the 2019-2020 flare. MNRAS, 513(1):611–623, June 2022. doi: 10.1093/mnras/stac892.

Henry A. Kobulnicky, Kenneth H. Nordsieck, Eric B. Burgh, Michael P. Smith, Jeffrey W. Percival, Ted B. Williams, and Darragh O'Donoghue. Prime focus imaging spectrograph for the Southern African large telescope: operational modes. In Masanori Iye and Alan F. M. Moorwood, editors, *Instrument Design and Performance for Optical/Infrared Ground-based Telescopes*, volume 4841 of *Society of Photo-Optical Instrumentation Engineers (SPIE) Conference Series*, pages 1634–1644, March 2003. doi: 10.1117/12.460315.

W. Kollatschny and M. Zetzl. The shape of broad-line profiles in active galactic nuclei. A&A, 549:A100, January 2013. doi: 10.1051/0004-6361/201219411.

G. La Mura. Fermi-LAT observations of flaring activity from PKS 0346-27 and PKS 0735+17. *The Astronomer's Telegram*, 15129:1, December 2021.

E. Landi Degl'Innocenti, S. Bagnulo, and L. Fossati. Polarimetric Standardization. In C. Sterken, editor, *The Future of Photometric, Spectrophotometric and Polarimetric Standardization*, volume 364 of *Astronomical Society of the Pacific Conference Series*, page 495, April 2007.

John D. Landstreet. Basics of spectropolarimetry. In Georges Meynet, Cyril Georgy, José Groh, and Philippe Stee, editors, *New Windows on Massive Stars*, volume 307, pages 311–320, January 2015. doi: 10.1017/S1743921314007017.

Juan Li, Jun-Hui Fan, and Yu-Hai Yuan. The parameters of binary black hole system in PKS 1510-089. *Chinese Physics*, 16(3):876–880, March 2007. doi: 10.1088/1009-1963/16/3/053.

Chao Lin, Jun-Hui Fan, and Hu-Bing Xiao. The intrinsic γ-ray emissions of Fermi blazars. *Research in Astronomy and Astrophysics*, 17(7):066, July 2017. doi: 10.1088/1674-4527/17/7/66.

Ioannis Liodakis, Abel L. Peirson, and Roger W. Romani. Prospects for Detecting X-Ray Polarization in Blazar Jets. ApJ, 880(1):29, July 2019. doi: 10.3847/1538-4357/ab2719.

Ioannis Liodakis, Alan P. Marscher, Iván Agudo, Andrei V. Berdyugin, Maria I. Bernardos, Giacomo Bonnoli, George A. Borman, Carolina Casadio, Víctor Casanova, Elisabetta Cavazzuti, Nicole R. Cavero, Laura Di Gesu, Niccoló Di Lalla, Immacolata Donnarumma, Steven R. Ehlert, Manel Errando, Juan Escudero, Maya García-Comas, Beatriz Agís-González, César Husillos, Jenni Jormanainen, Svetlana G. Jorstad, Masato Kagitani, Evgenia N. Kopatskaya, Vadim Kravtsov, Henric Krawczynski, Elina Lindfors, Elena G. Larionova, Grzegorz M. Madejski, Frédéric Marin, Alessandro Marchini, Herman L. Marshall, Daria A. Morozova, Francesco Massaro, Joseph R. Masiero, Dimitri Mawet, Riccardo Middei, Maxwell A. Millar-Blanchaer, Ioannis Myserlis, Michela Negro, Kari Nilsson, Stephen L. O'Dell, Nicola Omodei, Luigi Pacciani, Alessandro Paggi, Georgia V. Panopoulou, Abel L. Peirson, Matteo Perri, Pierre-Olivier Petrucci, Juri Poutanen, Simonetta Puccetti, Roger W. Romani, Takeshi Sakanoi, Sergey S. Savchenko, Alfredo Sota, Fabrizio Tavecchio, Samaporn Tinyanont, Andrey A. Vasiliev, Zachary R. Weaver, Alexey V. Zhovtan, Lucio A. Antonelli, Matteo Bachetti, Luca Baldini, Wayne H. Baumgartner, Ronaldo Bellazzini, Stefano Bianchi, Stephen D. Bongiorno, Raffaella Bonino, Alessandro Brez, Niccoló Bucciantini, Fiamma Capitanio, Simone Castellano, Stefano Ciprini, Enrico Costa, Alessandra De Rosa, Ettore Del Monte, Alessandro Di Marco, Victor Doroshenko, Michal Dovčiak, Teruaki Enoto, Yuri Evangelista, Sergio Fabiani, Riccardo Ferrazzoli, Javier A. Garcia, Shuichi Gunji, Kiyoshi Hayashida, Jeremy Heyl, Wataru Iwakiri, Vladimir Karas, Takao Kitaguchi, Jeffery J. Kolodziejczak, Fabio La Monaca, Luca Latronico, Simone Maldera, Alberto Manfreda, Andrea Marinucci, Giorgio Matt, Ikuyuki Mitsuishi, Tsunefumi Mizuno, Fabio Muleri, Stephen C. Y. Ng, Chiara Oppedisano, Alessandro Papitto, George G. Pavlov, Melissa Pesce-Rollins, Maura Pilia, Andrea Possenti, Brian D. Ramsey, John Rankin, Ajay Ratheesh, Carmelo Sgró, Patrick Slane, Paolo Soffitta, Gloria Spandre, Toru Tamagawa, Roberto Taverna, Yuzuru Tawara, Allyn F. Tennant, Nicolas E. Thomas, Francesco Tombesi, Alessio Trois, Sergey Tsygankov, Roberto Turolla, Jacco Vink, Martin C. Weisskopf, Kinwah Wu, Fei Xie, and Silvia Zane. Polarized Blazar X-rays imply particle acceleration in shocks. *arXiv e-prints*, art. arXiv:2209.06227, September 2022.

M. L. Lister, M. F. Aller, H. D. Aller, T. Hovatta, W. Max-Moerbeck, A. C. S. Readhead, J. L. Richards, and E. Ros. Why Have Many of the Brightest Radio-loud Blazars Not Been Detected in Gamma-Rays by Fermi? ApJ, 810(1):L9, September 2015. doi: 10.1088/2041-8205/810/1/L9.

B. Lott, D. Gasparrini, and S. Ciprini. The Fourth Catalog of Active Galactic Nuclei Detected by the Fermi Large Area Telescope – Data Release 2. *arXiv e-prints*, art. arXiv:2010.08406, October 2020.

F. Lucarelli, G. Piano, C. Pittori, F. Verrecchia, M. Tavani, A. Bulgarelli, P. Munar-Adrover, G. Minervini, A. Ursi, S. Vercellone, I. Donnarumma, V. Fioretti, A. Zoli, E. Striani, M. Cardillo, F. Gianotti, M. Trifoglio, A. Giuliani, S. Mereghetti, P. Caraveo, F. Perotti, A. Chen, A. Argan, E. Costa, E. Del Monte, Y. Evangelista, M. Feroci, F. Lazzarotto, I. Lapshov, L. Pacciani, P. Soffitta, S. Sabatini, V. Vittorini, G. Pucella, M. Rapisarda, G. Di Cocco, F. Fuschino, M. Galli, C. Labanti, M. Marisaldi, A. Pellizzoni, M. Pilia, A. Trois, G. Barbiellini, E. Vallazza, F. Longo, A. Morselli, P. Pi-

cozza, M. Prest, P. Lipari, D. Zanello, P. W. Cattaneo, A. Rappoldi, S. Colafrancesco, N. Parmiggiani, A. Ferrari, F. Paoletti, A. Antonelli, P. Giommi, L. Salotti, G. Valentini, and F. D'Amico. AGILE confirmation of gamma-ray activity from the IceCube-170922A error region. *The Astronomer's Telegram*, 10801:1, September 2017.

D. Lynden-Bell. Galactic Nuclei as Collapsed Old Quasars. Nature, 223(5207):690–694, August 1969. doi: 10.1038/223690a0.

D. Lynden-Bell and M. J. Rees. On quasars, dust and the galactic centre. MNRAS, 152: 461, January 1971. doi: 10.1093/mnras/152.4.461.

K. Mannheim. The proton blazar. A&A, 269:67–76, March 1993.

K. Mannheim and P. L. Biermann. Gamma-ray flaring of 3C 279 : a proton-initiated cascade in the jet ? A&A, 253:L21–L24, January 1992.

L. Maraschi, G. Ghisellini, and A. Celotti. A Jet Model for the Gamma-Ray–emitting Blazar 3C 279. ApJ, 397:L5, September 1992. doi: 10.1086/186531.

L. Maraschi, A. Ciapi, G. Fossati, G. Tagliafferi, and A. Treves. ROSAT Observations of the Two Radio-selected Blazars PKS 1034-293 and PKS 1335-127. ApJ, 443:29, April 1995. doi: 10.1086/175500.

A. P. Marscher. Turbulent Extreme Multi-Zone Model for Multi-Waveband Variations of Blazars. *arXiv e-prints*, art. arXiv:1304.2064, April 2013.

Alan P. Marscher. Turbulent, Extreme Multi-zone Model for Simulating Flux and Polarization Variability in Blazars. ApJ, 780(1):87, January 2014. doi: 10.1088/0004-637X/780/1/87.

Alan P. Marscher, Svetlana G. Jorstad, Francesca D. D'Arcangelo, Paul S. Smith, G. Grant Williams, Valeri M. Larionov, Haruki Oh, Alice R. Olmstead, Margo F. Aller, Hugh D. Aller, Ian M. McHardy, Anne Lähteenmäki, Merja Tornikoski, Esko Valtaoja, Vladimir A. Hagen-Thorn, Eugenia N. Kopatskaya, Walter K. Gear, Gino Tosti, Omar Kurtanidze, Maria Nikolashvili, Lorand Sigua, H. Richard Miller, and Wesley T. Ryle. The inner jet of an active galactic nucleus as revealed by a radio-to-γ-ray outburst. Nature, 452(7190):966–969, April 2008. doi: 10.1038/nature06895.

Alan P. Marscher, Svetlana G. Jorstad, Valeri M. Larionov, Margo F. Aller, Hugh D. Aller, Anne Lähteenmäki, Iván Agudo, Paul S. Smith, Mark Gurwell, Vladimir A. Hagen-Thorn, Tatiana S. Konstantinova, Elena G. Larionova, Liudmila V. Larionova, Daria A. Melnichuk, Dmitry A. Blinov, Evgenia N. Kopatskaya, Ivan S. Troitsky, Merja Tornikoski, Talvikki Hovatta, Gary D. Schmidt, Francesca D. D'Arcangelo, Dipesh Bhattarai, Brian Taylor, Alice R. Olmstead, Emily Manne-Nicholas, Mar Roca-Sogorb, José L. Gómez, Ian M. McHardy, Omar Kurtanidze, Maria G. Nikolashvili, Givi N. Kimeridze, and Lorand A. Sigua. Probing the Inner Jet of the Quasar PKS 1510-089 with Multi-Waveband Monitoring During Strong Gamma-Ray Activity. ApJ, 710(2): L126–L131, February 2010. doi: 10.1088/2041-8205/710/2/L126.

I. Mereu. Fermi-LAT detection of continuing gamma-ray activity from the FSRQ PKS 0346-27. *The Astronomer's Telegram*, 13521:1, February 2020.

I. Mereu and Fermi Large Area Telescope Collaboration. Fermi-LAT detection of enhanced gamma-ray activity from the FSRQ PKS 0837+012. *The Astronomer's Telegram*, 14433: 1, March 2021.

Eileen T. Meyer, Giovanni Fossati, Markos Georganopoulos, and Matthew L. Lister. From the Blazar Sequence to the Blazar Envelope: Revisiting the Relativistic Jet Dichotomy in Radio-loud Active Galactic Nuclei. ApJ, 740(2):98, October 2011. doi: 10.1088/0004-637X/740/2/98.

Razmik Mirzoyan. First-time detection of VHE gamma rays by MAGIC from a direction consistent with the recent EHE neutrino event IceCube-170922A. *The Astronomer's Telegram*, 10817:1, October 2017.

Rivay Mor, Hagai Netzer, and Moshe Elitzur. Dusty Structure Around Type-I Active Galactic Nuclei: Clumpy Torus Narrow-line Region and Near-nucleus Hot Dust. ApJ, 705(1):298–313, November 2009. doi: 10.1088/0004-637X/705/1/298.

Roberto Nesci. High optical state of the Gamma-ray flaring PKS 0346-27. *The Astronomer's Telegram*, 11269:1, February 2018a.

Roberto Nesci. X-rays follow-up of the Gamma-ray flaring FSRQ PKS 0346-27. *The Astronomer's Telegram*, 11455:1, March 2018b.

Roberto Nesci and Roopesh Ojha. Optical and gamma-ray brightening of the blazar PKS 0537-441. *The Astronomer's Telegram*, 12357:1, January 2019.

Hagai Netzer. Revisiting the Unified Model of Active Galactic Nuclei. ARA&A, 53: 365–408, August 2015. doi: 10.1146/annurev-astro-082214-122302.

C. Nigro, J. Sitarek, P. Gliwny, D. Sanchez, A. Tramacere, and M. Craig. agnpy: An open-source python package modelling the radiative processes of jetted active galactic nuclei. A&A, 660:A18, April 2022. doi: 10.1051/0004-6361/202142000.

Kenneth Nordsieck and Daniél Groenewald. Southern African Large Telescope Polarimetry Observer's Guide. Document number: SALT-3170AM0013, December 2019.

Kenneth H. Nordsieck, Kurt P. Jaehnig, Eric B. Burgh, Henry A. Kobulnicky, Jeffrey W. Percival, and Michael P. Smith. Instrumentation for high-resolution spectropolarimetry in the visible and far-ultraviolet. In Silvano Fineschi, editor, *Polarimetry in Astronomy*, volume 4843 of *Society of Photo-Optical Instrumentation Engineers (SPIE) Conference Series*, pages 170–179, February 2003. doi: 10.1117/12.459288.

Roopesh Ojha, Janeth Valverde, and Pfesesani Van Zyl. Fermi-LAT Detection of an Unusual Hard Spectrum and Enhanced Gamma-ray Emission from the FSRQ PKS 0131-522. *The Astronomer's Telegram*, 10987:1, November 2017.

D. E. Osterbrock. The nature and structure of active galactic nuclei. II. Rev. Mexicana Astron. Astrofis., 26:65–72, October 1993a.

Donald E. Osterbrock. The Nature and Structure of Active Galactic Nuclei. ApJ, 404: 551, February 1993b. doi: 10.1086/172307.

L. Pacciani and F. Ambrosino. Optical, X, HE gamma-ray activity of the FSRQ PKS 0035-252. *The Astronomer's Telegram*, 11874:1, July 2018.

P. Padovani and P. Giommi. A sample-oriented catalogue of BL Lacertae objects. MNRAS, 277:1477–1490, December 1995a. doi: 10.1093/mnras/277.4.1477.

P. Padovani, D. M. Alexander, R. J. Assef, B. De Marco, P. Giommi, R. C. Hickox, G. T. Richards, V. Smolčić, E. Hatziminaoglou, V. Mainieri, and M. Salvato. Active galactic nuclei: what's in a name? A&A Rev., 25(1):2, August 2017. doi: 10.1007/s00159-017-0102-9.

Paolo Padovani. The blazar sequence: validity and predictions. Ap&SS, 309(1-4):63–71, June 2007. doi: 10.1007/s10509-007-9455-2.

Paolo Padovani. Active Galactic Nuclei at all wavelengths and from all angles. *Frontiers in Astronomy and Space Sciences*, 4:35, November 2017a. doi: 10.3389/fspas.2017.00035.

Paolo Padovani. On the two main classes of active galactic nuclei. *Nature Astronomy*, 1: 0194, August 2017b. doi: 10.1038/s41550-017-0194.

Paolo Padovani and Paolo Giommi. The Connection between X-Ray– and Radio-selected BL Lacertae Objects. ApJ, 444:567, May 1995b. doi: 10.1086/175631.

Simona Paiano, Renato Falomo, Aldo Treves, and Riccardo Scarpa. The Redshift of the BL Lac Object TXS 0506+056. ApJ, 854(2):L32, February 2018. doi: 10.3847/2041-8213/aaad5e.

Vaidehi S. Paliya, Haocheng Zhang, Markus Böttcher, M. Ajello, A. Domínguez, M. Joshi, D. Hartmann, and C. S. Stalin. Leptonic and Hadronic Modeling of Fermi-LAT Hard Spectrum Quasars and Predictions for High-energy Polarization. ApJ, 863(1):98, August 2018. doi: 10.3847/1538-4357/aad1f0.

B. A. Peterson and J. G. Bolton. Identification of Southern Quasi-Stellar Objects-II. Astrophys. Lett., 10:105, January 1972.

G. Piano, A. Bulgarelli, M. Tavani, I. Donnarumma, C. Pittori, F. Verrecchia, F. Lucarelli, V. Fioretti, A. Zoli, S. Vercellone, E. Striani, M. Cardillo, F. Gianotti, M. Trifoglio, A. Giuliani, S. Mereghetti, P. Caraveo, F. Perotti, A. Chen, A. Argan, E. Costa, E. Del Monte, Y. Evangelista, M. Feroci, F. Lazzarotto, I. Lapshov, L. Pacciani, P. Soffitta, S. Sabatini, V. Vittorini, G. Pucella, M. Rapisarda, G. Di Cocco, F. Fuschino, M. Galli, C. Labanti, M. Marisaldi, A. Pellizzoni, M. Pilia, A. Trois, G. Barbiellini, E. Vallazza, F. Longo, A. Morselli, P. Picozza, M. Prest, P. Lipari, D. Zanello, P. W. Cattaneo, A. Rappoldi, S. Colafrancesco, N. Parmiggiani, A. Ferrari, A. Antonelli, P. Giommi, L. Salotti, G. Valentini, and F. D'Amico. AGILE detection of a gamma-ray flare from the FSRQ PKS 2023-07. *The Astronomer's Telegram*, 8879:1, March 2016.

G. Piano, C. Pittori, F. Verrecchia, G. Minervini, F. Lucarelli, P. Munar-Adrover, A. Ursi, A. Bulgarelli, V. Fioretti, N. Parmiggiani, M. Tavani, I. Donnarumma, S. Vercellone, E. Striani, M. Cardillo, F. Gianotti, M. Trifoglio, A. Giuliani, S. Mereghetti, P. Caraveo, F. Perotti, A. Chen, A. Argan, E. Costa, E. Del Monte, Y. Evangelista, M. Feroci, F. Lazzarotto, I. Lapshov, L. Pacciani, P. Soffitta, S. Sabatini, V. Vittorini, G. Pucella,

M. Rapisarda, G. Di Cocco, F. Fuschino, M. Galli, C. Labanti, M. Marisaldi, A. Pellizzoni, M. Pilia, A. Trois, G. Barbiellini, E. Vallazza, F. Longo, A. Morselli, P. Picozza, M. Prest, P. Lipari, D. Zanello, P. W. Cattaneo, A. Rappoldi, S. Colafrancesco, A. Ferrari, F. Paoletti, A. Antonelli, P. Giommi, L. Salotti, G. Valentini, and F. D'Amico. Enhanced gamma-ray emission from the FSRQ PKS 0131-522. *The Astronomer's Telegram*, 11003:1, November 2017.

G. Piano, P. Munar-Adrover, L. Pacciani, P. Romano, S. Vercellone, I. Donnarumma, F. Verrecchia, L. Carrasco, A. Porras, E. Recillas, and M. Tavani. The mid-2016 flaring activity of the flat spectrum radio quasar PKS 2023-07. A&A, 616:A65, August 2018. doi: 10.1051/0004-6361/201832812.

G. Piano, M. Cardillo, M. Tavani, C. Pittori, F. Verrecchia, F. Lucarelli, A. Ursi, C. Casentini, A. Bulgarelli, N. Parmiggiani, V. Fioretti, I. Donnarumma, S. Vercellone, F. Gianotti, M. Trifoglio, A. Giuliani, S. Mereghetti, P. Caraveo, F. Perotti, A. Chen, A. Argan, E. Costa, E. Del Monte, Y. Evangelista, M. Feroci, L. Pacciani, P. Soffitta, V. Vittorini, G. Di Cocco, F. Fuschino, M. Galli, C. Labanti, M. Marisaldi, A. Pellizzoni, M. Pilia, A. Trois, G. Barbiellini, E. Vallazza, F. Longo, A. Morselli, P. Picozza, M. Prest, P. Lipari, D. Zanello, P. W. Cattaneo, A. Rappoldi, A. Ferrari, F. Paoletti, L. A. Antonelli, P. Giommi, L. Salotti, G. Valentini, and F. D'Amico. AGILE detection of intense gamma-ray emission from the region of the FSRQ PKS 0035-252. *The Astronomer's Telegram*, 12763:1, May 2019.

L. Pigatto. Island Universes, Novae and Supernovae. A Great Debate of the XX Century. In M. Turatto, S. Benetti, L. Zampieri, and W. Shea, editors, *1604-2004: Supernovae as Cosmological Lighthouses*, volume 342 of *Astronomical Society of the Pacific Conference Series*, page 43, December 2005.

S. B. Potter, Ken Nordsieck, Encarni Romero-Colmenero, Steve Crawford, Petri Vaisanen, Éric Depagne, David Buckley, Anthony Koeslag, Janus Brink, Christian Hetlage, Keith Browne, Lisa Crause, Alan Schier, and James Allington. Commissioning the polarimetric modes of the Robert Stobie spectrograph on the Southern African Large Telescope. In Christopher J. Evans, Luc Simard, and Hideki Takami, editors, *Ground-based and Airborne Instrumentation for Astronomy VI*, volume 9908 of *Society of Photo-Optical Instrumentation Engineers (SPIE) Conference Series*, page 99082K, August 2016. doi: 10.1117/12.2232391.

G. Principe and R. Angioni. Fermi-LAT detection of enhanced gamma-ray activity from the FSRQ PMN J0231-4746. *The Astronomer's Telegram*, 13209:1, October 2019.

Tapio Pursimo, Julia Martikainen, and Roopesh Ojha. Optical flare observed in the flaring gamma-ray FSRQ PMN J0231-4746. *The Astronomer's Telegram*, 13248:1, October 2019.

Bindu Rani, Alok C. Gupta, R. Bachev, A. Strigachev, E. Semkov, F. D'Ammando, P. J. Wiita, M. A. Gurwell, E. Ovcharov, B. Mihov, S. Boeva, and S. Peneva. Spectral energy distribution variation in BL Lacs and flat spectrum radio quasars. MNRAS, 417(3): 1881–1890, November 2011. doi: 10.1111/j.1365-2966.2011.19373.x.

Grote Reber. Cosmic Static. ApJ, 100:279, November 1944. doi: 10.1086/144668.

Helena X. Ren, Matteo Cerruti, and Narek Sahakyan. Quasi-periodic oscillations in the γ-ray light curves of bright active galactic nuclei. *arXiv e-prints*, art. arXiv:2204.13051, April 2022.

A. W. Rodgers. Spectrum of AP Lib ($\equiv$ PKS 1514-24). *Nature Physical Science*, 233(39): 75, September 1971. doi: 10.1038/physci233075a0.

Gustavo E. Romero, M. Boettcher, S. Markoff, and F. Tavecchio. Relativistic Jets in Active Galactic Nuclei and Microquasars. Space Sci. Rev., 207(1-4):5–61, July 2017. doi: 10.1007/s11214-016-0328-2.

A. Roychowdhury, E. T. Meyer, M. Georganopoulos, and P. Breiding. What is the origin of the very high energy (VHE) emission from AP Librae? In *37th International Cosmic Ray Conference. 12-23 July 2021. Berlin*, page 804, March 2022.

John J. Ruan, Scott F. Anderson, Chelsea L. MacLeod, Andrew C. Becker, T. H. Burnett, James R. A. Davenport, Željko Ivezić, Christopher S. Kochanek, Richard M. Plotkin, Branimir Sesar, and J. Scott Stuart. Characterizing the Optical Variability of Bright Blazars: Variability-based Selection of Fermi Active Galactic Nuclei. ApJ, 760(1):51, November 2012. doi: 10.1088/0004-637X/760/1/51.

G. B. Rybicki and A. P. Lightman. *Radiative processes in astrophysics.* 1985.

E. E. Salpeter. Accretion of Interstellar Matter by Massive Objects. ApJ, 140:796–800, August 1964. doi: 10.1086/147973.

A. Savage. Identification of southern radio sources. MNRAS, 174:259–265, February 1976. doi: 10.1093/mnras/174.2.259.

B. Sbarufatti, A. Treves, R. Falomo, J. Heidt, J. Kotilainen, and R. Scarpa. ESO Very Large Telescope Optical Spectroscopy of BL Lacertae Objects. I. New Redshifts. AJ, 129(2):559–566, February 2005. doi: 10.1086/427138.

Edward F. Schlafly and Douglas P. Finkbeiner. Measuring Reddening with Sloan Digital Sky Survey Stellar Spectra and Recalibrating SFD. ApJ, 737(2):103, August 2011. doi: 10.1088/0004-637X/737/2/103.

David J. Schlegel, Douglas P. Finkbeiner, and Marc Davis. Maps of Dust Infrared Emission for Use in Estimation of Reddening and Cosmic Microwave Background Radiation Foregrounds. ApJ, 500(2):525–553, June 1998. doi: 10.1086/305772.

M. Schmidt. 3C 273 : A Star-Like Object with Large Red-Shift. Nature, 197(4872):1040, March 1963. doi: 10.1038/1971040a0.

Hester M. Schutte, Richard J. Britto, Markus Böttcher, Brian van Soelen, Johannes P. Marais, Amanpreet Kaur, Abraham D. Falcone, David A. H. Buckley, Andry F. Rajoelimanana, and Justin Cooper. Modeling the Spectral Energy Distributions and Spectropolarimetry of Blazars-Application to 4C+01.02 in 2016-2017. ApJ, 925(2):139, February 2022. doi: 10.3847/1538-4357/ac3cb5.

Carl K. Seyfert. Nuclear Emission in Spiral Nebulae. ApJ, 97:28, January 1943. doi: 10.1086/144488.

N. I. Shakura and R. A. Sunyaev. Black holes in binary systems. Observational appearance. A&A, 24:337–355, January 1973.

Zhaohui Shang, Michael S. Brotherton, Richard F. Green, Gerard A. Kriss, Jennifer Scott, Jessica Kim Quijano, Omer Blaes, Ivan Hubeny, John Hutchings, Mary Elizabeth Kaiser, Anuradha Koratkar, William Oegerle, and Wei Zheng. Quasars and the Big Blue Bump. ApJ, 619(1):41–59, January 2005. doi: 10.1086/426134.

Gregory A. Shields. A Brief History of Active Galactic Nuclei. PASP, 111(760):661–678, June 1999. doi: 10.1086/316378.

V. M. Slipher. On the Spectrum of the Nebula in the Pleiades. *Popular Astronomy*, 21: 186, January 1913.

Paul S. Smith. Extremely High Optical Polarization Observed in the Blazar PKS1502+106. *The Astronomer's Telegram*, 11047:1, December 2017.

J. Gregory Stacy, W. Thomas Vestrand, and P. Sreekumar. The Gamma-Ray Blazar PKS 0208-512 from MeV to GeV Energies. ApJ, 598(1):216–231, November 2003. doi: 10.1086/377632.

I. A. Steele. Optical Spectrum of TXS 0506+056 (possible counterpart to IceCube-170922A). *The Astronomer's Telegram*, 10799:1, September 2017.

A. Szostek. Fermi LAT detection of gamma ray activity from blazar PKS 0208-512. *The Astronomer's Telegram*, 3338:1, May 2011.

Yasuyuki T. Tanaka, Sara Buson, and Daniel Kocevski. Fermi-LAT detection of increased gamma-ray activity of TXS 0506+056, located inside the IceCube-170922A error region. *The Astronomer's Telegram*, 10791:1, September 2017.

A. M. Tanner, Jill Bechtold, C. E. Walker, John H. Black, and R. M. Cutri. A Study of Quasar Absorption-Line Systems With IRAS. AJ, 112:62, July 1996. doi: 10.1086/117988.

F. Tavecchio, M. Landoni, L. Sironi, and P. Coppi. Probing dissipation mechanisms in BL Lac jets through X-ray polarimetry. MNRAS, 480(3):2872–2880, November 2018. doi: 10.1093/mnras/sty1491.

Hien D. Tran. The Unified Model and Evolution of Active Galaxies: Implications from a Spectropolarimetric Study. ApJ, 583(2):632–648, February 2003. doi: 10.1086/345473.

C. Megan Urry. Multiwavelength properties of blazars. *Advances in Space Research*, 21 (1-2):89–100, January 1998. doi: 10.1016/S0273-1177(97)00619-4.

C. Megan Urry and Paolo Padovani. Unified Schemes for Radio-Loud Active Galactic Nuclei. PASP, 107:803, September 1995. doi: 10.1086/133630.

B. van Soelen, David A. H. Buckley, and Markus Boettcher. SALT-HRS observation of the blazar TXS 0506+056 associated with IceCube-170922A. *The Astronomer's Telegram*, 10830:1, October 2017.

K. Vollmann and T. Eversberg. Remarks on statistical errors in equivalent widths. *Astronomische Nachrichten*, 327(9):862, November 2006. doi: 10.1002/asna.200610645.

J. F. C. Wardle, D. C. Homan, C. C. Cheung, and D. H. Roberts. The Ultra-Fast Quasar PKS 1510-089: Direct Evidence for a Changing Orientation of the Central Engine. In J. Romney and M. Reid, editors, *Future Directions in High Resolution Astronomy*, volume 340 of *Astronomical Society of the Pacific Conference Series*, page 67, December 2005.

M. Wenger, F. Ochsenbein, D. Egret, P. Dubois, F. Bonnarel, S. Borde, F. Genova, G. Jasniewicz, S. Laloë, S. Lesteven, and R. Monier. The SIMBAD astronomical database. The CDS reference database for astronomical objects. A&AS, 143:9–22, April 2000. doi: 10.1051/aas:2000332.

B. J. Wilkes, A. E. Wright, D. L. Jauncey, and B. A. Peterson. An atlas of QSO spectra. PASA, 5(1):2–83, January 1983. doi: 10.1017/S1323358000021664.

L. Woltjer. Emission Nuclei in Galaxies. ApJ, 130:38, July 1959. doi: 10.1086/146694.

Jong-Hak Woo, C. Megan Urry, Roeland P. van der Marel, Paulina Lira, and Jose Maza. Black Hole Masses and Host Galaxy Evolution of Radio-Loud Active Galactic Nuclei. ApJ, 631(2):762–772, October 2005. doi: 10.1086/432681.

Thomas Wright. *An original theory or new hypothesis of the universe : founded upon general phaenomena of the visible creation; and particularly the Via the laws of nature, and solving by mathematical principles : the Lactea ...compris'd in nine familiar letters from the author to his friendand : illustrated with upward of thirty graven and mezzotinto plates ...* 1750. doi: 10.3931/e-rara-28672.

J. Wu, X. Zhou, B. Peng, J. Ma, Z. Jiang, and J. Chen. Optical monitoring of PKS 1510-089: a binary black hole system? MNRAS, 361(1):155–159, July 2005. doi: 10.1111/j.1365-2966.2005.09150.x.

Feng Yuan and Ramesh Narayan. Hot Accretion Flows Around Black Holes. ARA&A, 52:529–588, August 2014. doi: 10.1146/annurev-astro-082812-141003.

M. Zacharias. Blazar variability - expect the unexpected. In *High Energy Astrophysics in Southern Africa (HEASA2018*, page 33, August 2018.

Ya. B. Zel'dovich and I. D. Novikov. The Radiation of Gravity Waves by Bodies Moving in the Field of a Collapsing Star. *Soviet Physics Doklady*, 9:246, October 1964.

H. Zhang and M. Böttcher. X-Ray and Gamma-Ray Polarization in Leptonic and Hadronic Jet Models of Blazars. ApJ, 774(1):18, September 2013. doi: 10.1088/0004-637X/774/1/18.

Haocheng Zhang. Blazar Optical Polarimetry: Current Progress in Observations and Theories. *Galaxies*, 7(4):85, October 2019. doi: 10.3390/galaxies7040085.

Haocheng Zhang, Xuhui Chen, and Markus Böttcher. Synchrotron Polarization in Blazars. ApJ, 789(1):66, July 2014. doi: 10.1088/0004-637X/789/1/66.

Pengfei Zhang and Zhongxiang Wang. Polarized Optical Emission of the Blazar PKS 1222+216: Discovery of A 420-day Quasi-Periodic Signal. *arXiv e-prints*, art. arXiv:2207.10824, July 2022.

Appendix A

Additional Observational Results

Here, the observational results of the blazars not discussed in the main body of the text are given.

A.1 BL Lac-Type Objects

In this section, the spectropolarimetric and photometric observational data will be given for three BLLs (PKS 0426–380, PKS 0447–439, and PKS 1454–354) observed under the SALT transients monitoring campaign.

A.1.1 PKS 0426–380

PKS 0426–380 is a high-redshift ($z = 1.111$) BLL with an apparent visual magnitude of $V = 19.00$ and synchrotron peak frequency $\nu_{\rm sy} = 4.79 \times 10^{12}$ Hz. It has been associated with quasi-periodic oscillations in the γ-ray regime (Ait Benkhali et al., 2020; Covino et al., 2019; Ren et al., 2022).

In 2017, PKS 0426–380 was in an enhanced state of γ-ray activity (that started on ∼MJD 57509, and lasted to approximately MJD 58087), as shown in Figure A.1. It was observed with SALT on 2017 January 21 and February 20 in this enhanced state (Figure A.2). During the first spectropolarimetric observation, the averaged degree of polarisation was observed to be $\langle \Pi \rangle = 10.74 \pm 0.49\,\%$, with an averaged polarisation angle of $10.03 \pm 2.19^{\circ}$ (taken from $\lambda = 3900 - 9150$ Å). During the second observation, the γ-ray flux was slightly lower than that of the first observation, and showed $\langle \Pi \rangle = 10.77 \pm 0.99\,\%$ and polarisation angle $50.52 \pm 1.26^{\circ}$.

In the optical spectra shown in Figure A.2, two intervening [Mg II] absorption lines were detected at $\lambda \approx 4352.08$ Å and $\lambda \approx 5679.94$ Å, which is in agreement with Heidt et al. (2004) and Sbarufatti et al. (2005). These lines are not intrinsic to the BLL itself, but rather due to intervening systems located at $z = 1.030$ and $z = 0.559$. The only feature identified to be intrinsic to PKS 0426–380, was a weak forbidden [Mg II] emission line at $\lambda \approx 5870.20$ Å. Note that the feature at $\lambda \approx 5592.13$ Å is an artefact (remnant of a skyline) due to insufficient background subtraction that could not be removed successfully.

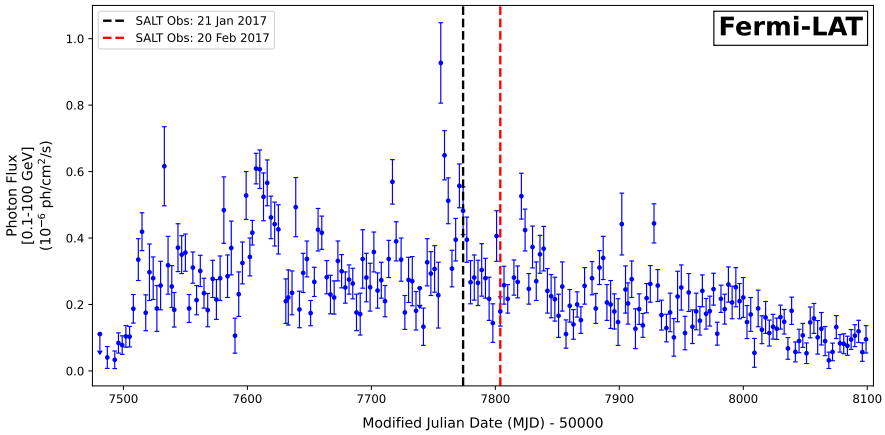

Figure A.1: Gamma-ray lightcurve for the BLL, PKS 0426–380, where the black and red dashed lines indicate the dates of the SALT spectropolarimetric observations.

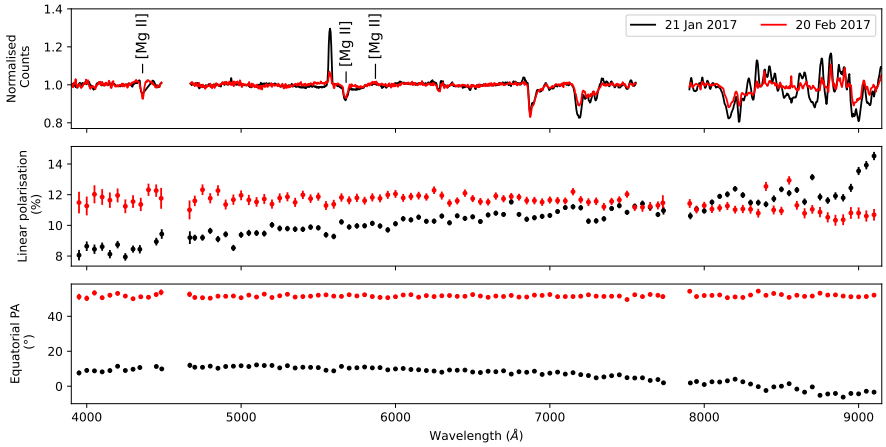

Figure A.2: Spectropolarimetric observations for the BLL, PKS 0426–380, observed on 2017 January 21 and 2017 February 20. The top panel gives the normalised counts spectra of the two observations, where the middle and bottom panels give the degree of linear polarisation, and the equatorial polarisation angle, respectively. The gaps in the spectra in the top panel from $\lambda = 7560 - 7730$ Å, $\lambda = 4485 - 4670$ Å, and $\lambda = 7730 - 7900$ Å are due to the removal of a skyline, and the two chip gaps of the CCD detector mosaic, respectively.

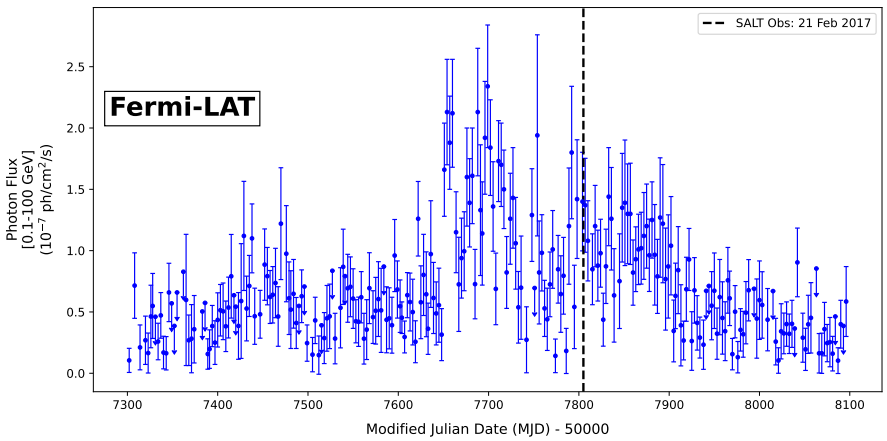

Figure A.3: Gamma-ray lightcurve for the BLL, PKS 0447–439, where the black dashed line indicates the date of the SALT spectropolarimetric observation.

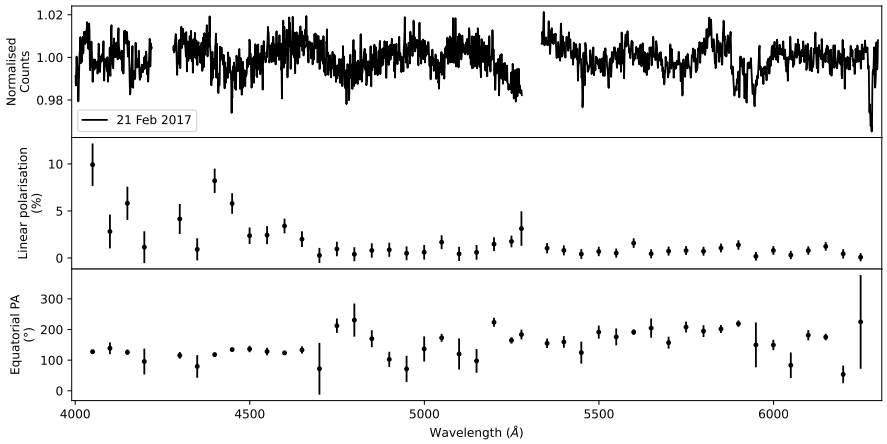

Figure A.4: Spectropolarimetric observations for the BLL, PKS 0447–439, observed on 2017 February 21. The top panel gives the normalised counts spectra of the observation, where the middle and bottom panels give the degree of linear polarisation, and the equatorial polarisation angle, respectively. The gaps in the spectrum in the top panel from $\lambda = 4220 - 4280\,\text{Å}$, $\lambda = 5280 - 5335\,\text{Å}$ are due to the removal of the two chip gaps of the CCD detector mosaic.

A.1.2 PKS 0447–439

PKS 0447–439 is a BLL with a redshift of $z = 0.107$, absolute visual magnitude $V = 15.24$, and synchrotron peak frequency of $\nu_{\text{sy}} = 4.47 \times 10^{15}\,\text{Hz}$. This source has also been associated with quasi-periodic oscillations in the γ-ray regime (Ait Benkhali et al., 2020).

For this source, a spectropolarimetric observation was performed on 2017 February 21 during an elevated γ-ray state, as shown in Figure A.3. The optical spectropolarimetric observation is given in Figure A.4, and revealed an averaged degree of polarisation of $\langle \Pi \rangle = 1.74 \pm 1.72\,\%$ and an averaged polarisation angle of $151.06 \pm 45.48°$.

A.1.3 PKS 1454–354

PKS 1454–354 is a distant BLL with redshift $z = 1.424$, absolute visual magnitude $V = 19.50$ and synchrotron peak frequency $\nu_{\text{sy}} = 1.01 \times 10^{13}\,\text{Hz}$. Renewed γ-ray activity was detected in 2021 June, with daily averaged fluxes increased by a factor of $\sim$75 when compared to the average flux recorded in the 4FGL-DR2 catalogue (D'Ammando and Garrappa, 2021; Garrappa, 2021). The γ-ray lightcurve during the flaring period is

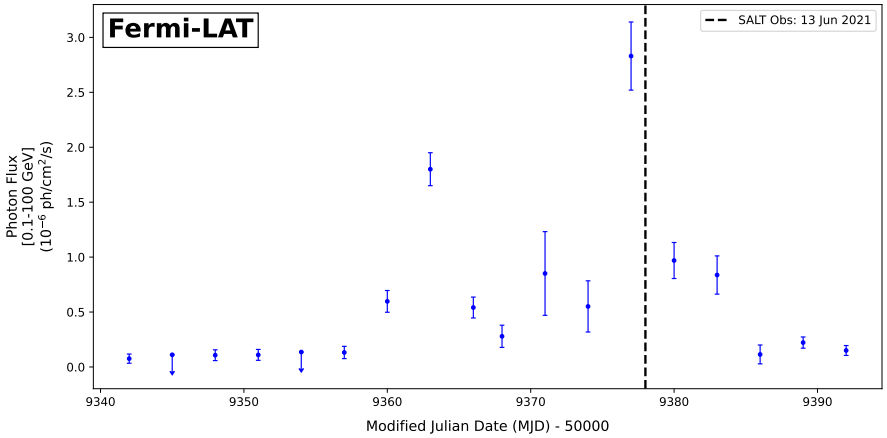

Figure A.5: Gamma-ray lightcurve for the BLL, PKS 1454–354, where the black dashed line indicates the date of the SALT spectropolarimetric observation.

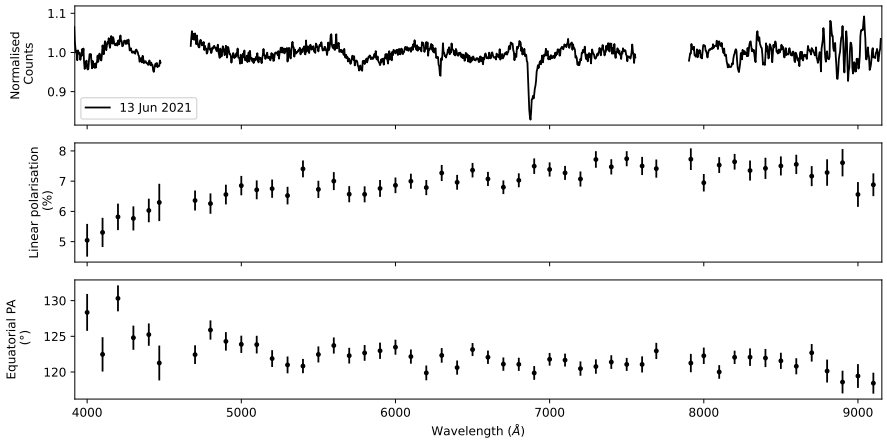

Figure A.6: Spectropolarimetric observations for the BLL, PKS 1454–354, observed on 2021 June 13. The top panel gives the normalised counts spectra of the observation, where the middle and bottom panels give the degree of linear polarisation, and the equatorial polarisation angle, respectively. The gaps in the spectrum in the top panel from $\lambda = 4480 - 4670$ Å, $\lambda = 7720 - 7900$ Å, and $\lambda = 7560 - 7720$ Å are due to the removal of the two chip gaps of the CCD detector mosaic, and a skyline, respectively.

shown in Figure A.5.

To observe this source during its flaring state, an optical spectropolarimetric observation was taken on 2021 June 13 (Figure A.6), just after the peak of the flare. It revealed a fairly low averaged degree of polarisation of $\langle \Pi \rangle = 6.89 \pm 0.64\,\%$ and averaged polarisation angle of $122.33 \pm 2.28°$, taken from $\lambda = 3900 - 9150$ Å.

A.2 Flat-Spectrum Radio Quasars

This section will outline the spectropolarimetric and photometric observational data of six FSRQs (PKS 0035–252, PKS 0346–279, PKS 0837+012, PKS 0907–023, 3C 273, and PKS 1424–418) observed under the SALT transients monitoring campaign.

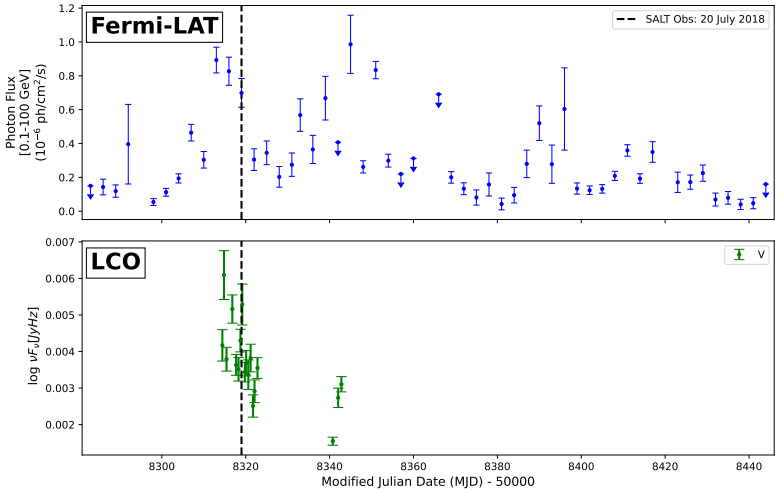

Figure A.7: Gamma-ray (top panel) and optical (bottom panel) lightcurves for the FSRQ, PKS 0035–252, where the black dashed line indicates the date of the SALT spectropolarimetric observation.

A.2.1 PKS 0035–252

PKS 0035–252 is an FSRQ with a redshift of $z = 0.498$, an apparent visual magnitude $V = 17.29$, and a synchrotron peak frequency of $\nu_{\rm sy} = 2.57 \times 10^{12}$ Hz. It was observed to have entered an optical, X-ray, and γ-ray flaring state on 2018 June 30, and reached a daily averaged γ-ray flux of > 120 times that of the average flux reported in the 3FGL catalogue (Angioni et al., 2018; Pacciani and Ambrosino, 2018; Piano et al., 2019).

The γ-ray and optical lightcurves for PKS 0035–252 are given in Figure A.7. The γ-ray lightcurve clearly shows the enhanced activity during the flaring state, and although the optical lightcurve does not provide good coverage, the optical fluxes also seemed to have been enhanced during the flaring event, reaching a maximum of $V = 14.48 \pm 0.12$ on MJD 58315, which decreased to $V = 15.97 \pm 0.08$ later, on MJD 58341.

An optical spectropolarimetric observation was taken on 2018 July 20, after the peak of the γ-ray flare, and is shown in Figure A.8. During this observation, the average degree of polarisation was $\langle \Pi \rangle = 7.31 \pm 0.67\,\%$ with an average polarisation angle of $78.00 \pm 1.40°$, taken from $\lambda = 3900 - 9150$ Å. Two absorption lines were observed in this spectrum; namely [Ne III] at $\lambda = 5797.04 \pm 7.20$ Å, and [O III] at $\lambda = 6549.80 \pm 6.40$ Å. An [Fe VII] emission line was also observed at $\lambda = 8570.40 \pm 4.36$ Å.

A.2.2 PKS 0346–279

PKS 0346–279 is an FSRQ with a redshift of $z = 0.991$, apparent visual magnitude $V = 18.63$, and synchrotron peak frequency of $\nu_{\rm sy} = 1.41 \times 10^{13}$ Hz. This source has been in an extended high state in the γ-ray, X-ray and optical regime since 2018 February (Angioni, 2018; Nesci, 2018a,b). Since 2018, regular outbursts/flares have occurred across the electromagnetic spectrum (e.g. Gokus and Angioni, 2019; La Mura, 2021; Mereu, 2020). The variable γ-ray lightcurve is shown in the top panel of Figure A.9, with the optical data given in the bottom panel of the figure.

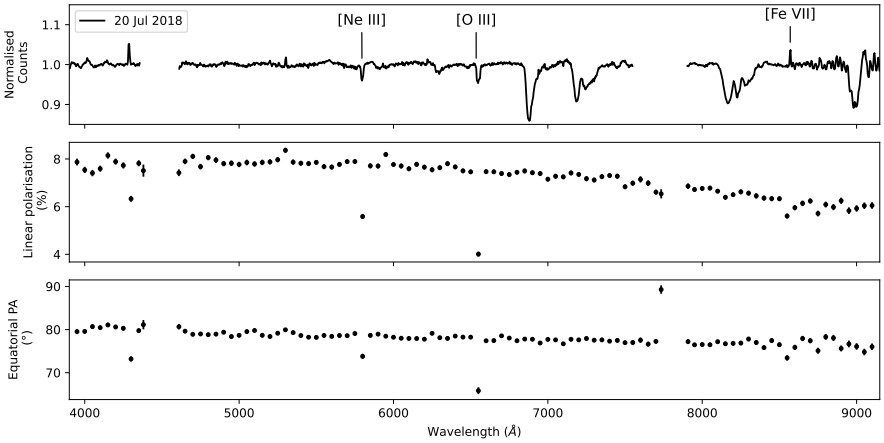

Figure A.8: Spectropolarimetric observation for the FSRQ, PKS 0035–252, observed on 2018 July 20. The top panel gives the normalised counts spectrum of the observation, where the middle and bottom panels give the degree of linear polarisation, and the equatorial polarisation angle, respectively. The gaps in the spectrum in the top panel from $\lambda = 4360 - 4610\,\text{Å}$, $\lambda = 7725 - 7900\,\text{Å}$, and $\lambda = 7550 - 7725\,\text{Å}$ are due to the removal of the two chip gaps of the CCD detector mosaic, and a skyline, respectively.

During two flaring periods (2018 February and 2021 November), optical spectropolarimetric observations were taken for PKS 0346–279, and are shown in Figure A.10. During the first observation on 2018 February 09, the observed average degree of polarisation was $\langle \Pi \rangle = 18.23 \pm 0.93\,\%$, and the average polarisation angle was $116.80 \pm 1.19°$. During the second observation on 2021 November 06, the average degree of polarisation was $\langle \Pi \rangle = 5.23 \pm 1.53\,\%$, with an average polarisation angle of $77.14 \pm 6.37°$ (from $\lambda = 3900 - 9150\,\text{Å}$). In both spectra, a [Mg II] emission line was detected at $\lambda = 5566.70 \pm 37.39\,\text{Å}$.

A.2.3 PKS 0837+012

PKS 0837+012 is an FSRQ with a redshift of $z = 1.123$, apparent visual magnitude $V = 19.09$, and synchrotron peak frequency of $\nu_{\text{sy}} = 3.24 \times 10^{12}\,\text{Hz}$. The source entered an active/high state in the γ-ray regime on 2021 March 01 (MJD 59274), and reached an averaged daily flux $\sim$150 times that of the average flux given in the 4FGL catalogue (Mereu and Fermi Large Area Telescope Collaboration, 2021). This follows after a larger γ-ray flare that occurred in 2020 December (Angioni, 2020), and both these flares can be seen in the γ-ray lightcurve Figure A.11. The optical fluxes shown in the bottom panel of Figure A.11 also show a high flux during the γ-ray flare (with $V = 17.02 \pm 0.21$ on MJD 59289), and decreases after the peak of the flare to an apparent visual magnitude of $V = 17.50 \pm 0.02$ on MJD 59293.

An optical spectropolarimetric observation on 2021 March 16 (Figure A.12) showed that the source had an average degree of polarisation of $\langle \Pi \rangle = 10.69 \pm 1.96\,\%$ (from $\lambda = 3900 - 9150\,\text{Å}$). The polarisation angle at the time of the observation was $132.09 \pm 3.63°$. A [C III] emission line was found at $\lambda = 4053.32 \pm 28.76\,\text{Å}$, as well as a [Mg II] at $\lambda = 5946.96 \pm 10.32\,\text{Å}$.

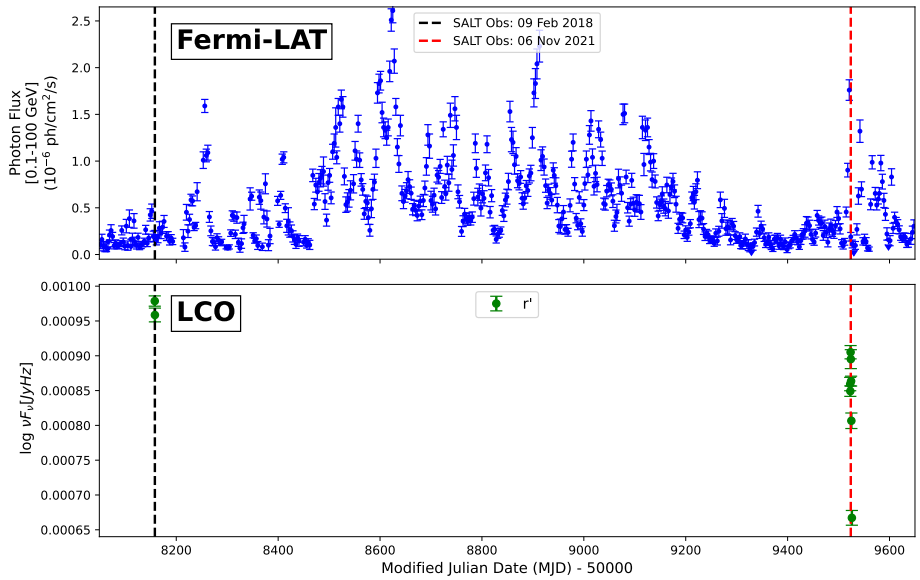

Figure A.9: Gamma-ray (top panel) and optical (bottom panel) lightcurves for the FSRQ, PKS 0346–279, where the black and red dashed lines indicate the dates of the SALT spectropolarimetric observations.

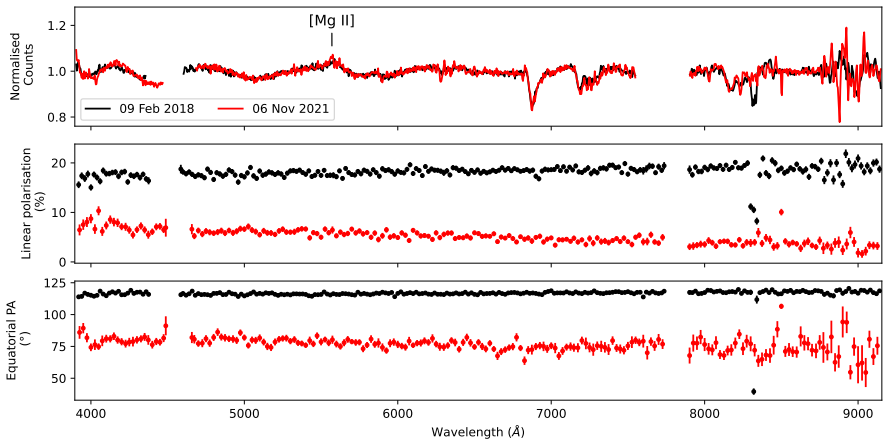

Figure A.10: Spectropolarimetric observations for the FSRQ, PKS 0346–279, observed on 2018 February 09 and 2021 November 06. The top panel gives the normalised counts spectra of the observations, where the middle and bottom panels give the degree of linear polarisation, and the equatorial polarisation angle, respectively. The gaps in the spectra in the top panel from $\lambda = 4360 - 4680$ Å, $\lambda = 7725 - 7900$ Å, and $\lambda = 7550 - 7725$ Å are due to the removal of the two chip gaps of the CCD detector mosaic, and a skyline, respectively.

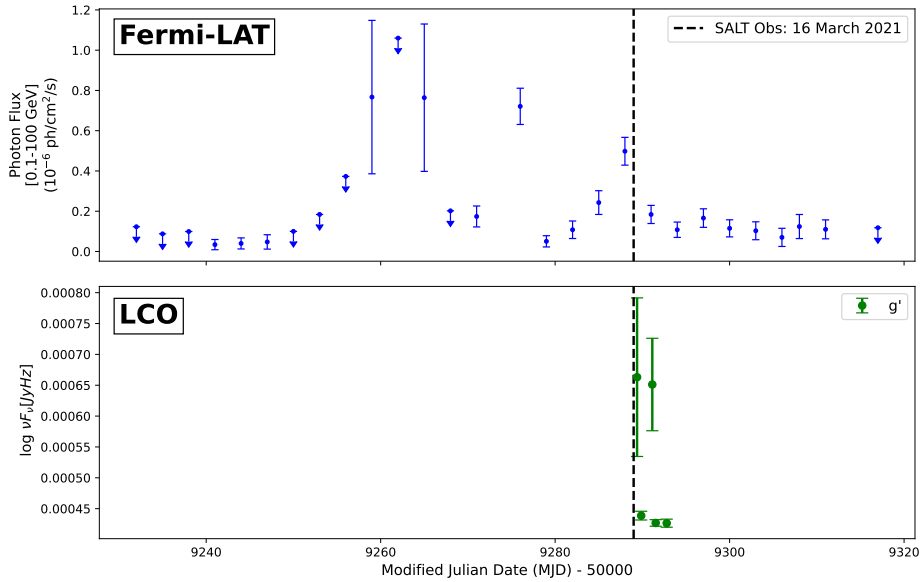

Figure A.11: Gamma-ray lightcurve for the FSRQ, PKS 0837+012, where the black dashed line indicates the date of the SALT spectropolarimetric observation.

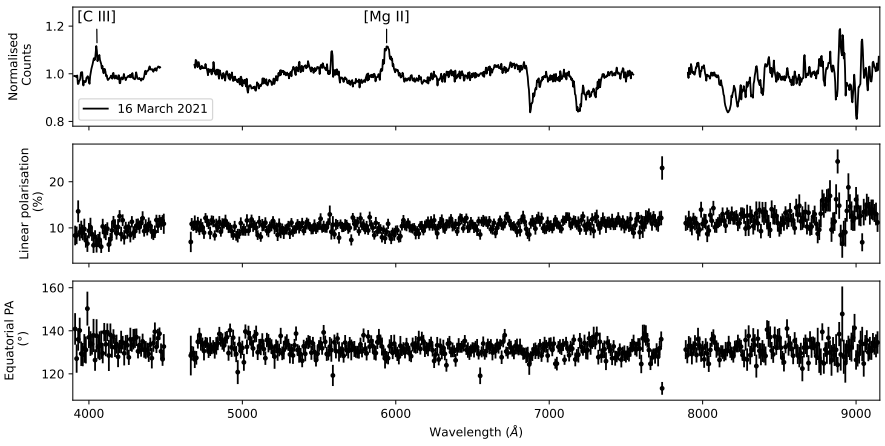

Figure A.12: Spectropolarimetric observations for the FSRQ, PKS 0837+012, observed on 2021 March 16. The top panel gives the normalised counts spectrum of the observation, where the middle and bottom panels give the degree of linear polarisation, and the equatorial polarisation angle, respectively. The gaps in the spectrum in the top panel from $\lambda = 4465 - 4685$ Å, $\lambda = 7725 - 7900$ Å, and $\lambda = 7550 - 7725$ Å are due to the removal of the two chip gaps of the CCD detector mosaic, and a skyline, respectively.

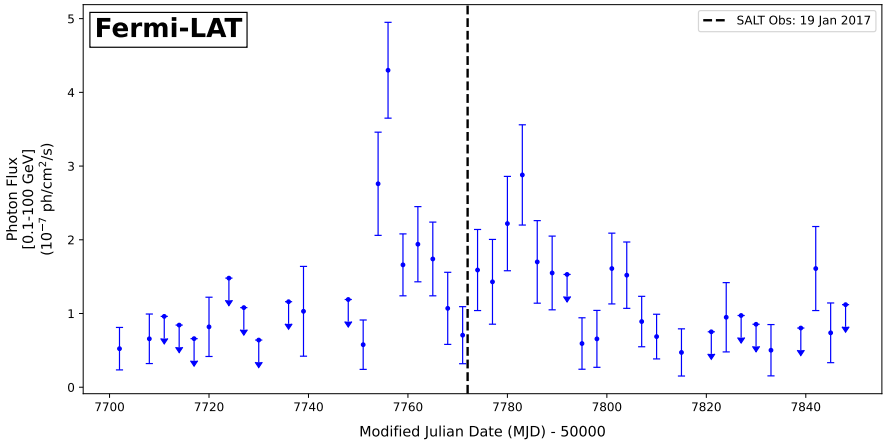

Figure A.13: Gamma-ray lightcurve for the FSRQ, PKS 0907–023, where the black dashed line indicates the date of the SALT spectropolarimetric observation.

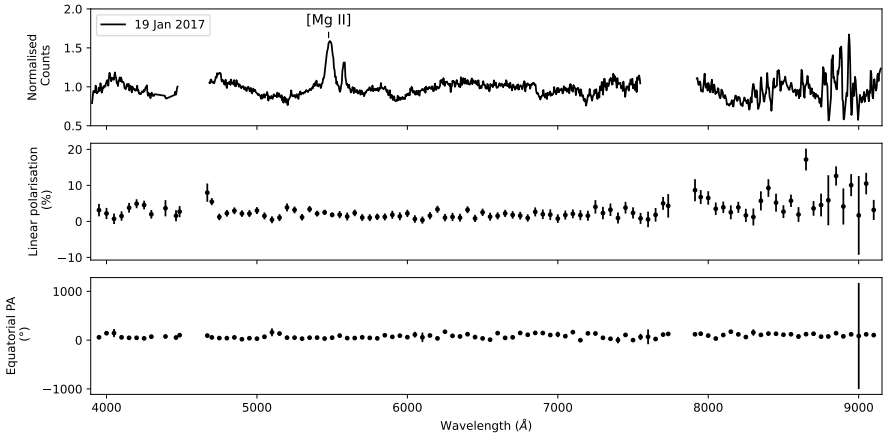

Figure A.14: Spectropolarimetric observations for the FSRQ, PKS 0907–023, observed on 2017 January 19. The top panel gives the normalised counts spectrum of the observation, where the middle and bottom panels give the degree of linear polarisation, and the equatorial polarisation angle, respectively. The gaps in the spectrum in the top panel from $\lambda = 4475 - 4680$ Å, $\lambda = 7725 - 7920$ Å, and $\lambda = 7550 - 7725$ Å are due to the removal of the two chip gaps of the CCD detector mosaic, and a skyline, respectively.

A.2.4 PKS 0907–023

PKS 0907–023 is an FSRQ with a redshift of $z = 0.957$, apparent visual magnitude $V = 18.56$, and synchrotron peak frequency of $\nu_{\rm sy} = 5.56 \times 10^{13}$ Hz. The γ-ray lightcurve is shown in Figure A.13, with the enhanced γ-ray activity visible from $\sim$ MJD 57740 to $\sim$ MJD 57800.

An optical spectropolarimetric observation was taken just after a γ-ray flare, on 2017 January 19 (MJD 57772), as shown in Figure A.14. This observation showed that the source had an averaged degree of polarisation of $\langle \Pi \rangle = 3.40 \pm 3.05\,\%$ and an average polarisation angle of $80.23 \pm 38.80°$ (taken from $\lambda = 3900 - 9150$ Å). A [Mg II] emission line was observed at $\lambda = 5483.61 \pm 5.61$ Å.

A.2.5 3C 273

The FSRQ 3C 273 has a redshift of $z = 0.158$, apparent visual magnitude $V = 14.83$ and synchrotron peak frequency of $\nu_{\rm sy} = 7.00 \times 10^{13}$ Hz. The γ-ray and optical lightcurves are

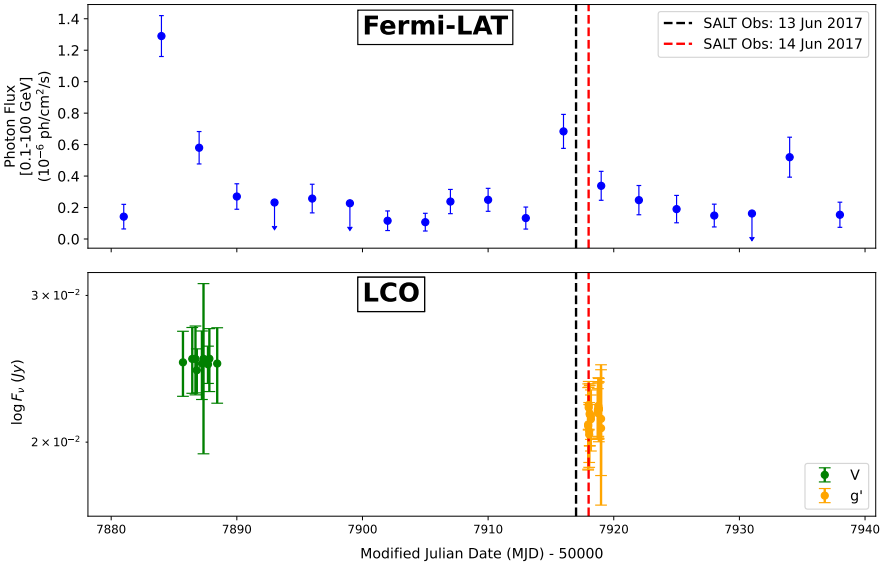

Figure A.15: Gamma-ray (top panel) and optical lightcurves (bottom panel) for the BLL, 3C 273, where the black and red dashed lines indicate the dates of the SALT spectropolarimetric observations.

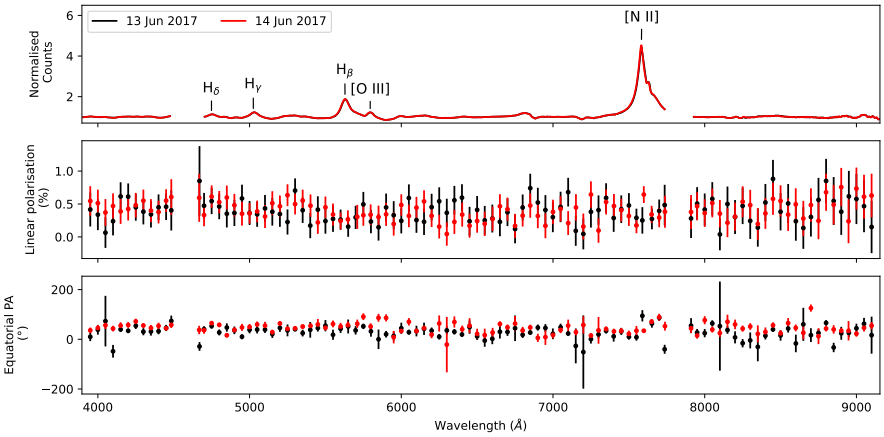

Figure A.16: Spectropolarimetric observations for the BLL, 3C 273, observed on 2017 June 13 and 14. The top panel gives the normalised counts spectra of the two observations, where the middle and bottom panels give the degree of linear polarisation, and the equatorial polarisation angle, respectively. The gaps in the spectra in the top panel from $\lambda = 4480 - 4700$ Å, $\lambda = 7740 - 7925$ Å are due to the removal of the two chip gaps of the CCD detector mosaic.

shown in Figure A.15. The γ-ray lightcurve show low levels of variability, with a small increase in flux between MJD 57910 and MJD 57930, reaching a maximum on MJD 57915 of 6.84×10^{-7} ph cm^{-2} s^{-1}.

Two spectropolarimetric observations were obtained for this source on 2017 June 13 and 14, as shown in Figure A.16. During both of these observations, the thermal emission component was dominant, and extremely low degrees of polarisation were observed, with averages of $\langle \Pi \rangle = 0.40 \pm 0.19\,\%$ and $\langle \Pi \rangle = 0.41 \pm 0.16\,\%$ (from $\lambda = 3900 - 9150$ Å), respectively. The polarisation angle fluctuated from $25.21 \pm 27.06°$ to $43.69 \pm 20.32°$ between the two observations. Five emission lines were observed in the optical spectra, namely H_δ at $\lambda = 4754.60 \pm 12.24$ Å, H_γ at $\lambda = 5030.75 \pm 6.39$ Å, H_β at $\lambda = 5633.38 \pm 2.47$ Å, [O III] at $\lambda = 5798.11 \pm 2.67$ Å, and lastly [N II] at $\lambda = 7596.49 \pm 6.74$ Å.

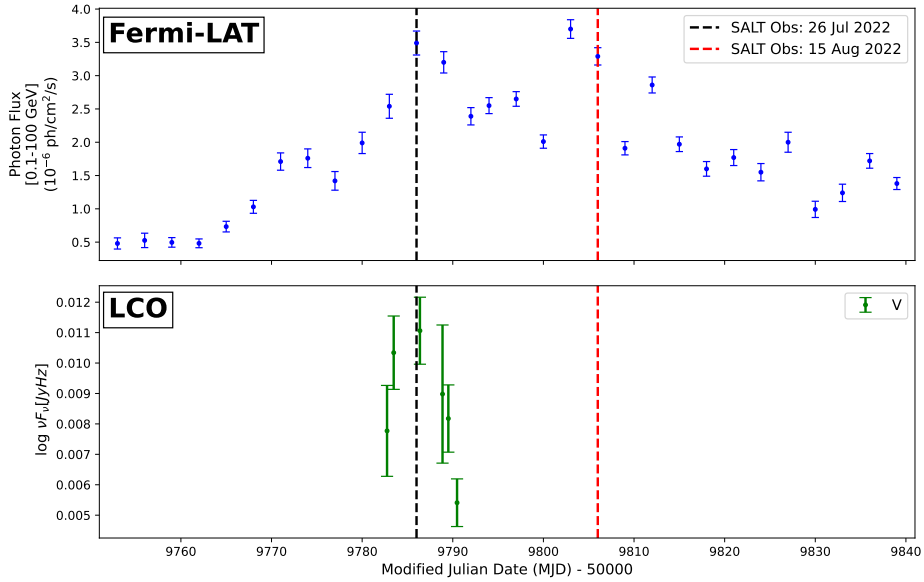

Figure A.17: Gamma-ray (top panel) and optical (bottom panel) lightcurves for the FSRQ, PKS 1424–418, where the black and red dashed lines indicate the dates of the SALT spectropolarimetric observations.

A.2.6 PKS 1424–418

PKS 1424–418 is an FSRQ with a redshift of $z = 1.522$, apparent visual magnitude $V = 17.70$, and synchrotron peak frequency of $\nu_{\rm sy} = 1.40 \times 10^{13}$ Hz. It is a highly variable blazar that is associated with quasi-periodic oscillations (Ren et al., 2022). In 2022 July, the source underwent a steady increase in brightness in the optical regime, coinciding with enhanced γ-ray flaring activity as observed by the *Fermi*-LAT (Jankowsky et al., 2022). In both the optical and γ-ray regimes, the 2022 July flare exceeded the highest historical fluxes recorded for this source. The γ-ray and optical lightcurves during the 2022 flaring period is shown in Figure A.17.

To investigate the polarisation signatures of this source during the 2022 flaring period, two optical spectropolarimetric observations were taken on 2022 July 26 (MJD 59786) and August 15 (MJD 59806), respectively, as shown in Figure A.18. During the first observation, the average degree of polarisation was found to be $\langle \Pi \rangle = 7.05 \pm 0.30\,\%$, taken from $\lambda = 3600 - 6250\,$Å. The average polarisation angle during this observation was $159.82 \pm 4.92°$. During the second observation, the average degree of polarisation decreased to $\langle \Pi \rangle = 3.23 \pm 0.58\,\%$, with an average polarisation angle of $140.54 \pm 4.80°$.

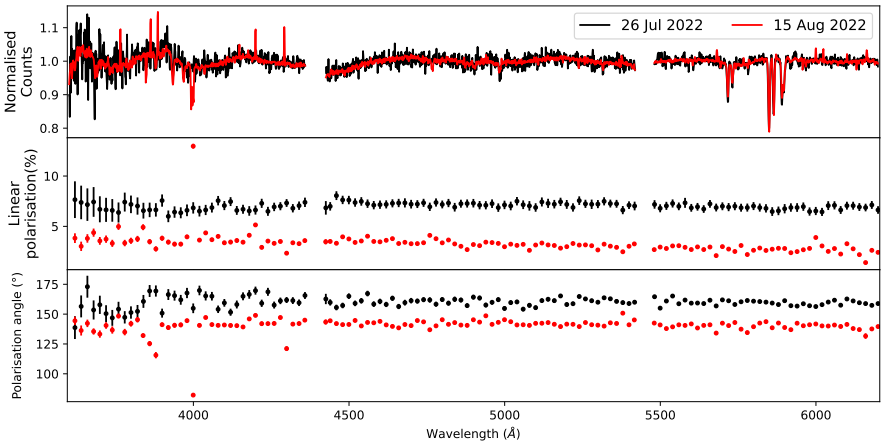

Figure A.18: Spectropolarimetric observations for the FSRQ, PKS 1424–418, observed on 2022 July 26 and 2022 August 15. The top panel gives the normalised counts spectra of the observations, where the middle and bottom panels give the degree of linear polarisation, and the equatorial polarisation angle, respectively. The gaps in the spectra in the top panel from $\lambda = 4360 - 4425$ Å, $\lambda = 5420 - 5480$ Å are due to the removal of the two chip gaps of the CCD detector mosaic.

Appendix B

Conferences and Proceedings

The research done for the duration of this study has been presented at several local and international conferences, and the proceedings submitted are as follows:

- Barnard, J., van Soelen, B., Cooper, J., Britto, R.J., Marais, J.P., van der Westhuizen, I.P., Buckley, D.A.H., Schutte, H.M., Böttcher, M., Vaidya, B., Acharya, S., and Martin-Carrillo, A. (2022), Optical spectropolarimetry monitoring of flaring blazars, *in* A. Prinsloo ed., *The Proceedings of SAIP2019, the 65th Annual Conference of the South African Institute of Physics, online conference*, 20 - 30 July, 2021, pp. 364 – 369.

- Barnard, J., van Soelen, B., Cooper, J., Britto, R.J., Marais, J.P., van der Westhuizen, I.P., Buckley, D.A.H., Schutte, H.M., Böttcher, M., Vaidya, B., Acharya, S., and Martin-Carrillo, (2022), Optical spectropolarimetry observations of the BL Lac-type object PKS 0537–441 after a period of quiescence, *9th Annual Conference on High Energy Astrophysics in Southern Africa (HEASA2021), online conference*, 13 - 17 September, 2021, PoS(HEASA2021)009.

More conference proceedings are expected to result from this work, due to be published in 2023, after having attended the following conferences in 2022:

- The 7th Heidelberg International Symposium on High-Energy Gamma-Ray Astronomy (Γ2022), Barcelona, Spain, 4 - 8 July 2022.

- The 10th Annual Conference on High Energy Astrophysics in Southern Africa (HEASA2022), Bloemfontein, South Africa, 28 September - 01 October 2022.

- The 10th International Fermi Symposium, Johannesburg, South Africa, 9 - 15 October, 2022.

Optical spectropolarimetry monitoring of flaring blazars

J Barnard[1], B van Soelen[1], J Cooper[1], R J Britto[1], J P Marais[1], I P van der Westhuizen[1], D A H Buckley[1,2], H M Schutte[3], M Böttcher[3], B Vaidya[4], S Acharya[4] and A Martin-Carrillo[5]

[1]Department of Physics, University of the Free State, Bloemfontein, 9300, South Africa
[2]South African Astronomical Observatory, PO Box 9, Observatory, Cape Town, 7935, South Africa
[3]Centre for Space Research, North-West University, Potchefstroom 2520, South Africa
[4]Discipline of Astronomy Astrophysics and Space Engineering, Indian Institute of Technology Indore, Khandwa Road, Simrol, Indore 453552, India
[5] Space Science Group, School of Physics, University College Dublin, Belfield, Dublin 4, Ireland

E-mail: ElsJ@ufs.ac.za

Abstract. Blazars are a subclass of radio-loud active galactic nuclei, with relativistic jets closely aligned with the line of sight. These sources are highly variable across all time-scales, and emit non-thermal emission across all wavelength regimes. Blazar-emission is characterised by a double-humped structure in its spectral energy distribution, indicating different emission mechanisms at play. At optical wavelengths, there is an underlying thermal component from the accretion disc, broad line region, and dusty torus, making it difficult to separate the different emission components. As part of a long term campaign, we are undertaking spectropolarimetric observations of flaring blazars, using the Southern African Large Telescope. This could be used to help disentangle the thermal from the non-thermal emission. We present results on the degree of linear polarisation of a selection of fourteen blazars observed between April 2016 and June 2021 , with emphasis on five sources of interest. Three sources, namely 4FGL J0231.2-4745, PKS 0537-441, and PKS 2023-07 were observed during/around periods of increased activity. The degree of linear polarisation for all three of the above sources was observed to be higher close to the peak of activity, and decreased as it returned to quiescence. Two sources, AP Lib (a BLL) and PKS 1034-293 (an FSRQ) was observed continually over a period spanning roughly one year. Both of these sources showed some variability in polarisation over the period in question.

1. Introduction

Active galactic nuclei (AGN), the central active cores of some galaxies, are believed to be powered by accretion of material onto a central supermassive black hole (SMBH). They display broad-band emission across the entire electromagnetic spectrum which, in some cases, outshines the host galaxy itself [1]. AGN present unique observational signatures across the different wavelength bands, which led to many different classes of AGN being identified [2]. The unified model suggests all AGN consist of a central SMBH and an accretion disc, a dusty absorber or torus, broad- and narrow-line regions, and in some cases, a strong, collimated jet [3], and the type of AGN observed depends strongly on the viewing angle of the observer.

Table 1. List of FSRQs and BLLs observed with the SALT . The mean linear polarisation was measured between 4000 Å and 8000 Å.

Target	Type	Obs. Date	Mean Pol. (%)	Target	Type	Obs. Date	Mean Pol. (%)
4FGL J0231.2-4745	FSRQ	22/10/2019	27.5	PKS 0208-512	FSRQ	05/12/2019	27.4
		29/10/2019	08.7			19/12/2019	05.3
AP Lib	BLL	14/05/2020	05.3	PKS 0346-279	FSRQ	09/02/2018	18.2
		08/06/2020	05.0	PKS 0426-380	BLL	17/01/2017	10.8
		24/06/2020	03.4			20/02/2017	10.9
		07/08/2020	08.9	PKS 0447-439	BLL	21/02/2017	05.1
		04/09/2020	06.3	PKS 0537-441	BLL	14/01/2019	37.4
		18/02/2021	03.4			05/03/2019	12.6
		12/03/2021	05.2	PKS 0837+012	FSRQ	16/03/2021	10.6
		04/04/2021	08.5	PKS 0907-023	FSRQ	19/01/2017	05.1
		11/04/2021	09.1	PKS 1034-293	FSRQ	15/05/2020	16.2
		21/04/2021	11.0			08/02/2021	17.9
		02/05/2021	08.6			17/03/2021	13.8
		08/05/2021	09.6			09/04/2021	12.7
		14/05/2021	07.1			05/06/2021	19.1
		03/06/2021	06.2	PKS 2023-07	FSRQ	14/04/2016	27.5
PKS 0035-252	FSRQ	20/07/2018	02.6			04/10/2018	09.1
PKS 0131-522	FSRQ	19/11/2017	07.8	TXS 0506+056	BLL	14/10/2017	10.7
		22/11/2017	06.4			20/10/2017	08.6

Blazars are a radio-loud subclass of AGN, with relativistic jets that propagate in a direction closely aligned with the observer's line of sight (viewing angle $< 10°$). As a result, the non-thermal emission originating in the jet is highly Doppler boosted, making blazars the brightest gamma-ray sources in the extragalactic sky [4]. Blazar emission is extremely variable on all time-scales (on time-scales from minutes up to several years), with dramatic variation present across the entire electromagnetic spectrum. Blazars are subdivided into two different categories, namely BL Lac type objects (BLLs) and Flat-Spectrum Radio Quasars (FSRQs). These can be distinguished by their optical spectral features: FSRQs display strong, broad emission lines , while BLLs display absorption or weak emission lines, or featureless spectra dominated by the non-thermal jet emission [2].

The spectral energy distributions (SEDs) of blazars are characterised by a double-humped structure. The lower-energy component (radio to optical/UV and sometimes soft X-rays) is powered by synchrotron emission from relativistic electrons in the jet. However, both leptonic and hadronic models have been previously postulated for the high-energy (X-ray to gamma-ray) component. The leptonic model assumes that the high-energy emission is dominated by Compton scattering of low-energy photons, whereas the hadronic model assumes that the high-energy component is produced through proton-synchrotron radiation or photomeson processes [4]. At optical wavelengths, there is also an underlying thermal contribution originating from the accretion disc, dusty torus, broad-line region (BLR) and host galaxy [5]. Since both the leptonic and hadronic models are able to reproduce blazar SEDs, separating the emission regions can be very difficult.

Polarimetry can be used as a diagnostic tool to disentangle the emission components in blazar SEDs. In the optical, it serves as a tool to separate the thermal (non-polarised) contributions from the non-thermal (polarised) contributions, allowing constraints to be placed on the jet's magnetic field structure, the non-thermal electron population, and the state of the accretion disc [5]. Here we present optical spectropolarimetry observations of a selection of blazars observed with the Southern African Large Telescope (SALT).

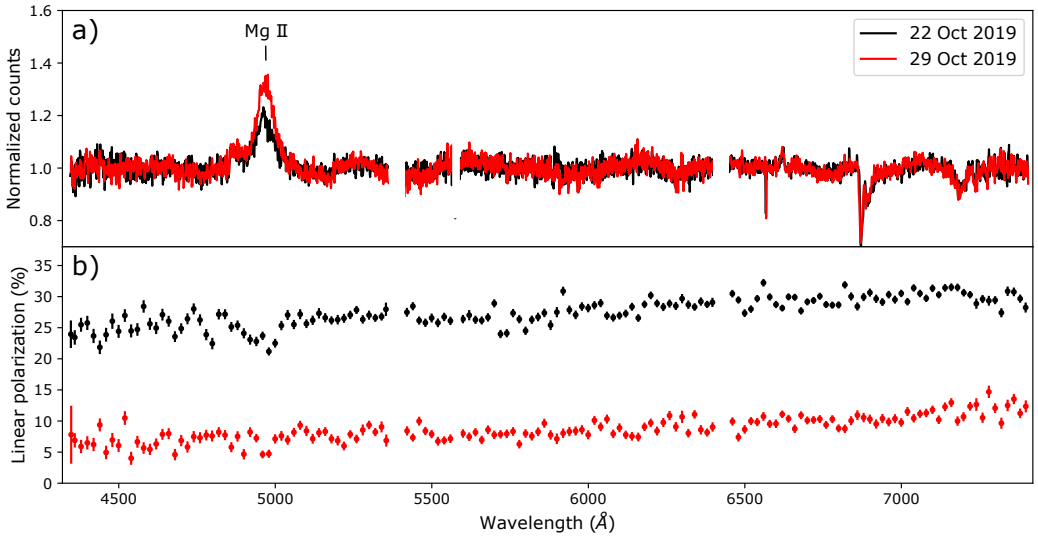

Figure 1. Spectropolarimetry observations of 4FGL J0231.2-4745 taken around a period of increased activity, where a) is the spectra and b) the observed degree of linear polarisation.

2. Observations

The spectropolarimetry observations (listed in Table 1) were taken with the SALT to observe blazars in different states, as well as track the long-term evolution of the degree of polarisation in both BLLs and FSRQs. The observations were performed using the Robert Stobie Spectrograph (RSS) in spectropolarimetry LINEAR mode to measure the degree of linear polarisation [6, 7]. The sources were observed using either the pg0300 grating (with a resolving power of $R = 190$–560 from 3400 Å to 9867 Å) or with two orientations of the pg0900 grating ($R = 620$–1655 from 3750 Å to 9000 Å), with either the argon or thorium-argon arc lamp used for wavelength calibration.

Data reduction was performed using a modified version of the POLSALT reduction pipeline (https://github.com/saltastro/polsalt.git). The modification allowed the wavelength calibration to be performed using the IRAF/NOAO package (http://ast.noao.edu/data/software). Additional cosmic-ray cleaning was performed in PYTHON using the LACOSMIC package (https://github.com/larrybradley/lacosmic.git). All other reductions followed the standard procedure given by the POLSALT pipeline. The two larger spaces in the spectra are due to gaps in the CCD detector mosaic, and the smaller missing region at ∼5600 Å is due to the removal of a skyline.

3. Results

3.1. Flaring Blazars

Figures 1 - 3 show the spectropolarimetry results on three blazars during both flaring and/or quiescent state. The spectra are normalised with respect to counts, and the degree of linear polarisation is represented as a percentage. Using the normalised spectra allows us to show the relative change in the emission/absorption line strengths. 4FGL J0231.2-4745 (Figure 1) was observed twice around a period of increased gamma-ray, X-ray and optical emission [8, 9, 10], where the gamma-ray flux increased by a factor of ∼60 with respect to the reported catalogue value [8] on 2019 October 19. The observations showed a significant decrease in linear polarisation from the first observation on 2019 October 22 to the second a week later (2019 October 29). There is also an increase in the equivalent width of the Mg II line, which indicates

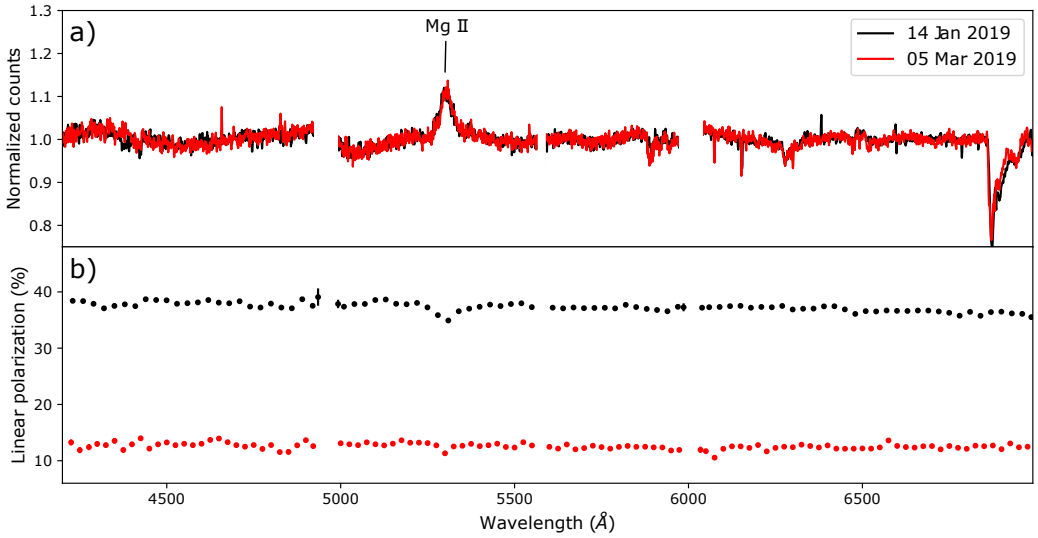

Figure 2. Spectropolarimetry observations of PKS 0537-441 taken around a period of increased activity, where a) is the spectra and b) the observed degree of linear polarisation.

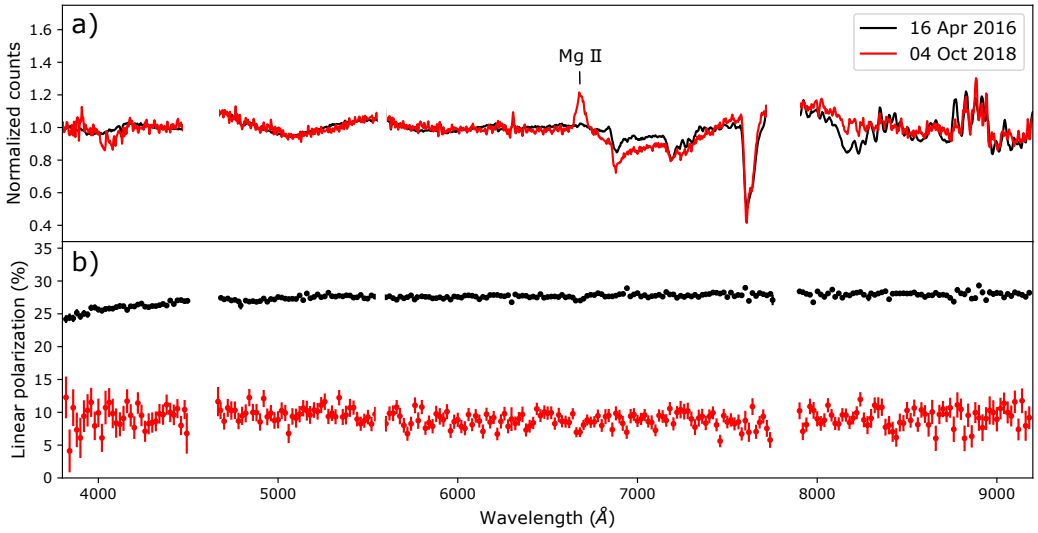

Figure 3. Spectropolarimetry observations of PKS 2023-07 taken during a flaring and non-flaring state, where a) is the spectra and b) the observed degree of linear polarisation.

a decrease of the non-thermal emission component between the two observations. In FSRQs, the non-thermal, beamed jet-emission often outshines the host galaxy, BLR, and accretion disc. Hence, a strengthening of the non-thermal component during a flare can cause the emission lines originating in these regions to appear less prominent/weaker than during quiescence [2].

PKS 0537-411 (Figure 2) was observed at the start of a period of increased activity following a quiescent period [11]. The two observations were taken 50 days apart. While the observations show no significant change in the equivalent width of the Mg II line, they show a large change in the degree of linear polarisation (decrease from 37% to 13%). The publicly available data from the monitoring of *Fermi*-LAT sources indicated that, in the weekly bins, there

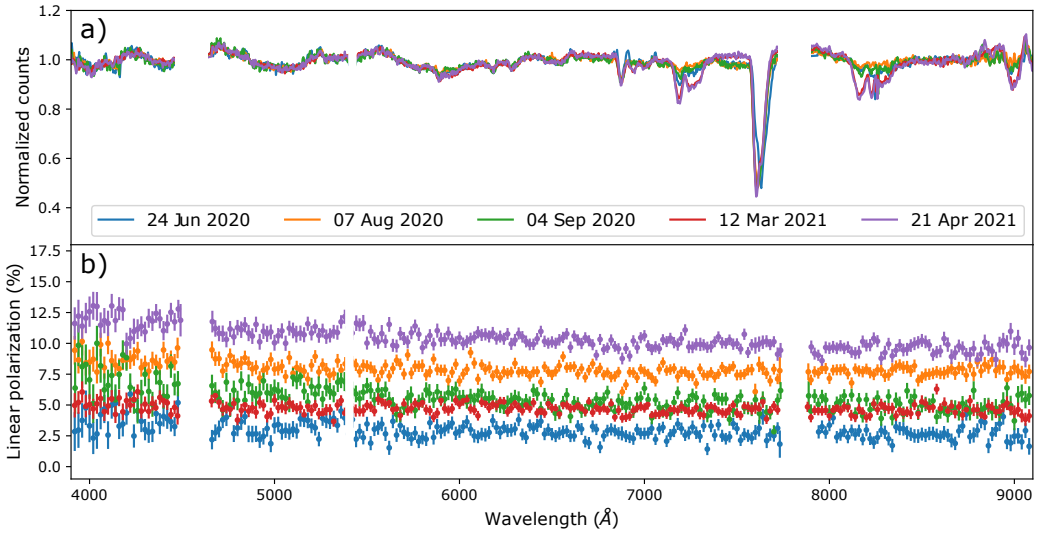

Figure 4. Long-term spectropolarimetry observations of AP Lib, a BLL. Observations were taken from 14 May 2020 to 3 June 2021 . Here, only a selection of five observations are shown, with each colour representing an observation date, and a) is the spectra and b) the observed degree of linear polarisation.

was a decrease in the flux (>100 MeV) by a factor of ∼1.8 between these two observations (https://fermi.gsfc.nasa.gov/ssc/data/access/lat/msl_lc/).

PKS 2023-07 (Figure 3) was observed once during a flaring state in April 2016 [12], and once during a quiescent state in October 2018. The optical spectrum clearly shows the switch from being dominated by the non-thermal synchrotron emission where no emission lines are observable during the flare, to showing a Mg II emission line during the quiescent state. The degree of polarisation changed by roughly 18% between the two observations.

3.2. Long-term Monitoring

Long-term monitoring of AP Lib (a BLL) and PKS 1034-293 (an FSRQ) has been performed over approximately one year (May 2020 to June 2021) to study the long-term variation in polarisation. Although there were no large changes in the degree of linear polarisation for either of the sources, there was definite variation over time. The spectropolarimetry results are shown in Figures 4 and 5, respectively, where the spectra are normalised with respect to counts.

4. Discussion and Conclusion

To date, the degree of polarisation has been successfully measured for fourteen blazars, both BLLs and FSRQs, during both flaring and/or non-flaring states. For the two sources presented in Figures 1 - 2, observations were taken during periods of increased activity. For these sources, the degree of linear polarisation decreased substantially after the initial observations. The blazar presented in Figure 3 was observed during a flare, along with a follow-up observation taken some time later during quiescence. We expect the thermal component to contribute more at shorter wavelengths. Therefore, there should be a general decrease in the degree of linear polarisation towards the bluer end, and it appears to be the case for the three blazars in question.

For the two long-term sources, both AP Lib (BLL, Figure 4) and PKS1034-293 (FSRQ, Figure 5), displayed some variability in polarisation over the observational period. The FSRQ source had a higher mean polarisation (12-20%) than the BLL (3-12%), while the BLL showed

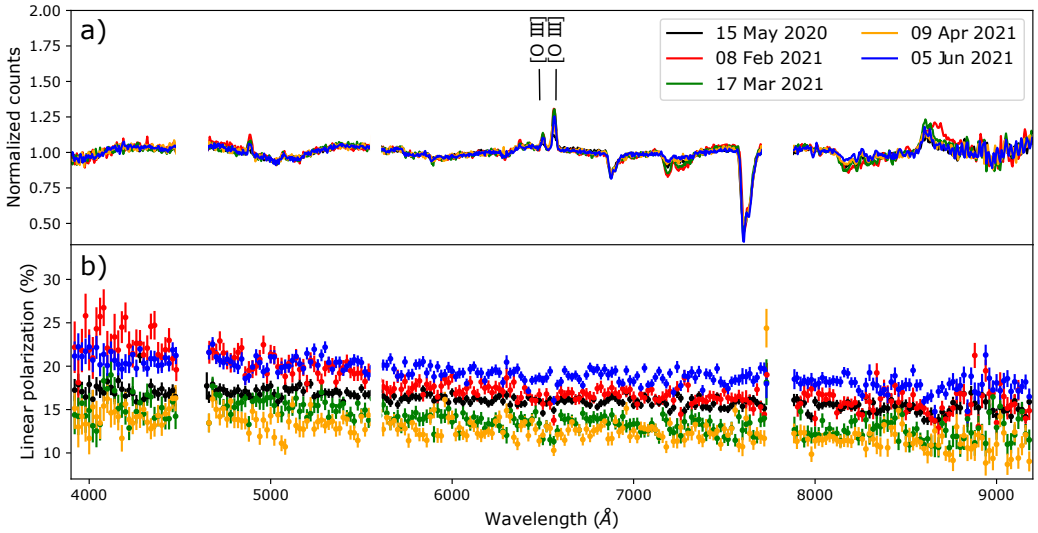

Figure 5. Long-term spectropolarimetry observations of PKS 1034-293, an FSRQ. Observations were taken from 14 May 2020 to 05 June 2021, with each colour representing an observation date, and a) is the spectra and b) the observed degree of linear polarisation.

a slightly larger range in polarisation. However, this may be due to observational bias and can only be confirmed through more observational data.

These are the initial results from an ongoing, long-term project. The variation found in the degree of linear polarisation will now be compared to the multi-wavelength behaviour of these sources. The change in the measured polarisation could be used in the modelling of the blazars' jet-behaviour.

Acknowledgments

All of the observations reported in this paper were obtained with the Southern African Large Telescope (SALT) under program 2018-2-LSP-001 (PI: DAH Buckley) and program 2019-2-MLT-001 (PI: B van Soelen).

References

[1] Padovani P 2017 *Front. Astron. Space Sci.* **4** 12-18
[2] Beckmann V and Shrader, C R 2012 *Active Galactic Nuclei* (Weinheim: Wiley)
[3] Urry C M and Padovani P 1995 *PASP* **107** 803-45
[4] Böttcher M 2019 *Galaxies* **7** 20-56
[5] Böttcher M, van Soelen B, Britto R J, Buckley D A H, Marais J P and Schutte H 2017 *Galaxies* **5** 52-58
[6] Burgh E B, Nordsieck K H, Kobulnicky H A, Williams T B, O'Donoghue D, Smith M P and Percival J W 2003 *SPIE* **4841** 1463-71
[7] Kobulnicky H A, Nordsieck K H, Burgh E B, Smith M P, Percival J W, Williams T B and O'Donoghue D 2003 *SPIE* **4841** 1634-44
[8] Principe G and Angioni, R 2019 *ATel* **13209**
[9] D'Ammando F, Principe G and Angioni, R 2019 *ATel* **13212**
[10] Pursimo T, Martikainen J and Ojha R 2019 *ATel* **13248**
[11] Nesci R and Ojha R 2019 *ATel* **12357**
[12] Emery G, Jankowsky F, Lenain J P, Marais J P, Mbonani T, Romoli C, van Soelen B, Wierzcholska A, Zacharias M and Meyer M 2019 *Proc. of the 36th Int. Cosmic Ray Conf. (Madison)* PoS(ICRC2019) 669

PROCEEDINGS OF SCIENCE

Optical spectropolarimetry observations of the BL Lac-type object PKS 0537−441 after a period of quiescence

J Barnard,[a,*] **B van Soelen,**[a] **J Cooper,**[a] **R J Britto,**[a] **J P Marais,**[a] **I P van der Westhuizen,**[a] **D A H Buckley,**[a,b] **H M Schutte,**[c] **M Böttcher,**[c] **B Vaidya,**[d] **S Acharya**[d] **and A Martin-Carrillo**[e]

[a] *Department of Physics, University of the Free State, Bloemfontein, South Africa*
[b] *South African Astronomical Observatory, Cape Town, South Africa*
[c] *Center for Space Research, North West University, Potchefstroom, South Africa*
[d] *Discipline of Astronomy Astrophysics and Space Engineering, Indian Institute of Technology Indore, Indore, India*
[e] *Space Science Group, School of Physics, University College Dublin, Dublin, Ireland*

E-mail: ElsJ@ufs.ac.za

Blazars are a radio-loud subclass of active galactic nuclei with relativistic jets closely aligned with our line of sight. They are highly variable across all time-scales, and display rapid flares across multiple wavelength bands. At optical wavelengths, the observed emission is a superposition of non-thermal emission arising from the jet, and thermal emission that originates from the accretion disc, broad-line region, dust torus and host galaxy. Optical spectropolarimetry observations of blazars can be used to disentangle the thermal non-polarised and non-thermal polarised emission components in blazar emission during flaring and quiescent states. As part of a long-term monitoring campaign, spectropolarimetry observations have been taken with the Southern African Large Telescope of a selection of blazars during periods of increased activity. Here we focus on spectropolarimetry results and *Fermi*-LAT light curve of the BL-Lac type object PKS 0537−441 observed around a period of increased activity. It was observed to be active at both optical and gamma-ray energies after recovering from a faint state in late 2018. Spectropolarimetry observations were taken twice, with the degree of linear polarisation being between 35% and 40% during the first observation, and between 10% and 15% during the second, while there was no significant change in the strength of the emission line.

**** High Energy Astrophysics in Southern Africa (HEASA2021) ****
**** 13 - 17 September, 2021 ****
**** Online ****

[*] Speaker

© Copyright owned by the author(s) under the terms of the Creative Commons Attribution-NonCommercial-NoDerivatives 4.0 International License (CC BY-NC-ND 4.0).

1. Introduction

The central active cores of some galaxies, or active galactic nuclei (AGN), which are powered by the accretion of material onto a central supermassive black hole, display non-thermal, broad-band emission across the entire electromagnetic spectrum [1]. Blazars are a radio-loud subclass of AGN with a prominent jet-emission component, as the jet propagates in a direction that is within $\sim 10^{\circ}$ of the observer's line of sight, resulting in highly Doppler boosted emission. Blazar emission is extremely variable on minute up to year time-scales, with large variations observable across multiple wavelength bands [2].

Blazar spectral energy distributions (SEDs) typically consist of two broad, non-thermal components. The lower-energy component spans the radio to optical/UV and sometimes soft X-ray wavelength bands. Two different emission components contribute in the lower-energy component: a non-thermal, polarised component and an underlying thermal, non-polarised component. The non-thermal component is produced by synchrotron emission from the jet, while the underlying thermal emission originates from the accretion disc, dust torus, broad-line region (BLR) and host galaxy itself [3]. The higher-energy component, extending from the X-ray to the gamma-ray wavelength bands, can be reproduced by both leptonic and hadronic models [3].

For flaring blazars, optical polarimetry can serve as a diagnostic tool that separates the thermal and non-thermal contributions from one another. This, in turn, allows for constraints to be placed on various SED- and jet-model parameters [4]. Here we present optical spectropolarimetry observations of a blazar, PKS 0537−441, obtained around a period of increased gamma-ray activity, following a quiescent state [5]. These observations form part of a long-term observing campaign that aims at monitoring the optical spectropolarimetric behaviour of a large selection of blazars.

2. Observations

Spectropolarimetry observations were undertaken with the Southern African Large Telescope (SALT) under the long-term transient observing programme 2018-2-LSP-001, that observes various transients, including novae, gamma-ray bursts, cataclysmic variables, and flaring blazars [4]. In the case of blazars, observations are normally triggered by an increase in gamma-ray activity detected by the *Fermi* Large Area Telescope (LAT). From 2016 April to 2021 May, the transient programme has collected SALT spectropolarimetry observations of 21 different blazars, consisting of 14 Flat-Spectrum Radio Quasars (FSRQs), 6 BL Lac type objects (BLLs), and 1 Blazar Candidate of Uncertain Type (BCU). In the following we limit the discussion to one BLL observed during a period of increased activity as it was recovering from a faint state, namely PKS 0537−441 ($z = 0.894$) [6].

2.1 Optical Spectropolarimetry

The SALT observations were performed using the Robert Stobie Spectrograph (RSS) in spectropolarimetry LINEAR mode to measure the degree of linear polarisation [7, 8]. Data reduction was performed using a modified version of the POLSALT reduction pipeline,[1] which allows the wave-

[1] https://github.com/saltastro/polsalt.git

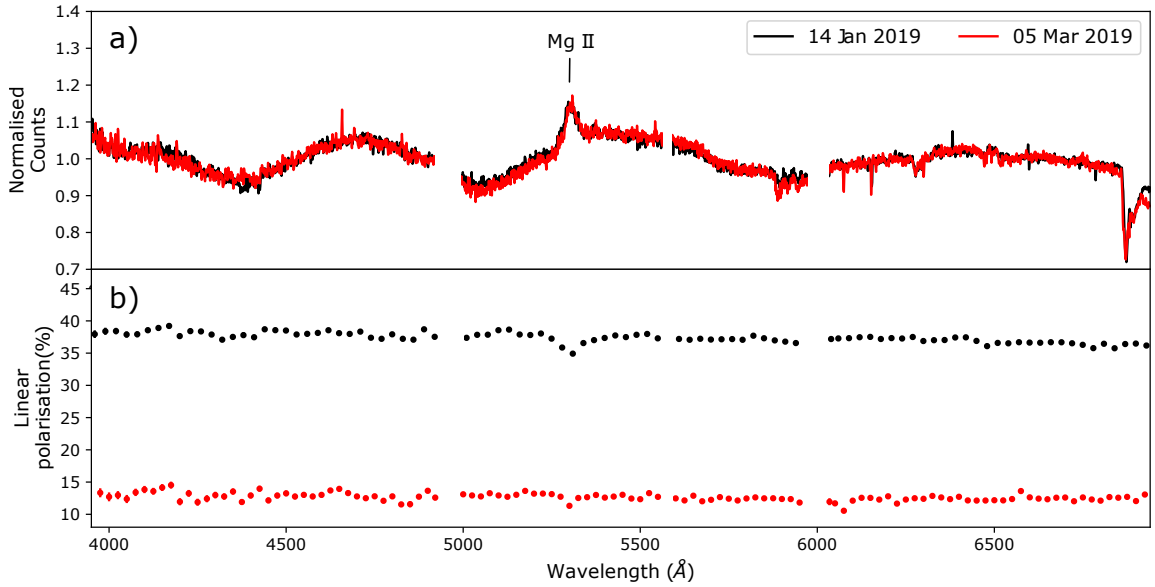

Figure 1: Spectropolarimetry observations of PKS 0537−441 taken around a period of increased activity after quiescence, where (a) is the normalised counts, and (b) the observed degree of linear polarisation.

length calibration to be performed using the IRAF/NOAO package.[2] After the wavelength calibration, the modified pipeline performs additional cosmic-ray cleaning using the LACOSMIC package.[3] The spectra in Figure 1 show two empty regions due to the chip gaps, and a smaller gap at ~5600 Å due to the removal of a strong skyline.

The spectropolarimetry observation of the BLL was performed using the pg0900 grating at an angle of 14.375°, covering a wavelength range from 4500 Å to 7500 Å (with a resolving power of $R = 870 - 1200$). For wavelength calibration, the Argon arc lamp was used.

2.2 Gamma-ray Observations

The *Fermi*-LAT gamma-ray light curves were obtained from the *Fermi*-LAT Light Curve Repository (LCR).[4] The data for PKS 0537−441 was obtained with a 3-day binned data cadence, within an energy range of 0.1 - 100 GeV. The minimum detection significance, or upper limit, was set at a Test Statistic (TS) value of 4 ($\approx 2\sigma$), and the spectral fitting was done with a free photon index.

3. Results

Figure 1 shows the spectropolarimetry results of PKS 0537−441 after the target has recovered from a quiescent state (since 2018 December 13, MJD 58465) and showed activity in both optical and gamma-ray since [5]. The degree of linear polarisation during the first observation was between 35% and 40%. Seven weeks later, the degree of polarisation was observed to have decreased to between

[2]http://ast.noao.edu/data/software
[3]https://github.com/larrybradley/lacosmic.git
[4]https://fermi.gsfc.nasa.gov/ssc/data/access/lat/LightCurveRepository/

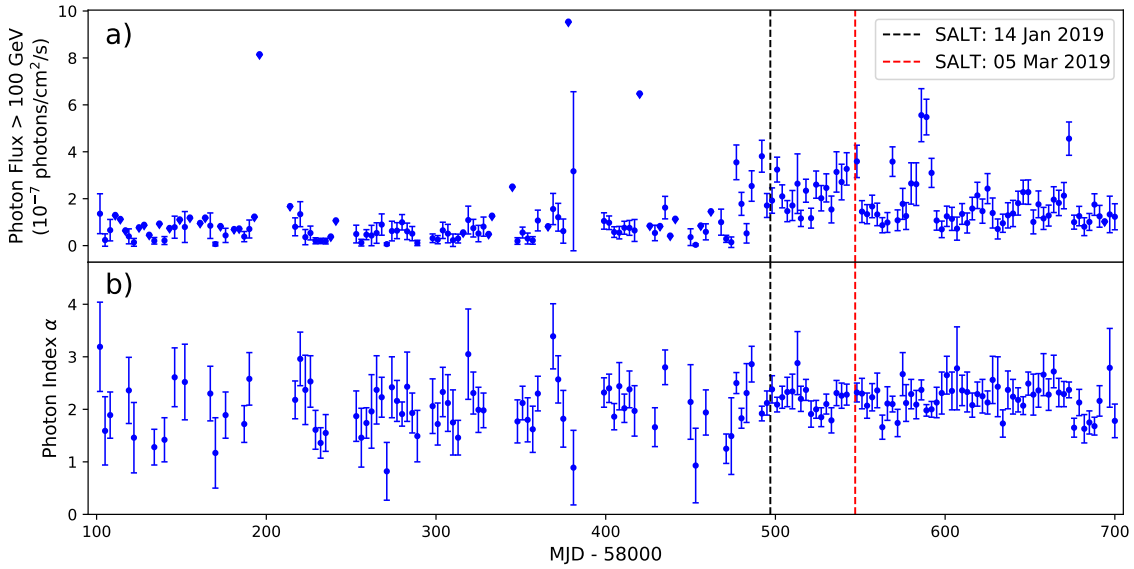

Figure 2: The *Fermi*-LAT light curve (a), and photon spectral index (b) for PKS 0537−441. The flux was measured at $E > 100$ GeV in 3-day bins, spanning the period of 2017 December 15 to 2019 August 05 (MJD 58102 to 58700). The dashed lines in (a) indicate the dates at which the SALT spectropolarimetry observations were taken.

10% and 15%, thus showing substantial variability. The *Fermi*-LAT light curve (Figure 2) spanning a period of 2017 December – 2019 August clearly shows the transition from a quiescent to an active state, increasing from an average photon flux ($E > 100$ GeV) of below 1×10^{-7} photons cm^{-2} s^{-1} to a varying flux of up to six times higher. On 2019 January 14 (MJD 58497), the gamma-ray photon flux ($E > 100$ GeV) reached $(1.92 \pm 0.54) \times 10^{-7}$, and reached $(3.36 \pm 0.771) \times 10^{-7}$ photons cm^{-2} s^{-1} on 2019 March 05 (MJD 58547). Hence, there is an increase in the gamma-ray photon flux while a decrease in optical polarisation is observed.

4. Discussion and Conclusion

For the BLL, PKS 0537−441, SALT spectropolarimetry observations were performed during a period of increased gamma-ray and optical activity following a period of quiescence (see Figure 1). It can be seen from Figure 1 that the degree of linear polarisation has decreased between the two observations. The gamma-ray light curve (Figure 2) obtained from the *Fermi* LCR show the increased gamma-ray activity during the period in question. This trend is in agreement with what is known about blazar jets: non-thermal synchrotron emission in the jet increases due to turbulence in jet's magnetic field, and therefore increases degree of linear polarisation. Hence, polarisation studies can link directly to the jet's magnetic field structure and can place constraints on model parameters.

These observations form part of a long-term monitoring campaign that aims at contemporaneous, multi-wavelength observations of blazars during both flaring and quiescent states in an attempt

to gain a better understanding of blazar jets, the jet's magnetic field, the state of the accretion discs, as well as the nature of the electron population in the jet.

Acknowledgments

All of the spectropolarimetry observations reported in this paper were obtained with the Southern African Large Telescope (SALT) under program 2018-2-LSP-001 (PI: DAH Buckley). B. van Soelen acknowledges support by the National Research Foundation of South Africa (Grant Number: 116300)

References

[1] Padovani P 2017 *Front. Astron. Space Sci.* **4** 12-18

[2] Beckmann V and Shrader, C R 2012 *Active Galactic Nuclei* (Weinheim: Wiley)

[3] Böttcher M, Reimer A, Sweeney K and Prakash A 2013 *ApJ* **768**

[4] Böttcher M, van Soelen B, Britto R J, Buckley D A H, Marais J P and Schutte H 2017 *Galaxies* **5** 52-58

[5] Nesci R and Ojha R 2019 *ATel* **12357**

[6] Mao L S 2011 *New Astronomy* **16** 8

[7] Burgh E B, Nordsieck K H, Kobulnicky H A, Williams T B, O'Donoghue D, Smith M P and Percival J W 2003 *SPIE* **4841** 1463-71

[8] Kobulnicky H A, Nordsieck K H, Burgh E B, Smith M P, Percival J W, Williams T B and O'Donoghue D 2003 *SPIE* **4841** 1634-44